Design and kinematic analysis of a cable-driven anthropomimetic robotic arm

Mustafa Shabbir Kurbanhusen

2008

Mustafa, S. K. (2008). Design and kinematic analysis of a cable-driven anthropomimetic robotic arm. Doctoral thesis, Nanyang Technological University, Singapore.

https://hdl.handle.net/10356/6172

https://doi.org/10.32657/10356/6172

Design and Kinematic Analysis of a Cable-Driven Anthropomimetic Robotic Arm

Mustafa Shabbir Kurbanhusen

School of Mechanical & Aerospace Engineering

A thesis submitted to the Nanyang Technological University
in fulfillment of the requirement for the degree of
Doctor of Philosophy

2008

Abstract

In recent years, robotic arms are being realized as potential tools to help the elderly and disabled people in gaining some independence and improving their quality of life. These assistive robotic arms are mostly serial rigid-link arms with actuators mounted onto the joints, and are designed to perform assistive tasks with the end-effector. However, the rigid-link arms are massive with high moments of inertia, and therefore unsafe for the users who are within the working envelopes. The objective of this research is to design and develop a robotic arm that is light-weight, and having similar working envelope as the human arm.

In this report, the design and kinematic analysis of the robotic arm are presented. Based on the *anthropomimetic* design approach, three basic cable-driven modules are proposed for the 3-DOF shoulder joint, the 1-DOF elbow joint and the 3-DOF wrist joint. These cable-driven joint modules are parallel mechanisms with the joints at the centre and the driving cables at the side, resulting in a unique hybrid configuration. The basic modules are then assembled to form a 7-DOF cable-driven anthropomimetic robotic arm. For the forward displacement analysis, the closed-form solutions for the shoulder and wrist modules are obtained. A task decomposition approach with a dimension reduction optimization technique is proposed for the inverse displacement analysis of the 7-DOF cable-driven robotic arm. Convex theory is applied to evaluate the positive tension conditions of the cable-driven joint modules. The orientation workspace of the 3-DOF shoulder/wrist modules is obtained using an equi-volumetric partition approach based on the T-&-T angle parameterization. It is found that the proposed approach provides an effective way in representing the workspace boundaries and in generating the human joint workspace templates. Using these templates, a joint-level design optimization is carried out to synthesize a 7-DOF robotic arm having a workspace that closely matches the workspace of human arm. Calibration is also addressed to improve the positioning accuracy of the 7-DOF arm. Linear self-calibration models based on differential kinematics are formulated for the cable-driven joint modules, while a linear calibration model is formulated based on *product-of-exponential* (POE) formula for the complete 7-DOF arm assembly.

A prototype of the synthesized 7-DOF cable-driven robotic arm is then developed for experimental investigations. The dimensions of the 7-DOF prototype arm are similar to the human arm. The arm weighs about 1 kg, with a payload of 5 kg and a repeatability of $\pm 2.5mm$ at the tool-tip. From experimental studies, the proposed calibration algorithm is shown to be effective as the errors of the 7-DOF arm are precisely recovered with a minimum of 15 measurement poses, resulting in a positioning accuracy of $5mm$.

"It is not the critic who counts, not the man who points out how the strong man stumbled, or where the doer of deeds could have done them better. The credit belongs to the man who is actually in the arena; whose face is marred by dust and sweat and blood; who strives valiantly; who errs and comes up short again and again; who knows the great enthusiasm, the great devotions; who spends himself in a worthy cause; who, at best, knows in the end the triumph of high achievement, and who, at the worst, if he fails, at least fails while daring greatly; so that his place shall never be with those cold and timid souls who know neither victory or defeat."

- Theodore Roosevelt

Acknowledgment

Embarking on a tertiary education is analogous to embarking on a treasure hunt. Undergraduate teaches one the basic survival skills but postgraduate teaches one to explore and discover hidden treasures using these basic survival skills. It requires one to have great determination and perseverance, and more importantly, people to guide you in this journey. Likewise, my PhD endeavour was made possible with the great people around me who have patiently given me the guidance and encouragement to discover these *treasures*. I would like to express my sincere appreciation and heartfelt gratitude to the following:

1. Associate Professor Yeo Song Huat, my main supervisor from the NTU School of Mechanical and Aerospace Engineering, for his insightful guidance and constant encouragement throughout my research. He trusted in my abilities by creating an atmosphere that permitted independent thinking in researching the various issues.

2. Dr Lin Wei, my co-supervisor from the Singapore Institute of Manufacturing Technology, for his invaluable guidance, informative comments and unwavering support of my research. His industrial expertise brought fresh perspectives to my research.

3. Dr Yang Guilin, my co-supervisor from the Singapore Institute of Manufacturing Technology, for his expert technical guidance, infinite patience and insightful suggestions rendered throughout my research. He took an active and conscientious role in guiding my research efforts.

4. Associate Professor Chen I-Ming, from the NTU School of Mechanical and Aerospace Engineering, for his belief in my potential research abilities and his informative comments.

5. Associate Professor Low Kin Huat from the NTU School of Mechanical and Aerospace Engineering, for introducing me to the world of research, which might not have been possible if not for his initial encouragement.

6. Assistant Professor John Gerard Heng Kok Hui from the NTU School of Mechanical and Aerospace Engineering, and my two external examiners for their insightful comments and suggestions made on this thesis. These comments have enabled me to produce a thesis with a complete overview of all the research issues in the design and analysis of a cable-driven anthropomimetic robotic arm.

7. My fellow research colleagues at the Robotics Research Centre and the SIMTech Research Collaboration Cluster, for their suggestions and assistance rendered during my research and especially for making research an enjoyable journey of learning and discovery. We shared many memorable moments, which will always be cherished.

8. The staff of Robotics Research Centre, NTU and Mechatronics Group, SIMTech for providing an excellent and conducive research environment.

9. My 'final year project' students, for giving me the opportunity to share my passion with them and their assistance rendered in my research investigations.

10. My childhood buddy, Mr Ang Wee Chong, for his faith in my abilities to pursue a PhD.

11. His Holiness, Syedna wa Maulana Abul Qaid Johar Mohammed Burhanuddin (TUS), for his spiritual guidance and giving me the faith to keep on persevering when it became overwhelming and challenging at times.

12. My parents and my brother, for their unwavering support, encouragement, patience and understanding in all my endeavors. They are always there to lend a listening ear and offer a helping hand.

13. Agency for Science, Technology and Research for awarding my PhD scholarship and financially supporting my research endeavors.

14. Nanyang Technological University for their financial support of this research under the Academic Research Fund Project (RG24/06).

15. Finally, to all those who have assisted me in my PhD studies in some ways or another.

Contents

List of Figures

List of Tables

List of Notations

$\mathbf{a}_i$	i^{th} Column vector of the cable structure matrix matrix
Ad	Adjoint representation
$\mathbf{A}$	Cable structure matrix $(n \times m)$
$\mathbf{A}^{\#}$	Pseudo-inverse of the cable structure matrix
b_{xi}, b_{yi}, b_{zi}	Global coordinates of B_i
$\mathbf{b}_i$	Positional vector of i^{th} base cable attachment point
$\widehat{\mathbf{b}}_i$	Skew-symmetric matrix of $\mathbf{b}_i$ (3×3)
B_i	Cable attachment point i on the base
d, d_v, d_ω	Uniformly-distributed deviations
D	Calibration Jacobian matrix
$\bar{e}_{\{\phi,\theta,\sigma\}}$	Average error of $\{\phi, \theta, \sigma\}$
$\mathbf{E}_{T\&T}$	T-&-T angle Jacobian matrix
$\mathbf{E}_\phi, \mathbf{E}_\theta$	Partial derivative matrices of $\mathbf{E}_{T\&T}$ relative to ϕ, θ
f_{ijk}	Feature point
$\mathbf{F}'(\mathbf{X})$	Newton-Raphson Jacobian matrix
h_a	Number of achievable poses
h_{total}	Total number of poses
I_d	Internal passive DOF of a mechanism
I_v	Volume-associated integral factor
$\mathbf{J}_{//}$	Jacobian matrix $(m \times n)$
$\mathbf{J}_X$	Forward Jacobian matrix
$\mathbf{J}_L$	Inverse Jacobian matrix
$\mathbf{K}$	Stiffness matrix $(n \times n)$
l_i	Length of i^{th} cable
$\dot{l}_i$	Spooling velocity of i^{th} cable
$\ddot{l}_i$	Spooling acceleration of i^{th} cable
$\mathbf{l}_i$	Unit vector of i^{th} cable
$\dot{\mathbf{L}}$	Cable spooling velocity vector

$\ddot{\mathbf{L}}$	Cable spooling acceleration vector
m	Number of cables
m_J	Manipulability of a pose
M	Mobility of a mechanism
n	Number of task-based dimension (degrees-of-freedom)
n_v, n_ω	Uniformly-distributed measurement noise deviation
$\mathbf{N}$	Null vector
$\mathbf{N}_{force}$	Row vector components of $\mathbf{N}$ for cables under force control
$\mathbf{N}_{position}$	Row vector components of $\mathbf{N}$ for cables under position control
p_{xi}, p_{yi}, p_{zi}	Global coordinates of P_i
$p^p_{xi}, p^p_{yi}, p^p_{zi}$	Local coordinates of P_i
$\mathbf{p}_i$	Positional vector of i^{th} moving platform cable attachment point relative to inertial frame
$\mathbf{p}^p_i$	Positional vector of i^{th} moving platform cable attachment point relative to local body frame
P_i	Cable attachment point i on the moving platform
$\mathbf{R}_{XY}$	Rotation matrix of frame {Y} relative to frame {X}
$\mathbf{S}_{T\&T}$	Inverse of $\mathbf{E}_{T\&T}$
$\mathbf{S}_\phi, \mathbf{S}_\theta$	Partial derivative matrices of $\mathbf{S}_{T\&T}$ relative to ϕ, θ
t_i	Tension of i^{th} cable
$\mathbf{T}$	Cable tension vector $(m \times 1)$
$\mathbf{T}_{force}$	Cable tension vector under force control
$\mathbf{T}_{position}$	Cable tension vector under position control
$\mathbf{T}_{XY}$	Transformation matrix of frame {Y} relative to frame {X}
$V_{Cartesian}$	Geometrical volume of cylindrical workspace
$V_{SO(3)}$	Workspace volume of $SO(3)$
$\mathbf{W}_{Ext}$	External wrench vector $(n \times 1)$
$\mathbf{x}$	Design variable vector
X	Gross error vector
$\mathbf{X}$	Pose of the moving platform in cartesian space
$\dot{\mathbf{X}}$	Velocity of the moving platform in cartesian space
$\ddot{\mathbf{X}}$	Acceleration of the moving platform in cartesian space
Y	Measurement residue vector
$\mathbf{Z}$	Arbitrary column vector in homogeneous solution
α	Rotational angle about y-axis
χ	Random factor from 0 to 1
δE	Error deviation metric
δp	Average quantified position deviation metric

δR	Average quantified orientation deviation metric
λ	Arbitrary scalar
ν	Reflection parameter
$\omega_x, \omega_y, \omega_z$	Angular velocity components of the moving platform
$\dot{\omega}_x, \dot{\omega}_y, \dot{\omega}_z$	Angular acceleration components of the moving platform
$\{\phi, \theta, \sigma\}$	Tilt and Torsion angle representation parameters
\$	Twist vector (6×1)
ε, ξ	User defined tolerance

List of Abbreviations

ADL	Activities of Daily Living
CDM	Cable-Driven Mechanism
CDPM	Cable-Driven Parallel Mechanism
CDRA	Cable-Driven Robotic Arm
CI	Conditioning Index
DOF	Degree-of-Freedom
GCI	Global Conditioning Index
GH	Glenohumeral
GSCI	Global Stiffness Conditioning Index
GSPI	Global Stiffness Performance Index
HU	Humeroulnar
MWS	Maneuverable Workspace
RU	Radioulnar
$se(3)$	*Lie Algebra* of $SE(3)$
$so(3)$	*Lie Algebra* of $SO(3)$
SCI	Stiffness Conditioning Index
$SE(3)$	Special Euclidean Group
$SO(3)$	Special Orthogonal Group
S$\underline{\text{P}}$S	Spherical-Prismatic-Spherical Joint Configuration (active Prismatic Joint)
T-&-T	Tilt and Torsion Angles
WMI	Workspace Matching Index

Chapter 1

Introduction

Section 1.1 presents the background for the need of assistive robotics in the present situation. Section 1.2 presents a brief overview of the current state of research in assistive robotics, in particular assistive robotic arms, and lists the main research challenges to address. Section 1.3 presents the objective and the scope of this research, while Section 1.4 outlines the structure of this thesis.

1.1 Background

Over the next decade, most of the industrialized nations will face a significant growth in the aging population with people over 60 years, with the elderly-dependency ratio growing from about 22% to more than 45% [1, 2]. This is because the advancement in medical and healthcare are enabling people to live longer, while extremely demanding work-life environments are discouraging many working couples from starting families. The consequence is a shift in the demographics which raises the profile of infirmity and disability in the world's population. Current solutions in providing care for this segment of the population include support from caregivers, or placing them in healthcare facilities like senior citizen centers or nursing homes. However, these solutions are fast becoming inadequate and expensive [3]. According to an economic study conducted in the US [4], it was found that more than three billion US dollars could be saved annually if all elderly US-citizen were to stay at home for just three more months before joining a senior citizen center. This is because high costs for individual treatment in healthcare centers can be eliminated if individuals that need support in daily life activities can continue to live at home, resulting in significant savings. Service robotics technology, especially assistive robots, can play a vital role in providing technological solutions to facilitate living at home, and have potential for commercial success due to the following incentives [4]:

- Innovative automation solutions from manufacturing plants that are readily available for use
- Development of sophisticated sensors and control techniques to enhance the intelligence of service robots
- Greater affordability to purchase service robots due to:
  - A decrease in costs of mechanical and electronic devices
  - An increase in income due to a greater range of healthcare plans (i.e., insurance, healthcare welfare packages, etc.)

Hence significant research efforts have been carried out in assistive robotics for the elderly population [5, 6]. Countries like Japan, Korea and the European Union have already embarked on national campaigns in robotics [7], with a focus on using assistive robots to enable people to continue leading active and productive lives in their old age, without being a burden to others. In addition to the elderly population, assistive robotic efforts have also been focused on people with disabilities [5, 8] because an estimated 10% of the world population[1] are living with disabilities, and these people require supervision or assistance in most of their daily life activities. With the availability of assistive robotics technology (in particular assistive robotic arms), this opens up whole new possibilities to enhance their quality of life.

1.2 Research in Assistive Robotic Arms

Assistive robots are being realized as potential tools for millions of elderly and disabled people to gain some independence and improve their quality of life. Hence, significant research has been conducted in assistive robotics technology and their efforts have resulted in devices such as wheelchair-mounted manipulators [10, 11, 12], desktop manipulators [13, 14], powered prosthesis [15], powered upper-limb orthosis [16, 17], powered lower-limb orthosis [18, 19, 20], transfer aid systems [21], therapeutic robots [8, 22, 23], and monitoring or companion robots [24, 25, 26].

Among the various assistive robotic devices developed, assistive robotic arms have received significant amount of interest and attention by the research community. This is because robotic arms have the potential to provide the elderly and the disabled with a means to carry out tasks in their daily living[2]. Hence researchers have developed various robotic arms in order to achieve similar functionality as the human arm. These arms are usually in the form of serial chain of rigid links, designed to perform a task with its end-effector. Other

[1] According to the World Health Organization, this amounts to approximately 600 million people [9].

[2] There are five common Activities of Daily Living (ADL): (i) transferring to and from the bed, (ii) dressing, (iii) feeding, (iv) bathing, and (v) toileting.

than the well-known commercially successful assistive arms like Handy 1 [13] and MANUS [10], there are also numerous innovatively designed assistive robotic arms that are still under research development (see Fig. 1.1). Notable examples include the MATS robotic arm [27], the ARMAR anthropomorphic arm [28], the Stanford Arm using 'Distributed Elastically Coupled Macro Mini Parallel' actuation system [29], the magneto-rheological (MR) Safe Arm [30], the 'Safety Serve Manipulator' (SSM) system [31], and the 7R anthropomorphic robot-arm driven by pneumatic artificial muscles [32].

(a) MATS robotic arm [27]

(b) ARMAR Robot with anthropomorphic arms [28]

(c) Safe Arm with MR-based passive compliant joints [30]

Figure 1.1: Novel designed assistive robotic arm prototypes

1.2.1 General Classification

Assistive robotic arms are generally classified based on their mounting schemes (see Fig. 1.2), which is in turn dependent on the task requirements. There are three main mounting schemes and they are categorized as follows:

(a) Static Workstation-based Mounting Scheme

This method is usually employed when a user requires assistance for manipulation tasks that do not need a change in the environment. These tasks include eating, drinking and

even static-based employment tasks. One of the well-known workstation-based robotic arm system is the 'Handy 1' robot arm [13], as shown in Fig. 1.2(a). It uses an relatively cheap 5-DOF industrial robot arm (Cyber 310) to mainly perform programmed feeding tasks. It is operated via a chin switch to select and activate the task process. Such systems have good stability but they also occupy valuable floor space and have limited maneuverability.

(b) Wheelchair-based Mounting Scheme

This method is usually employed when a user requires assistance for manipulation tasks and at the same time require mobility due to a change in the living environment. These tasks include cooking, washing, and mobile-based employment tasks. One of the well-known wheelchair-based robotic arm is the MANUS [10], as shown in Fig. 1.2(b). The MANUS is a 7-DOF robot that easily folds up into an unobstructive position at the side of the wheelchair. It uses a 16 button keypad, a track-ball and a joystick to carry out task space control. For such a system, stability and coordination with the wheelchair controls must be carefully taken into consideration. In addition, current designs are inflexible in construction, by being exclusively right or left handed, and the arm may be obstructive when not in use.

(c) Mobile Robot-based Mounting Scheme

This method is employed to serve as a companion to the user when carrying out his/her daily tasks and it has the ability to move independently from the user. One of the well-known mobile robot-based robotic system is the Care-O-bot II [25], as shown in Fig. 1.2(c). Built in 2002, it is a mobile service robot equipped with an assistive arm to provide handling capabilities for typical objects in the home. It also has an adjustable walking support with a hand-held control panel to carry out certain tasks. However, such robotic systems have greater autonomy which in turn increases the complexity and costs.

(a) Static workstation-based mounting: Handy 1 [13]

(b) Wheelchair-based mounting: MANUS [10]

(c) Mobile robot-based mounting: Care-O-bot II [25]

Figure 1.2: Typical assistive robotic arm mounting schemes

1.2.2 Research Issues

The development of assistive service robots involve a 'human-in-the-loop' systems approach. As explained by Bien [33], in this approach, the human acts as a user and the robot becomes an active provider of service, with the human existing in the common working space (see Fig. 1.3). Human-robot interaction is inevitable and will pose significant technical challenges to ensure complete protection of the human from any mishaps or malfunctions. This is unlike industrial robots where the human acts as an operator, functioning outside the working space of the robot, and the robot is simply a passive recipient of service from the human. Furthermore, the safety of the human operator in industrial settings is achieved by isolating the robot from the human. Hence human-robot interaction and human-robot interface issues[3] will be the greatest challenge to overcome in the design of assistive service robots.

A robotic arm system with 'user-friendly' human-robot interface and 'safe' human-robot interaction will be useless if it cannot be reliable to execute its tasks (i.e., issue of dependability). Implementation issues such as path planning, kinematic calibration and motion

[3] In general, human-robot interaction refers to the form of communication between the user and the robot in order to accomplish tasks, while human-robot interface refers to the device or system to facilitate the interaction. These issues involve addressing several requirements such as safety, reliability, robustness, maintainability, ease of operations, aesthetic appearance and cost.

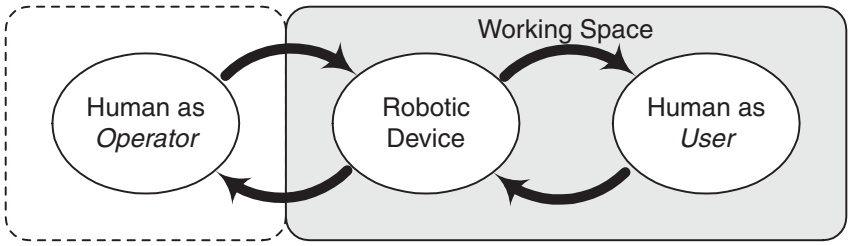

Figure 1.3: Human-robot interaction model [34]

control techniques, must also be taken into consideration in order to attain satisfactory performance. Path planning is vital to achieve completion of the task requirements, while kinematic calibration is vital to improve upon the inaccuracies introduced in the physical prototype due to the manufacturing and assembly processes. Motion control techniques, on the other hand, are critical for the successful execution of the motion planning tasks. Issues like mechanism design, kinematics, dynamics and performance must also be considered for systematic analysis and development of robotic arms.

While most assistive robotic arms possess some fundamental features of a human arm, such as the number of DOF, the types of joints, anthropocentric-based link lengths and scaling, and the motion characteristics, their mechanism designs and driving schemes are still quite different from the human arm. Thus, their actual performances are still quite distant from the human arm's remarkable manipulation capabilities and there is still room for improvement in this aspect.

1.3 Objective and Scope of Thesis

Past efforts in developing assistive robotic arms aim to create a robotic substitute for the human arm. Their attempts, while unique in their own way, do not compare to the human arm's remarkable characteristics and still require improvements. In this research, instead of addressing this issue using the conventional mechanism design approach, we will turn to biological solutions in the human arm to provide us with unique mechanical design solutions.

Thus, the objective of this research is to design a novel robotic arm with anthropomimetic features, for assistive applications. The aim is to achieve a lightweight and intrinsically-safe design with comparable dexterity and motion characteristics as that of a human arm (mainly in terms of its workspace).

The anthropomimetic assistive robotic arm design is cable-driven[4]. In this case, well-developed kinematics, workspace evaluation, performance evaluation and motion control techniques for conventional rigid-link mechanisms cannot be directly applied to cable-driven mechanisms (CDMs). This is because cables have a unique unilateral driving property i.e., cables can carry payloads only when in tension. This thesis will establish fundamental tools for the systematic analysis and design of such a robotic arm, including kinematic analysis, workspace-related analysis, design optimization and kinematic calibration. This will be followed by the development of an optimally designed 7-DOF cable-driven robotic arm (CDRA) prototype for the purpose of experimental investigations.

The scope of this thesis is as follows:

- A novel design for a cable-driven anthropomimetic robotic arm will be proposed. This design will be of a hybrid structure, where it will contain both open-loop and closed-loop kinematic chains, and will be made up of both rigid-links and cables.
- Kinematic analysis of the individual cable-driven parallel mechanisms (CDPMs) and the complete 7-DOF cable-driven robotic arm will be developed, including displacement analysis, velocity analysis and acceleration analysis.
- Workspace-related analysis of CDPMs will be addressed in order to obtain relevant information to evaluate feasible CDPM designs. This includes the formulation of a cable tension analysis procedure using the convex analysis theory.

[4] The cable-driven concept has various names in different geographical locations. The Americans generally referred to it as cables, while the Japanese refer to it as wires, and the Europeans generally refer to it as tendons. In this thesis, the term 'cables' has been adopted.

- Based on the joint motion limits, workspace templates of the human arm joints will be generated for subsequent design optimization. An equi-volumetric partition scheme based on the Tilt-&-Torsion angles parameterization will be proposed for the 3-DOF orientation workspace. Workspace evaluation, involving both quantitative and qualitative approaches, will be proposed for design optimization.

- Design optimization of the individual CDPMs will be carried out with the formulation of an optimization model. The aim is to have a robotic arm design whose workspace will be as close as possible as to that of the human arm. This will be followed by the development of the 7-DOF cable-driven robotic arm prototype, for the purpose of experimental investigations.

- Kinematic calibration issues will be addressed with the formulation of suitable calibration models for CDPMs and CDRA. This will be followed by simulation studies and calibration experiment verifications of the individual CDPM modules and the whole 7-DOF cable-driven robotic arm prototype.

In this thesis, several assumptions are made and they are as follows:

- Each cable length is precisely controlled by one motor.

- Cable attachment points at the base and moving platform are assumed to behave as spherical joints.

- For the proposed cable-driven robotic arm, the cables are assumed to be massless as the cables in each CDPM will be less than a metre in length.

- Cables in tension are assumed to behave as rigid links.

- Vibrations in cables will not be taken into account.

1.4 Organization of Thesis

The remaining chapters of this thesis are organized as follows:

Chapter 2 addresses the concepts adopted for design of assistive robotic arms and introduces a novel conceptual design of a cable-driven assistive robotic arm based on an anthropomimetic approach.

Chapter 3 addresses the kinematic analysis of the modular CDPMs and the whole 7-DOF cable-driven robotic arm.

Chapter 4 addresses the workspace-related analysis of CDMs, focusing on cable-tension analysis, stiffness analysis, workspace generation and performance evaluation measures.

Chapter 5 presents the design optimization of the 7-DOF CDRA, followed by its prototype development. A unique hybrid position-force based control scheme is proposed for future works, and the development of a novel designed tension sensor prototype is presented for such force based control applications.

Chapter 6 addresses the kinematic calibration of the modular CDPMs and the 7-DOF CDRA, including simulation studies and experimental verifications of the proposed calibration models.

Finally, Chapter 7 concludes this thesis, summarizing the contributions of this thesis and outlining the future work.

Chapter 2

Conceptual Design of a 7-DOF Cable-Driven Anthropomimetic Robotic Arm

---

Section 2.1 highlights the design philosophy adopted for current assistive robotic arms and the key design requirements. It also discusses about the approaches adopted to develop 'safe' robotic arms. Section 2.2 presents the recent anthropomimetic design philosophy adopted by robot designers today, and looks at the human arm anatomy and the biological solutions that can be observed for design of novel mechanisms. Section 2.3 presents the proposed conceptual design of the 7-DOF cable-driven anthropomimetic robotic arm, and highlights its advantages. Section 2.4 presents the mobility analysis of the proposed conceptual design to verify its mobility with that of the human arm. Section 2.5 discusses the possible related research extensions based on the anthropomimetic design concept, followed by discussion in Section 2.6 regarding the salient points in this chapter.

2.1 Background

2.1.1 *Human-Centered* Design Approach

Designing an assistive robotic arm to assist the elderly and the disabled is significantly different from designing a robotic manipulator to operate in manufacturing plants. Industrial robotic systems design focuses on precision, accuracy and repeatability, and has a highly structured working environment. In contrast, assistive robotic arms will be operating in less structured and unsupervised human environments, and will exist in close proximity to, or even coming in physical contact with the users. Here the task requirements on the accuracy and precision of the system will also be lower. In addition, the target users of such assistive robots are mostly elderly and disabled people, which place additional constraints to the design process. Instead, a *human-centered* design approach would be more appropriate than a machine-centered approach. The aim of the human-centered approach is to develop assistive robotic systems that provide 'safe' human-robot interaction through 'user-friendly' human-robot interfaces [33, 35, 36, 37]. This is a multi-disciplinary work, involving various aspects of robotic systems development such as mechanism design, locomotion and manipulation capabilities, calibration, path planning, motion control techniques and cognitive capabilities.

2.1.2 Design Requirements

There are several design requirements which must be met in order to develop a successful assistive robotic arm. These requirements include:

- **Safety**

  In industrial robot applications, traditional metrics such as bandwidth, maximum force, maximum torque, and reachable workspace are used to evaluate the performance [29]. However, for assistive robots, these traditional performance metrics are secondary design considerations. The primary design consideration is safety, as humans will be in

close physical contact with the robot. In order to achieve the highest safety performance, all facets of robot design must be considered, including mechanical, electrical and software.

- **Robustness and Reliability**

  The elderly and the disabled users will need to rely on these assistive robotic arms for long periods of time. Hence, in order for the robotic arm to ensure safety, it must also have robust and reliable mechanical, electrical and software components. In addition, these users are unskilled operators and cannot provide any form of technical support. The implications of these are that much more autonomy is required of the system and these robots must have robust and reliable autonomous error recovery features that can handle any complex error situations.

- **Flexibility**

  The human user environment is unstructured and varies with each user. Mass produced systems should not come with fixed configurations. Instead, it should have certain flexibility to be able to customize to individual user needs.

- **Maintainability**

  A robot requiring little or no maintenance throughout its service life with ease in repair will make it more readily accepted by its users [36]. This can be achieved by having maintenance-free subsystems and reliable stock components with modular designs. Modular designed subsystems also allow for future modifications without jeopardizing the system integrity.

- **Ease of Operations**

  In biological organisms, interaction is usually by verbal or visual means through dialogs and gestures, respectively. Hence, these are possible solutions for users to be able to interact and utilize the robot in a natural and intuitive way. In addition, the target users are the elderly and the disabled. Hence the user requirements are even stricter with very constrained modes of communication. Any complexity in the system must be

made hidden and the system must have a very easy-to-use, user-friendly and intuitive user interface. The human-robot interface must also be designed in such a way that no specialized training would be required for any person who might (voluntarily or non-voluntarily) encounter a robot, and would feel comfortable using it.

- **Aesthetic Appearance**

  Aesthetic appearance of a robot greatly influences the user confidence and its acceptance [38]. Interacting with a much more 'tidy' and aesthetic looking robotic arm would make users feel more comfortable and relaxed. Hence this requires a human-factors approach.

- **Cost**

  Low costs are essential for successful acceptance of assistive robots as majority of the target users (i.e., elderly and disabled) may not be financially well-off. Hence, low costs can be achieved by using readily available stock components, reducing complexity of the mechanical design by transferring more functionality to the sensors and software, and trading precision with robustness.

Although efforts have been made in addressing the other requirements, safety is perhaps most widely researched out of the various requirements mentioned, followed by reliability [35, 36, 37]. This is because from the viewpoint of human-robot interaction, it is crucial to take utmost care and precautions to ensure the human beings in close proximity to these robots are not harmed under any circumstances.

2.1.3 Means to Achieve 'Safe' Designs

Due to the close proximity of the human users to these robots, the starting point in the design phase must always be an evaluation of the probability and consequences of a system failure. This is to ensure safety precautions are taken so that the humans are not harmed

under any circumstances. Various safety precautions have been proposed and implemented by researchers on three main areas, namely mechanical, electrical and software.

Mechanical-based precautions include: (i) Designing arms with minimal weight possible (i.e., removing auxiliary devices [39], using lightweight materials and redistributing the actuation system based on the performance requirements in each link [29]), (ii) Developing compliant links and actuation systems(i.e., Braided Pneumatic Artificial muscles [32] and Magneto-Rheological-based passive compliant joints [30]), and (iii) Designing ergonomic features (i.e., eliminating sharp edges and protrusions, addition of padding to minimize the effect of collision [30, 40]).

Electrical-based precautions include: (i) Monitoring and limiting of torques acting on robotic arm joints and end-effector [41], (ii) Active monitoring and controlling of robot workspace using sensors and avoiding collisions [42], (iii) Employing feedback sensor redundancy to monitor kinematic irregularities and actively controlling forces in joints [31], and (iv) Having conveniently located emergency-stop switches.

Software-based precautions include: (i) Implementing software-based limits on motor torque and velocity [43], (ii) Compliant control schemes (i.e., Joint space or Cartesian space) [44], (iii) Impedance control schemes [45], (iv) Collision detection algorithms to detect presence of humans and implementing strategies to make robots behave in a natural and human-friendly way [46], (v) Predicting human position and changing the robot arm trajectory so as to minimize the danger [47], (vi) Information sharing by the robot on its intended motion before execution [48], and (vii) Fault-tolerance architecture and operating systems [49].

While each of these precautions have their own merits, electrical and software-based precautions require complex feedback systems with real-time capabilities which significantly increase the computation burden and developmental costs, and most importantly, in the event of unforeseen system failure, it poses great danger to its human users as these solutions are not intrinsic to the mechanical components. Mechanical-based precautions offer

intrinsically-safe features and this will be the main focus of the proposed assistive robotic arm design in this chapter.

2.2 *Anthropomimetic* Design Approach

Nature has created highly complex, efficient and dependable systems in the form of many living organisms we see today. The design and functionality of these organisms have evolved progressively over billions of years to become highly optimized and efficient. Hence, it would be a wise choice to tap into this readily available pool of nature's solutions and apply it to today's engineering problems, as design constraints and objectives are very similar in terms of functionality, optimization and cost-effectiveness. The key to successfully utilizing these biological solutions is to find analogous means of transferring these biological ideas into technical solutions, instead of directly copying nature's ideas. This anthropomimetic design concept is widely applicable to many fields, and robotics technology would certainly benefit by applying good design principles and concepts from nature into mechanism designs and control strategies.

Indeed, the last several years has seen several robot designers who have started observing solutions-in-nature and mimicking these biological solutions. These developments range from control strategies [50] to manipulator designs. For the manipulator, these designs mimic elephant trunks [51], tentacles [52], snakes [53] and even the human arm [32, 54]. This has brought about several interesting and novel robotic arm solutions (see Fig. 2.1), with the aim of achieving a design with better mobility, versatility, redundancy and compliance.

Does the Human Arm Offer any Solutions?

In order to come up with an anthropomimetic robotic arm design, the most obvious choice to observe for design ideas is the human arm. As shown in Fig. 2.2, the human arm skeleton consists of an assemblage of the scapula (shoulder), humerus (upper arm), radius & ulna

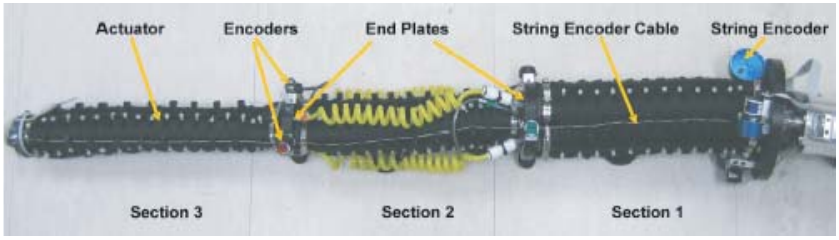

(a) Octopus Arm [52]

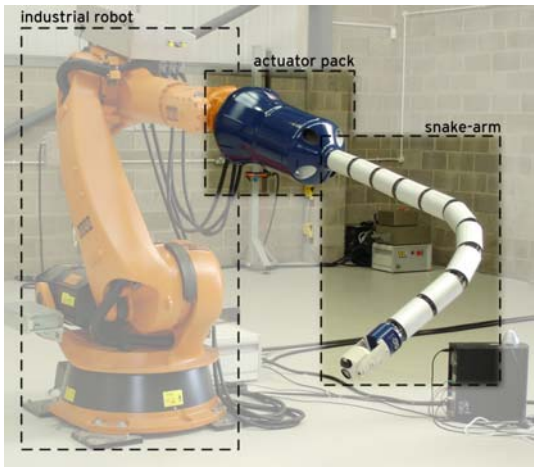

(b) Snake Arm [53]

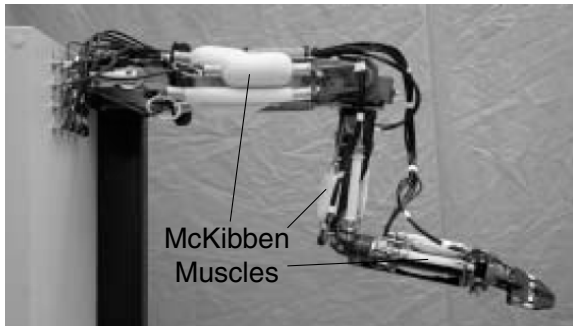

(c) 7-DOF Pneumatic Robotic Arm [32]

Figure 2.1: Biologically-inspired manipulator designs

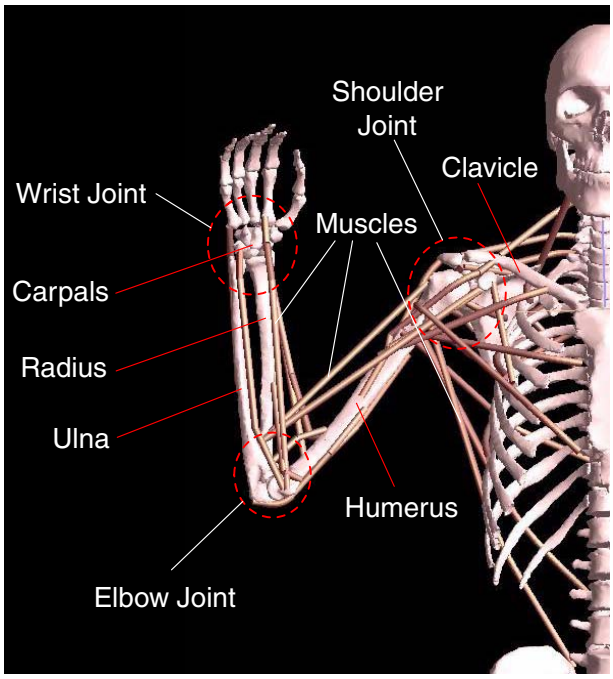

Figure 2.2: Human arm anatomical structure

(forearm), and carpals (wrist). Its fundamental roles are to support the weight of the human arm and to serve as a place for muscles attachment. The relative displacement of these bones contribute to the arm's major movement and the connections between these bones form four basic synovial joints, namely glenohumeral (shoulder), humeroulnar (elbow), radioulnar (forearm) and radiocarpal & midcarpal (wrist) joints. Although the structures of these synovial joints are different, these joints provide similar motions as those in conventional mechanical joints. Simplifications have been made to kinematically model anatomical joints by using revolute joints, universal joints and spherical joints. In addition, all the joints are modeled with fixed centre of rotations since the movements in the human joints' instantaneous centers of rotation are small [55].

(a) The Shoulder Joint

The human shoulder consists of a collarbone (clavicle) and a shoulder blade (scapula). These bones project out from the body forming a scaffold for the arm to hang from. The collarbone and the shoulder blade meet at the end to form a shoulder socket (also known as the glenohumeral (GH) joint) where the head of the humerus fits into the concave recess of the scapula, as shown in Fig. 2.3(a). The surface motion at the GH joint is primarily rotational, but with slight translations of $\pm 2mm$ [56] occurring due to loading conditions. Nevertheless, anatomical features (such as cartilage, ligaments, structure of the bones and stabilizing muscles) help minimize translation of the humeral head [57]. Hence, the kinematic model of the shoulder joint is generally modeled as a spherical joint with a fixed rotation centre [58, 59] (see Fig. 2.3(a)).

(b) The Elbow Joint

The arm is made up of three long bones, namely the humerus in the upper arm and the ulna and radius in the lower arm. The upper and lower arms are connected at the elbow by the humeroulnar (HU) joint (between the humerus and ulna) and the radioulnar (RU) joint

(between the radius and ulna). The HU joint permits rotation between the upper and lower arm, while the RU joint permits rotation of the hand and forearm. The HU joint is modeled as a revolute joint whose line of rotation passes through the centre of the trochlea (see Fig. 2.3(b)), while the RU joint is modeled as a cylindrical joint whose axis of rotation passes through the distal end of the ulna and the centre of the capitulum [55] (see Fig. 2.3(c)).

(c) The Wrist Joint

The wrists consist of eight small nugget shaped bones, more commonly known as carpals. They are arranged in two irregular rows that are held together by ligaments. These bones form a 'gliding' joint that permit sliding motion between the surfaces of carpals. The complexity of the joint motion at the wrist makes it difficult to exactly identify the instant center of motion. However the trajectories of the hand during flexion/extension and radial/ulna flexion show that they occur in a fixed plane and the rotation in each plane takes place about a fixed axis. These axes are located within the head of the capitate and are not altered by the position of the hand in the plane of rotation [57]. As shown in Fig. 2.3(d), the wrist joint is modeled as a universal joint since the flexion-extension and the radial-ulna flexion axes are believed to intersect [55].

Hence, the basic human arm has a total of seven DOFs. The shoulder joint is a 3-DOF rotational joint, while the elbow and the wrist joints are 2-DOF rotational joints [90]. However, the rotational DOF of the RU joint at the elbow has its axes passing through the distal end of the ulna and the centre of the capitulum to the capitate, as shown in Fig. 2.3(c). Thus, the wrist joint is analogous to a 3-DOF spherical joint while the elbow joint is analogous to a 1-DOF revolute joint. Together, these three joints are arranged in series to form the basic 7-DOF human arm structure.

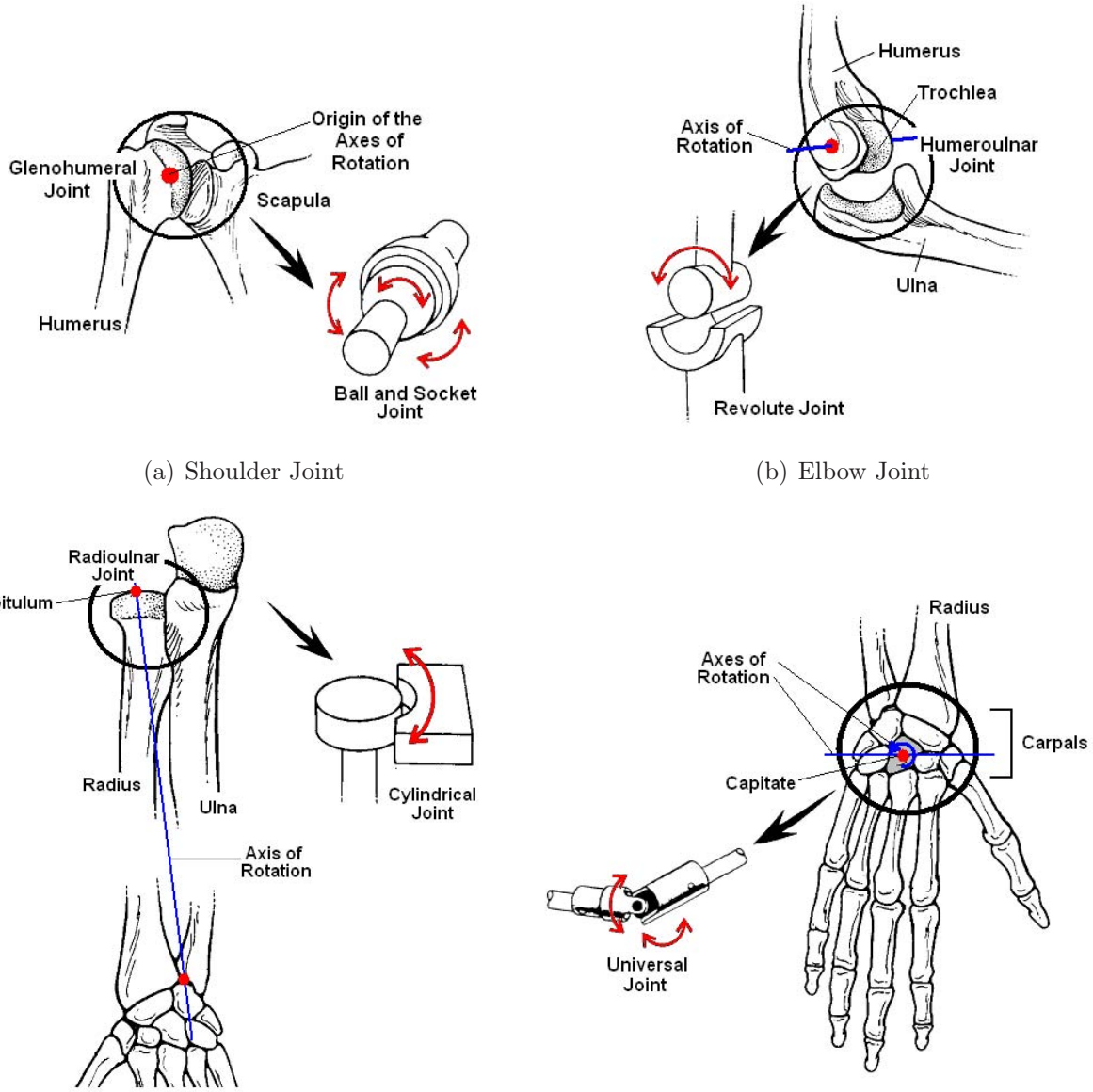

(a) Shoulder Joint

(b) Elbow Joint

(c) Forearm Joint

(d) Wrist Joint

Figure 2.3: The joints in the human arm and their equivalent kinematic models

(d) The Human Muscles

The human muscular system, is a kind of 'engine' that causes the body to propel itself. Muscles are generally distributed in pairs and their unilateral driving ability to contract not only enables the body to move but also provides the force that pushes substances, such as blood and food, through the body. Muscles are controlled by the central nervous system through motor units attached to the muscle fibers. Depending on the type of load to be lifted, a differing number of motor units will be recruited into the contraction process. The

more fibers that contract, the bigger and harder the muscle will be. As muscles rarely acts in isolation, there are four functional roles that are assumed by them, namely as an agonist (to cause movement), an antagonist (to stop movement), a stabilizer (to stabilize a body part against unknown forces) and a neutralizer (to eliminate any unwanted motion produced by the agonist). Muscles performing the agonist and antagonist roles are often positioned on the opposite sides of a joint. For example, during elbow flexion, the biceps act as agonists while the triceps act as antagonists, as shown in Fig. 2.4. Hence the muscle driving scheme consists of numerous muscles working in pairs with redundant pairs of muscle. These pairs of muscles are also arranged in a closed-loop fashion, similar to that of parallel mechanisms. The human muscle physiology is also observed to be of similar characteristics with cables (both having the unilateral driving property of being able to only exert tension).

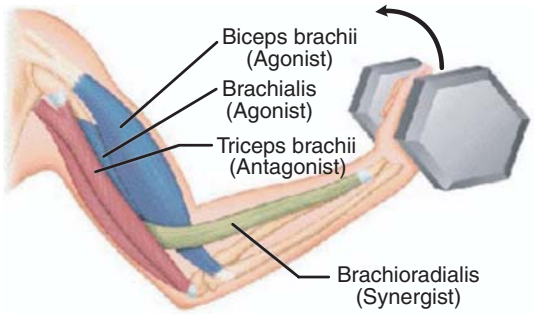

Figure 2.4: Agonist and antagonist in action

2.3 Proposed Conceptual Design

From the previous section, the human arm is observed to resemble a hybrid mechanism consisting of local parallel mechanisms (i.e., 3-DOF shoulder joint, 1-DOF elbow joint and 3-DOF wrist joint, with their relevant muscles arranged in a parallel manner), attached adjacently to form a serial mechanism with 7-DOF. In addition, the human arm muscle arrangement consists of numerous muscles working in pairs with a redundant actuation scheme, similar to that of parallel mechanisms. Hence, based on these biological solution

observations and the need for an intrinsically-safe 'human-centered' solution, the design of the assistive robotic arm is conceptualized to be of similar structure as the human arm. A novel design is proposed which combines under-deterministic cable-driven parallel mechanisms (CDPMs) with a central 7-DOF rigid-link (i.e., consisting of three sequentially connected joints). The outcome is a deterministic 7-DOF cable-driven robotic arm (CDRA), as shown in Fig. 2.5. This design is considered a *hybrid* structure because it contains both open-loop and closed-loop kinematic chains, and it consists of both rigid-links and cables.

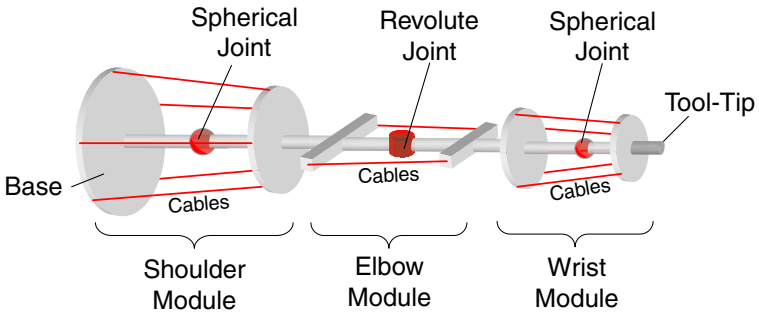

Figure 2.5: Conceptual design of the 7-DOF cable-driven anthropomimetic robotic arm

There are two basic *sufficiently restrained*[1] CDPMs that are proposed to form the whole 7-DOF cable-driven robotic arm, as observed from Fig. 2.5. These basic CDPMs are the 1-DOF CDPM (i.e., elbow module) and the 3-DOF CDPM (i.e., shoulder and wrist modules). For the 1-DOF CDPM, its moving platform possesses a revolute motion due to the existence of the central revolute jointed constraint link. Thus this mechanism is similar to a four-bar linkage in which the moving platform is treated as the output link and the cables are employed as the inputs. For the 3-DOF CDPM, its moving platform possesses a spherical motion due to the existence of the central constraint link with a spherical joint. Thus this mechanism is similar to an orientating device in which the moving platform is treated as the output link and the cables are employed as the inputs. These basic cable-driven joint modules (i.e., 3-DOF shoulder module, 1-DOF elbow module and 3-DOF wrist module) bear

[1] Ming and Higuchi [60] were one of the first few to provide classifications for CDMs based on the relation between the number of cables (m) attached to the moving platform and the DOF (n) of the mechanism. Without loss of generality, CDMs utilizing 'greater than or equals to' $(n+1)$ cables to control the pose of the moving platform were classified as sufficiently restrained, while the rest (i.e., utilizing 'less than' $(n+1)$ cables) were classified as insufficiently restrained and require external forces (i.e., gravity) to control the pose of the moving platform.

resemblance to the respective human arm joints with their central rigid-link bone structure. These modules are then connected alongside to form a global serial structure with 7-DOF, similar to that of the human arm. Another resemblance is that these joint modules are cable-driven with a redundant actuation scheme, based on the observation of the human muscles' unilateral driving property (i.e., being able to exert only tension), and the redundant muscle driving scheme.

This design offers the following benefits:

- **Intrinsically-Safe**

  The flexible nature of cable allows the arm to have a natural compliance. This makes the arm intrinsically safer as compared to its rigid-link equivalent.

- **Lightweight**

  Cables are lighter than most mechanical transmission systems such as linkages, gear trains and belt-&-pulley, and have negligible inertia. In addition, the cable actuation units are mounted on the base rather than onto the linkages. Hence, the hybrid cable-driven arm has a lower moment of inertia and is much lighter, compared to its rigid-link equivalent.

- **Dexterous with a Large Workspace**

  Since cables can be rolled into a spool, they allow a large range of motion, compared to the conventional hydraulic or pneumatic actuators. In addition, it is possible to have redundant cables due to its lightweight nature. Hence this allows the proposed arm to have a larger and more dexterous workspace.

- **Higher Payload-to-Weight Ratio**

  The hybrid parallel-in-series cable arrangement of the 7-DOF CDRA and the light-weight structure of its individual modular CDPMs allows it to have a higher payload-to-weight ratio, as compared to the conventional rigid-link serial arms.

- **Variable Stiffness**

  End-effector stiffness can be modified to meet the task requirements by adjusting the cable tension, the number of cables used and their arrangement scheme.

- **Modular in Design**

  The 7-DOF cable-driven arm is modular in design where the actuation of each modular CDPM is decoupled and hence, these modules can be easily interchanged, leading to versatility and simplicity of repair.

- **Reliable with High Fault Tolerance**

  The cable actuation units are mechanically designed with simplicity, and are therefore expected to exhibit strong reliability. In addition, the presence of redundant cables ensure the arm is still able to function in the event of cable failure.

- **Aesthetically Appealing Appearance**

  Proposing a design which resembles a human arm makes the robotic arm look less intimidating and more friendly. Replacing rigid and bulky actuators with thin cables also makes it more look more aesthetically appealing.

- **Low Cost**

  The simplicity of the mechanical actuation of cables and the arm design allow the fabrication and maintenance costs to be relatively low, as compared to conventional robotic arms with 'safe' but complex actuation modules [61, 62]. Although having one motor for one cable can increase the costs due to the redundant nature of CDPMs, this can be minimized through the use of low-cost motion controllers.

Hence, the benefits offered by the proposed cable-driven anthropomimetic robotic arm meet most of the key design requirements mentioned in Section 2.1.2. However, several challenges exist in the successful implementation of cable-driven robots, due to the unilateral driving property (i.e., ability to only exert tension) and flexible nature of cables. These include: (i) Designing and analyzing configurations without encountering cable interference, (ii) Effective control of end-effector without losing positive cable tensions, and (iii) Calibrating

the cable-driven robot for subsequent path planning and motion control tasks. Based on these challenges, this thesis aims to develop a systematic framework to design a suitable cable-driven anthropomimetic robotic arm for real-world applications.

2.4 Mobility Analysis

In this section, mobility analysis is carried out for the basic 1-DOF and 3-DOF CDPMs proposed in the conceptual design of the assistive robotic arm. This is to verify that the mobility of the individual CDPMs are the same as that of their respective human joints. For rigid-link mechanisms, mobility analysis is carried out using the Gruebler-Kutzback criterion [63]. However, for cable-driven mechanisms, this criterion can also be utilized to analyze its mobility, provided we convert the cable-driven design to its rigid-link equivalent structure. Ming and Higuchi [60] proposed a kinematically equivalent rigid-link mechanism for an active cable, consisting of passive spherical joint at both ends of an active prismatic joint (S$\underline{\text{P}}$S)[2] as shown in Fig. 2.6. The Gruebler-Kutzback Criterion is given as:

$$M = \lambda(l - j - 1) + \sum_{i}^{m} f_i - I_d \tag{2.1}$$

Where M is the mobility of a mechanism, λ is the DOF of the space in which the mechanism is intended to function, l is the total number of links in a mechanism (inclusive of the base and the moving platform), j is the total number of joints, f_i is the DOF permitted by joint i, I_d is the internal passive DOF of the mechanism and m is the number of cables. Note that each end of the 'cable equivalent' rigid-link leg is connected to a spherical joint. Hence, a passive rotational DOF exists whose axis passes through both of the spherical joints, resulting in one passive DOF for each leg. This means that although the prismatic joint in each leg has the ability to transmit forces about its axis, it has however, no torque transmission capability about the passive axis.

[2] 'S' represents the spherical joint while 'P' represents the prismatic joint. The order of the letters indicate the order of arrangement of the joints, while an underlined letter indicates that it is an active joint.

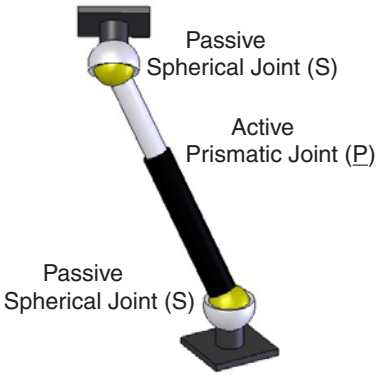

Figure 2.6: Equivalent Spherical-Prismatic-Spherical (SPS) rigid link for a cable in positive tension

2.4.1 1-DOF CDPM Module

Based on Eqn. (2.1) and Fig. 2.7(a), the mobility of the cable equivalent rigid-link kinematic model of the 1-DOF CDPM module with m cables, is given by:

$$M = 6\{(2m+2) - (3m+1) - 1\} + \{m \times (3+3+1) + 1\} - m = 1 \tag{2.2}$$

2.4.2 3-DOF CDPM Module

Based on Eqn. (2.1) and Fig. 2.7(b), the mobility of the cable equivalent rigid-link kinematic model of the 3-DOF CDPM module with m cables, is given by:

$$M = 6\{(2m+2) - (3m+1) - 1\} + \{m \times (3+3+1) + 3\} - m = 3 \tag{2.3}$$

From Eqns. (2.2) and (2.3), it is seen that by converting the cable-driven design to its rigid-link equivalent, the modified Gruebler-Kutzback Criterion from Eqn. (2.1) is still suitable for mobility analysis of cable-driven mechanisms. In addition, regardless of the number of cables used, the proposed basic 1-DOF and 3-DOF CDPMs have the same mobility as the human arm joints.

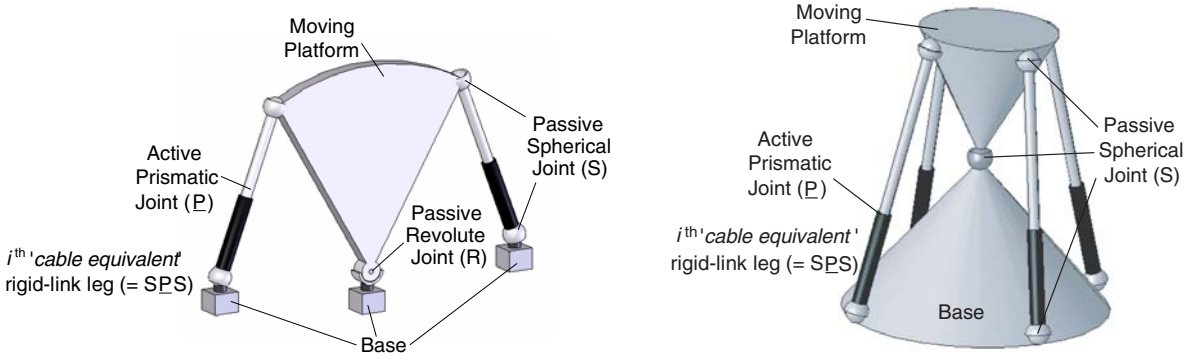

(a) One-DOF 'Cable Equivalent' Rigid-Link Parallel Mechanism

(b) Three-DOF 'Cable Equivalent' Rigid-Link Parallel Mechanism

Figure 2.7: 'Cable equivalent' rigid-link parallel mechanisms

2.5 Related Research Areas

Other than being developed as an assistive robotic arm (see Fig. 2.8), the 'anthropomimetic' design concept can be extended to other related research areas.

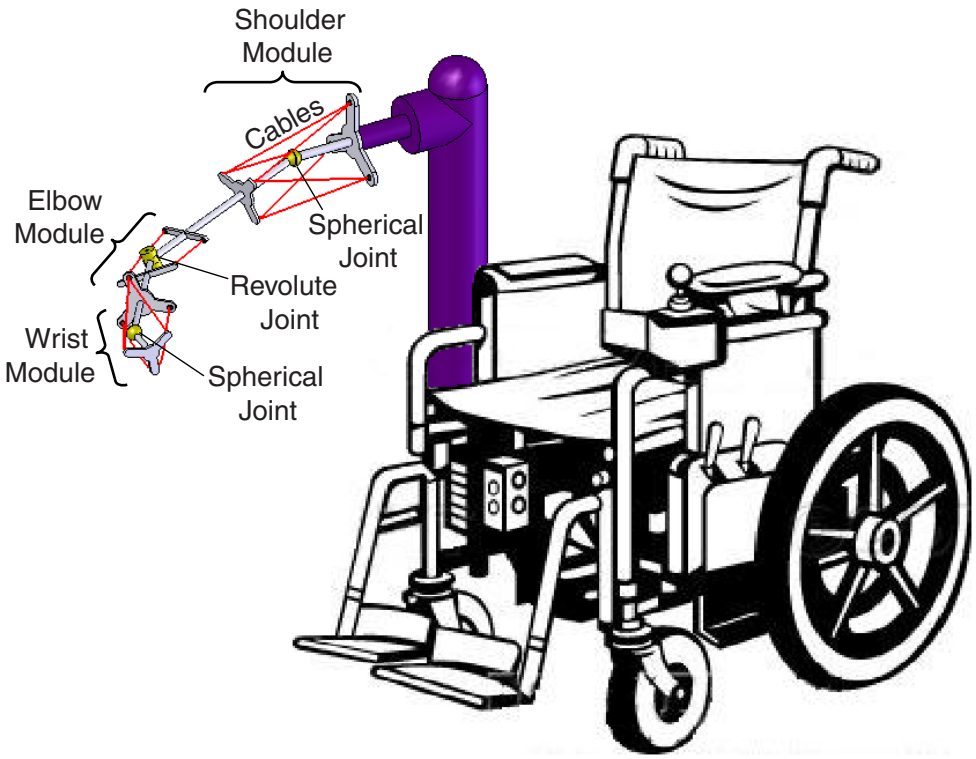

Figure 2.8: Conceptual design of a wheelchair-mounted assistive robotic arm

2.5.1 Medical Applications

(a) Prosthesis

Prosthesis can be developed based on the 'anthropomimetic' design concept for patients who have lost their limbs. Figure 2.9 presents the conceptual design of a cable-driven wrist prosthesis. Compared to current prosthesis available in the market, the proposed cable-driven prosthesis can offer the advantages of being intrinsically-safe with natural compliance due to the lightweight and flexible nature of cables. The main challenges would be to develop a low-powered compact cable actuation unit and an effective control method, possible through the use of electromyograph signals from the remaining skeletal muscle nerves. Readers may refer to a publication by the author in [64] for more details on the cable-driven wrist prosthesis design methodology and prototype development.

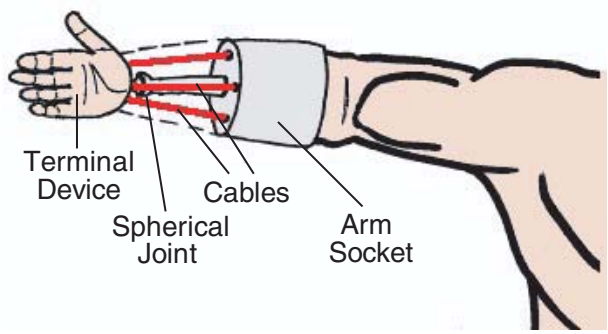

Figure 2.9: Conceptual design of a cable-driven wrist prosthesis

(b) Rehabilitation

In the mechanotherapy of human joint injuries, wearable limb rehabilitators can be developed with a bio-kinematic structure based on the 'human-centered' and 'anthropomimetic' design concept. This means that under-deterministic cable-driven mechanisms are combined with the human limbs to form a complete deterministic structure. Figure 2.10 presents the conceptual design of a wearable arm rehabilitator. Compared to current arm rehabilitators, the cable-driven wearable arm rehabilitator conforms to the human arm joints and produces motion which are about the human joints itself. This makes the rehabilitation process much

more comfortable and safer as it minimizes unnecessary stress to be created at the joints during the rehabilitation exercises. This is unlike the case for current rehabilitators as the human joint is forced to conform to the mechanisms motion characteristics. Since safety is critical for such rehabilitation devices, the cable-driven concept is ideal as it also provides a natural protection due to its inherent compliance characteristic and flexible nature of cables. Readers may refer to a publication by the author in [65] for more details on the cable-driven wearable arm rehabilitator design methodology and the optimal design solution.

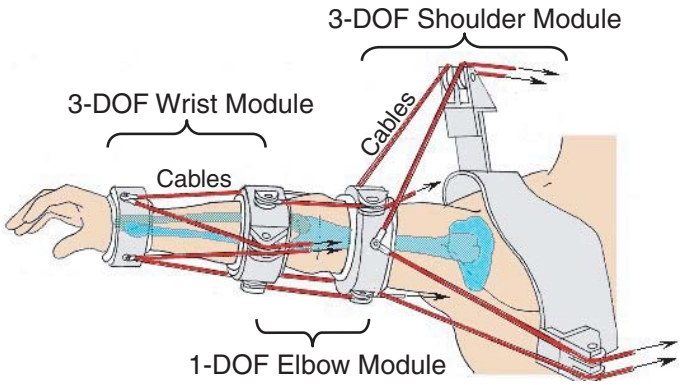

Figure 2.10: Conceptual design of a cable-driven wearable arm rehabilitator

2.5.2 Haptic Applications

The concept of a cable-driven anthropomimetic wearable robotic arm can be extended to haptic applications such as teleoperation, virtual reality and entertainment. The wearable arm can be used for teleoperation as a 'macro to micro' man-machine interface in manipulation of tiny objects (i.e., assembly of MEMS components, micromanipulation of biological stem cells, etc.) or it can also be used to remotely control a slave robotic manipulator in hazardous environments (i.e., nuclear plants, bomb disposal, etc.). The wearable arm can be used in tactile feedback system for interface with virtual environments, as well as in entertainment, as a game control input and feedback system. Game players will be able to have a more realistic experience with force-feedback on their arms when playing games with combat scenarios.

2.6 Discussion

In this chapter, the human-centered design approach for current assistive robotic arms is addressed and its key design requirements are highlighted in order to develop a successful assistive robotic arm that will be widely accepted by its target users. The 'anthropomimetic' design philosophy is also discussed which involves observation of biological organisms for engineering solutions. The human arm is observed for biological solutions and a novel cable-driven design for a 7-DOF assistive robotic arm is proposed. Basic anthropomimetic parallel mechanism modules are proposed to be arranged in series to form the whole 7-DOF arm. These modules are also cable-driven in order to have a similar muscle driving scheme. Mobility analysis is also carried out to verify the mobility of the proposed cable-driven mechanisms with that of the human arm joints. Several related research directions for the 'anthropomimetic' cable-driven concept are also discussed.

In conclusion, the proposed 7-DOF cable-driven robotic arm design offers numerous benefits over conventional articulated assistive robotic arms. However, several challenges exist in the development and implementation of cable-driven robots, due to the unilateral driving property (i.e., ability to only exert tension) and flexible nature of cables. These issues will be addressed in this thesis in order to establish a systematic framework to design and analyze such hybrid cable-driven manipulators.

Chapter 3

Kinematic Analysis

Section 3.1 presents an overview of the kinematic analysis of cable-driven mechanisms and highlights the important issues for such mechanisms, including the relevant geometric background. Section 3.2-3.4 presents the kinematic analyses of the 1-DOF, 3-DOF and 7-DOF cable-driven mechanisms respectively, including the displacement, velocity and acceleration analyses. Section 3.5 then concludes with the discussion of the salient points in this chapter.

3.1 Background

Kinematics deals with the aspect of motion without giving consideration to the forces and torques that are causing it. Hence, the purpose of kinematic analysis is to determine the kinematic relations (i.e., displacement, velocity and acceleration) between the pose of the moving platform and the joint variables. For rigid link mechanisms, the joint displacement of the legs determine the pose of the moving platform. Likewise, for cable-driven mechanisms (CDMs), it is the length of the cables that determine the pose of the moving platform. The results from kinematic analysis will be utilized in the selection of suitable motors for the cable actuation units and during the motion control implementation phase, where the cable actuation units will need to deliver the required kinematic relations of the cables, based on the desired tool-tip kinematic requirements.

3.1.1 Kinematics of Parallel Mechanisms

Unlike serial mechanisms, the forward kinematics[1] of parallel mechanisms is challenging as it is expressed in highly nonlinear equations with multiple solutions due to the closed-loop nature of the parallel mechanisms [66]. The inverse kinematics on the other hand, is relatively straightforward, simply requiring direct substitution to obtain the unique set of joint displacement solutions for a given pose. Previous research efforts on forward kinematics have focused on three main approaches: the polynomial-based [67, 68], the extra-sensor [69, 70] and the numerical-iterative approach [71, 72]. In the polynomial-based approach, a polynomial solution for the direct kinematics of parallel mechanisms is obtained. However, the process of reducing the set of constraint equations into a univariate high-order polynomial equation is complex, and in the end, if the order of the resultant polynomial equation if greater than four, a numerical method has to be utilized to find their solutions. In the extra-sensor approach, in addition to the sensors installed on the actuated joints,

[1] This refers to the determination of the pose of a moving platform, given the joint displacements.

redundant sensors are also installed on the passive joints of the mechanisms. These redundant information allows the simplification of the forward kinematics. However, this involves high implementation costs and hardware complexities. As a result, the numerical-iterative approach has been widely utilized. This is because numerical-iterative methods generally results in a faster generation of the forward displacement solution. One such widely employed method is the Newton-Raphson method due to its property of quadratic convergence. However, this approach also poses a potential problem of reliability and accuracy, as it is highly sensitive to the initial estimate values and the nature of the resulting constraint equations, but this is generally minimized by using the previous point of the trajectory as a good initial guess.

3.1.2 Kinematics of 'Cable-Driven' Parallel Mechanisms

In 1994, Ming and Higuchi [60, 73] provided a basic understanding of the kinematics of CDMs. In relation to the unique characteristic of CDMs (i.e., the unilateral driving property of cables to be able to only exert tension), their work presented the necessary and sufficient conditions for positioning by cables. In their work, *it was mathematically proven that a sufficiently-restrained n-DOF CDM, requires a minimum of* $(n+1)$ *cables in positive tension*[2]*, to fully restrain its moving platform.* A positive-tensioned cable functions similarly as a rigid-link mechanism and has a kinematically equivalent form, consisting of passive spherical joints at both ends of an active prismatic joint (S$\underline{\text{P}}$S) [60] (see Fig. 2.6). Hence, it has been realized that the kinematic analysis of CDMs is similar to that of rigid-link mechanisms, provided the positive tension of the cables are maintained.

Similar to rigid-link parallel mechanisms, the kinematic analysis of cable-driven parallel mechanisms (CDPMs) is also very complicated. However, unlike the parallel mechanisms where closed-form solutions for the forward kinematics have been found, this is highly im-

[2] The set of cables in positive tension must also satisfy the tension-closure condition. This will be further elaborated in Chapter 4.

possible for CDPMs. This is because the resulting matrix of equation is over-constrained due to the unilateral driving property of cables that require a minimum of m $(= n + 1)$ cables to completely restrain the moving platform of a n-DOF CDPM and attain the required pose. Hence numerical-iterative methods using the Newton-Raphson algorithm have been generally utilized [71]. An extended forward kinematics was also presented by Ming and Higuchi [74]. This was done by obtaining the pose of the n-DOF CDPM from n cable lengths, followed by utilizing inverse kinematics to obtain the lengths of the remaining $(m - n)$ cable lengths. The inverse kinematics of a CDPM on the other hand, is relatively straightforward, simply requiring direct substitution of a given pose parameters to obtain a unique set of cable lengths. However, whether the pose is realizable depends on the cable tension conditions and the ability to obtain a set of positive cable tension to sufficiently restrain the moving platform (i.e., tension-closure condition).

3.1.3 Geometric Background on Rigid-Body Kinematics

In kinematic analysis of rigid body motions, the *Special Euclidean Group*, or $SE(3)$, is commonly used to describe the configuration of a rigid body with regards to certain coordinate frames. If $\{K_A\}$ is a fixed inertial coordinate frame and $\{K_B\}$ is a body-attached coordinate frame, the configuration of $\{K_B\}$ with respect to $\{K_A\}$ is expressed either as an ordered pair or a 4×4 homogeneous matrix:

$$\mathbf{T}_{ab} = (\mathbf{p}_{ab}, \mathbf{R}_{ab}) = \begin{bmatrix} \mathbf{R}_{ab} & \mathbf{p}_{ab} \\ 0 & 1 \end{bmatrix} \tag{3.1}$$

Where $\mathbf{R}_{ab} \in SO(3)$ is the rigid body rotation of $\{K_B\}$ with respect to $\{K_A\}$ and $\mathbf{p}_{ab} \in \Re^{3\times1}$ is the initial location of the origin of $\{K_B\}$ with respect to $\{K_A\}$. Note that $SO(3)$ or *Special Orthogonal Group*, refers to the 3×3 rotation matrices group. The group operation on $SE(3)$ allows the configuration of a frame $\{K_C\}$ to be described with respect to $\{K_A\}$ via an intermediate frame $\{K_B\}$ as $\mathbf{T}_{ac} = \mathbf{T}_{ab}.\mathbf{T}_{bc} = (\mathbf{p}_{ab}, \mathbf{R}_{ab}).(\mathbf{p}_{bc}, \mathbf{R}_{bc}) = (\mathbf{p}_{ab}+\mathbf{R}_{ab}.\mathbf{p}_{bc}, \mathbf{R}_{ab}.\mathbf{R}_{bc})$.

Since $SE(3)$ is a Lie Group, the *Lie Algebra* of $SE(3)$, denoted by $se(3)$, consists of matrices

in the form:

$$\widehat{\$} = \begin{bmatrix} \widehat{\omega} & \upsilon \\ 0 & 0 \end{bmatrix} \tag{3.2}$$

Where $\widehat{\omega}$ is a 3×3 real skew-symmetric matrix which forms the Lie algebra of $SO(3)$, denoted by $so(3)$, and $\upsilon \in \Re^{3\times 1}$. An element of $\widehat{\omega} \in so(3)$ is regarded as a vector $\omega \in \Re^{3\times 1}$, while an element of $se(3)$ is represented as a 6×1 vector $\$ = (\upsilon, \omega) \in \Re^{6\times 1}$, termed as a *twist*. Interpreted using the theory of screws, a twist describes a general rigid body motion, simultaneously rotating and translating about a screw axis. ω is the unit directional vector of the screw axis and υ is the position of the screw axis relative to the origin.

On matrix Lie algebras, the *Lie bracket* is given by the matrix commutator: if A and B are elements of a matrix Lie algebra, then $[A, B] = AB - BA$. In particular, on $so(3)$, the Lie bracket of two elements correspond to their vector product: $[\omega_1, \omega_2] = \omega_1 \times \omega_2$. On $se(3)$, the Lie bracket of two elements (υ_1, ω_1) and (υ_2, ω_2) is given by:

$$[(\upsilon_1, \omega_1), (\upsilon_2, \omega_2)] = (\omega_1 \times \upsilon_2 - \omega_2 \times \upsilon_1, \omega_1 \times \omega_2) \tag{3.3}$$

An element of a Lie group can also be identified with a linear mapping between its Lie algebra via its *adjoint* representation, denoted by the symbol Ad. Suppose $\mathbf{T}_{ab}$ is a matrix Lie group with Lie algebra t. For every $X \in \mathbf{T}_{ab}$, the adjoint mapping $Ad_X : t \to t$ is defined by $Ad_X(V) = XVX^{-1}$ for $V \in t$. If $X = (\mathbf{p}_{ab}, \mathbf{R}_{ab})$ is an element of $SE(3)$, then its adjoint map acting on an element $V = (\upsilon_{ab}, \omega_{ab})$ of $se(3)$ is described as either:

$$Ad_X(V) = (\mathbf{p}_{ab} \times \mathbf{R}_{ab}\omega_{ab} + \mathbf{R}_{ab}\upsilon_{ab}, \mathbf{R}_{ab}\omega_{ab}) \tag{3.4}$$

Or its 6×6 matrix representation:

$$Ad_X(V) = \begin{bmatrix} \mathbf{R}_{ab} & \widehat{\mathbf{p}}_{ab}\mathbf{R}_{ab} \\ 0 & \mathbf{R}_{ab} \end{bmatrix} \begin{bmatrix} \upsilon_{ab} \\ \omega_{ab} \end{bmatrix} \tag{3.5}$$

Additional properties:

1. $Ad_X^{-1} = Ad_{X^{-1}}$

2. $Ad_X Ad_Y = Ad_{XY}$ for any $X, Y \in SE(3)$.

Elements of Lie algebra can also be identified with a linear mapping between its Lie algebra via the Lie bracket. Given an element $V \in t$, its adjoint representation is the linear map $ad_X : t \to t$, defined by $ad_X(V) = [X, V]$. If $X = (v_1, \omega_1)$ and $V = (v_2, \omega_2)$ are elements of $se(3)$, then the adjoint representation can be described as either:

$$ad_X V = (\omega_1 \times v_2 - \omega_2 \times v_1, \omega_1 \times \omega_2) \tag{3.6}$$

Or its 6×6 matrix representation:

$$ad_X V = \begin{bmatrix} \widehat{\omega}_1 & \widehat{v}_1 \\ 0 & \widehat{\omega}_1 \end{bmatrix} \begin{bmatrix} v_2 \\ \omega_2 \end{bmatrix} \tag{3.7}$$

Additional property:

1. $ad_X V = -ad_V X$

In robot kinematics, Lie algebra is applied to determine the generalized velocities of rigid bodies [75]. A tangent vector $\dot{X}(t)$ of a curve $X(t) = (\mathbf{p}_{ab}(t), \mathbf{R}_{ab}(t)) \in SE(3)$ can be identified with an element of $se(3)$ in two ways:

1. If $X(t)$ describes the motion of a rigid body with regards to the body-attached frame, then $\widehat{V}^b_{ab} = X^{-1}\dot{X} = (\mathbf{R}^{-1}_{ab}\dot{\mathbf{p}}_{ab}, \mathbf{R}^{-1}_{ab}\dot{\mathbf{R}}_{ab})$ is an element of $se(3)$. $\widehat{V}^b_{ab}$ is referred to as the *body velocity* representation of $\dot{X}$ since $\mathbf{R}^{-1}_{ab}\dot{\mathbf{R}}_{ab}$ and $\mathbf{R}^{-1}_{ab}\dot{\mathbf{p}}_{ab}$ are the angular and translational velocities of the rigid body expressed in its body-attached frame respectively.

2. If the description is with regards to a spatial[3] reference frame, then $\widehat{V}^s_{ab} = \dot{X}X^{-1} = (\dot{\mathbf{p}}_{ab} - \dot{\mathbf{R}}_{ab}\mathbf{R}^{-1}_{ab}\mathbf{p}_{ab}, \dot{\mathbf{R}}_{ab}\mathbf{R}^{-1}_{ab})$ is also an element of $se(3)$. $\widehat{V}^s_{ab}$ is referred to as the *spatial velocity* representation of $\dot{X}$. A vital difference in the interpretation of the spatial

[3] The word 'spatial' is sometimes used to distinguish planar motions in $\Re^2$ and general (spatial) motions in $\Re^3$. For this description, 'spatial' is used to describe the fixed or inertial reference frame.

velocity is that $\dot{\mathbf{R}}_{ab}\mathbf{R}_{ab}^{-1}$ is the angular velocity of the rigid body expressed in the spatial frame, while the translational velocity expressed in the spatial frame is not $\dot{\mathbf{p}}_{ab} - \dot{\mathbf{R}}_{ab}\mathbf{R}_{ab}^{-1}\mathbf{p}_{ab}$, but simply $\dot{\mathbf{p}}_{ab}$.

Thus, from the above-mentioned descriptions, it is observed that $V_{ab}^{s} = (\upsilon_{ab}^{s}, \omega_{ab}^{s})$ and $V_{ab}^{b} = (\upsilon_{ab}^{b}, \omega_{ab}^{b})$ are related by the adjoint transformation as follows:

$$V_{ab}^{s} = Ad_{\mathbf{T}_{ab}} V_{ab}^{b} \tag{3.8}$$

Where:

$$\omega_{ab}^{s} = \mathbf{R}_{ab}\omega_{ab}^{b} \tag{3.9}$$

$$\upsilon_{ab}^{s} = \mathbf{p}_{ab} \times \mathbf{R}_{ab}\omega_{ab}^{b} + \mathbf{R}_{ab}\upsilon_{ab}^{b} \tag{3.10}$$

Additional properties:

1. $V_{ab}^{b} = -V_{ba}^{s}$

2. $V_{ab}^{b} = -Ad_{\mathbf{T}_{ba}} V_{ba}^{b}$.

(Please refer to [75, 76] for more details on Lie group rigid body kinematic descriptions and properties.)

In the following sections, the kinematic analyses of three types of CDMs are presented: the 1-DOF CDPM, the 3-DOF CDPM and the 7-DOF CDRA (which consists of serially connected CDPMs). This will include the forward/inverse displacement analyses and the derivation of equations for the velocity and acceleration analysis. It is assumed that *a minimum of* $(n+1)$ *cables are in positive tension* such that the moving platform is sufficiently restrained and the cables can be represented by kinematically equivalent SPS rigid-links [60].

3.2 Kinematic Analysis of the 1-DOF CDPM

The kinematic diagram of a sufficiently restrained 1-DOF CDPM is shown in Fig. 3.1, where the moving platform is connected to the base by a central constraint leg with a revolute joint, and a minimum of two driving cables. This is to ensure that the moving platform is constrained to produce a 1-DOF rotary motion about the revolute joint axis at point O. B_i are cable attachment points on the base, while P_i are cable attachment points on the moving platform.

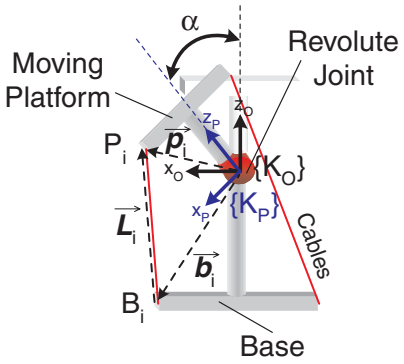

Figure 3.1: Kinematic diagram of a 1-DOF CDPM

3.2.1 Displacement Analysis

The purpose of displacement analysis is to determine the relationship between the pose of the moving platform and the cable lengths. From Fig. 3.1, an inertial frame $\{K_O\}$ is attached to the base and a local frame $\{K_P\}$ is attached to the moving platform. The origin of both frames are located at the revolute joint. By convention, all quantities are written in frame $\{K_O\}$ unless specified by a trailing superscript p to denote that it is in frame $\{K_P\}$. Hence, the orientation of the moving platform with respect to the inertial base frame is given by:

$$\mathbf{T}_{OP} = \begin{bmatrix} \mathbf{R}_{OP} & \mathbf{p}_{op} \\ 0 & 1 \end{bmatrix} \tag{3.11}$$

Where:

$\mathbf{R}_{OP} = \mathbf{R}_y(\alpha) = \begin{bmatrix} \cos\alpha & 0 & \sin\alpha \\ 0 & 1 & 0 \\ -\sin\alpha & 0 & \cos\alpha \end{bmatrix}$: The orientation of frame $\{K_P\}$ about the y axis with respect to the inertial frame $\{K_O\}$

$\mathbf{p}_{op} = \{0, 0, 0\}^T$: The position vector of point P with respect to point O expressed in the inertial frame

The vector-closure equation for each cable is written as:

$$\overrightarrow{OB_i} + \overrightarrow{B_iP_i} = \overrightarrow{OP_i} \qquad (i = 1, \ldots, m) \tag{3.12}$$

Hence, the cable lengths l_i are related to the pose of the moving platform via the length (Euclidean norm) of the vector $\mathbf{L}_i$ $\left(= \overrightarrow{B_iP_i}\right)$, as:

$$\begin{aligned} l_i &= \left\| \overrightarrow{OP_i} - \overrightarrow{OB_i} \right\| \\ &= \|\mathbf{R}_{OP} \cdot \mathbf{p}_i{}^p - \mathbf{b}_i\| \\ &= \sqrt{(\mathbf{b}_i)^2 + (\mathbf{p}_i{}^p)^2 - 2(\mathbf{b}_i)^T(\mathbf{R}_{OP} \cdot \mathbf{p}_i{}^p)} \end{aligned} \tag{3.13}$$

Where:

$\mathbf{b}_i = \{b_{ix}, b_{iy}, b_{iz}\}^T$: Fixed coordinates of point B_i with respect to frame $\{K_O\}$

$\mathbf{p}_i{}^p = \{p_{ix}^p, p_{iy}^p, p_{iz}^p\}^T$: Local coordinates of point P_i with respect to frame $\{K_P\}$

(a) Forward Displacement Analysis

The 1-DOF CDPM is very similar to a four-bar linkage mechanism except that the moving platform is constrained by a revolute joint. Having one unknown (i.e., orientation α), the closed form solution of its forward displacement is relatively straightforward and it is obtained by expanding Eqn. (3.13) as:

$$\begin{aligned} l_i{}^2 &= \left(b_{ix}{}^2 + b_{iz}{}^2\right) + \left((p_{ix}^p)^2 + (p_{iz}^p)^2\right) - 2\cos\alpha.\,(b_{ix}.p_{ix}^p + b_{iz}.p_{iz}^p) \\ &\quad -2\sin\alpha.\,(b_{ix}.p_{iz}^p - b_{iz}.p_{ix}^p) \qquad (i = 1, 2, \ldots \text{ or } m) \end{aligned} \tag{3.14}$$

By letting $t = \tan\frac{\alpha}{2}$, the sine and cosine of the unknown variable are expressed as:

$$\sin\alpha = \frac{2t}{1+t^2} \tag{3.15}$$

And,

$$\cos\alpha = \frac{1-t^2}{1+t^2} \tag{3.16}$$

Substituting Eqn. (3.15) and (3.16) into Eqn. (3.14), a second order polynomial equation is obtained as:

$$\mathbf{a}_i t^2 + \mathbf{b}_i t + \mathbf{c}_i = 0 \tag{3.17}$$

Where:

$$\mathbf{a}_i = {l_i}^2 - ({b_{ix}}^2 + {b_{iz}}^2) - ((p_{ix}^p)^2 + (p_{iz}^p)^2) - 2.(b_{ix}.p_{ix}^p + b_{iz}.p_{iz}^p)$$

$$\mathbf{b}_i = 4.(b_{ix}.p_{iz}^p - b_{iz}.p_{ix}^p)$$

$$\mathbf{c}_i = {l_i}^2 - ({b_{ix}}^2 + {b_{iz}}^2) - ((p_{ix}^p)^2 + (p_{iz}^p)^2) + 2.(b_{ix}.p_{ix}^p + b_{iz}.p_{iz}^p)$$

The solutions of Eqn. (3.17) are given as:

$$t_1, t_2 = \frac{-\mathbf{b}_i \pm \sqrt{{\mathbf{b}_i}^2 - 4.\mathbf{a}_i.\mathbf{c}_i}}{2\mathbf{a}_i} \tag{3.18}$$

Where:

$$\alpha_1 = 2.\arctan t_1$$

$$\alpha_2 = 2.\arctan t_2$$

The univariate polynomial Eqn. (3.17) is very significant because from a single cable length, only two possible solutions (α_1 *or* α_2) can be obtained, but the real solutions have to be examined using Eqn. (3.14) to see if they are within the mechanical joint limits. However, for a 1-DOF CDPM with m cable lengths, the forward displacement procedure is slightly different. This procedure will involve utilizing any one cable length to determine the pose, and from the obtained pose, the remaining cable lengths are verified if the calculated and actual lengths are equal.

However, in practical applications, there will seldom be the case where the calculated length will match the actual length. Hence, for practical implementations, this approach can be modified to ensure that a pose is always feasible, provided the other design constraints are satisfied. Instead of verifying whether the calculated and actual lengths are equal, these remaining cable lengths can be adjusted to be equal to the required calculated lengths, and thus satisfying the kinematic displacement criterions.

(b) Inverse Displacement Analysis

In the inverse displacement analysis, the orientation of the moving platform of the 1-DOF CDPM is given. Hence, the cable lengths $(l_1, \ldots, l_m)$ need to be determined. This is done by direct substitution of the orientation angle α into Eqn. (3.13).

3.2.2 Velocity Analysis

The objective of velocity analysis is to determine the instantaneous kinematic relationship between the velocity of the moving platform with the spooling velocity of the cables. The Jacobian Matrix, $\mathbf{J}_{//}$, indicates this relationship which is a function of the orientation of the moving platform, and it holds with the assumption of *positive cable tension* such that the cables can be represented by its kinematically equivalent SPS rigid link.

In order to derive the instantaneous kinematic relationship of the 1-DOF CDPM, Eqn. (3.13) must first be differentiated with respect to time, which results in the following:

$$l_i.\dot{l}_i = -(\mathbf{b}_i)^T(\dot{\mathbf{R}}_{OP}.{\mathbf{p}_i}^p) + (\mathbf{R}_{OP}.{\mathbf{p}_i}^p)^T(\dot{\mathbf{R}}_{OP}.{\mathbf{p}_i}^p) \tag{3.19}$$

From differential kinematics of rigid body [63], the differential of an orthogonal matrix results in $\dot{\mathbf{R}}_{OP} = \widehat{\boldsymbol{\omega}}\mathbf{R}_{OP}$, where $\widehat{\boldsymbol{\omega}}$ is a 3×3 skew-symmetric matric consisting of the angular velocity components relative to the inertial frame $\{K_O\}$. Utilizing this observation in Eqn. (3.19)

and rearranging it, this results in a simplified form as follows:

$$\dot{l}_i = (\mathbf{p}_i \times \mathbf{l}_i)\boldsymbol{\omega} \tag{3.20}$$

Where $\mathbf{l}_i = \mathbf{L}_i / \| \mathbf{L}_i \|$ is a unit vector along the i^{th} cable and $\mathbf{p}_i = \mathbf{R}_{OP}.{\mathbf{p}_i}^p$ is the position vector of P_i with respect to the inertial frame $\{K_O\}$. From Eqn. (3.20), m scalar equations can be rearranged to form the instantaneous kinematic relationship, which is generally expressed as:

$$\dot{\mathbf{L}} = \mathbf{J}_{//}\ \dot{\mathbf{X}} \tag{3.21}$$

Where:

$\dot{\mathbf{L}} = \{\dot{l}_1 \quad \cdots \quad \dot{l}_m\}^T$: The spooling velocity of the cables

$\mathbf{J}_{//} = {\mathbf{J}_L}^{-1}\ \mathbf{J}_X$

$\mathbf{J}_X = \begin{bmatrix} (\mathbf{p}_1 \times \mathbf{L}_1)^T \\ \vdots \\ (\mathbf{p}_m \times \mathbf{L}_m)^T \end{bmatrix}$: Also known as the $(m \times n)$ Forward Jacobian Matrix

$\mathbf{J}_L = \begin{bmatrix} l_1 & 0 & 0 \\ 0 & \ddots & 0 \\ 0 & 0 & l_m \end{bmatrix}$: Also known as the $(m \times m)$ Inverse Jacobian Matrix

$\dot{\mathbf{X}} = \boldsymbol{\omega} = \{0, \omega_y, 0\}^T$: The rotational velocity of the moving platform of the 1-DOF CDPM, expressed in frame $\{K_O\}$

3.2.3 Acceleration Analysis

The objective of the acceleration analysis is to determine the relationship between the acceleration of the moving platform with the spooling acceleration of the cable. This analysis will be critical when carrying out the dynamic analysis of the cable-driven parallel mechanism. The spooling acceleration of the cables is obtained by directly differentiating Eqn. (3.21) once, with respect to time. This results in the following:

$$\ddot{\mathbf{L}} = \mathbf{J}_{//}\ \ddot{\mathbf{X}} + \dot{\mathbf{J}}_{//}\ \dot{\mathbf{X}} \tag{3.22}$$

Where:

$\ddot{\mathbf{L}} = \{\ddot{l}_1 \quad \cdots \quad \ddot{l}_m\}^T$: The spooling acceleration of the cables

$$\dot{\mathbf{J}}_{//} = \left(\dot{\mathbf{J}_L}^{-1}\right) \mathbf{J}_X + \mathbf{J}_L{}^{-1}\, \dot{\mathbf{J}}_X$$

$$= \begin{bmatrix} -\dot{l}_1.{l_1}^{-2} & 0 & 0 \\ 0 & \ddots & 0 \\ 0 & 0 & -\dot{l}_m.{l_m}^{-2} \end{bmatrix} . \begin{bmatrix} (\mathbf{p}_1 \times \mathbf{L}_1)^T \\ \vdots \\ (\mathbf{p}_m \times \mathbf{L}_m)^T \end{bmatrix}$$

$$+ \begin{bmatrix} {l_1}^{-1} & 0 & 0 \\ 0 & \ddots & 0 \\ 0 & 0 & {l_m}^{-1} \end{bmatrix} . \begin{bmatrix} (\mathbf{b}_1 \times (\boldsymbol{\omega} \times \mathbf{p}_1))^T \\ \vdots \\ (\mathbf{b}_m \times (\boldsymbol{\omega} \times \mathbf{p}_m))^T \end{bmatrix}$$

$\ddot{\mathbf{X}} = \dot{\boldsymbol{\omega}} = \{0, \dot{\omega}_y, 0\}^T$: The rotational acceleration of the moving platform of the 1-DOF CDPM, expressed in frame $\{K_O\}$

3.3 Kinematic Analysis of the 3-DOF CDPM

The kinematic diagram of a sufficiently restrained 3-DOF CDPM is shown in Fig. 3.2, where the moving platform is connected to the base by a central constraint leg with a spherical joint, and a minimum of four driving cables. This is to ensure that the moving platform is constrained to produce a 3-DOF spherical motion about the spherical joint at point O. B_i are cable attachment points on the base, while P_i are cable attachment points on the moving platform.

3.3.1 Displacement Analysis

Similar to the displacement analysis of the 1-DOF CDPM, an inertial frame $\{K_O\}$ is attached to the base and a local frame $\{K_P\}$ is attached to the moving platform, as shown in Fig. 3.2. The origin of both frames are located at the spherical joint. The orientation of the moving

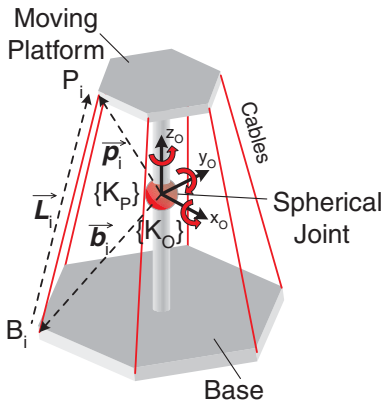

Figure 3.2: Kinematic diagram of a 3-DOF CDPM

platform with respect to the inertial base frame is given by:

$$\mathbf{T}_{OP} = \begin{bmatrix} \mathbf{R}_{OP} & \mathbf{p}_{op} \\ 0 & 1 \end{bmatrix} \tag{3.23}$$

Where:

$$\begin{aligned} \mathbf{R}_{OP} &= \mathbf{R}_z(\phi)\mathbf{R}_y(\theta)\mathbf{R}_z(-\phi)\mathbf{R}_{z'}(\sigma) = \mathbf{R}_z(\phi)\mathbf{R}_y(\theta)\mathbf{R}_z(\sigma-\phi) \\ &= \begin{bmatrix} c\phi c\theta c(\sigma-\phi) - s\phi s(\sigma-\phi) & -c\phi c\theta s(\sigma-\phi) - s\phi c(\sigma-\phi) & c\phi s\theta \\ s\phi c\theta c(\sigma-\phi) + c\phi s(\sigma-\phi) & -s\phi c\theta s(\sigma-\phi) + c\phi c(\sigma-\phi) & s\phi s\theta \\ -s\theta c(\sigma-\phi) & s\theta s(\sigma-\phi) & c\theta \end{bmatrix} \end{aligned}$$

(Cosine and Sine of the angles are denoted by c and s respectively.)

The Tilt-&-Torsion angles representation (Tilt Angles (ϕ and θ) and Torsion Angle (σ)), also known as the modified Z-Y-Z Euler angles [77] (see Fig. 3.3), is adopted for the displacement analysis of the 3-DOF CDPM due to its intuitive and compact visualization. The angles ϕ, θ and σ are described as:

ϕ: The angle between the base x-axis and the projection of the approach vector onto the base xy-plane

θ: The angle between base z-axis and the moving z'-axis

σ: The angle of rotation about the moving z'-axis with respect to a predefined x'-axis reference line

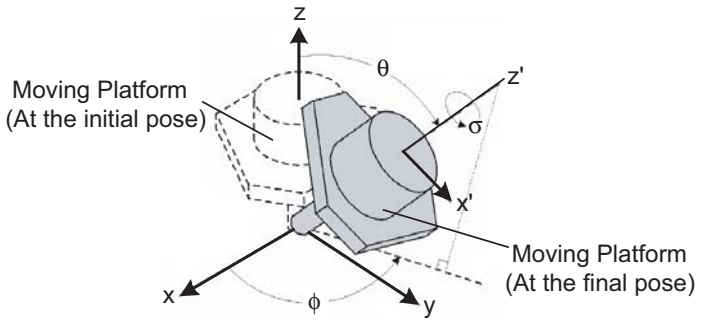

Figure 3.3: Tilt-&-Torsion angles representation [77]

(a) Forward Displacement Analysis

Numerous efforts have been made in obtaining the closed-form solution of rigid-linked spherical mechanisms, resulting in an eight-degree univariate polynomial equation [78, 79]. However, for a 3-DOF CDPM, the redundant link poses additional constraints in obtaining a closed-form solution and such solutions generally do not exist over most of the poses. Geometrical methods using tetrahedrons have also been proposed by Song and Kwon [80], by special arrangement of the links and using a novel numerical method using two unknown link lengths. Forward displacement analysis was carried out using the tetrahedron approach but it was realized that these methods are most suitable for parallel mechanisms with specific arrangement of links and require complex formulations that are more time-consuming than the numerical-iterative approach. Ceccarelli [81, 82, 83] also proposed a coordinate-free forward displacement solution using the tetrahedron observations in a 3-2-1 configured pose estimation device. This was formulated based on the Cayley-Menger determinants which was mathematically more tractable as the terms were determinants with geometric meanings. Ming and Higuchi [60] proposed an approach to utilize n cable lengths, of a n-DOF CDPM, to obtain the possible poses based on the closed-form solutions. After which, the remaining $(m-n)$ cable lengths are determined from the inverse displacement analysis, using the previously obtained possible poses. Hence, this is a very suitable approach to adopt in the forward displacement analysis especially during the motion control implementation phase. In this section, a closed-form solution is formulated for the optimal designed 3-DOF CDPM configuration (i.e., 3-3 six-cable). The numerical forward displacement analysis of

the general 3-DOF CDPM configuration will not be addressed as it can be easily formulated based on the Newton-Raphson numerical approach presented by Williams [71].

Closed-Form Solution for a 3-3 six-cable CDPM configuration

Although a numerical method is available to address the forward displacement analysis of a general 3-DOF CDPM case, a closed-form solution is always preferred. For the optimal designed 3-DOF CDPM (see Fig. 3.4), the 3-3 six-cable configuration forms the vertex of three tetrahedrons i.e., the cable end-points P_i $(i = 1, 2, 3)$. Thus, by utilizing this tetrahedron observation, we propose a closed-form forward kinematics solution. Frame $\{K_O\}$ is the inertial coordinate frame located at the spherical joint centre. Frame $\{K_P\}$ is the local coordinate frame on the moving platform and also located at the spherical joint centre, but it undergoes a 3-DOF (orientation) rigid-body rotation $\mathbf{R}_{OP}$ with respect to $\{K_O\}$. $\overrightarrow{OB_j}^{\{O\}} = \{b_{xj}, b_{yj}, b_{zj}\}^T$ $(j = 1, 2, 3)$ are base cable attachment point position vectors that are fixed with respect to $\{K_O\}$, while $\overrightarrow{OP_i}^{\{P\}} = \{{p_{xi}}^p, {p_{yi}}^p, {p_{zi}}^p\}^T$ $(i = 1, 2, 3)$ are the moving platform cable attachment point position vectors that are fixed with respect to $\{K_P\}$.

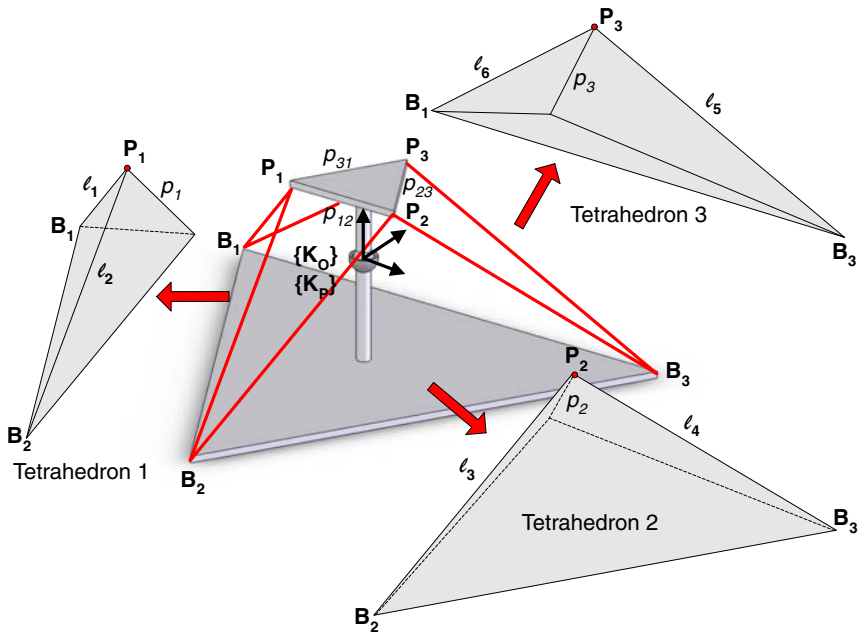

Figure 3.4: Kinematic diagram of the 3-3 six-cable 3-DOF CDPM with observed tetrahedrons

As shown in Fig. 3.4, the 3-DOF CDPM module is redundantly driven by six cables to generate 3-DOF rotational motions about the spherical joint. In fact, three cable lengths are enough to determine $\mathbf{R}_{OP}$. Here, for ease of computation, four cable lengths (i.e., l_1, l_2, l_3 and l_4) are chosen. Suppose P_i with respect to the inertial frame $\{K_O\}$ is given by $\overrightarrow{OP_i} = \{p_{xi}, p_{yi}, p_{zi}\}^T$ $(i = 1, 2, 3)$, then for the Tetrahedron '1', we have the following:

$$p_1^2 = p_{x1}^2 + p_{y1}^2 + p_{z1}^2 \tag{3.24}$$

$$l_1^2 = (p_{x1} - b_{x1})^2 + (p_{y1} - b_{y1})^2 + (p_{z1} - b_{z1})^2 \tag{3.25}$$

$$l_2^2 = (p_{x1} - b_{x2})^2 + (p_{y1} - b_{y2})^2 + (p_{z1} - b_{z2})^2 \tag{3.26}$$

In Eqns. (3.24)-(3.26), only $\{p_{x1}, p_{y1}, p_{z1}\}$ is unknown. Solving these three equations, at most two set of solutions can be obtained for $\{p_{x1}, p_{y1}, p_{z1}\}$. Similarly, for Tetrahedron '2', another two sets of solutions can be determined for $\{p_{x2}, p_{y2}, p_{z2}\}$. Suppose the known local coordinates of point P_i with respect to frame $\{K_S\}$ are given (i.e., $\overrightarrow{OP_i}^{\{P\}}$), then under $\mathbf{R}_{OP}$, we obtain the following:

$$\mathbf{R}_{OP}\ \overrightarrow{OP_1}^{\{P\}} = \overrightarrow{OP_1} \tag{3.27}$$

$$\mathbf{R}_{OP}\ \overrightarrow{OP_2}^{\{P\}} = \overrightarrow{OP_2} \tag{3.28}$$

$$\mathbf{R}_{OP}\ \left(\overrightarrow{OP_1}^{\{P\}} \times \overrightarrow{OP_2}^{\{P\}}\right) = \overrightarrow{OP_1} \times \overrightarrow{OP_2} \tag{3.29}$$

From Eqns. (3.27)-(3.29), we obtain the following:

$$\mathbf{R}_{OP} = \left[\overrightarrow{OP_1}, \overrightarrow{OP_2}, \left(\overrightarrow{OP_1} \times \overrightarrow{OP_2}\right)\right] \left[\overrightarrow{OP_1}^{\{P\}}, \overrightarrow{OP_2}^{\{P\}}, \left(\overrightarrow{OP_1}^{\{P\}} \times \overrightarrow{OP_2}^{\{P\}}\right)\right]^{-1} \tag{3.30}$$

Since both $\overrightarrow{OP_1}$ and $\overrightarrow{OP_2}$ may have two set of solutions, at most four set of solutions can be obtained for $\mathbf{R}_{OP}$. However, these solutions have to be checked with the other two remaining cable lengths (i.e., l_5 and l_6) through inverse kinematics and the tension-closure condition. Normally, only one solution will be valid.

(b) Inverse Displacement Analysis

Similar to the inverse displacement analysis of the 1-DOF CDPM, the orientation $\{\phi,\ \theta,\ \sigma\}$ of the moving platform of the 3-DOF CDPM is given. Hence, the cable lengths $(l_1, \ldots, l_m)$ need to be determined. This is done by direct substitution of $\{\phi,\ \theta,\ \sigma\}$ into Eqn. (3.13).

3.3.2 Velocity Analysis

Similar to the velocity analysis of the 1-DOF CDPM, the Jacobian matrix of the 3-DOF CDPM which gives the instantaneous kinematic relationship, is similar to that given in Eqn. (3.21). The only difference is that the velocity $\dot{\mathbf{X}}$ of the moving platform consists of three rotational velocity components $\{\omega_x,\ \omega_y,\ \omega_z\}$.

Transformation between $(\omega_x, \omega_y, \omega_z)$ ***and*** $(\dot{\phi},\ \dot{\theta},\ \dot{\sigma})$

From rigid body kinematics, the mapping from the angular velocity $(\omega_x, \omega_y, \omega_z)$ to the instantaneous values of the Tilt-&-Torsion angles $(\dot{\phi},\ \dot{\theta},\ \dot{\sigma})$ is expressed as:

$$\begin{Bmatrix} \omega_x \\ \omega_y \\ \omega_z \end{Bmatrix} = \boldsymbol{E}_{T\&T} \begin{Bmatrix} \dot{\phi} \\ \dot{\theta} \\ \dot{\sigma} \end{Bmatrix} \tag{3.31}$$

Where:

$$\boldsymbol{E}_{T\&T} = \begin{bmatrix} -\cos\phi\sin\theta & -\sin\phi & \cos\phi\sin\theta \\ -\sin\phi\sin\theta & \cos\phi & \sin\phi\sin\theta \\ (1-\cos\theta) & 0 & \cos\theta \end{bmatrix}$$

(Refer to Appendix A for formulation details.)

Alternatively, the instantaneous values of the Tilt-&-Torsion angles $(\dot{\phi},\ \dot{\theta},\ \dot{\sigma})$ is obtained from the given angular velocity $(\omega_x, \omega_y, \omega_z)$ from Eqn. (3.31) as follows:

$$\begin{Bmatrix} \dot{\phi} \\ \dot{\theta} \\ \dot{\sigma} \end{Bmatrix} = \boldsymbol{S}_{T\&T} \begin{Bmatrix} \omega_x \\ \omega_y \\ \omega_z \end{Bmatrix} \tag{3.32}$$

Where:

$$\boldsymbol{S}_{T\&T} = \boldsymbol{E}_{T\&T}{}^{-1} = \begin{bmatrix} \frac{-\cos\phi\cos\theta}{\sin\theta} & \frac{-\sin\phi\cos\theta}{\sin\theta} & 1 \\ -\sin\phi & \cos\phi & 0 \\ \frac{\cos\phi\sin\theta}{(1+\cos\theta)} & \frac{\sin\phi\sin\theta}{(1+\cos\theta)} & 1 \end{bmatrix}$$

The velocity transformations obtained in this section will be useful during the motion control and path planning stage.

3.3.3 Acceleration Analysis

Similar to the acceleration analysis of the 1-DOF CDPM, the instantaneous kinematic relationship of the 3-DOF CDPM is similar to Eqn. (3.22). The only difference is that the acceleration $\ddot{\mathbf{X}}$ of the moving platform consists of three rotating acceleration components $\{\dot{\omega}_x,\ \dot{\omega}_y,\ \dot{\omega}_z\}$.

Transformation between $(\dot{\omega}_x, \dot{\omega}_y, \dot{\omega}_z)$ ***and*** $(\ddot{\phi},\ \ddot{\theta},\ \ddot{\sigma})$

The transformation mapping from the angular acceleration $(\dot{\omega}_x, \dot{\omega}_y, \dot{\omega}_z)$ to the instantaneous acceleration values of the Tilt-&-Torsion angles $(\ddot{\phi},\ \ddot{\theta},\ \ddot{\sigma})$ can be obtained by differentiating Eqn. (3.31) once with respect to time. This is given as:

$$\begin{aligned} \begin{Bmatrix} \dot{\omega}_x \\ \dot{\omega}_y \\ \dot{\omega}_z \end{Bmatrix} &= \dot{\boldsymbol{E}}_{T\&T} \begin{Bmatrix} \dot{\phi} \\ \dot{\theta} \\ \dot{\sigma} \end{Bmatrix} + \boldsymbol{E}_{T\&T} \begin{Bmatrix} \ddot{\phi} \\ \ddot{\theta} \\ \ddot{\sigma} \end{Bmatrix} \\ &= \left(\boldsymbol{E}_{\phi}\dot{\phi} + \boldsymbol{E}_{\theta}\dot{\theta}\right) \begin{Bmatrix} \dot{\phi} \\ \dot{\theta} \\ \dot{\sigma} \end{Bmatrix} + \boldsymbol{E}_{T\&T} \begin{Bmatrix} \ddot{\phi} \\ \ddot{\theta} \\ \ddot{\sigma} \end{Bmatrix} \end{aligned} \tag{3.33}$$

Where:

$$\boldsymbol{E}_{\phi} = \frac{\partial \boldsymbol{E}_{T\&T}}{\partial \phi} = \begin{bmatrix} \sin\phi\sin\theta & -\cos\phi & -\sin\phi\sin\theta \\ -\cos\phi\sin\theta & -\sin\phi & \cos\phi\sin\theta \\ 0 & 0 & 0 \end{bmatrix}$$

$$\boldsymbol{E}_\theta = \frac{\partial \boldsymbol{E}_{T\&T}}{\partial \theta} = \begin{bmatrix} -\cos\phi\cos\theta & 0 & \cos\phi\cos\theta \\ -\sin\phi\cos\theta & 0 & \sin\phi\cos\theta \\ \sin\theta & 0 & -\sin\theta \end{bmatrix}$$

Alternatively, the instantaneous acceleration terms $(\ddot{\phi},\ \ddot{\theta},\ \ddot{\sigma})$ can be obtained from the given angular acceleration terms $(\dot{\omega}_x, \dot{\omega}_y, \dot{\omega}_z)$ by differentiating Eqn. (3.32) once with respect to time. This is given by:

$$\begin{Bmatrix} \ddot{\phi} \\ \ddot{\theta} \\ \ddot{\sigma} \end{Bmatrix} = \dot{\boldsymbol{S}}_{T\&T} \begin{Bmatrix} \omega_x \\ \omega_y \\ \omega_z \end{Bmatrix} + \boldsymbol{S}_{T\&T} \begin{Bmatrix} \dot{\omega}_x \\ \dot{\omega}_y \\ \dot{\omega}_z \end{Bmatrix}$$

$$= \left(\boldsymbol{S}_\phi \dot{\phi} + \boldsymbol{S}_\theta \dot{\theta}\right) \begin{Bmatrix} \omega_x \\ \omega_y \\ \omega_z \end{Bmatrix} + \boldsymbol{S}_{T\&T} \begin{Bmatrix} \dot{\omega}_x \\ \dot{\omega}_y \\ \dot{\omega}_z \end{Bmatrix}$$

$$= \left(\boldsymbol{S}_\phi \boldsymbol{E}_{T\&T(1)} \begin{Bmatrix} \omega_x \\ \omega_y \\ \omega_z \end{Bmatrix} + \boldsymbol{S}_\theta \boldsymbol{E}_{T\&T(2)} \begin{Bmatrix} \omega_x \\ \omega_y \\ \omega_z \end{Bmatrix} \right) \begin{Bmatrix} \omega_x \\ \omega_y \\ \omega_z \end{Bmatrix} + \boldsymbol{S}_{T\&T} \begin{Bmatrix} \dot{\omega}_x \\ \dot{\omega}_y \\ \dot{\omega}_z \end{Bmatrix} \tag{3.34}$$

Where:

$$\boldsymbol{S}_\phi = \frac{\partial \boldsymbol{S}_{T\&T}}{\partial \phi} = \begin{bmatrix} \frac{\sin\phi\cos\theta}{\sin\theta} & \frac{-\cos\phi\cos\theta}{\sin\theta} & 0 \\ -\cos\phi & -\sin\phi & 0 \\ \frac{-\sin\phi\sin\theta}{(1+\cos\theta)} & \frac{\cos\phi\sin\theta}{(1+\cos\theta)} & 0 \end{bmatrix}$$

$$\boldsymbol{S}_\theta = \frac{\partial \boldsymbol{S}_{T\&T}}{\partial \theta} = \begin{bmatrix} \frac{\cos\phi}{\sin^2\theta} & \frac{\sin\phi}{\sin^2\theta} & 0 \\ 0 & 0 & 0 \\ \frac{\cos\phi}{(1+\cos\theta)} & \frac{\sin\phi}{(1+\cos\theta)} & 0 \end{bmatrix}$$

$\boldsymbol{E}_{T\&T(i)}$: i^{th} row vector of $\boldsymbol{E}_{T\&T}$

The acceleration transformations obtained in this section will be useful during the motion control and path planning stage.

3.4 Kinematic Analysis of the 7-DOF CDRA

In order to develop a robotic arm with similar functionality as the human arm, a 'parallel-in-series' structured 7-DOF cable-driven robotic arm is proposed, which consists of serially connected set of a 3-DOF CDPM (i.e., representing the shoulder module), a 1-DOF CDPM (i.e., representing the elbow module) and another 3-DOF CDPM (i.e., representing the wrist module), as shown in Fig. 3.5. This section will address the kinematic analysis of this 7-DOF CDRA.

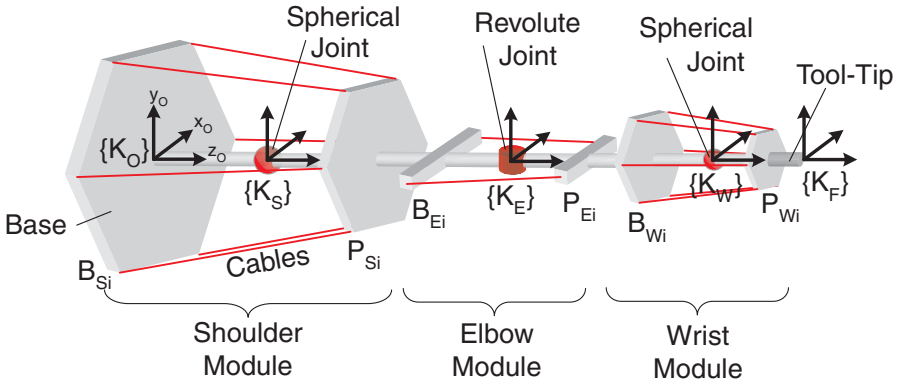

Figure 3.5: Kinematic diagram of a 7-DOF CDRA

3.4.1 Displacement Analysis

The purpose of displacement analysis is to determine the kinematic relationship between the cable lengths and the tool-tip poses of the 7-DOF CDRA. To facilitate the kinematic formulations, a number of global and local frames are attached to the 7-DOF CDRA, as shown in Fig. 3.5. (Kindly note that all of the local frames are parallel to each other in the arm's initial home configuration.)

The position and orientation of the tool-tip frame $\{K_F\}$ on the moving platform of the wrist module with respect to the inertial base frame $\{K_O\}$ is given by:

$$\mathbf{T}_{OF} = \mathbf{T}_{OS}\ \mathbf{T}_{SE}\ \mathbf{T}_{EW}\ \mathbf{T}_{WF} \tag{3.35}$$

Where:

$$\mathbf{T}_{OF} = \begin{bmatrix} \mathbf{R}_{OF} & \mathbf{p}_{of} \\ \mathbf{0} & 1 \end{bmatrix} \in SE(3), \mathbf{R}_{OF} \in SO(3) \text{ and } \mathbf{p}_{of} \in \Re^3$$

$$\mathbf{T}_{OS} = \begin{bmatrix} \mathbf{R}_{OS} & \mathbf{p}_{os} \\ \mathbf{0} & 1 \end{bmatrix} \in SE(3), \mathbf{R}_{OS} \in SO(3) \text{ and } \mathbf{p}_{os} \in \Re^3$$

$$\mathbf{T}_{SE} = \begin{bmatrix} \mathbf{R}_{SE} & \mathbf{p}_{se} \\ \mathbf{0} & 1 \end{bmatrix} \in SE(3), \mathbf{R}_{SE} \in SO(2) \text{ and } \mathbf{p}_{se} \in \Re^3$$

$$\mathbf{T}_{EW} = \begin{bmatrix} \mathbf{R}_{EW} & \mathbf{p}_{ew} \\ \mathbf{0} & 1 \end{bmatrix} \in SE(3), \mathbf{R}_{EW} \in SO(3) \text{ and } \mathbf{p}_{ew} \in \Re^3$$

$$\mathbf{T}_{WF} = \begin{bmatrix} \mathbf{I}_{3\times3} & \mathbf{p}_{wf} \\ \mathbf{0} & 1 \end{bmatrix} \in SE(3) \text{ and } \mathbf{p}_{wf} \in \Re^3$$

(a) Forward Displacement Analysis

The major issue in the forward displacement analysis of the 7-DOF CDRA is the determination of $\mathbf{T}_{OS}$ (i.e., $\mathbf{R}_{OS}$), $\mathbf{T}_{SE}$ (i.e., $\mathbf{R}_{SE}$) and $\mathbf{T}_{EW}$ (i.e., $\mathbf{R}_{EW}$), given the cable lengths of the individual CDPMs. This has been addressed in the previous sections. Hence, once the cable lengths for the three modular CDPMs are known, the tool-tip pose can then be uniquely determined. In a general simulation case, although the forward displacement solution may not exist due to the cable redundancy, the analysis algorithm is more appropriate for on-line computation of the tool-tip pose of a moving arm as the forward solution already exists.

(b) Inverse Displacement Analysis

The aim of inverse displacement analysis is to determine the lengths of the driving cables, given tool-tip pose $\mathbf{T}_{OF}$ and plays a key role in determining if this $\mathbf{T}_{OF}$ is reachable. In robotics, an inverse kinematic problem for a serial mechanism is cast into a system of non-linear equations or an optimization problem which is usually solved using an iterative numerical algorithm. In general, most conventional robotic arms have less than 6-DOF. However, in this case, the 7-DOF cable-driven robotic arm has a redundant DOF and the inverse solution

will be infinite.

In this redundant system, for a given tool-tip pose $\mathbf{T}_{OF}$, the joints are still free to move along a constrained surface in joint space, known as the *self-motion manifold* [84]. A simple physical interpretation of this redundant DOF is that if the joint of the wrist module is held fixed, the elbow module is free to swivel about a circular arc whose normal vector is parallel to the axis passing through the joints of the shoulder and wrist modules. This can be explained based on the early works on the workspace of such a 7-DOF robotic arm by Korein [85]. It was observed that the shoulder and the wrist joint limits restrict the elbow joint to lie on two spherical polygons, each with its centre located at the shoulder and wrist joints respectively. The intersection of these two polygons results in a circular arc with a set of feasible elbow pose as a function of the joint limits of the shoulder and wrist joints (see Fig. 3.6).

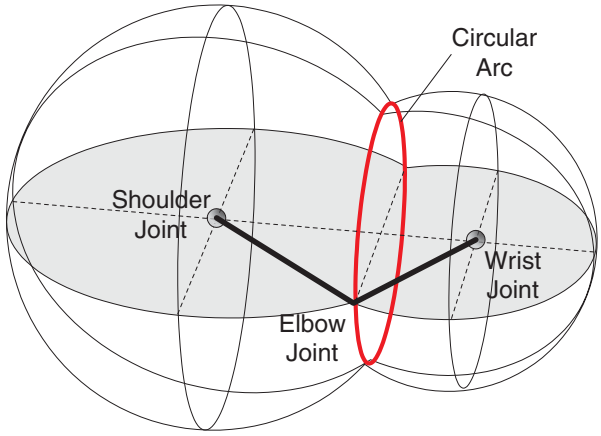

Figure 3.6: Intersection of two spherical polygons resulting in a circular arc

In this analysis, a task-decomposition technique is adopted such that the position of the wrist module joint is determined by the shoulder and elbow modules, while the orientation of frame $\{K_W\}$ is accommodated by the joint of the wrist module. Even after doing so, the 4-DOF shoulder-elbow assembly still has 1-DOF redundancy to identify a 3D point. Hence, an optimal solution approach, which optimizes the manipulability of the shoulder module, is proposed to obtain a unique inverse displacement solution.

For an inverse displacement problem, all the position vectors of the coordinates frames are known, and $\mathbf{T}_{OF}$ is user-specified. In addition, since $\mathbf{T}_{WF}$ is a known fixed transformation, right-multiplying both sides of Eqn. (3.35) with $\mathbf{T}_{WF}^{-1}$ results in:

$$\mathbf{T}_{OW} = \mathbf{T}_{OS}\ \mathbf{T}_{SE}\ \mathbf{T}_{EW} \tag{3.36}$$

Where:

$$\mathbf{T}_{OW} = \begin{bmatrix} \mathbf{R}_{OW} & \overrightarrow{OW}_{(Final)} \\ \mathbf{0} & 1 \end{bmatrix} \in SE(3)$$

$$\mathbf{R}_{OW} = \mathbf{R}_{OF}.{\mathbf{R}_{WF}}^{-1} \in SO(3)$$

$$\overrightarrow{OW}_{(Final)} = \overrightarrow{OF} - \mathbf{R}_{OW}\overrightarrow{WF} \in \Re^3$$

From these information, the next step is to determine the rotation matrices for the various CDPMs. The inverse displacement analysis is then carried out as follows (see Figs. 3.7 and 3.8):

- **Step 1:** (Figure 3.8(b))

  Determine the rotation matrix $\mathbf{R}_{SE}$ of the elbow module which is based on:

$$\begin{aligned} \mathbf{R}_{SE} &= \mathbf{R}_y(\theta_{se}) \\ &= \begin{bmatrix} \cos\theta_{se} & 0 & \sin\theta_{se} \\ 0 & 1 & 0 \\ -\sin\theta_{se} & 0 & \cos\theta_{se} \end{bmatrix} \end{aligned} \tag{3.37}$$

  Where:

$$\theta_{se} = \pi - \arccos\left(\frac{\left\|\overrightarrow{SE}\right\|^2 + \left\|\overrightarrow{EW}\right\|^2 - \left\|\overrightarrow{OW}\right\|^2}{2.\left\|\overrightarrow{SE}\right\|.\left\|\overrightarrow{EW}\right\|}\right)$$

  Determine feasibility of the pose by checking if the elbow module joint angle limits are not exceeded and a set of positive cable tension with tension-closure exists. Continue if and only if both conditions are satisfied.

- **Step 2:**

  Determine the rotation matrix $\mathbf{R}_{OS}$ of the shoulder module which is composed of two

rotation sequences[4]:

$$\mathbf{R}_{OS} = \mathbf{R}_{OS2}\ \mathbf{R}_{OS1} \tag{3.38}$$

Where $\mathbf{R}_{OS1}$ and $\mathbf{R}_{OS2}$ are based on the Equivalent Angle-Axis rotation matrix representation, which is described as:

$\mathbf{R}_{\text{Equiv. Angle-Axis}}(\{k_x, k_y, k_z\}^T, \psi) =$

$$\begin{bmatrix} k_xk_x(1-c\psi)+c\psi & k_xk_y(1-c\psi)-k_zs\psi & k_xk_z(1-c\psi)+k_ys\psi \\ k_xk_y(1-c\psi)+k_zs\psi & k_yk_y(1-c\psi)+c\psi & k_yk_z(1-c\psi)-k_xs\psi \\ k_xk_z(1-c\psi)-k_ys\psi & k_yk_z(1-c\psi)+k_xs\psi & k_zk_z(1-c\psi)+c\psi \end{bmatrix} \tag{3.39}$$

- **Step 2a:** (Figure 3.8(c))

  Determine the rotation matrix $\mathbf{R}_{OS1}$ of the shoulder module such that the wrist module joint centre reaches the desired point $\overrightarrow{OW}_{(Final)}$. This is given by:

$$\mathbf{R}_{OS1} = \mathbf{R}_{\text{Equiv. Angle-Axis}}(Axis_{os1}, \theta_{os1}) \tag{3.40}$$

  Where:

  $Axis_{os1} : \left(\mathbf{R}_{SE}\overrightarrow{OW}\right) \times \overrightarrow{OW}_{(Final)}$

  $\theta_{os1} = \arccos\left(\dfrac{\left(\mathbf{R}_{SE}\overrightarrow{OW}\right)^T\overrightarrow{OW}_{(Final)}}{\left\|\mathbf{R}_{SE}\overrightarrow{OW}\right\|\left\|\overrightarrow{OW}_{(Final)}\right\|}\right)$: Angle between $\mathbf{R}_{SE}\overrightarrow{OW}$ and $\overrightarrow{OW}_{(Final)}$

- **Step 2b:** (Figure 3.8(d))

  Determine the rotation matrix $\mathbf{R}_{OS2}$ of the shoulder module such that the configuration has optimal manipulability. This is given by:

$$\mathbf{R}_{OS2} = \mathbf{R}_{\text{Equiv. Angle-Axis}}(Axis_{os2}, \theta_{os2}) \tag{3.41}$$

  Where:

  $Axis_{os2} : \overrightarrow{OW}_{(Final)}$

  θ_{os2} : It ranges from 0 to 2π

[4] $\mathbf{R}_{OS2}$ is pre-multiplied as the subsequent rotation sequence is about the fixed inertial axis.

Rotating θ_{os2} from 0 to 2π will not change the position of the wrist module joint centre and each pose is a possible solution. Hence, an optimization criteria has to be adopted to obtain an ideal solution for $\mathbf{R}_{OS2}$. Numerous optimization criterions have been proposed such as minimum potential energy and minimum rotation angle, but for this 7-DOF cable-driven robotic arm, the maximum manipulability is adopted as the objective is to achieve an assistive robotic arm that is as dexterous as the human arm. The manipulability of a pose is determined by using the pose dependent Jacobian matrix $\mathbf{J}$ of the shoulder module (given in Section 3.3.2) as follows:

$$m_J = \sqrt{det(\mathbf{J}^T\mathbf{J})} \tag{3.42}$$

Note that m_J is a local measure and it is dependent on $\mathbf{R}_{OS2}$. Hence, the optimal $\mathbf{R}_{OS2}$ (i.e., optimal θ_{os2}) is determined by maximizing m_J.

Determine feasibility of the pose by checking if the shoulder module joint angle limits are not exceeded and a set of positive cable tension with tension-closure exists. Continue if and only if both conditions are satisfied.

- **Step 3:** (Figure 3.8(e))

  Determine the rotation matrix $\mathbf{R}_{EW}$ of the wrist CDPM from Eqn. (3.36) which results in:

$$\mathbf{R}_{EW} = (\mathbf{R}_{SE})^{-1} \ (\mathbf{R}_{OS})^{-1} \ \mathbf{R}_{OW} \tag{3.43}$$

  Where:

  $\mathbf{R}_{SE}$: Determined from Step 1

  $\mathbf{R}_{OS}$: Determined from Step 2

  Determine feasibility of the pose by checking if wrist module joint angle limits are not exceeded and a set of positive cable tension with tension-closure exists.

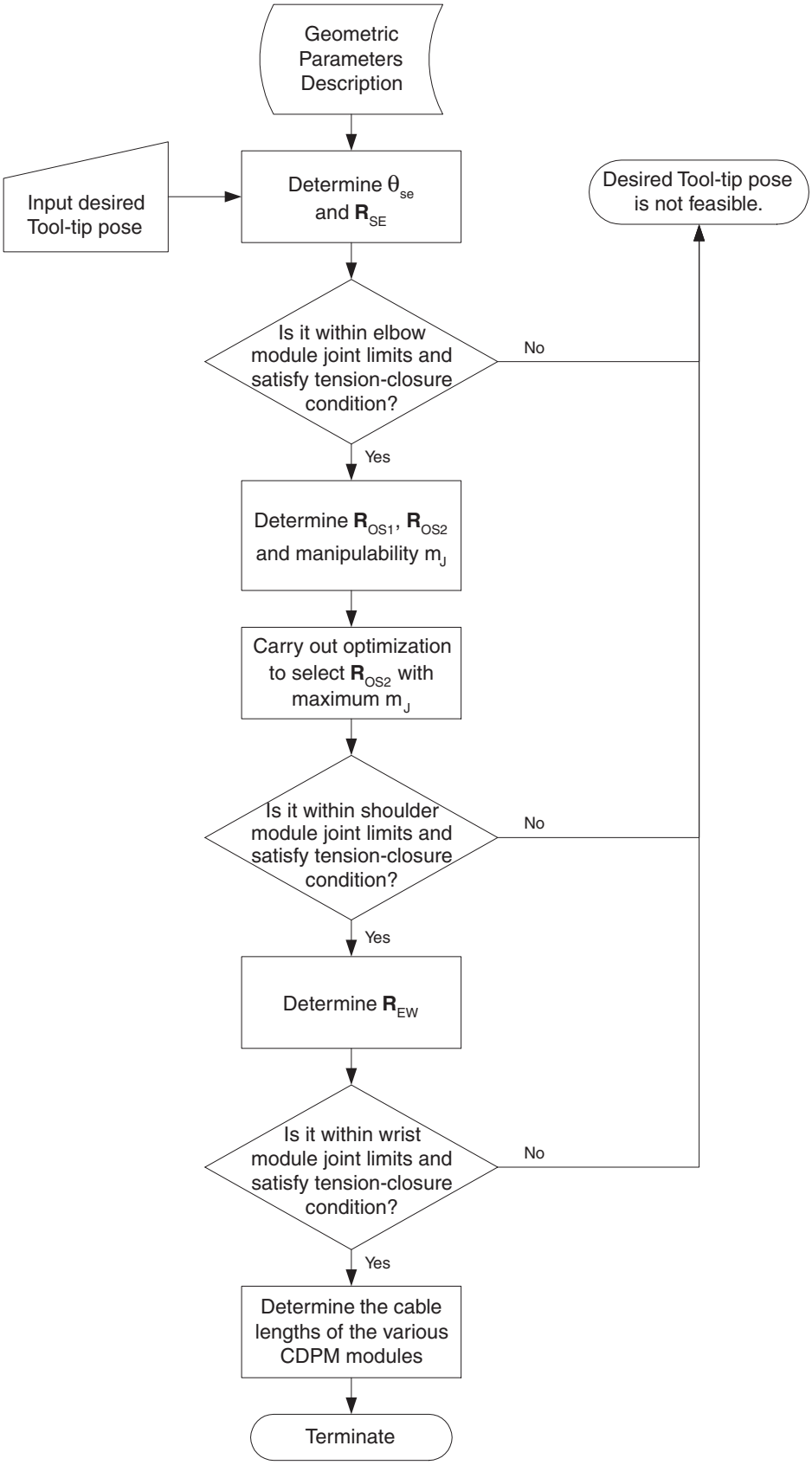

Figure 3.7: Flowchart of the inverse displacement analysis of the 7-DOF CDRA

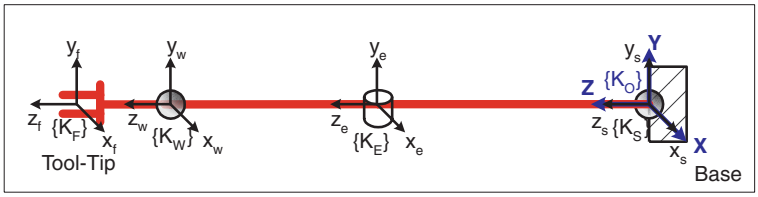

(a) Home pose of the 7-DOF CDRA

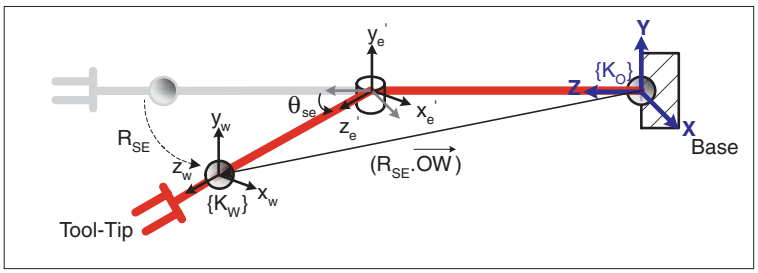

(b) Step 1 - Rotation ($\mathbf{R}_{SE}$) of the elbow module

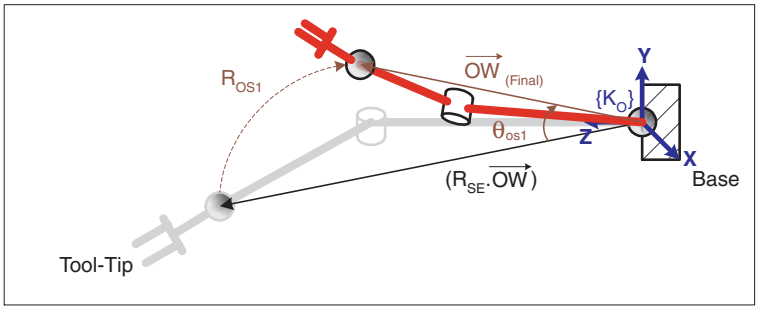

(c) Step 2a - Rotation ($\mathbf{R}_{OS1}$) of shoulder module to $\mathbf{OW}_{(Final)}$

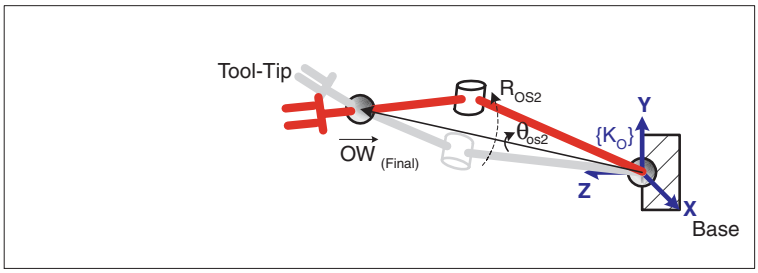

(d) Step 2b - Rotation ($\mathbf{R}_{OS2}$) of shoulder module about $\mathbf{OW}_{(Final)}$ with optimal manipulability

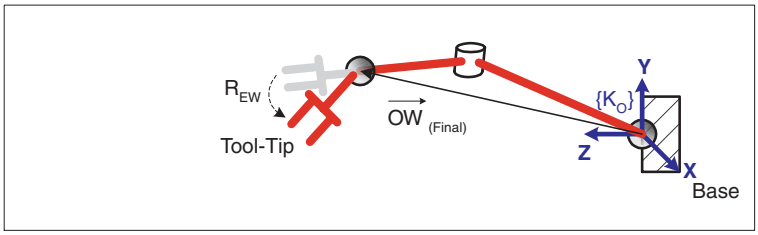

(e) Step 3 - Rotation ($\mathbf{R}_{EW}$) of wrist module

Figure 3.8: Inverse kinematics sequence steps for the 7-DOF CDRA

Computation Example: In order to verify the proposed inverse kinematics algorithm, simulation studies are carried out on a 7-DOF cable-driven robotic arm with a 3-3 six-cable configuration for the shoulder and wrist modules, and a 2-2 two-cable configuration for the elbow module (see Fig. 3.9). The kinematic parameters for the various individual modules at home pose are as follows:

$$
\begin{cases}
\mathbf{p}_{os} = \{0, 0, 72\}, & \mathbf{b}_{s1}^{\{O\}} = \mathbf{b}_{s2}^{\{O\}} = \{0, 129, 0\}, & \mathbf{b}_{s3}^{\{O\}} = \mathbf{b}_{s4}^{\{O\}} = \{-111.7, -64.5, 0\}, \\
 & \mathbf{b}_{s5}^{\{O\}} = \mathbf{b}_{s6}^{\{O\}} = \{111.7, -64.5, 0\}, & \mathbf{p}_{s1}^{\{S\}} = \mathbf{p}_{s6}^{\{S\}} = \{42.4, 24.5, 51\}, \\
 & \mathbf{p}_{s2}^{\{S\}} = \mathbf{p}_{s3}^{\{S\}} = \{-42.4, 24.5, 51\}, & \mathbf{p}_{s4}^{\{S\}} = \mathbf{p}_{s5}^{\{S\}} = \{0, -49, 51\} \\
\mathbf{p}_{se} = \{0, 0, 300\}, & \mathbf{b}_{e1}^{\{S\}} = \{-55, 0, 57\}, & \mathbf{b}_{e2}^{\{S\}} = \{19, 0, -82\}, \\
 & \mathbf{p}_{e1}^{\{E\}} = \{-51.5, 0, 80\}, & \mathbf{p}_{e2}^{\{E\}} = \{28.5, 0, 80\} \\
\mathbf{p}_{ew} = \{0, 0, 200\}, & \mathbf{b}_{w1}^{\{E\}} = \mathbf{b}_{w2}^{\{E\}} = \{39, 22.5, 150\}, & \mathbf{b}_{w3}^{\{E\}} = \mathbf{b}_{w4}^{\{E\}} = \{-39, 22.5, 150\}, \\
 & \mathbf{b}_{w5}^{\{E\}} = \mathbf{b}_{w6}^{\{E\}} = \{0, -45, 150\}, & \mathbf{p}_{w1}^{\{W\}} = \mathbf{p}_{w6}^{\{W\}} = \{34.6, -20, 50\}, \\
 & \mathbf{p}_{w2}^{\{W\}} = \mathbf{p}_{w3}^{\{W\}} = \{0, 40, 50\}, & \mathbf{p}_{w4}^{\{W\}} = \mathbf{p}_{w5}^{\{W\}} = \{-34.6, -20, 50\} \\
\mathbf{p}_{wf} = \{0, 0, 75\} & & \text{(All dimensions are in } \textit{millimeters}.\text{)}
\end{cases}
$$

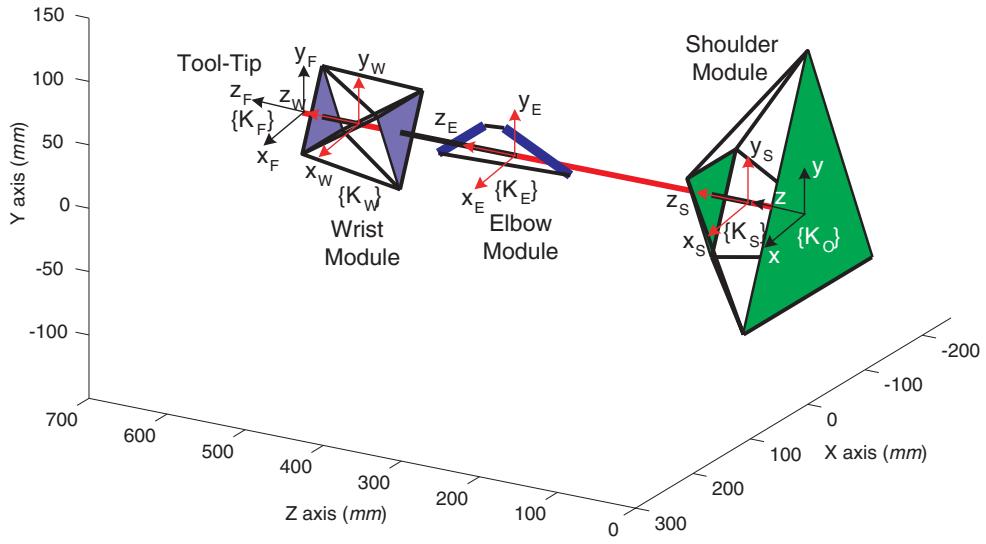

Figure 3.9: Home pose description of 7-DOF CDRA used for simulation study

Table 3.1 presents the inverse kinematics solution at various desired tool-tip poses and the cable lengths required in each module, while Fig. 3.10 presents the inverse kinematics solution for each pose in Table 3.1. The inverse displacement analysis algorithm was implemented in MATLAB using the 'fmincon' function. The optimal solutions for the various desired tool-tip poses were obtained within five to six iterations.

Table 3.1: Simulation results for the inverse kinematics of the 7-DOF CDRA

Desired Tool-Tip Pose Description	Cable Lengths (mm)		
	Shoulder	Elbow	Wrist
Pose (i): $\begin{bmatrix} 0.6155 & -0.2282 & 0.7544 & 0 \\ 0.1970 & 0.9713 & 0.1330 & 0 \\ -0.7631 & 0.0668 & 0.6428 & 572 \\ 0 & 0 & 0 & 1 \end{bmatrix}$	$L_{S1} = 173.9$ $L_{S2} = 156.8$ $L_{S3} = 142.1$ $L_{S4} = 147.2$ $L_{S5} = 178.5$ $L_{S6} = 189.4$	 $L_{E1} = 89.6$ $L_{E2} = 127.2$ 	$L_{W1} = 85.9$ $L_{W2} = 98.8$ $L_{W3} = 108.7$ $L_{W4} = 123.8$ $L_{W5} = 114.4$ $L_{W6} = 104.8$
Pose (ii): $\begin{bmatrix} 0.8206 & 0.1087 & 0.5610 & -25 \\ -0.0498 & 0.9916 & -0.1193 & 75 \\ -0.5693 & 0.0699 & 0.8192 & 522 \\ 0 & 0 & 0 & 1 \end{bmatrix}$	$L_{S1} = 158.4$ $L_{S2} = 154.2$ $L_{S3} = 123.9$ $L_{S4} = 153.2$ $L_{S5} = 184.7$ $L_{S6} = 201.9$	 $L_{E1} = 118.9$ $L_{E2} = 100.7$ 	$L_{W1} = 108.7$ $L_{W2} = 118.7$ $L_{W3} = 118.0$ $L_{W4} = 105.3$ $L_{W5} = 95.1$ $L_{W6} = 94.9$
Pose (iii): $\begin{bmatrix} 0.0911 & -0.1361 & 0.9865 & 300 \\ -0.0224 & 0.9901 & 0.1386 & -100 \\ -0.9956 & -0.0348 & 0.0872 & 372 \\ 0 & 0 & 0 & 1 \end{bmatrix}$	$L_{S1} = 180.7$ $L_{S2} = 176.4$ $L_{S3} = 174.8$ $L_{S4} = 154.4$ $L_{S5} = 159.5$ $L_{S6} = 152.1$	 $L_{E1} = 125.8$ $L_{E2} = 92.9$ 	$L_{W1} = 111.5$ $L_{W2} = 94.5$ $L_{W3} = 102.4$ $L_{W4} = 102.4$ $L_{W5} = 119.4$ $L_{W6} = 115.5$
Pose (iv): $\begin{bmatrix} 0.8434 & -0.0886 & -0.5299 & -75 \\ 0.1045 & 0.9945 & 0 & -100 \\ 0.5270 & -0.0554 & 0.8480 & 572 \\ 0 & 0 & 0 & 1 \end{bmatrix}$	$L_{S1} = 184.6$ $L_{S2} = 164.9$ $L_{S3} = 141.7$ $L_{S4} = 139.6$ $L_{S5} = 169.9$ $L_{S6} = 185.3$	 $L_{E1} = 94.1$ $L_{E2} = 123.7$ 	$L_{W1} = 128.8$ $L_{W2} = 104.4$ $L_{W3} = 68.2$ $L_{W4} = 68.1$ $L_{W5} = 85.2$ $L_{W6} = 119.5$

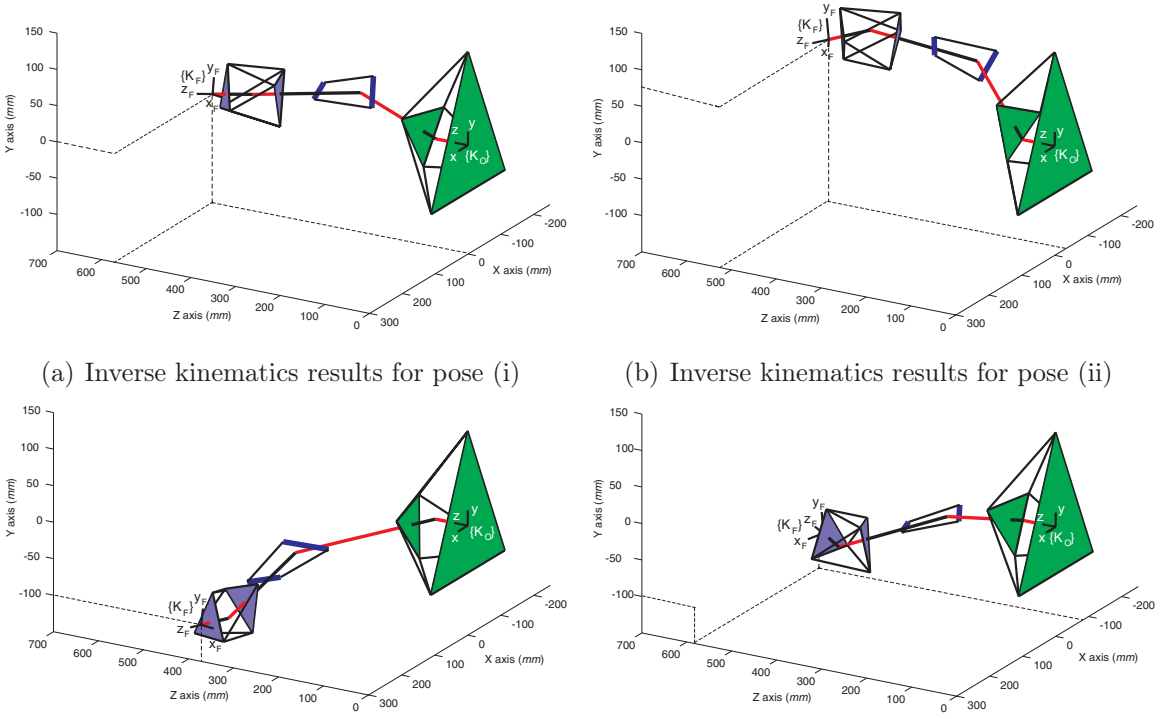

(a) Inverse kinematics results for pose (i)

(b) Inverse kinematics results for pose (ii)

(c) Inverse kinematics results for pose (iii)

(d) Inverse kinematics results for pose (iv)

Figure 3.10: Simulation results for inverse kinematics of the 7-DOF CDRA

3.4.2 Velocity Analysis

The objective of velocity analysis for the 7-DOF cable-driven robotic arm is to determine the instantaneous kinematic relationship between the tool-tip velocity and the spooling velocity of the cables of the various CDPMs connected serially to form the 7-DOF structure. The velocity analysis will be based on Lie algebra as described in Section 3.1.3. Differentiating Eqn. (3.35) once with respect to time results in the following:

$$\begin{aligned}\dot{\mathbf{T}}_{OF} &= \dot{\mathbf{T}}_{OS}\,\mathbf{T}_{SE}\,\mathbf{T}_{EW}\,\mathbf{T}_{WF} + \mathbf{T}_{OS}\,\dot{\mathbf{T}}_{SE}.\mathbf{T}_{EW}\,\mathbf{T}_{WF} + \\ &\quad \mathbf{T}_{OS}\,\mathbf{T}_{SE}\,\dot{\mathbf{T}}_{EW}\,\mathbf{T}_{WF} + \mathbf{T}_{OS}\,\mathbf{T}_{SE}\,\mathbf{T}_{EW}\,\dot{\mathbf{T}}_{WF} \end{aligned} \tag{3.44}$$

Note that $\dot{\mathbf{T}}_{WF} = 0$ as $\mathbf{T}_{WF}$ is a fixed transformation that does not change relative to time. Right-multiplying both sides of Eqn. (3.44) by $\mathbf{T}_{OF}^{-1}$ results in:

$$\begin{aligned}\dot{\mathbf{T}}_{OF}\,\mathbf{T}_{OF}^{-1} &= \dot{\mathbf{T}}_{OS}\,\mathbf{T}_{OS}^{-1} + \mathbf{T}_{OS}\,\dot{\mathbf{T}}_{SE}\,\mathbf{T}_{SE}^{-1}\,\mathbf{T}_{OS}^{-1} + \\ &\quad \mathbf{T}_{OS}\,\mathbf{T}_{SE}\,\dot{\mathbf{T}}_{EW}\,\mathbf{T}_{EW}^{-1}\,(\mathbf{T}_{OS}\,\mathbf{T}_{SE})^{-1} \end{aligned} \tag{3.45}$$

Equation (3.45) is termed as the differential kinematic equation of the 7-DOF CDRA. Geometrically, it describes the differential change in the tool-tip pose resulting from the differential changes in the cable length, viewed from the spatial (inertial) coordinate reference frame. Converting Eqn. (3.45) into its adjoint representation (expressed in the spatial coordinate frame) results in the following:

$$V^s_{OF} = V^s_{OS} + Ad_{T_{OS}}\ V^s_{SE} + Ad_{T_{OE}}\ V^s_{EW} \tag{3.46}$$

Where:

$V^s_{OF} = \begin{bmatrix} \upsilon^s_{of} \\ \omega^s_{of} \end{bmatrix}$: Tool-tip velocity expressed in spatial frame $\{K_O\}$

$V^s_{OS} = \begin{bmatrix} \upsilon^s_{os} \\ \omega^s_{os} \end{bmatrix}$: Velocity of the moving platform of the shoulder module expressed in frame $\{K_O\}$

$Ad_{T_{OS}} = \begin{bmatrix} \mathbf{R}_{OS} & \widehat{\mathbf{p}}_{os}\mathbf{R}_{OS} \\ 0 & \mathbf{R}_{OS} \end{bmatrix}$: Adjoint mapping of $\mathbf{T}_{OS}$

$\widehat{\mathbf{p}}_{os}$: Skew-symmetric matrix of $\mathbf{p}_{os}$

$V^s_{SE} = \begin{bmatrix} \upsilon^s_{se} \\ \omega^s_{se} \end{bmatrix}$: Velocity of the moving platform of the elbow module expressed in frame $\{K_S\}$

$Ad_{T_{OE}} = \begin{bmatrix} \mathbf{R}_{OS}\mathbf{R}_{SE} & \widehat{\mathbf{p}}_{oe}(\mathbf{R}_{OS}\mathbf{R}_{SE}) \\ 0 & \mathbf{R}_{OS}\mathbf{R}_{SE} \end{bmatrix}$: Adjoint mapping of $\mathbf{T}_{OE}$

$\widehat{\mathbf{p}}_{oe}$: Skew-symmetric matrix of $\mathbf{p}_{oe}(= \mathbf{p}_{os} + \mathbf{R}_{OS}\mathbf{p}_{se})$

$V^s_{EW} = \begin{bmatrix} \upsilon^s_{ew} \\ \omega^s_{ew} \end{bmatrix}$: Velocity of the moving platform of the wrist module expressed in frame $\{K_E\}$

(Refer to Appendix B for the details of the various velocity terms.)

3.4.3 Acceleration Analysis

The objective of acceleration analysis for the 7-DOF cable-driven robotic arm is to determine the relationship between the acceleration of the tool-tip located on the moving platform of the wrist module to the spooling accelerations of the cables, which will be critical when

carrying out dynamic analysis. The acceleration expression is obtained by differentiating Eqn. (3.46) once, with respect to time. This results in the following expression:

$$\dot{V}^s_{OF} = \dot{V}^s_{OS} + \dot{A}d_{T_{OS}}\ V^s_{SE} + Ad_{T_{OS}}\ \dot{V}^s_{SE} + \dot{A}d_{T_{OE}}\ V^s_{EW} + Ad_{T_{OE}}\ \dot{V}^s_{EW} \tag{3.47}$$

Where:

$\dot{V}^s_{OF} = \begin{bmatrix} \dot{\upsilon}^s_{of} \\ \dot{\omega}^s_{of} \end{bmatrix}$: Tool-tip acceleration expressed in spatial frame $\{K_O\}$

$\dot{V}^s_{OS} = \begin{bmatrix} \dot{\upsilon}^s_{os} \\ \dot{\omega}^s_{os} \end{bmatrix}$: Acceleration of the moving platform of the shoulder module expressed in spatial frame $\{K_O\}$

$\dot{A}d_{T_{OS}} = 2\ ad_{V^s_{OS}} Ad_{T_{OS}}$: First derivative of the adjoint mapping of $\mathbf{T}_{OS}$

$\dot{V}^s_{SE} = \begin{bmatrix} \dot{\upsilon}^s_{se} \\ \dot{\omega}^s_{se} \end{bmatrix}$: Acceleration of the moving platform of the elbow module expressed in spatial frame $\{K_S\}$

$\dot{A}d_{T_{OE}} = 2\ ad_{V^s_{OE}} Ad_{T_{OE}}$: First derivative of the adjoint mapping of $\mathbf{T}_{OE}$

$\dot{V}^s_{EW} = \begin{bmatrix} \dot{\upsilon}^s_{ew} \\ \dot{\omega}^s_{ew} \end{bmatrix}$: Acceleration of the moving platform of the wrist module expressed in spatial frame $\{K_E\}$

(Refer to Appendix B for the acceleration formulation and details of the various acceleration terms.)

3.5 Discussion

In this chapter, the kinematic analysis of the individual 1-DOF and 3-DOF CDPM modules as well as the entire 7-DOF cable-driven robotic arm, are presented.

The forward displacement solutions for the various CDMs are presented. The forward displacement of the 1-DOF CDPM is derived analytically due to its similarity to that of a four-bar linkage, while a closed-form forward displacement solution is formulated for the unique 3-3 six-cable configuration of the optimized 3-DOF CDPM modules (i.e., shoulder and wrist modules), and thus simplifying the computational effort. On the other hand, the

forward displacement for the 7-DOF CDRA is very straightforward, simply requiring direct substitution of the orientation parameters of each individual CDPM modules to determine the tool-tip pose.

The inverse displacement solution of the various CDMs are presented. The inverse displacement solutions of the 1-DOF and 3-DOF CDPM modules are straightforward, simply requiring direct substitution of the orientation to obtain the cable lengths. However, due to the redundancy of the 7-DOF CDRA, the inverse displacement analysis for the entire arm is not straightforward. Contributions are made in proposing an effective inverse displacement analysis approach using a task decomposition method in conjunction with a dimension reduction technique, which is computationally efficient. Given desired tool-tip poses, computational examples are given for the inverse displacement solution of a 7-DOF CDRA, which demonstrated the effectiveness of the task decomposition method in achieving suitable arm postures. However, it should be noted that the feasible displacement solutions must be checked for tension-closure conditions due to the unilateral driving property of cables, which will be addressed in the next chapter.

Velocity and acceleration analyses are carried out for both the individual CDPM modules and the entire 7-DOF arm. The result from these analyses will be useful for velocity-based control, dynamic formulation and tension-based control of the CDMs.

Chapter 4

Workspace-Related Analysis

Section 4.1 presents a brief overview on the workspace analysis of CDPMs, including the relevant workspace evaluation tools (i.e., cable tension, stiffness and singularity) and workspace generation. After defining the workspace of CDPMs in Section 4.2, Section 4.3 proposes a tension-closure approach to analyze the positive cable tension condition of the CDPMs, while Section 4.4 presents the stiffness matrix of the CDPM modules for subsequent use as a workspace quality measure. This is followed by workspace generation of the various human arm joints in Section 4.5 based on their motion ranges, while Section 4.6 proposes both quantitative and qualitative workspace performance measures. Section 4.7 then concludes with the discussion of the salient points in this chapter.

4.1 Background

Performance analysis plays a vital role in obtaining the fundamental tools to evaluate and carry out optimal designing of a mechanism. In literature, this has been generally done by analyzing certain workspace-related performance measures based on the kinematic properties of mechanisms. Hence, workspace analysis is a pertinent issue to address for subsequent development of performance measures and design optimization. In general, workspace analysis consists of three main components, namely: (i) workspace definition, (ii) workspace evaluation approaches, and (iii) workspace generation.

4.1.1 Workspace Definition

Before a workspace can be analyzed, it has to be given a definition to allow for subsequent development of evaluation tools and generation of the feasible workspace. From literature, the workspace of CDPMs have been classified into four main types, namely: (i) *Controllable* or *wrench-closure* workspace, which consists of a collection of poses where force and torque at end-effector can be controlled [86, 87], (ii) *Wrench-feasible* workspace, which is a subset of the wrench-closure workspace, but with the additional condition of being within the allowable cable tension bounds [88], (iii) *Statically reachable* workspace, which consists of a collection of poses that can be reached statically [89], and (iv) *Dynamic* workspace, which consists of a collection of poses which takes dynamics and the end-effector accelerations into consideration [90]. Based on these classifications, different workspace are generated, but all workspace evaluation still require cable tension analysis due to the unilateral driving property of cables.

4.1.2 Workspace Evaluation Tools

The definition of a workspace enables the subsequent development of evaluation tools to analyze a workspace pose. For parallel mechanisms, the workspace tools are based on the constraints imposed by the joint parameters and the closed-loop kinematic chains. For cable-driven parallel mechanisms (CDPMs), the joint parameters, namely the cable lengths, generally do not constraint the workspace since it can be considered infinite by rolling the cables into spools. Instead, the workspace is constrained due to the unilateral driving property of cables. Hence, the workspace of CDPMs have a pre-requisite of having a set of positive cable tension to sufficiently restraint the moving platform at each pose (i.e., tension-closure condition). In addition, the flexible nature of cables cause CDPMs to have relatively low stiffness and introduces vibration, thereby affecting the positional accuracy significantly. Hence, it is also crucial to carry out stiffness analysis to establish if a CDPM has sufficient stiffness at a particular pose.

(a) Cable Tension Analysis

In general, two main approaches have been adopted to analyze and determine the cable tension conditions of CDPMs, namely: (i) the *null space* approach, and (ii) the *geometrical* approach. Both methods utilize the Jacobian matrix transpose (also known as the Cable Structure matrix obtained through kinetostatic equilibrium analysis) in their calculations. The only difference is that the null space approach represents kinematic constraints in terms of subspaces (linear combination of spatial vectors) as compared to convexes (positive combination of contact forces) in the geometrical approach [91, 92]. However, an important observation to highlight between these two approaches is that the former approach is able to determine both the magnitude and sign of the cable tension, while the latter method is able to only determine the sign of the cable tension.

In the null space approach, linear algebraic tools are utilized to analyze the transpose of the

Jacobian matrix to determine the cable tension values. This is only possible if a homogenous solution exists to be able to obtain positive cable tensions, and thus leading to a conclusion that a n-DOF CDPM[1] must have a minimum of m $(= n + 1)$ cables in positive tension (One of the earliest works to present a mathematical proof for this observation was by Ming and Higuchi [60]). This approach has been adopted by several researchers to carry out cable tension analysis [74], feasible workspace construction [86] and optimal workspace determination [93, 94]. However, as the number of cables increase, this approach is no longer straightforward to check the positive cable tension condition and formulate the workspace boundaries.

In the geometrical approach, the cable tension vectors form convex hulls and the external wrench is checked to see if it lies inside the convex set. In this approach, the convexes represent the positive combinations of the pulling force. This approach has been adopted by several researchers to carry out analytical workspace boundary generation [95, 96] and theoretical study of the workspace [97, 90]. Zlatanov [98] also proposed an alternative method to study the geometrical features of convex 2-cones and 3-cones in screw spaces, which is limited when extended to cones of four or more independent screws. In addition, the complexity of such approaches increases for CDPMs having greater than 3-DOF. This issue was addressed by Bang [99], who proposed a recursive dimension reduction method to check tension-closure of high-dimensional task space and redundantly-restrained CDPMs (i.e., $m > n + 1$). This method reduces the space dimension and checks if the origin belongs to the convex hull.

In recent years, tools from multi-fingered grasping (i.e., Antipodal Grasping Theorem) have also been employed for cable tension analysis of CDPMs. This is because grasping involves a unidirectional constraint (i.e., can only exert compression, whereas it is the case of exerting tension for CDPMs), as pointed out by several researchers [91, 100, 101, 102]. However, in order to precisely match the grasping model to CDPMs, the effect of friction at the contact

[1] Such a CDPM is classified as sufficiently restrained and this thesis will only focus on such CDPM designs.

points is not truly present in CDPMs (i.e., no sliding involved). In addition, the surface normals must match the direction of the corresponding cables, unless two or more cables are attached at the same point on the moving platform. For such cases, these coincident cable attachments points are modeled as a single contact with friction. As pointed out by Ebert-Uphoff [91], there are some limitations to these analogies. In the CDPM analogy with frictionless grasping, the analogy is valid instantaneously as the grasped object shape changes, depending upon the pose of the moving platform. However, in the CDPM analogy with a parallel mechanism, the analogy is valid instantaneously and for only finite motion. As such, grasping tools are only valid for certain CDPM configurations and extensive research still needs to be conducted before grasping tools can be adopted for use in general CDPMs.

(b) Stiffness Analysis

The flexible nature of cables cause CDPMs to have relatively low stiffness and thereby significantly affecting the positional accuracy. For stiffness analysis, the pretension of cables is assumed to be large enough for the cables to be in tension and in the linear region of the stress-strain curve. In principle, a finite-element analysis will reveal more or less the complete information about the mechanism's elastic properties. However, such finite-element analyses are not only computationally expensive and time-consuming, but they are also not suitable for design iteration and optimization. Hence, kinematic approaches are preferred without resorting to computationally intensive procedures. One of the first few works in the field of CDPMs to address stiffness analysis was by Kawamura [101, 103, 104]. These works mainly investigated the influence of cable pretension on the stiffness of a CDPM with the aim of addressing the issue of vibration. Verhoeven [86] formulated a simplified stiffness matrix which was a function of the cable stiffness and cable length, and analyzed its eigenvalues to determine the nearness to singularity poses. Behzadipour [105] introduced a new approach to calculate the total stiffness matrix of a CDPM and to subsequently determine the stability of the moving platform, adapted from the work done by Svinin [106, 107] on rigid-link gough-stewart platforms. However, there still lacks a unified systematic approach for stiffness

analysis of CDPMs.

(c) Singularity Analysis

Another important aspect of workspace evaluation is the examination of singularity. The notion of singularity refers to configurations in which a parallel mechanism has uncontrollable DOFs instantaneously. In other words, a parallel mechanism loses its working capability at singularity configurations. The occurrence of singularity configurations in parallel mechanisms must be avoided at all costs during motion, as the actuators cannot control the motion even in the neighborhood of these singular configurations. As a consequence, knowledge of singular configurations is vital for motion control and singularity-free path planning. It also represents the basic information for the synthesis of a desired mechanism workspace, free from singularities.

One of the early works that addressed the singularity analysis was by Ma and Angeles [108]. In this work, singularities of parallel manipulators were classified into three categories, namely *architecture* singularity, *configuration* singularity and *formulation* singularity. Architecture singularity is a special case of configuration singularity, while formulation singularity is a trivial case because it is always avoidable by changing the associated kinematic model. Therefore, configuration singularity is the most pertinent singularity category as its avoidance is only possible at the trajectory-planning stage. One of the notable recent works to address configuration singularity was by Ottaviano and Ceccarelli [82, 83] through the use of an innovative 3-2-1 configured cable-based pose estimation device. Based on the unique tetrahedron geometry formed by the device configuration and through the use of Cayley-Menger determinants, the tetrahedron volume was utilized to identify singularity poses and the performance of the device. In [82], errors in cable length measurements were also taken into consideration to investigate its effects in pose estimation and the performance of the device.

Similar to parallel mechanisms, the configuration singularities of a CDPM can be classified

into three main groups, namely: (i) forward, (ii) inverse, and (iii) combined singularity. Based on Eqn. (3.21), forward singularity occurs when $\mathbf{J}_X$ loses rank, inverse singularity occurs when $\mathbf{J}_L$ loses rank, and combined singularity occurs when both matrices lose rank simultaneously. Matrix $\mathbf{J}_L$ is a diagonal matrix and it will lose rank only when one of the cable lengths become zero. For certain configurations, this may never happen due to the physical constraints imposed by the constraint links, and even if the configuration allow cables lengths to reach zero, this usually occurs at the workspace boundary. As a result, the inverse and combined singularity do not exist and only the forward singularity need to be investigated.

Forward singularity poses can be identified through rank analysis of matrix $\mathbf{J}_X$. For CDPMs, this matrix is usually a non-square matrix which complicates its rank analysis. In addition, the Jacobian matrix is meaningful only when all the driving cables are in positive tension. So if any of the driving cables become slack, the Jacobian matrix becomes invalid. Hence, in order to analyze the singularity of CDPMs, the unilateral property of cables need to be taken into account and hence, cable tension analysis is paramount before checking for singularity. If tension-closure condition is not satisfied, it means that the cable structure matrix $\mathbf{A}(= -\mathbf{J}_{//}^T)$ does not have full rank, which means that the Jacobian matrix also does not have full rank (since the rank of a matrix and its transpose are the same). Hence, cable tension analysis automatically determines if a particular pose is in singularity without the need for forward singularity analysis. Nevertheless, analysis of the conditioning of forward singularity is still required to identify if the CDPM is approaching neighboring areas that may experience loss in manipulability and dexterity. It also allows the analysis of the quality of the overall workspace.

(d) Workspace Performance Measures

The most widely studied performance measures are based on workspace quantity (i.e., volume) and workspace quality (i.e., manipulability, condition index, dexterity, stiffness). Al-

though majority of design optimization utilize workspace volume as a performance measure, a mechanism designed for maximum workspace may lead to undesirable kinematic characteristics such as poor dexterity or manipulability [109, 110]. Hence, it is also important to determine the quality of the workspace in addition to workspace quantization. A variety of workspace quality measures have been proposed such as manipulability, dexterity, condition index and stiffness, but most of them are equivalent to one another as they all depend on the conditioning of the Jacobian matrix [66]. A more commonly used workspace quality measure is the global condition index (GCI), which is a measure of the kinematic dexterity of the robot over the whole workspace [111]. Large values for GCI (close to one) ensure good performance with respect to force and velocity transmission. Regardless of the quality indices used, a mechanism far from singularities will always have a high workspace quality measure. For CDPMs, GCI has also been employed to study the workspace quality [93, 94]. However, Jacobian-based indices do not reflect the stiffness of the cables. Hence, several other measures have been proposed. Bosscher [112] proposed a slope-based measure to analyze the stability of an under-constrained CDPM (i.e., No. of cables $\leq$ DOF), while Verhoeven [113] proposed a tension factor which reflects the tension distribution among the cables. Bang [99] proposed a similar tension factor, but it utilized a linear programming approach. Hence, there is a need to look into an appropriate workspace quality measure for CDPMs which will take both cable stiffness and manipulability into consideration.

4.1.3 Workspace Generation

In tandem with the development of workspace evaluation tools, it is also vital to generate the overall workspace boundary of a mechanism. The workspace generated will represent the possible poses a mechanism can achieve provided it can satisfy certain criterions.

In literature, there have been two main approaches for the workspace generation of CDPMs, namely: (i) analytical and (ii) numerical approaches. The analytical approach derives the workspace from the closed-form solutions of the kinematic constraints, and the workspace

boundary is generally characterized by the occurrence of the loss of tension-closure condition[2]. Bosscher [96] characterized the wrench-feasible workspace boundary based on geometrical properties of the available net wrench set. Ethan [114] derived the closed-form expression for the workspace boundary based on convex analysis and using tools from semi-definite programming. Verhoeven [115] developed a method to find closed-form expressions of the conservative bounds for the controllable workspace. Oh and Agrawal [116, 117] proposed an interesting approach to analytically generate feasible workspace through the choice of a control law, which considered input constraints and disturbances. Based on a given initial condition, this method allowed recursive calculations of subsequent feasible domains, which is useful in extending the end-effector motion range. Although analytical methods have an explicit expression and high computational efficiency, they are more suited for lower DOF CDPMs with simpler kinematic constraints and architectures. Such approaches become complex and computationally challenging when incorporating actual implementation issues (such as mechanical interferences, task-specific kinematic constraints, cable tension bounds and CDPM configurations with redundant cables) due to the increasing number of inequalities to consider. Hence numerical approaches are generally more effective in coping with such cases, and are demonstrated in works by Ceccarelli [118], Pusey [94], Alp [119], Gosselin [120], and Bang [121].

The numerical approach generally involves using of discretization algorithms to quantify the workspace, solving the inverse kinematics at each pose, and verifying the constraints that limit the workspace. For CDPMs, this involves cable tension analysis. Such numerical approaches can be applied to any type of CDPM architectures. However, this approach requires proper representation of the pose parameters in the workspace with an equi-volumetric finite partitioning scheme. Ceccarelli [118] proposed such an equi-volumetric finite partition scheme based on a binary matrix formulation. This formulation divided the cross-section of the workspace into small rectangles, represented by a feature point. An efficient workspace boundary determination algorithm was also developed, which is based on the geometry of

[2] This is usually considered as a singularity pose is based on the conventional singularity definition as a pose where the moving platform has uncontrollable DOFs instantaneously.

the grid and the number of surrounding feature points.

There are two main categories of pose parameters, namely translational and orientation pose parameters [66]. Translational pose parameters can be easily visualized in 3-dimensional space and the visualization in $\Re^3$ represents the actual task space. However, is it not so trivial for the case of orientation pose parameters, especially $SO(3)$ orientations. There are several conventions that have been developed to represent and parameterize rigid body rotations, such as the Cayley-Rodrigues parameters, axis-angle parameters, unit quaternions, Euler angles, T-&-T angles, and exponential coordinates [77, 120, 122, 123]. Hence, there are two basic requirements to be considered in selection of the appropriate parameterization method: (i) the parametric domain must have a closed boundary so as to make finite partition possible, and (ii) the parameterization needs at most three parameters so that the embodied orientation workspace can be readily visualized in three-dimensional space.

There are three parameterization methods (among the various mentioned previously) which fulfill these two requirements, i.e., the Euler angles, the T-&-T angles, and the exponential coordinates. The rigid body rotation group $SO(3)$ can be represented as a rectangular parallelepiped [124], a solid cylinder [77] and a solid sphere [123] when using the Euler angles, the T-&-T angles and exponential parameterizations, respectively. Various partition schemes have been proposed for these three parameterization methods based on their geometries[3]. Nevertheless, these three partition schemes possess the same essential features, i.e., they are all equi-volumetric, parametric, proportional, and exact partitions of their corresponding geometric identities. However, as a result of the parameterization, integration measures have to be introduced when computing the workspace volume from its parametric domain. Consequently, the orientation workspace volume is numerically computed as a weighted sum of the equi-volumetric elements in which the weightages are the element associated integration measures [124]. Following this approach, various global performance measures of the orientation workspace can also be readily computed.

[3] Readers may refer to a related paper by the author [125] for details on the partition schemes proposed and the workspace analysis of the different parameterization methods.

4.2 'Maneuverable' Workspace

Extending from the various terminologies of workspace, the 'maneuverable workspace' (*MWS*) of a CDPM is generally described as a set of poses where the moving platform can be positioned and is able to maintain static equilibrium under any external wrenches. Therefore, a pose in the *MWS* must fulfill these criterions:

- The forward/inverse displacement solutions must exist
- A set of cables must be in positive tension to maintain the moving platform's pose in equilibrium (i.e., *tension-closure*)
- The pose must not be in singularity configuration
- The cables must not intersect with each other

In the above criterions, mechanical joint limits, minimum stiffness requirements, cable tension bounds, limitation of actuator power and motion controller capabilities are not listed because these depend on the working environment and practical implementation, rather than just theoretical limits.

4.3 Cable Tension Analysis

In this thesis, the proposed 7-DOF cable-driven robotic arm consists of serially attached 1-DOF and 3-DOF CDPM modules (presented earlier in Chapter 2). Hence, the tool-tip of the 7-DOF CDRA will be able to maintain its pose under any arbitrary external wrench with positive cable tensions in each of its individual CDPM modules (i.e., tension-closure) if and only if all the individual CDPM modules can achieve tension-closure. Hence, this thesis will focus on the cable tension analysis for only these two types of sufficiently restrained orientation CDPMs.

4.3.1 Cable Structure Matrix

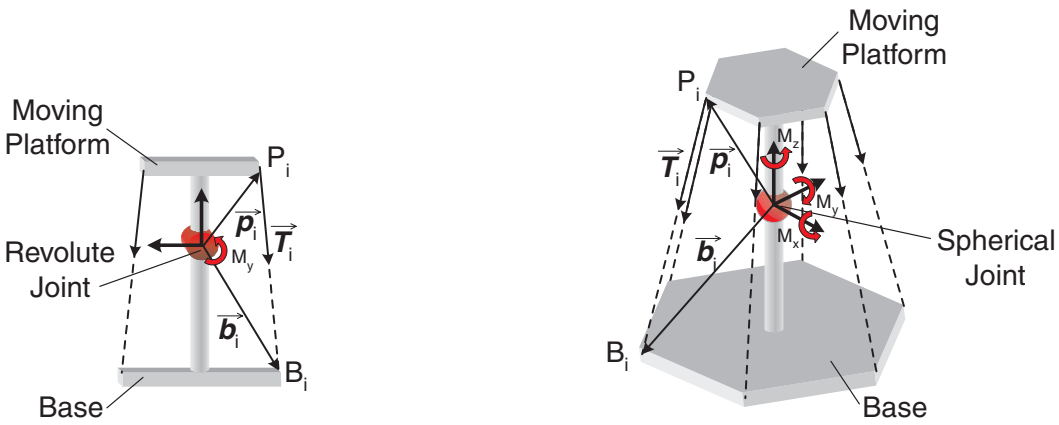

(a) 1-DOF CDPM (b) 3-DOF CDPM

Figure 4.1: Free body diagrams of the basic orientation CDPMs used to form the 7-DOF CDRA

The first step in cable tension analysis is to obtain a model which will enable the analysis of a particular pose to maintain equilibrium of the moving platform with positive cable tensions $\{t_1, \ldots, t_m\}$ under the influence of an arbitrary external wrench $\mathbf{W}_{Ext}$. Figure 4.1 shows the free body diagrams of both the 1-DOF and 3-DOF CDPMs. For a n-DOF orientation CDPM with m cables, the relationship between the cable tension vector, $\mathbf{T}$ and the external wrench, $\mathbf{W}_{Ext}$ under kinetostatic equilibrium is given by:

$$\mathbf{A}.\mathbf{T} = \mathbf{W}_{Ext} \tag{4.1}$$

Where:

$\mathbf{A} = [\mathbf{a}_1, \ldots, \mathbf{a}_m] \in \Re^{n \times m}$: The cable structure matrix

$\mathbf{a}_i = \mathbf{l}_i \times \mathbf{p}_i \in \Re^{n \times 1}$: The column vector of $\mathbf{A}$

$\mathbf{l}_i$: The unit vector of the i^{th} cable

$\mathbf{p}_i$: The position vector of i^{th} moving platform cable attachment point with respect to the base frame $\{K_O\}$

$\mathbf{T} = \{t_1, \ldots, t_m\}^T \in \Re^{m \times 1}$: The cable tension vector

For the 1-DOF CDPM, $\mathbf{W}_{Ext} = \{M_y\} \in \Re^{1 \times 1}$, while $\mathbf{W}_{Ext} = \{M_x, M_y, M_z\}^T \in \Re^{3 \times 1}$ for the

3-DOF CDPM. This is because the revolute and spherical joints on the central rigid links restraint all the external forces. The cable structure matrix $\mathbf{A}$ is dependent on the pose of the moving platform, and it is related to the Jacobian matrix $\mathbf{J}_{//}$ based on the following relationship:

$$\mathbf{A} = -\mathbf{J}_{//}{}^{T} \tag{4.2}$$

This relationship can be easily made by observation of the two matrices formulated in Eqns. (3.21) and (4.1).

4.3.2 Definition of Tension-Closure

A CDPM is said to be in *tension-closure* at a particular pose $\mathbf{X} \in SE(3)$ if and only if the moving platform can withstand any arbitrary external wrench $\mathbf{W}_{Ext}$ with a set of positive cable tensions under equilibrium conditions. This is without any bounds on the cable tension, and it is mathematically described as:

$$\forall\ \mathbf{W}_{Ext} \in \Re^n : \exists\ \mathbf{T} > 0, \ni\ \ \mathbf{A}.\mathbf{T} = \mathbf{W}_{Ext} \tag{4.3}$$

Where $\mathbf{T} \in \Re^m_+$ is referred to as a positive solution, where each component of cable tension vector $\mathbf{T}$=$\{t_1, \ldots, t_m\}^T$ is greater than zero. From Eqn. (4.3), tension-closure is achieved if and only if the column vectors of $\mathbf{A}$ (i.e., $\mathbf{a}_1, \ldots, \mathbf{a}_m$) are able to positively span $\Re^n$ and thus any arbitrary external wrench $\mathbf{W}_{Ext} \in \Re^n$ can be expressed as $\mathbf{W}_{Ext} = t_1\mathbf{a}_1 + \cdots + t_m\mathbf{a}_m$. For any set of vectors to positively span $\Re^n$, it must also be positively dependent (by selecting $\mathbf{W}_{Ext} = 0$) such that:

$$rank(\mathbf{A}) = n \tag{4.4}$$

$$\sum_{i=1}^{m} t_i\mathbf{a}_i = 0 \tag{4.5}$$

4.3.3 Tension-Closure Approach

Adapted from Murray [75], the tension-closure condition has an equivalent form and is defined as follows:

> *A pose is said to be in tension-closure if and only if there does NOT exist a vector* $v \in \Re^m$, $v \neq 0$, *such that for* $i = 1, \ldots, m$, $v^T \boldsymbol{a}_i = 0$ *or have the same sign.*

This tension-closure approach is based on convex analysis using Minkowski-Farka's Lemma and Stiemke's Theorem, and its proof can be found in [114, 126]. Geometrically, this statement can be interpreted as follows:

> For any hyperplane[4] passing through the origin of $\Re^n$, there should NOT exist a *supporting*[5] hyperplane such that all the columns of $\mathbf{A}$ (i.e., $\mathbf{a}_1, \ldots, \mathbf{a}_m$), except those on the hyperplane point (i.e., $\mathbf{a}_i$s used to form the hyperplane), lie on one side of the hyperplane. Instead, one of these remaining $(m - n + 1)$ $\mathbf{a}_i$s should lie on the other side of the hyperplane. Hence, for tension-closure, either no supporting hyperplanes should be found, or equivalently, all hyperplanes should be *separating*[6].

The next step in this tension-closure approach is the formulation of the associated hyperplanes and checking if any of these hyperplanes are supporting. For the 1-DOF CDPM, this becomes a very straightforward case of checking if the signs of the elements in the cable structure matrix $\mathbf{A}$ are of different signs.

[4] A hyperplane, which is affine and convex, divides a space into two half-spaces, where these half-spaces are convex sets.

[5] A hyperplane H is said to be a 'supporting' hyperplane to a convex set Y if Y is contained within one of the half-spaces of H and the boundary of Y has points in common with H.

[6] A hyperplane H is said to be a 'separating' hyperplane such that two convex sets, A and B, belong to different half-spaces of H.

For the 3-DOF CDPM, the hyperplanes are represented by planes and its normal vector is simply the cross-product of two vectors lying in the plane. Hence, in order to determine if a particular hyperplane is supporting, dot product is carried out between the hyperplane's normal vector v, and the remaining $(m-n+1)$ columns of $\mathbf{A}$ (n is equals to three for the 3-DOF CDPM, and these column vectors exclude those used to form v). The signs of their dot product solutions determine which half-space does the remaining a_is lie. If these dot product solutions are of the same signs, it means that these $(m-n+1)$ remaining columns lie on one half-plane of the hyperplane defined by v. Hence, this hyperplane is of the supporting type and tension-closure cannot be achieved for a CDPM (whose configuration is defined by the cable structure matrix $\mathbf{A}$) at a particular pose. Hence, using the cable structure matrix $\mathbf{A}$ of the 3-DOF CDPM, the tension-closure approach is carried out in the following manner [127]:

1. Generate all the associated plane's normal vectors v_i by taking the cross-product of any two column vectors $\mathbf{a}_j$ and $\mathbf{a}_k$ $(j = 1, \ldots, m; k = 1, \ldots, m; j \neq k)$. This results in a total of ${}^mC_2$ v_is $(i = 1, \ldots, {}^mC_2)$.

2. Take dot products of v_i with $\mathbf{a}_q$ $(q = 1, \ldots, m; q \neq j; q \neq k)$, where a column vector w_q with $(m-2)$ elements is formed. In total, ${}^mC_2$ w_qs are formed.

3. Check the elements of each w_q. If and only if the elements of each w_q have different signs (i.e at least one positive and one negative element), this means that the tension-closure condition is satisfied. Else, it is not satisfied.

This approach results in a simple and fast computation method to determine the positive cable tension condition for the 3-DOF CDPMs. However, this approach does not consider certain special configurations. This may occur in redundantly-restrained CDPM configurations with parallel or coinciding cables, or when the base and the moving platform cable attachment points coincide with each other. To handle these cases, a pre-requisite checking of the column vectors $\mathbf{a}_i$ need to be carried out as follows:

1. Check the column vectors $\mathbf{a}_i$, one at a time. If there exist zero column vectors, remove these column vectors from the cable structure matrix $\mathbf{A}$.

2. Check the column vectors $\mathbf{a}_i$, two at a time. If the cross product of any pair of column vectors is a zero vector, it means these two column vectors are linearly dependent. In this case, if these parallel vectors are of the opposite direction, skip the checking of this column. Else, remove one of these column vectors from the cable structure matrix $\mathbf{A}$ (as these are identical vectors).

3. Check if there are a minimum of four column vectors $\mathbf{a}_i$ in the reduced cable structure matrix $\mathbf{A}$ and the rank of $\mathbf{A}$ is three. If there are less than four $\mathbf{a}_i$s or rank is less than three, then this pose cannot satisfy tension-closure condition. Else continue with tension-closure approach.

These three pre-requisite steps can be embedded into the proposed tension-closure approach. Note that if the pose can achieve tension-closure (i.e., a set of positive cable tension), it means that the mechanism does not suffer from any singularities at this pose. Hence, singularity analysis is not required.

4.3.4 Null Space Approach

The tension-closure approach results in a systematic, generic and fast computation to determine tension-closure as compared to utilizing conventional null space tension-closure approach. However, this approach is unable to provide a numerical value to the positive cable tension. Hence, the null space approach has to be utilized during the motion control and path planning phase. This approach is nevertheless briefly mentioned in this thesis to provide the readers with a complete cable tension analysis. Based on Eqn. (4.1), the cable tension solution of a sufficiently restrained CDPM using a pseudo-inverse matrix[7] is given by:

$$\mathbf{T} = \mathbf{A}^{\#}.\mathbf{W}_{Ext} + (\mathbf{I} - \mathbf{A}^{\#}.\mathbf{A})\mathbf{Z} \tag{4.6}$$

[7] Readers may refer to [128] for details on the formulation of pseudo-inverse matrices.

Where:

$\mathbf{A}^{\#} = \mathbf{A}^T(\mathbf{A}.\mathbf{A}^T)^{-1} \in \Re^{m\times n}$: The underconstrained Moore-Penrose pseudo inverse of the cable structure matrix $\mathbf{A}$

$\mathbf{I} \in \Re^{m\times m}$: Identity matrix

$\mathbf{Z} = \left\{ \begin{array}{cccc} z_1 & z_2 & \cdots & z_m \end{array} \right\}^T$: An arbitrary column vector

Equation. (4.6) is regarded as an equation with redundancy, as there are infinite cable tension solutions for the sufficiently-restrained (i.e., $m > n$) CDPM modules. The first term $\mathbf{A}^{\#}.\mathbf{W}_{Ext}$ is a tension solution satisfying the first constraint (also known as the *particular* solution), while the second term $(\mathbf{I} - \mathbf{A}^{\#}.\mathbf{A})\mathbf{Z}$ (also known as the *homogeneous* solution) is the redundancy after the first constraint is satisfied. For such CDPMs , there are two cases to consider in order to determine the sufficient condition to keep tension of each cable positive, i.e., $(m = n + 1)$ and $(m > n + 1)$.

- **Case 1:** Minimum number of cables $(m = n + 1)$

  In this case, the equivalent expression of Eqn. (4.6) is written as:

  $$\mathbf{T} = \mathbf{A}^{\#}.\mathbf{W}_{Ext} + \lambda.\mathbf{N} \tag{4.7}$$

  Where the homogeneous solution is expressed as the kernel vector of $\mathbf{A}$ (i.e., $\mathbf{N} = \{n_1 \quad n_2 \quad \cdots \quad n_m\}^T$) multiplied by an arbitrarily scalar λ.

  If every components of $\lambda.\mathbf{N}$ are positive, then it is possible to provide an arbitrary positive compensation from the second term to the solution satisfying the first constraint in Eqn. (4.7). All the elements in $\mathbf{N}$ must be positive as an arbitrary value of λ can be selected to ensure that any negative components of the particular solution $\mathbf{A}^{\#}.\mathbf{W}_{Ext}$ can be cancelled out by addition and thereby making the tension in every cable to be positive. Hence the sufficient condition to satisfy the second constraint is $n_i > 0$ $(i = 1, \ldots, m)$.

- **Case 2:** Redundant cables $(m > n + 1)$

When $m > n+1$, $\text{rank}(\mathbf{I}-\mathbf{A}^{\#}.\mathbf{A}) = m-n$. Hence, the tension solution can be written as Eqn. (4.8) which includes $(m-n)$ independent vectors $\mathbf{N}_i$ $(i = 1, 2, \ldots, (m-n))$, such that:

$$\mathbf{T} = \mathbf{A}^{\#}.\mathbf{W}_{Ext} + \lambda_1.\mathbf{N}_1 + \lambda_2.\mathbf{N}_2 + \ldots + \lambda_{m-n}.\mathbf{N}_{m-n} \tag{4.8}$$

Comparing with the minimum cable case, there are more redundancy given by $(m-n)$ arbitrary coefficients. As a result, it will be easier to keep the tension of each cable positive.

4.3.5 Cable Tension Analysis of the CDPM Modules

(a) Cable Tension Analysis of the 1-DOF CDPM Module

For the 1-DOF CDPM, the arbitrary external wrench $\mathbf{W}_{Ext}$ spans $\Re^1$. Hence, based on the tension-closure approach, the hyperplane becomes a point and this becomes a very simple and straightforward analysis of checking the signs of each columns of $\mathbf{A}$. Different signs indicate that tension-closure is satisfied and that a null vector solution consisting of positive components, exist.

Computation Example: This example utilizes the tension-closure approach to determine if the pose of a 1-DOF two-cable CDPM (see Fig. 4.2) is achievable. Its kinematic parameters at home pose are as follows:

$$\begin{cases} \mathbf{b}_1^{\{O\}} = \{-100, 0, -100\}, & \mathbf{b}_2^{\{O\}} = \{100, 0, -100\}, \\ \mathbf{p}_1^{\{P\}} = \{-75, 0, 50\}, & \mathbf{p}_2^{\{P\}} = \{75, 0, 50\} \end{cases}$$

(All dimensions are in *millimeters*.)

The poses of the 1-DOF two-cable CDPM in Fig. 4.2 are not singularity poses if the cables were replaced with rigid links. However, the unilateral driving property of cables makes the second pose unfeasible (see Fig. 4.2(b)) as it is unable to withstand external clockwise moments about the y_O axis (indicated by red arrow).

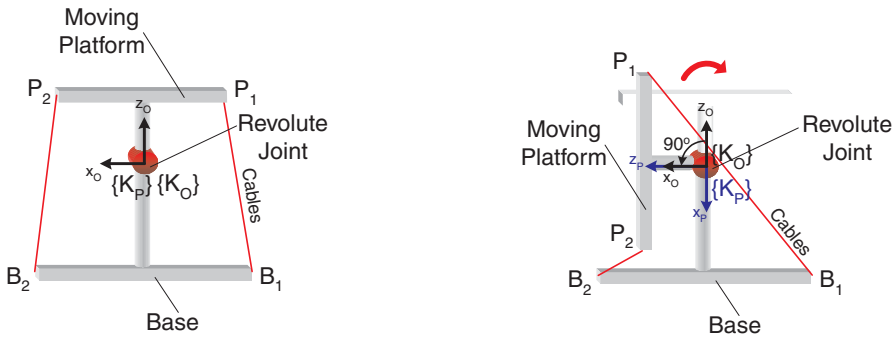

(a) At a pose satisfying tension-closure

(b) At a pose not satisfying tension-closure (after rotation of 90° about y-axis from home pose)

Figure 4.2: Tension-closure example for the 1-DOF two-cable CDPM

Pose I of the 1-DOF CDPM, as shown in Fig. 4.2(a), is in the home pose such that it satisfies the tension-closure condition. Using Eqns. (3.11) and (3.21), the cable structure matrix is obtained as $\mathbf{A} = [-82.19, 82.19]$. From observation, the components in each columns of $\mathbf{A}$ are of different signs. Hence the tension-closure statement is satisfied and all two cables can achieve positive tension. This pose is also checked for tension-closure using the null space approach described in Section 4.3.4. Using Eqn. (4.7) and the row-reduced echelon form, the null vector of matrix $\mathbf{A}$ is determined as $\{0.707, 0.707\}^T$. This null vector contains only positive components and hence, this pose can achieve tension-closure condition.

Pose II of the 1-DOF CDPM, as shown in Fig. 4.2(b), is a pose which undergoes a rotation of 90° about the y-axis of the base frame $\{K_O\}$ such that it does not satisfy the tension-closure condition. The figure shows an exaggerated pose which is obviously unable to restraint the moving platform but this is mainly for illustration purpose. Using Eqns. (3.11) and (3.21), the cable structure matrix is obtained as $\mathbf{A} = [-10.85, -44.72]$. From observation, the components in each columns of $\mathbf{A}$ are of same signs. Hence the tension-closure statement is not satisfied and the two cables cannot achieve positive tension. This pose is also checked for tension-closure using the null space approach described in Section 4.3.4. Using Eqn. (4.7) and the row-reduced echelon form, the null vector of matrix $\mathbf{A}$ is determined as $\{-0.972, 0.236\}^T$. This null vector contains both negative and positive components and hence, this pose clearly cannot achieve tension-closure condition.

(b) Cable Tension Analysis of the 3-DOF CDPM Module

For the 3-DOF CDPM, the arbitrary external wrench $\mathbf{W}_{Ext}$ spans $\Re^3$. Hence, based on the tension-closure approach, the hyperplane becomes a plane and the induced vector v_i is simply the cross product of two columns of the cable structure matrix $\mathbf{A}$.

Computation Example: This example utilizes the tension-closure approach to determine if the pose of a 3-DOF four-cable CDPM (see Fig. 4.3) is achievable. Its kinematic parameters at home pose are as follows:

$$\begin{cases} \mathbf{b}_1^{\{O\}} = \{50, 50, -100\}, & \mathbf{b}_2^{\{O\}} = \{-50, 50, -100\}, \\ \mathbf{b}_3^{\{O\}} = \{-50, -50, -100\}, & \mathbf{b}_4^{\{O\}} = \{50, -50, -100\} \\ \mathbf{p}_1^{\{P\}} = \{30, 0, 75\}, & \mathbf{p}_2^{\{P\}} = \{-30, 0, 75\} \end{cases}$$

(All dimensions are in *millimeters*.)

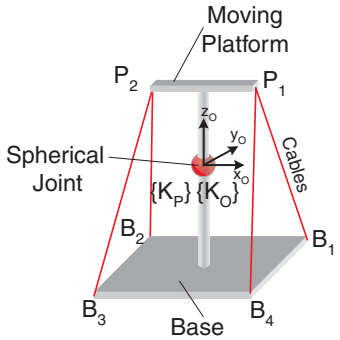

(a) At a pose satisfying tension-closure (at home pose)

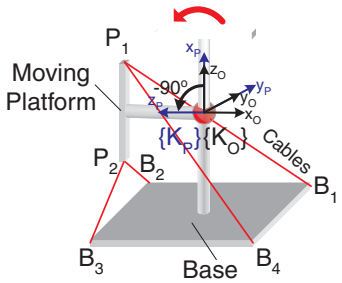

(b) At a pose not satisfying tension-closure (after rotation of -90° about y-axis from home pose)

Figure 4.3: Tension-closure example for the 3-DOF four-cable CDPM

The poses of the 3-DOF four-cable CDPM in Fig. 4.3 are not singularity poses if the cables were replaced with rigid links. However, the unilateral driving property of cables makes the second pose unfeasible (see Fig. 4.3(b)) as it is unable to withstand external counter-clockwise moments about the y_O axis (indicated by red arrow).

Pose I of the 3-DOF CDPM, as shown in Fig. 4.3(a), is in the home pose such that it satisfies the tension-closure condition. Pose II as shown in Fig. 4.3(b), is a pose which undergoes a

rotation of -90° about the y-axis of the base frame $\{K_O\}$ such that it does not satisfy the tension-closure condition. This figure shows an exaggerated pose which is clearly beyond the joint limits but this is mainly for illustration purpose. Based on the tension-closure approach in Section 4.3.3, a total of ${}^4C_{3-1}(=6)$ induced vectors v_i are obtained for a four-cable 3-DOF CDPM.

Table 4.1: Tension-closure results for the 3-DOF four-cable CDPM at different poses

	Pose I	Pose II
Cable structure matrix, $\mathbf{A}$ $=[\mathbf{a}_1\ \mathbf{a}_2\ \mathbf{a}_3\ \mathbf{a}_4]$	$\begin{bmatrix} -20.48 & -20.48 & 20.48 & 20.48 \\ 36.87 & -36.87 & -36.87 & 36.87 \\ 8.19 & -8.19 & 8.19 & -8.19 \end{bmatrix}$	$\begin{bmatrix} -8.02 & 16.74 & -16.74 & 8.02 \\ -32.06 & -66.98 & -66.98 & -32.06 \\ -20.04 & -41.86 & 41.86 & 20.04 \end{bmatrix}$
$w_1 = \{v_1.\mathbf{a}_3, v_1.\mathbf{a}_4\}$ (with $v_1 = \mathbf{a}_1 \times \mathbf{a}_2$)	$\{24742, -24742\}$	$\{89888, 43026\}$
$w_2 = \{v_2.\mathbf{a}_2, v_2.\mathbf{a}_4\}$ (with $v_2 = \mathbf{a}_1 \times \mathbf{a}_3$)	$\{-24742, 24742\}$	$\{-89888, -43026\}$
$w_3 = \{v_3.\mathbf{a}_2, v_3.\mathbf{a}_3\}$ (with $v_3 = \mathbf{a}_1 \times \mathbf{a}_4$)	$\{24742, -24742\}$	$\{-43026, 43026\}$
$w_4 = \{v_4.\mathbf{a}_1, v_4.\mathbf{a}_4\}$ (with $v_4 = \mathbf{a}_2 \times \mathbf{a}_3$)	$\{24742, -24742\}$	$\{89888, -89888\}$
$w_5 = \{v_5.\mathbf{a}_1, v_5.\mathbf{a}_3\}$ (with $v_5 = \mathbf{a}_2 \times \mathbf{a}_4$)	$\{-24742, 24742\}$	$\{43026, 89888\}$
$w_6 = \{v_6.\mathbf{a}_1, v_6.\mathbf{a}_2\}$ (with $v_6 = \mathbf{a}_3 \times \mathbf{a}_4$)	$\{24742, -24742\}$	$\{-43026, -89888\}$

Table 4.1 presents the computation details of the induced vectors v_i and their respective w_is. At Pose I, the components in each w_is are of different signs. Hence the tension-closure statement is satisfied and all four cables can achieve positive tension. This pose is also checked for tension-closure using the null space approach described in Section 4.3.4. Using Eqn. (4.7) and the row-reduced echelon form, the null vector of matrix $\mathbf{A}$ is determined as $\{0.5, 0.5, 0.5, 0.5\}^T$. This null vector contains only positive components and hence, this pose can achieve tension-closure condition.

At Pose II, the components in several w_is are of same signs. Hence the tension-closure statement is not satisfied as some of the cables cannot achieve positive tension. This pose is also checked for tension-closure using the null space approach described in Section 4.3.4. Using Eqn. (4.7) and the row-reduced echelon form, the null vector of matrix $\mathbf{A}$ is determined as $\{0.6378, -0.3053, -0.3053, 0.6378\}^T$. This null vector contains negative components and hence, this pose cannot achieve tension-closure condition.

4.4 Stiffness Analysis

When a cable-driven mechanism approaches singularity poses or poses in which cables are unable to maintain positive tension, stiffness analysis can play a vital role in identifying such poses [86, 105]. The stiffness matrix maps the change of applied wrench $\delta\mathbf{W}_{Ext} \in \Re^n$ with the infinitesimal deflection δX of a mechanism's moving platform pose. This is a linear relationship [129, 118] and is given by:

$$\delta\mathbf{W}_{Ext} = \mathbf{K}\delta X \tag{4.9}$$

Where $\mathbf{K}$ is known as the cartesian stiffness matrix, which is usually posture-dependent.

By representing k_i as the stiffness of the i^{th} cable, the stiffness equation in the joint space is given as:

$$\delta\mathbf{T} = diag(k_1, \ldots, k_m)\delta\mathbf{L} \tag{4.10}$$

Based on the assumption of cables behaving as linear springs, the stiffness of a cable at a particular cable tension t_i is given as [86]:

$$k_i = k'.\left(1 + \frac{t_i}{k'}\right).l_i^{-1} \approx k'.l_i^{-1} \tag{4.11}$$

Where k' the stiffness per reciprocal unit length (i.e., the proportionality factor) which is a constant and l_i is the cable length at a particular pose. In typical applications, the $\frac{t_i}{k'}$ terms

are normally less than 0.5% [86] and can be neglected as the contribution of the actuator and joint compliance are much higher.

Hence, from Eqns. (4.1), (4.9), (4.10) and (4.11), the cartesian stiffness matrix is determined as:

$$\mathbf{K} = k'\mathbf{A}\mathbf{L}_O^{-1}\mathbf{A}^T \tag{4.12}$$

Where $\mathbf{L}_O^{-1}$=diag$(l_1^{-1}, \ldots, l_m^{-1})$ is a diagonal matrix whose elements are the reciprocal of the original cable lengths at that particular pose.

Based on Eqn. (4.12), the stiffness matrix of the 1-DOF CDPM is determined as:

$$\mathbf{K}_{1DOF} = k'\mathbf{A}\mathbf{L}_O^{-1}\mathbf{A}^T \tag{4.13}$$

Where $\mathbf{K}_{1DOF} = k_{\theta_{yy}} \in \Re^{1\times1}$, and represents the stiffness about the revolute y axis.

Based on Eqn. (4.12), the stiffness matrix of the 3-DOF CDPM is determined as:

$$\mathbf{K}_{3DOF} = k'\mathbf{A}\mathbf{L}_O^{-1}\mathbf{A}^T \tag{4.14}$$

Where $\mathbf{K}_{3DOF} = \begin{bmatrix} k_{\theta_{xx}} & k_{\theta_{xy}} & k_{\theta_{xz}} \\ k_{\theta_{yx}} & k_{\theta_{yy}} & k_{\theta_{yz}} \\ k_{\theta_{zx}} & k_{\theta_{zy}} & k_{\theta_{zz}} \end{bmatrix} \in \Re^{3\times3}$, and represents the 3-DOF orientation stiffness in the Cartesian space.

The stiffness matrices in Eqns. (4.13) and (4.14) are functions of cable stiffness, cable length and pose. These matrices are presented in this section, mainly to be used as an evaluation tool for workspace quality over an entire workspace. They will be utilized for the design optimization process as a design constraint, and for future works, when carrying out stiffness-based motion control implementation.

4.5 Workspace Generation

For the proposed 7-DOF cable-driven robotic arm, optimal design is mainly focused on a task-based problem with a goal of designing a 7-DOF robotic arm that is similar to the human

arm in terms of its workspace and dexterity. Hence, the workspace of each of the individual 1-DOF and 3-DOF CDPM modules must be optimized to have similar motion characteristics as their respective human arm joints. The first step is to generate workspace templates based on the motion ranges of the human arm joints. However, due to the complex nature of the human arm joint motion, an analytical approach becomes complicated and ineffective. Hence a numerical approach is proposed to determine the human arm joint workspace template as well as to represent the workspace of the individual CDPM modules.

4.5.1 1-DOF CDPM Module

The basic 1-DOF CDPM module will form the elbow joint structure of the proposed 7-DOF cable-driven robotic arm. Since there is only one orientation parameter (i.e., α), the $SO(2)$ workspace is straightforward. The range of α is discretized based on a user-defined interval, and each point is evaluated for tension-closure condition. The elbow joint can produce one basic motion of Extension/Flexion, as shown in Fig. 4.4. Hence, the motion range for the 1-DOF elbow joint is $\alpha \in [0°, 140°]$. Figure 4.5 shows the description of the inertial and moving coordinate frames at the right-hand elbow joint. The origin of the inertial frame coordinate system is at the elbow joint centre (i.e., centre of trochlea) with orthogonal axes x, y and z (i.e., x is pointing to the frontal direction of the body; y is pointing to the upward direction of the body; and z is the cross product of x with y). As for the moving frame coordinate system, its origin is also at the elbow joint centre (i.e., centre of trochlea) with the orthogonal axes x', y' and z' (i.e., x' is the cross product of y' with z'; y' is the same as the inertial frame y axis; and z' is pointing along the forearm axis of rotation).

4.5.2 3-DOF CDPM Module

The basic 3-DOF CDPM module will form the shoulder and wrist modules of the proposed 7-DOF cable-driven robotic arm. These 3-DOF CDPMs are in fact cable-driven spherical

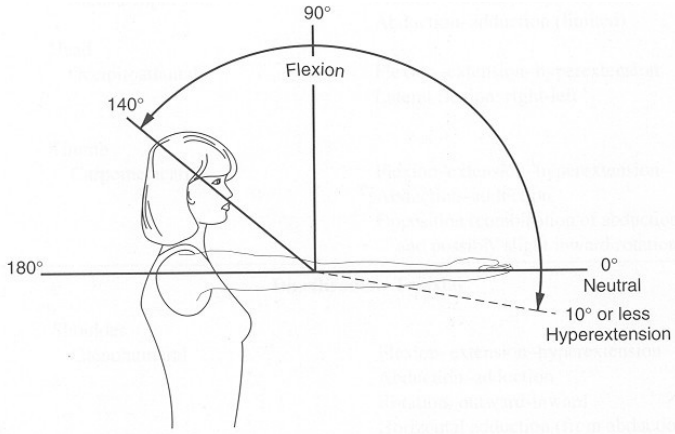

Figure 4.4: Types of motion at the elbow joint and its joint limits [130]

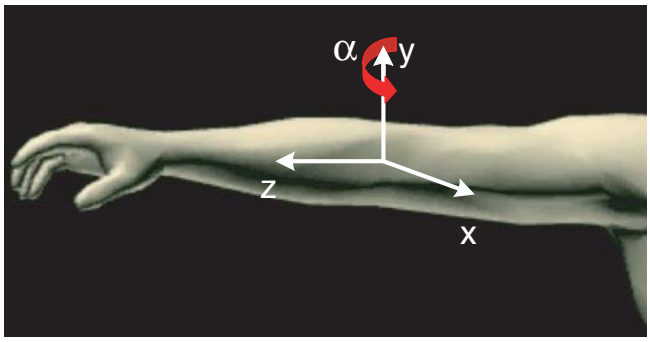

Figure 4.5: Inertial frame description of the right-hand elbow joint at home pose

mechanisms. Hence, the $SO(3)$ orientation workspace analysis is not as straightforward. In addition, workspace representation for the purpose of defining the range of motion of human 'spherical' joints is approached differently as compared to mechanisms or computer animations. While quaternion seems to be used as the standard method for representing motion in computer animations, they are not so often used in biomechanics. Quaternion has the advantages in terms of lack of gimbal lock and insensitivity to round-off errors, but they suffer from problems of interpretation in terms of meaningfully clinical or anatomical angles. Euler angles, on the other hand, allow some degree of intuition for the rotation angles, but suffer from singularities. Representations using equivalent angle-axis have also been proposed [85] but the main issue is that interpretation of joint motions must have an intuitive feel while being mathematically tractable at the same time. Hence, there is a great debate as to the use of Euler angles with quaternion and equivalent angle-axis for workspace representations.

For the 3-DOF CDPM, the Tilt-&-Torsion angles parameterization is adopted to represent the workspace of the human shoulder and wrist joints based on their joint range of motion limits. The advantage of this representation is that it is able to separate the 3-DOF orientation into two components: the 2-DOF tilt and the 1-DOF twist. The tilt component (ϕ and θ) determines the direction of the axis, while the twist component (σ) determines the rotation about the axis itself, as shown in Fig. 3.3. This representation is intuitive and the joint motion limit boundaries can be identified using this representation.

Gosselin [120] proposed an intuitive way to display orientation workspace using a cylindrical coordinate system. Adopting a similar approach, the orientation workspace of the 3-DOF CDPM is displayed using a system of cylindrical coordinates $\{r, \gamma, h\}$. ϕ, θ and σ will be the polar angle γ, the polar radius r, and the height h respectively. In this section, an equi-volumetric partition scheme of the cylindrical workspace of radius π and height 2π (with $\phi \in$[-180°,180°], $\theta \in$[0°,180°] and $\sigma \in$[-180°,180°]) is proposed. The following is the partition scheme of the top half of the cylinder [65] (The partition of the bottom half of the cylinder will be similar to that of the top half as presented here.).

- **Step 1:** As shown in Fig. 4.6(a), the solid cylinder is divided along z-axis into p identical circular discs of height $\delta h = \frac{\pi}{p}$. Starting from the bottom, the discs are then labeled from 1 to p, i.e., $i = 1, \ldots, p$. This results in p circular discs.

- **Step 2:** As shown in Fig. 4.6(b), each circular disc i is then divided into p circular bands of thickness $\delta r = \frac{\pi}{p}$ along the radial direction. Note that the first circular band is actually a circular disc of radius $\frac{\pi}{p}$ and height $\frac{\pi}{p}$. Starting from this central circular disc, the circular bands are labeled from 1 to p, i.e., $j = 1, \ldots, p$. This results in p circular bands.

- **Step 3:** As shown in Fig. 4.6(c), the central circular disc (i.e., $j = 1$) is divided into four quadrants, where each quadrant is regarded as the basic element of volume $\delta V_{Cartesian} = \frac{\pi^4}{4p^3}$. For each circular band j (i.e., $j = 2, \ldots, p$), it is circumferentially divided into $4(2j - 1)$ equi-volumetric element of volume $\delta V_{Cartesian}$ with the same

spacing angle of $\frac{\pi}{2(2j-1)}$, as shown in Fig. 4.6(d). Starting from the x-axis, the elements are labeled counter-clockwise from 1 to $4(2j-1)$, i.e., $k = 1, \ldots, 4(2j-1)$. This results in $\sum_{j=1}^{p} 4(2j-1) = 4p^2$ elements for each circular disc.

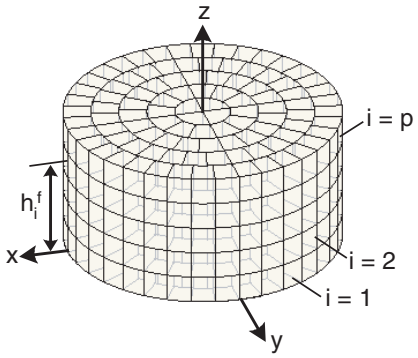

(a) Partition scheme of a solid cylinder

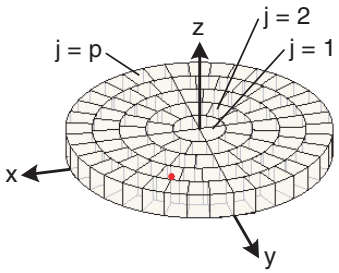

(b) Partition scheme of ith circular disc

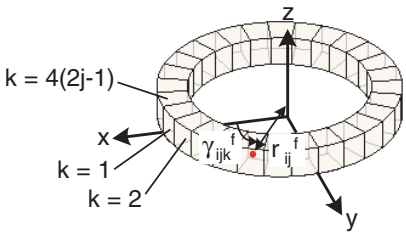

(c) Partition scheme of jth circular band in ith disc

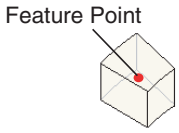

(d) Element in the partition scheme

Figure 4.6: Equi-volumetric partition scheme of a solid cylinder

In total, there are $4p^3$ elements in the cylindrical workspace and each element is specified by its feature point f_{ijk} using a triplet index (i, j, k). f_{ijk} is selected as the intersection point of the three neutral planes of the element and is given in cylindrical coordinates as:

$$f_{ijk} = [r_{ij}^f, \gamma_{ijk}^f, h_i^f] \tag{4.15}$$

Where $h_i^f = \frac{(2i-1)\pi}{2p}$, $r_{ij}^f = \frac{(2j-1)\pi}{2p}$ and $\gamma_{ijk}^f = \frac{(2k-1)\pi}{4(2j-1)}$ (for $i = 1, \ldots, p$; $j = 1, \ldots, p$; and $k = 1, \ldots, 4(2j-1)$). When the number of elements is sufficiently large, each element can be locally represented by f_{ijk}. The advantage of this division scheme is that the singularity points for the T&T angles at $\theta = 0$ and π are avoided. It has a 'one-to-one' mapping between the points in the cylindrical plot and the poses in the task space. In addition, all elements

are geometrically identical, with simplified analysis and computational effort. Given the joint motion limits, the workspace templates for the shoulder and wrist joints can be easily determined.

(a) Shoulder Joint Workspace Representation

In order to determine the shoulder joint workspace representation in cylindrical coordinates, the shoulder joint is observed for its motion characteristics. Figure 4.7 shows the types of motion at the shoulder joint and its joint limits. The shoulder joint can produce four basic motions, namely Extension/Flexion, Horizontal Extension/Flexion, Abduction/Adduction and Outward/Inward Rotation. It can also produce a fifth motion, known as Circumduction, which is a combination of the four basic movements. Based on the shoulder joint motion range, the approximated maximum range of the tilt angles and twist angles are $\phi \in$[-180°,180°], $\theta \in$[0°,140°] and $\sigma \in$[-90°,90°] respectively. These values are approximated as they vary slight between each individual.

Figure 4.8 shows the description of the inertial and moving coordinate frames at the right-hand shoulder joint based on the T-&-T angles parameterization. The origin of the inertial frame coordinate system is at the shoulder joint centre with orthogonal axes x, y and z (i.e., x is pointing to the frontal direction of the body; y is pointing to the upward direction of the body; and z is the cross product of x with y). As for the moving frame coordinate system, its origin is also at the shoulder joint centre with the orthogonal axes x', y' and z' (i.e., x' is the pointing along the predefined forearm axis of rotation based on the initial pose of the upper arm; y' is the cross product of z' with x'; and z' is pointing along the longitudinal axis of the humerus bone at any pose).

Based on the shoulder joint motion limits and the shoulder joint coordinate frame descriptions, the right-hand shoulder joint workspace representation using T-&-T angles is a cylinder of height π (i.e., $-\frac{\pi}{2}$ to $\frac{\pi}{2}$) with an irregular shaped cross-section. Fig. 4.9 shows the 3D view and the irregular shaped cross-section of the right-hand shoulder joint workspace, as

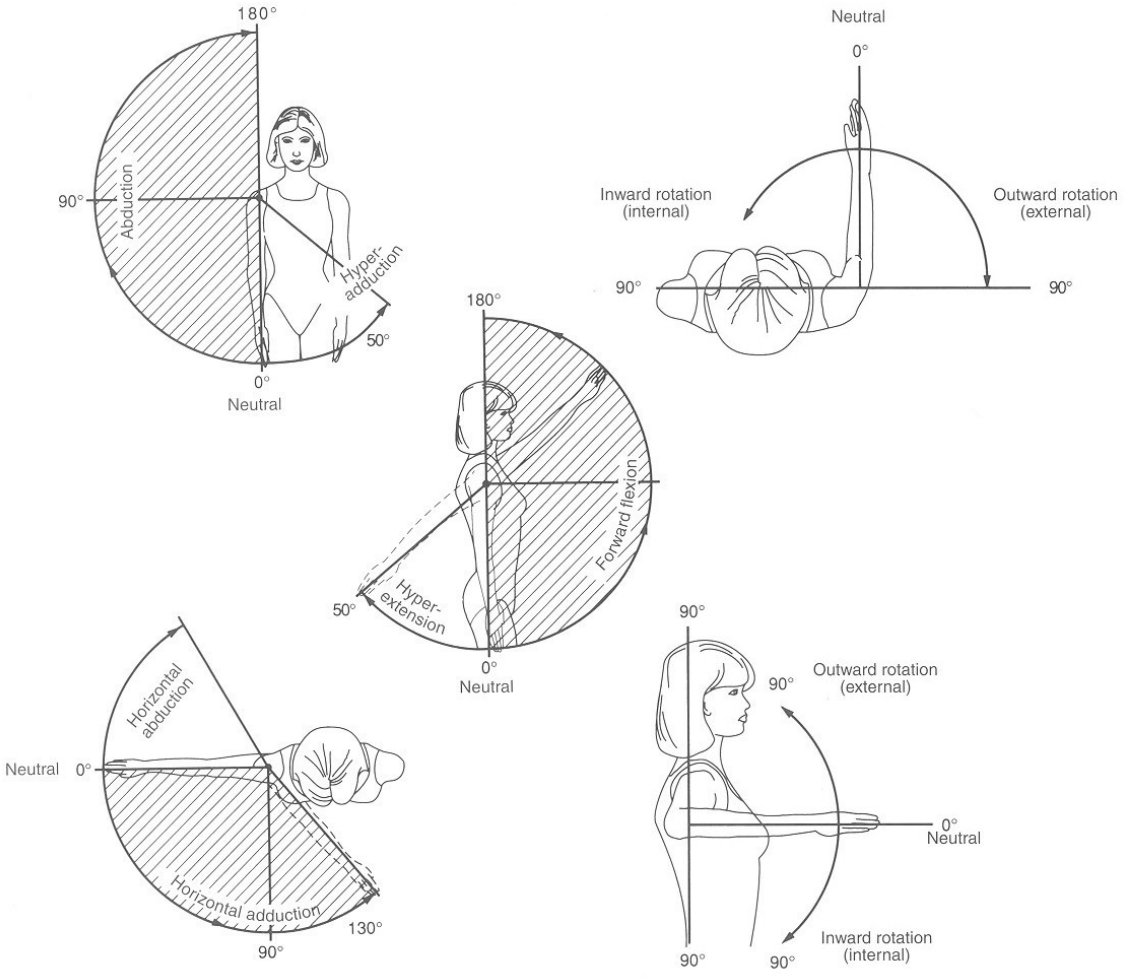

Figure 4.7: Types of motion at the shoulder joint and its joint limits [130]

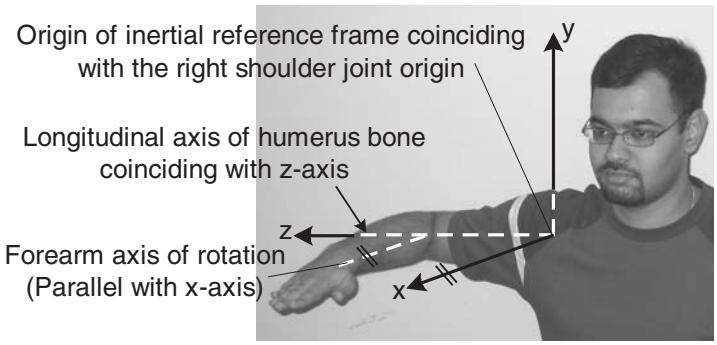

Figure 4.8: Inertial frame description of the right-hand shoulder joint at home pose

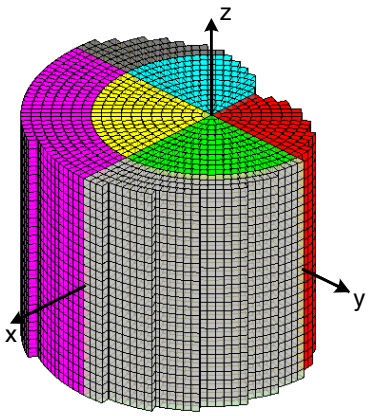

(a) 3D view of the right-hand shoulder joint workspace

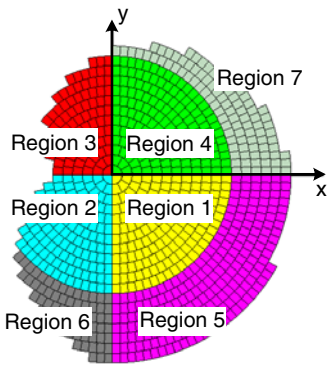

(b) Cross-sectional view of the ith disc

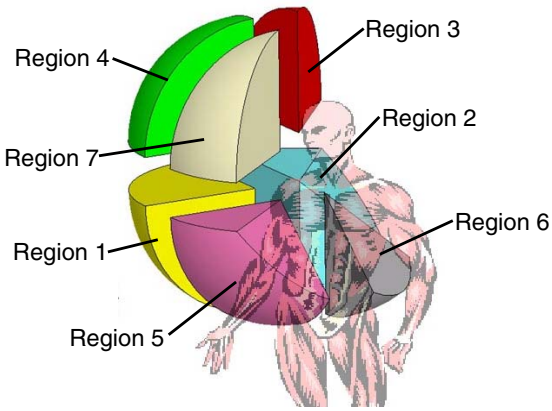

(c) The corresponding regions in the Cartesian task space at $\sigma = 0$

Figure 4.9: Representation of the right-hand shoulder joint workspace based on its motion range limits (The colours indicate the regions in the cylindrical workspace plot to the corresponding regions in the cartesian task space.)

well as the corresponding regions in the Cartesian task space.

(b) Wrist Joint Workspace Representation

Similar to the approach adopted for the shoulder joint, the wrist joint is observed for its motion characteristics. Figure 4.10 shows the types of motion at the 'equivalent' wrist joint and its joint limits[8]. The wrist can produce two basic motions: Extension/Flexion and Radial/Ulnar Flexion. It has also a third motion due to the pronation/supination about the

[8] The wrist joint is actually a 2-DOF joint. However, it has a motion about the forearm axis and hence, it is equivalent to a 3-DOF joint when combined with the forearm joint.

forearm axis. Based on the 'equivalent' wrist joint motion range, the approximated maximum range of the tilt angles and twist angles are $\phi \in$[-180°,180°], $\theta \in$[0°,90°] and $\sigma \in$[-80°,80°] respectively.

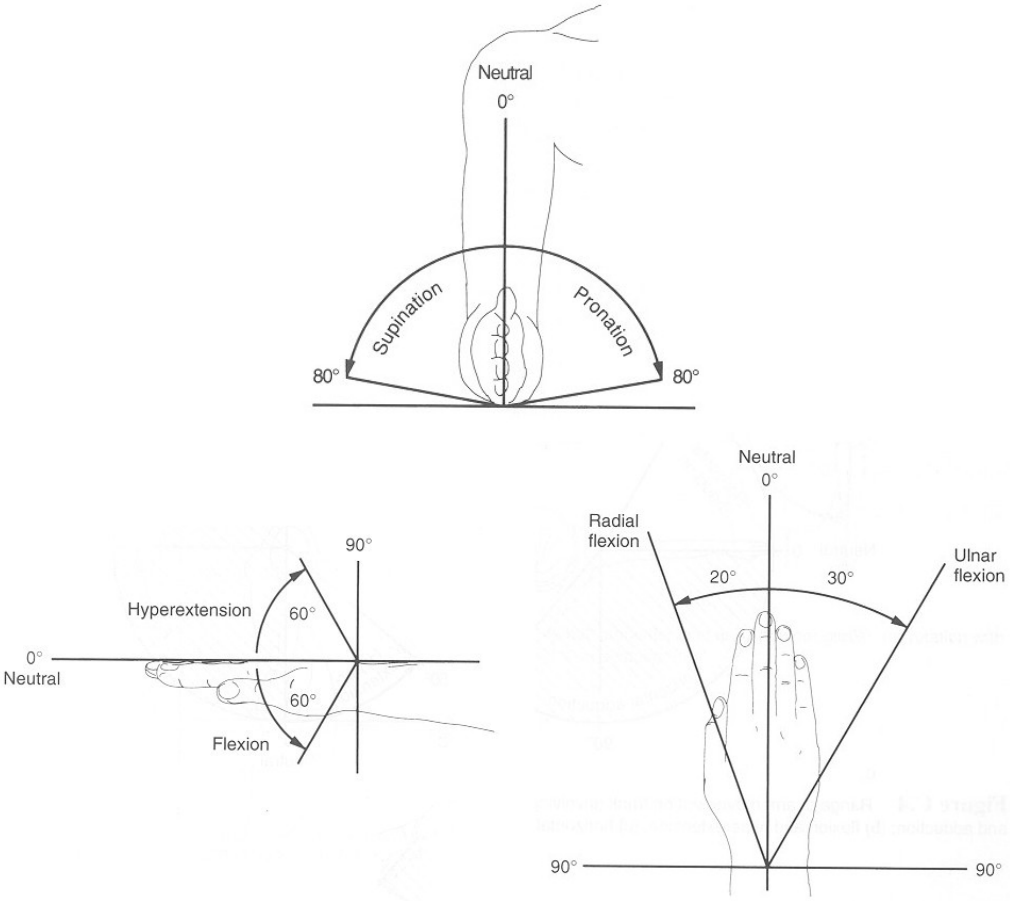

Figure 4.10: Types of motion at the wrist joint and its joint limits [130]

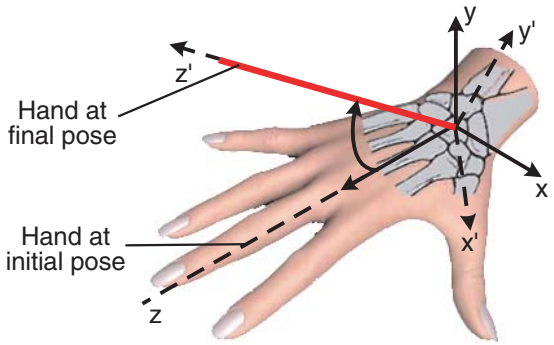

Figure 4.11: Inertial frame description of the right-hand wrist joint at home pose

Figure 4.11 shows the description of the inertial and moving coordinate frames at the right-hand wrist joint based on the T-&-T angles parameterization. The origin of the inertial frame coordinate system is at the capitate bone with the orthogonal axes x, y and z (i.e., x is the cross product of y with z; y is pointing to the upward direction of the hand (perpendicular to the palm); and z is pointing along the centre metacarpal (i.e., middle finger) and aligned with forearm axis of rotation). As for the moving frame coordinate system, its origin is also at the capitate bone with the orthogonal axes x', y' and z' (i.e., x' is the cross product of y' with z'; y' is pointing to the upward direction of the moved hand (perpendicular to the palm); and z' is pointing along the centre metacarpal (i.e., middle finger) in the final pose).

Based on the wrist joint motion limits and the wrist joint coordinate frame descriptions, the workspace representation using T-&-T angles is a cylinder of height $\frac{8}{9}\pi$ (i.e., $-\frac{4}{9}\pi$ to $\frac{4}{9}\pi$) with an irregular shaped cross-section. Fig. 4.12 shows the 3D view and the irregular shaped cross-section of the right-hand wrist joint workspace, as well as the corresponding regions in the Cartesian task space.

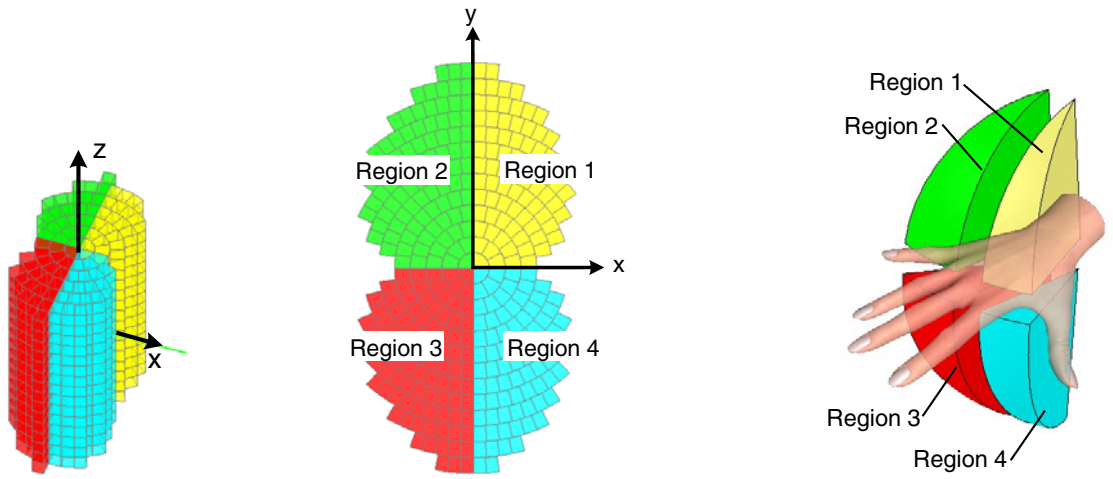

(a) 3D view of the right-hand wrist joint workspace

(b) Cross-sectional view of the ith disc

(c) The corresponding regions in the Cartesian task space at $\sigma = 0$

Figure 4.12: Representation of the right-hand wrist joint workspace based on its motion range limits (The colours indicate the regions in the cylindrical workspace plot to the corresponding regions in the Cartesian task space.)

4.5.3 Workspace Volume

The workspace volume of the 1-DOF CDPM module is a straightforward case of adding up the discretized feasible poses, as compared to the 3-DOF CDPM module. When quantifying the workspace volume of $SO(3)$, $V_{SO(3)}$ is not equal to the geometrical volume of the cylindrical workspace (i.e., $V_{Cartesian}$) due to the non-linear parameterization. Hence, a volume-associated integral factor (I_v) has to be introduced to accurately determine $V_{SO(3)}$ from $V_{Cartesian}$. From the concept of metrics, I_v is defined as the absolute value of the Jacobian matrix which relates the rate of change of the orientation parameters to describe the rotation to the angular velocity of the rigid body. When computing the volume of $SO(3)$ from the cylindrical coordinate representation of T-&-T angles, an equivalent I_v is determined as $\frac{\sin\theta}{\theta}$ by adopting a similar approach presented by Chirikjian [124] (refer to Appendix C for formulation details.). The volume for the discretized $SO(3)$ workspace is now given as:

$$\begin{aligned} V_{SO(3)} &= \left(\sum_{i=1}^{h_{total}} I_{vi}\right) \Delta V_{Cartesian} \\ &= \left(\sum_{i=1}^{h_{total}} \frac{\sin\theta_i}{\theta_i}\right) \left(\frac{\pi^4}{4p^3}\right) \end{aligned} \tag{4.16}$$

Where h_{total} is the total number of poses (i.e., feature point) and θ_i is the θ angle at the ith feature point, with respect to the cylindrical workspace as shown in Fig. 4.6. Using Eqn. (4.16), the workspace volumes of the human shoulder and wrist joint are given by 23.024 rad^2 and 8.199 rad^2 respectively.

4.6 Workspace Performance Measures

4.6.1 Quantitative Measure

For the 7-DOF cable-driven robotic arm design, the main objective is to achieve a workspace that closely matches the actual 7-DOF human arm workspace. This can be achieved by

designing CDPMs whose workspace will closely match the workspace of their respective human arm joints, through the generated human arm joint workspace templates in Section 4.5. Hence, a performance evaluation measure is proposed that will quantitatively determine how much workspace volume of the human arm joints have been matched by their respective CDPM modules. The proposed performance quantity measure, known as the Workspace Matching Index (WMI), is described as:

$$WMI = \frac{\text{Maneuverable Workspace Volume of a CDPM module}}{\text{Total Workspace Volume of the respective human arm joint}} \tag{4.17}$$

For the 1-DOF elbow module, Eqn. (4.17) is numerically given as:

$$WMI = \frac{\sum_{i=1}^{h_a} \Delta V_{SO(2)}}{\sum_{i=1}^{h_{total}} \Delta V_{SO(2)}} = \frac{h_a}{h_{total}} \tag{4.18}$$

For the 3-DOF shoulder and wrist modules, Eqn. (4.17) is numerically given as:

$$WMI = \frac{\sum_{i=1}^{h_a} \Delta V_{SO(3)}}{\sum_{i=1}^{h_{total}} \Delta V_{SO(3)}} = \frac{\sum_{i=1}^{h_a} \frac{\sin\theta_i}{\theta_i}}{\sum_{i=1}^{h_{total}} \frac{\sin\theta_i}{\theta_i}} \tag{4.19}$$

Where h_a is the number of poses achievable by the CDPM and is a subset of h_{total}, while h_{total} is the total number of poses in the human arm joint workspace. WMI ranges from 0 to 1. A WMI value 1 (ideal) indicates that the CDPM module is able to achieve all the poses in its corresponding human arm joint workspace.

4.6.2 Qualitative Measure

Besides workspace quantization, it is also important to determine the quality of the workspace. In addition, the 7-DOF cable-driven robotic arm utilizes cables which are flexible and greatly affects the tool-tip stiffness. Hence it is very critical to maintain sufficient stiffness. As shown by Strang [131], the condition number of a matrix is used in numerical analysis to estimate the error generated in the solution of a linear system of equations by the error on the data. When applied to the Jacobian Matrix, the condition number gives a measure of the accuracy

of the Cartesian velocity and the static load acting on the end of the end-effectors. Similarly, the condition number of the stiffness matrix $\mathbf{K}$ (determined in Section 4.4) can also be used to give a measure of accuracy for cable-driven mechanisms, which includes the effect of cable stiffness. The Stiffness Condition Index i.e., *SCI*, (which is the reciprocal of the condition number) is given as the ratio of the minimum to the maximum singular value of $\mathbf{K}$ at a given pose. *SCI* ranges from 0 to 1. Large values for *SCI* (close to 1) ensure good stiffness with respect to force and velocity transmission, while *SCI* values close to 0 indicate poor stiffness.

Adopting a similar approach as the Global Conditioning Index proposed by Yang [110], the Global Stiffness Conditioning Index (*GSCI*) is proposed as a performance quality measure. *GSCI* is the integration of *SCI* over the whole workspace, and is given by:

$$GSCI = \frac{\int_V SCI(\mathbf{K})dV}{\int_V dV} \tag{4.20}$$

Where V represents the workspace volume of the mechanism.

For the 1-DOF elbow module, the global stiffness performance index (*GSPI*) is numerically given as:

$$\begin{aligned} GSPI &= \frac{\sum_{q=1}^{h_a}(\mathbf{K}_{1DOF})_q \cdot \Delta V_{SO(2)}}{\sum_{q=1}^{h_a}\Delta V_{SO(2)}} \\ &= \frac{\sum_{q=1}^{h_a}(k_{\theta_{yy}})_q}{h_a} \end{aligned} \tag{4.21}$$

GSPI represents the average stiffness with respect to the total $SO(2)$ workspace.

For the 3-DOF shoulder and wrist modules, Eqn. (4.20) is numerically given as:

$$\begin{aligned} GSCI &= \frac{\sum_{q=1}^{h_a} SCI(\mathbf{K}_{3DOF})_q \cdot \Delta V_{SO(3)}}{\sum_{q=1}^{h_a}\Delta V_{SO(3)}} \\ &= \frac{\sum_{q=1}^{h_a}\left(SCI(\mathbf{K}_{3DOF})_q \frac{\sin\theta_q}{\theta_q}\right)}{\sum_{q=1}^{h_a}\frac{\sin\theta_q}{\theta_q}} \end{aligned} \tag{4.22}$$

GSCI ranges from 0 to 1. Large values for *GSCI* (close to 1) ensure good overall stiffness with respect to force and velocity transmission, while *GSCI* values close to 0 indicate poor overall stiffness.

GSCI and *GSPI* will be crucial when a task requires a minimum amount of stiffness in each pose. These indices are presented in this thesis to provide a workspace quality evaluation tool, and will be used as a design constraint during the design optimization process to ensure certain workspace quality. It will also be considered during future works when carrying out stiffness-based motion control implementation.

4.7 Discussion

In this chapter, three workspace-related analysis (i.e., cable tension analysis, stiffness analysis and workspace generation with its performance measures) of the CDPM modules are addressed. These analyses will be crucial for the subsequent design optimization process.

From the various definitions of workspace in literature, a definition for the 'maneuverable' workspace of the CDPM modules is presented. This is followed by addressing the cable tension analysis of CDPMs. Contributions are made in proposing a computationally effective approach for the tension-closure analysis of the CDPM modules based on the theory of convex analysis. Computational examples demonstrate the effectiveness of the proposed approach over the conventional 'null-space' approach in terms of its computation efforts and simplicity. This will be crucial during design optimization in order to obtain a result without going through computationally intensive algorithms. However, it is also noted that this approach can only evaluate the tension-closure condition, but not the magnitude of the required cable tension. Hence, the 'null-space' approach has to be adopted during the motion control implementation phase.

Workspace generation is carried out to determine the template of the various human arm

joints based on their motion ranges. This is for the subsequent design optimization process where the aim is to design a 7-DOF cable-driven robotic arm whose motion capabilities will match with that of the human arm, in terms of it workspace. Due to the complex nature of the human arm joint motion, an analytical approach for workspace generation becomes complicated and ineffective. Hence, a numerical approach is adopted in this thesis. The workspace generation for the 1-DOF revolute joint is trivial unlike the 3-DOF spherical joint. Hence, more effort is carried out on the workspace generation of the 3-DOF spherical joint. There are several approaches to represent the $SO(3)$ workspace but the Tilt-&-Torsion angles parameterization is chosen due to its advantage of being able to separate the 3-DOF orientation into two tilt components, and one twist component. Hence, this representation becomes intuitive and the joint motion limit boundaries can be easily identified. In addition, the $SO(3)$ workspace is represented in the cylindrical coordinates which is intuitive and has a 'one-to-one' mapping from the points in the cylindrical plot to the pose in the task space. Hence, contributions are made to propose an equi-volumetric workspace discretization scheme which ensures each element in the cylindrical workspace converges to its feature point when the number of elements become sufficiently large. In addition, the singularity points of the T-&-T angles are avoided due to the proposed division scheme.

Similar to the workspace generation, the workspace volume of the 1-DOF CDPM is a trivial case. However, for the 3-DOF CDPM, the volume of $SO(3)$ workspace is not equal to the geometric volume of the cylindrical workspace. Hence, integration measures are introduced when computing the $SO(3)$ workspace from its parametric domain. This is to ensure the volume generated are mathematically tractable. A 'Workspace Matching Index' which utilizes the workspace volume, is subsequently proposed to evaluate the various CDPM module designs during design optimization where the aim is to come up with a 7-DOF CDRA that has similar workspace as the human arm. This measure determines the percentage the workspace of a CDPM matches with that of its corresponding human arm joint.

Due to the flexible nature of cables, CDPMs have relatively low stiffness which affect the

positional accuracy. Hence, a new global performance quality measure is proposed by utilizing the conditioning index of the stiffness matrix over the entire workspace. Although this index will not be necessary during the design optimization at this stage, it will prove useful when coming up with a design whose task requires a certain amount of stiffness.

Chapter 5

Design Optimization & Prototype Development

Section 5.1 presents the design optimization methodology for the individual CDPM modules with its optimized results. Section 5.2 presents the developed prototype and its various components, while Section 5.3 proposes a hybrid position-force based control scheme for future work, and presents a novel designed tension sensor prototype for such force-based control applications. Finally, Section 5.4 discusses the highlights of this chapter.

5.1 Design Optimization

In the past, a naive optimal design was achieved by comparing a few alternative design solutions created based on a priori problem knowledge. However, the objective of designing the optimum mechanism was never guaranteed, as an exhaustive search was not conducted. Hence, design optimization became essential for such cases. Optimization algorithms have gained popularity in the engineering design field mainly because of the availability and affordability of high-speed computers. Optimization involves either minimization or maximization of an objective. In any mechanism design process, the idea of optimality is challenging to realize, as there is no single global criterion that will include all the objective functions. It is practically impossible to include workspace quantity and quality measures together as a single performance measure. However, it is also desired to have the best conditioning of the workspace, but these two goals are often conflicting. For CDPMs, the unilateral property of cables further restrict the limited and complex workspace. Hence, efforts have mainly been focused on enlarging the workspace by investigating the number of cables attached to the moving platform, the configuration of the cable suspending and cable attachment points [132, 133, 134]. There have been works that also investigated the trends in the workspace under the effect of design parameters [95].

5.1.1 Methodology

The design optimization for the 7-DOF cable-driven robotic arm is to determine the optimal configuration which renders the closest performance as the human arm. However, analysis of the operational workspace of a redundant 7-DOF arm is complicated because it involves the analysis of both position workspace and orientation workspace that are often coupled with each other. In addition, there is no effective way to present and characterize the 6-dimensional operational workspace. Hence, in order to simplify the analysis, a joint-level workspace optimization approach is employed. By analyzing the individual workspace of

the three joint CDPM modules and comparing to their respective counterparts in a human arm, we are able to evaluate the workspace properties of the 7-DOF CDRA design. For this purpose, the workspace of the individual human arm joints were generated in Section 4.5, to be used as templates for these joint CDPM modules to achieve and the design optimization is aimed at maximizing the *WMI* (formulated in Section 4.6.1) of each CDPM modules. Stiffness will be utilized as a design constraint to ensure certain workspace quality, as well as a secondary criterion to assist in selecting the better design should there be a case of two optimized CDPMs having similar *WMI*.

5.1.2 Optimization Model

The design optimization model consists of three main parts: (i) objective function, (ii) design variables, and (ii) design constraints.

1. **Objective Function**

   The objective function is the *WMI* of a CDPM module (with the aim of maximizing *WMI*).

2. **Design Variables**

   The design variables include the number of cables, the cable attachment points arrangement and the mechanism dimensions (i.e., d_1, d_2, r_1 and r_2, which are the length of the base and moving platform constraint links, and the radius of the base and moving platform respectively, as shown in Fig. 5.1). However, these design variables will result in an infinite number of configurations to investigate. With an aim of finding a realizable solution, the optimization process is subjected to the several constraints.

3. **Design Constraints**

   (a) Configuration of CDPM modules are restricted to those with symmetric designs (i.e., with regular polygonal shapes for the cable attachment points on the base

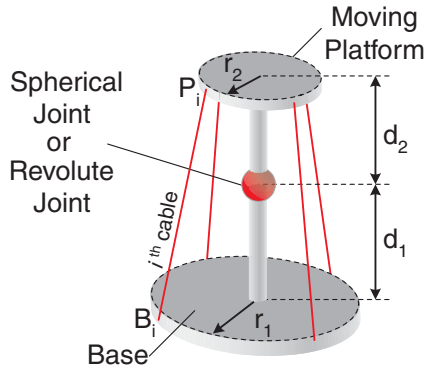

Figure 5.1: Mechanism dimension parameters

and moving platform) with the same number of cables in each attachment point group. Symmetric designs minimize cable interference, while asymmetric designs cause anisotropy of dynamic characteristics and may result in unexpected motion of the moving platform under interaction with external wrenches. The suitable range for the minimum number of cables needed to manipulate a CDPM is determined based on Caratheodory and Steinitz theorems [75]. For a n-DOF CDPM, Caratheodory's theorem implies that a minimum of $(n + 1)$ cables in positive tension are required, while Steinitz's theorem implies that at most $2n$ cables in positive tension are sufficient. Hence, the minimum number of cables needed to effectively manipulate the 1-DOF CDPM is two (see Fig. 4.2(a)), while it ranges from four to six for the 3-DOF CDPM. Figure 5.2 shows the topological synthesis of symmetric four-, five- and six-cable 3-DOF CDPMs.

(b) Dimensional constraints are imposed on the design variables d_1, d_2, r_1 and r_2. They are based on the human arm anthropometric data [135] and ensure that the 7-DOF CDRA design will not be too large for practical application or incur physical interference with the mechanical components. It will also ensure that it will bear similar resemblance to the human arm for aesthetic purposes.

- Shoulder module dimension constraints

  $15 \leq r_1 \leq 130mm$, $15 \leq r_2 \leq 50mm$, $50 \leq d_1 \leq 125mm$ and $50 \leq d_2 \leq 200mm$

- Elbow module dimension constraints

$15 \leq r_1 \leq 50mm$, $10 \leq r_2 \leq 45mm$, $50 \leq d_1 \leq 100mm$ and $50 \leq d_2 \leq 100mm$

- Wrist module dimension constraints

  $10 \leq r_1 \leq 45mm$, $10 \leq r_2 \leq 45mm$, $50 \leq d_1 \leq 100mm$ and $50 \leq d_2 \leq 100mm$

(c) Qualitative workspace performance constraints are imposed to ensure that the workspace is of certain quality. Due the flexible nature of cables, the stiffness of the tool-tip is critical to maintain. Hence, the stiffness matrix performance indices (see Section 4.6.2) will be used as the workspace quality constraint. For the 3-DOF CDPM, the minimum SCI for each pose in the design to achieve is set to $1e^{-6}$, while the 1-DOF CDPM must achieve a minimum torsional stiffness of 500 Nm/rad at each pose.

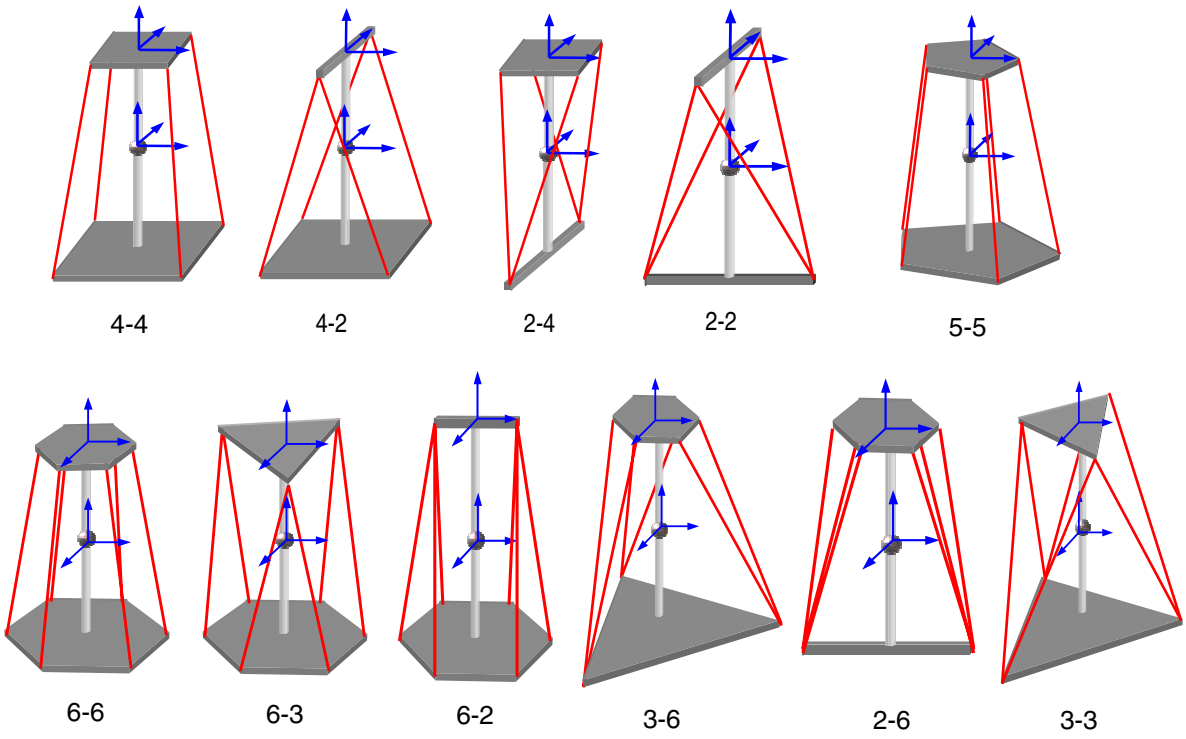

Figure 5.2: Topological synthesis of symmetric four-, five- and six-cable 3-DOF CDPMs

5.1.3 Optimization Algorithm

A direct optimization approach is adopted as the objective function as the optimization model constraints are highly nonlinear. In this investigation, the complex optimization

algorithm [136] is used to search for the optimal design solution due to the non-linearity of the objective function. This algorithm begins with a number of randomly created feasible points. If an unfeasible point is found, a new point is created using the previously generated feasible point. The unfeasible point is pushed towards the centroid of the previously found feasible points. Once a set of feasible points is found, the worst point is reflected about the centroid of the rest of the points to determine the new point. The new point is further modified and accepted, depending on the feasibility and function value of the new point. If this new point falls outside the variable boundaries, the point is modified to fall on the violated boundary. If the new point is feasible, the point is retracted towards the feasible points. This new feasible point replaces the worst point in the simplex and the algorithm continues for the next iteration.

For the algorithm to succeed, the feasible region must be of convex type. Otherwise retraction of the centroid point may result in unfeasible points. This method is slightly modified to obtain the optimized values effectively. Figure 5.3 shows the flowchart of the modified complex search optimization procedure. The optimization procedure is described as follows:

- **Step 1**: Set a bound for design variable vector $\mathbf{x}$ $(\mathbf{x}_L, \mathbf{x}_U)$, reflection parameter ν and termination parameters ε, and ξ. Point $\mathbf{x}$ consists of k design variables that satisfy the design constraints.

- **Step 2**: Randomly generate an initial set of $2k$ feasible points: $\mathbf{x}_i = \mathbf{x}_L + \chi(\mathbf{x}_H - \mathbf{x}_L)$ where χ is a random factor from 0 to 1.

- **Step 3**: Calculate the respective function values $(f_1, \ldots, f_{2k})$, as given in Eqns. (4.18) and (4.19).

- **Step 4**: Carry out the reflection step:

  (a) Select $\mathbf{x}_{min}$ such that $f(\mathbf{x}_{min}) = \min\,(f_1, f_2, \ldots, f_{2k}) = f_{min}$; and $\mathbf{x}_{max}$ such that $f(\mathbf{x}_{max}) = \max\,(f_1, f_2, \ldots, f_{2k}) = f_{max}$

(b) Calculate the centroid $\mathbf{x}_c$ (of all points except $\mathbf{x}_{min}$):

$$\mathbf{x}_c = \left(\sum_{i=1}^{2k} \mathbf{x}_i - \mathbf{x}_{min} \right) / (2k-1)$$

And determine the new point $\mathbf{x}_m$: $\mathbf{x}_m = \mathbf{x}_c + \nu(\mathbf{x}_c - \mathbf{x}_{min})$

(c) If $\mathbf{x}_m$ is feasible and $f(\mathbf{x}_m) \leq f_{min}$, retract half the distance to the centroid $\mathbf{x}_c$ (if $f(\mathbf{x}_c) > f_{min}$) or half the distance to $\mathbf{x}_{max}$ (if $f(\mathbf{x}_c) \leq f_{min}$). Continue this until $f(\mathbf{x}_m) > f_{min}$.

(d) Else if $\mathbf{x}_m$ is feasible and $f(\mathbf{x}_m) > f_{min}$, proceed to Step 6.

(e) Else if $\mathbf{x}_m$ is infeasible, proceed to Step 5.

- **Step 5**: Check for feasibility of the solution and reset violated variable bounds:

$$\begin{cases} \text{If } \mathbf{x}_m < \mathbf{x}_L \text{ set } \mathbf{x}_m = \mathbf{x}_L \\ \text{If } \mathbf{x}_m > \mathbf{x}_U \text{ set } \mathbf{x}_m = \mathbf{x}_U \end{cases}$$

- **Step 6**: Replace $\mathbf{x}_{min}$(or $\mathbf{x}_{max}$) by $\mathbf{x}_m$ and check for termination.

(a) Calculate $\bar{f} = \dfrac{1}{2k} \sum_{i=1}^{2k} f(\mathbf{x}_i)$ and $\bar{\mathbf{x}} = \dfrac{1}{2k} \sum_{i=1}^{2k} \mathbf{x}_i$.

(b) If $\sqrt{\sum_{i=1}^{2k} (f(\mathbf{x}_i) - \bar{f})^2} \leq \varepsilon$ and $\sqrt{\sum_{i=1}^{2k} \|\mathbf{x}_i - \bar{\mathbf{x}}\|^2} \leq \xi$, then terminate optimization process.

(c) Else continue optimization process in Step 4(a)).

The algorithm (based on the flowchart in Fig. 5.3) is coded in MATLAB and it is run on a PIV 3Ghz desktop PC to obtain the optimization results.

5.1.4 Optimization Results

The design optimization is carried out with the various ranges of the dimension parameters as defined in Section 5.1.3.

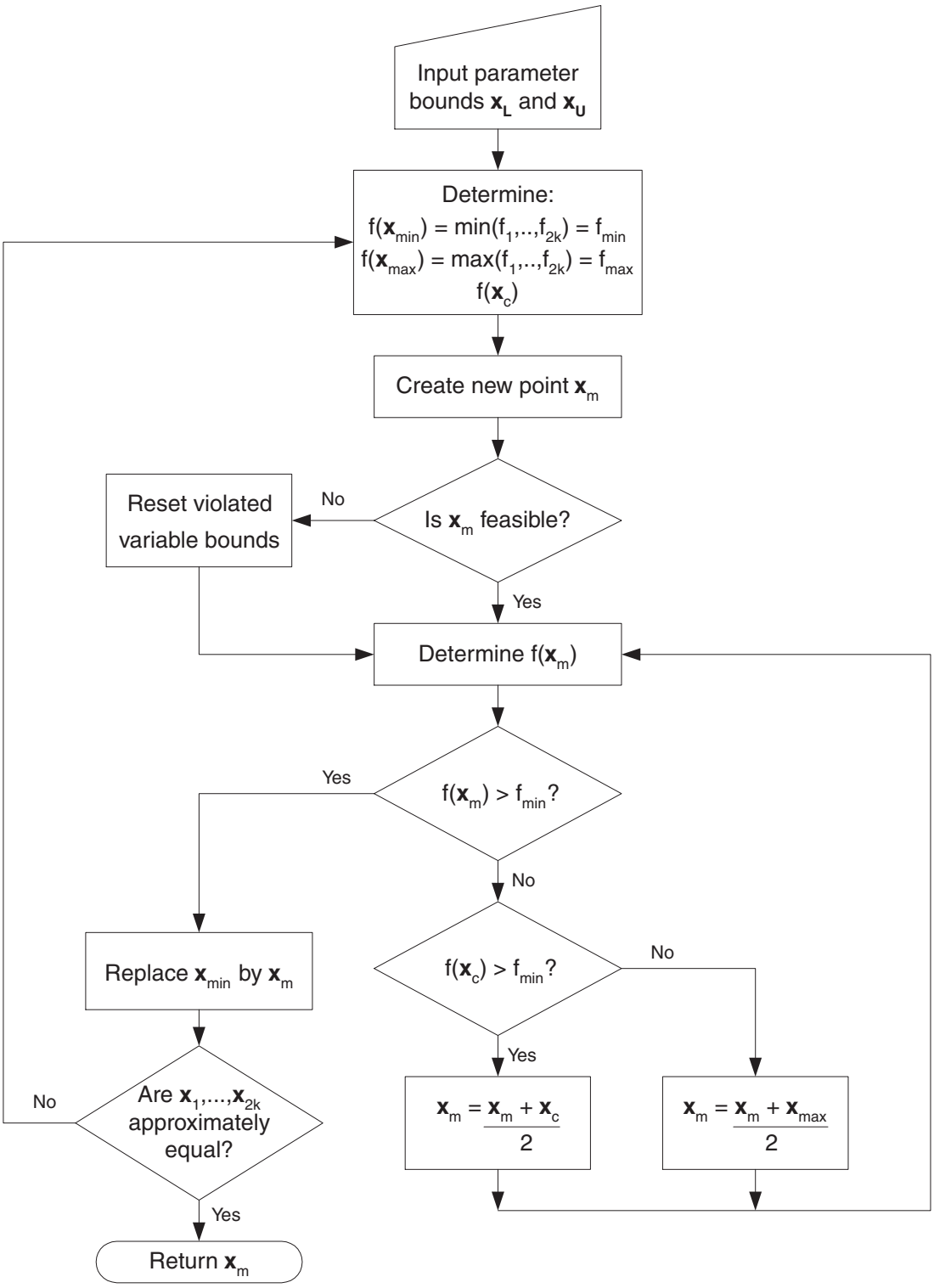

Figure 5.3: Modified complex search optimization algorithm flowchart

(a) Optimized Result of the Shoulder Module

There are four ($= k$) design variables for the optimization algorithm (i.e., r_1, r_2, d_1 and d_2). Optimization was carried out on the various symmetric four-, five- and six-cable configurations (see Fig. 5.2). Based on the optimization results (see Table 5.1), the optimized shoulder module is a 3-3 six-cable configuration with $r_1 = 129mm$, $r_2 = 49mm$, $d_1 = 72mm$, $d_2 = 51mm$, *WMI* of 0.686 and *GSCI* of 0.358. Figure 5.4 shows the configuration dimensions and workspace plot of the optimized shoulder module. The result was obtained within 100 iterations in approximately 30 minutes (with number of divisions, $p = 10$).

Table 5.1: Optimization results for the various symmetric shoulder module configurations

Number of Cables	Configuration	*WMI* $(0-1)$	*GSCI* $(0-1)$
Four	4-4	0.098	0.023
	4-2	0.194	0.031
	2-4	0.168	0.096
	2-2	0.221	0.293
Five	5-5	0.131	0.038
Six	6-6	0.181	0.054
	6-3	0.360	0.137
	6-2	0.433	0.114
	3-6	0.352	0.199
	3-3	0.686	0.358
	2-6	0.225	0.081

(b) Optimized Result of the Elbow Module

There are four ($= k$) design variables for the optimization algorithm (i.e., r_1, r_2, d_1 and d_2). After the optimization process, the optimized elbow module is a 2-2 two-cable configuration with $r_1 = 50mm$, $r_2 = 45mm$, $d_1 = 50mm$, $d_2 = 50mm$, and *WMI* of 0.617, as shown in Fig. 5.5.

However, since the elbow module is a planar case with a relatively straightforward configu-

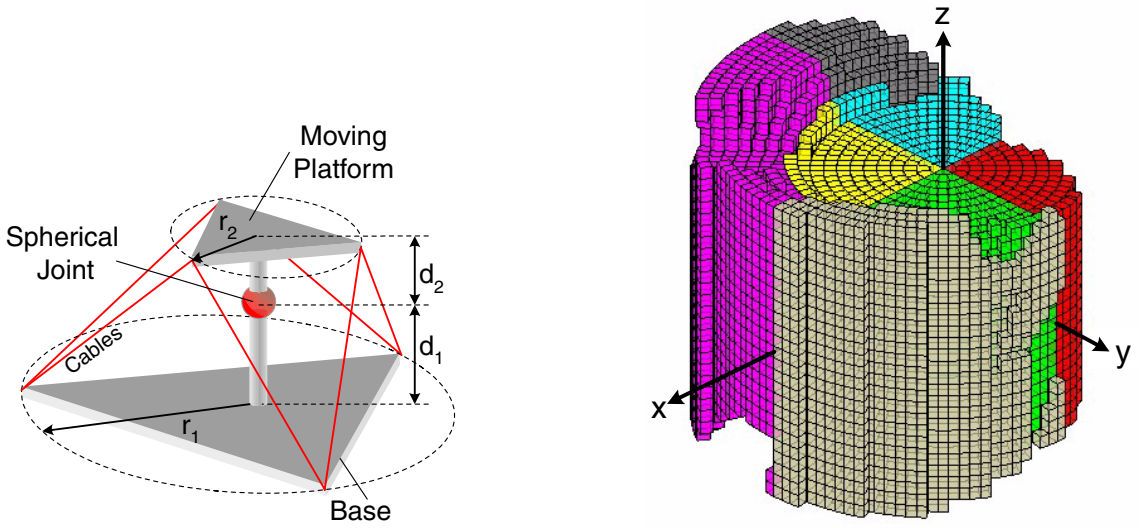

(a) Optimized 3-3 six-cable configuration with $r_1 = 129mm$, $r_2 = 49mm$, $d_1 = 72mm$ and $d_2 = 51mm$

(b) Optimized cylindrical workspace plot with WMI=0.686

Figure 5.4: Optimized shoulder module

ration, the design variables are increased in order to achieve an elbow module with better WMI. Hence the modified design optimization problem for the elbow module is described as follows:

- **Design Variables**: The mechanism dimensions ($k = 8$) now include two components for each cable attachment point (i.e., $\{x_{bi}, z_{bi}\}$ and $\{x_{pi}, z_{pi}\}$, $i = 1, 2$)
- **Design Constraints**: These design constraints are still based on the previous design constraints for the elbow module, except that now, they are set to ensure that the two cables do not intersect or cross-over each other during the elbow joint motion range.
  - $-50 \leq x_{b1} \leq -15mm$, $15 \leq x_{b2} \leq 50mm$, $-45 \leq x_{p1} \leq -10mm$ and $10 \leq x_{p2} \leq 45mm$
  - $50 \leq z_{b1}, z_{p1}, z_{p2} \leq 100mm$ and $-100 \leq z_{b2} \leq -50mm$
  - In addition, $z_{p1} > z_{b1}$

The same modified complex search optimization algorithm is utilized, but for this case, the number of generated initial set of feasible points in Step 2 are 16 (i.e., $k = 8$). After the

modified optimization process, the optimized elbow module is a 2-2 two-cable configuration with $x_{b1} = -50mm$, $z_{b1} = 57mm$, $x_{b2} = 21mm$, $z_{b2} = -82mm$, $x_{p1} = -44mm$, $z_{b1} = 79mm$, $x_{p2} = 28.5mm$, $z_{p2} = 78mm$, WMI of 1 and $GSPI$ of 1.48 kNm/rad, as shown in Fig. 5.5(b). The result was obtained within 40 iterations in approximately 30 seconds (with angular increment of $\pi/180°$).

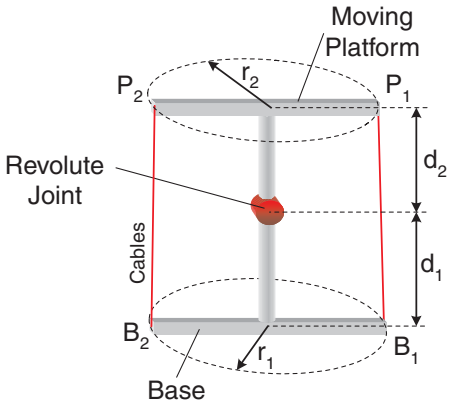

(a) Optimized 2-2 two-cable configuration with $r_1 = 50mm$, $r_2 = 45mm$, $d_1 = 50mm$, $d_2 = 50mm$, and WMI=0.617

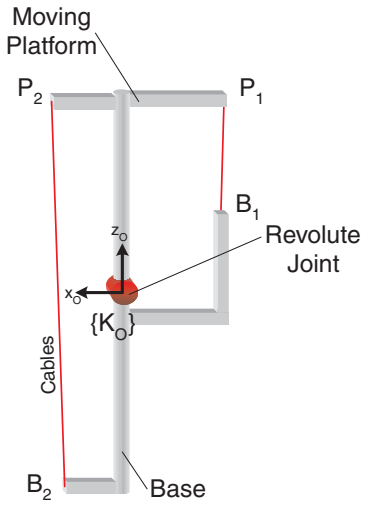

(b) Optimized 2-2 two-cable configuration (based on modified optimization problem) with $x_{b1} = -50mm$, $z_{b1} = 57mm$, $x_{b2} = 21mm$, $z_{b2} = -82mm$, $x_{p1} = -44mm$, $z_{p1} = 79mm$, $x_{p2} = 28.5mm$, $z_{p2} = 78mm$, and WMI=1

Figure 5.5: Optimized elbow module

(c) Optimized Result of the Wrist Module

There are four (= k) design variables for the optimization algorithm (i.e., r_1, r_2, d_1 and d_2). Optimization was carried out on the various symmetric four-, five- and six-cable configurations (see Fig. 5.2). Based on the optimization results (see Table 5.2), the optimized wrist module is a 3-3 six-cable configuration with $r_1 = 39mm$, $r_2 = 44mm$, $d_1 = 57mm$, $d_2 = 51mm$, WMI of 0.555 and $GSCI$ of 0.209. Figure 5.6 shows the configuration dimensions and workspace plot of the optimized wrist module. The result was obtained within 50

iterations in approximately 10 minutes (with number of divisions, $p = 10$).

Table 5.2: Optimization results for the various symmetric wrist module configurations

Number of Cables	Configuration	WMI $(0-1)$	$GSCI$ $(0-1)$
Four	4-4	0.019	$2.13e^{-6}$
	4-2	0.229	0.049
	2-4	0.198	0.055
	2-2	0.373	0.271
Five	5-5	0.040	$1.87e^{-5}$
Six	6-6	0.054	$3.93e^{-5}$
	6-3	0.267	0.080
	6-2	0.408	0.066
	3-6	0.280	0.092
	3-3	0.555	0.209
	2-6	0.227	0.082

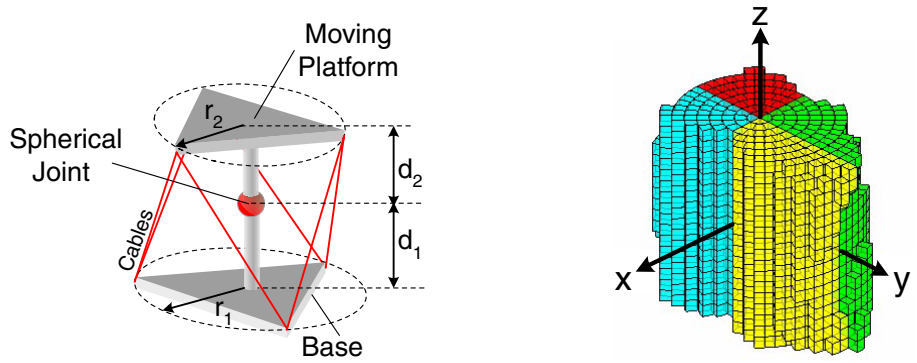

(a) Optimized 3-3 six-cable configuration with $r_1 = 39mm$, $r_2 = 44mm$, $d_1 = 57mm$ and $d_2 = 51mm$

(b) Optimized cylindrical workspace plot with WMI=0.555

Figure 5.6: Optimized wrist module

From the optimization results, the shoulder and wrist modules achieved WMI of 60-70%, while the elbow module achieved WMI of 100%. The optimization process for the shoulder module was the longest as the prescribed workspace was almost three times larger than that of the wrist module, while the optimization for the elbow was the shortest as it only had one orientation parameter. In addition, it is observed that the results obtained are consistent with results reported in literature [133, 137], in terms of the number of cables

and cable attachment points (i.e., workspace increases with increasing number of cables and decreasing number of cable attachment points). The next section will present the prototype development of these optimized CDPM modules and the 7-DOF cable-driven robotic arm.

5.2 Prototype Development

The prototype of the 7-DOF cable-driven robotic arm is developed for the purpose of carrying out experimental investigations. This prototype is also based on achieving a 7-DOF assistive robotic arm with a workspace matching as closely possible as the human arm. This section will present the various components of the 7-DOF CDRA prototype.

5.2.1 Cable Actuation Unit

The cable actuation unit (CAU) consists of a DC servo motor from Servodynamics® (Model number: IG23CS-22-EPC1000-F with quadrature count of 4000 pulses per revolution) connected to a cable winding drum through a 4:1 belt-&-pulley transmission system, as shown in Fig. 5.7. Each DC servo motor is driven by a Kollmorgen® amplifier (Model: Silverline SO-4004). Based on the motor specifications and the transmission system design, the CAU was determined to withstand cable tension of approximately 250N, and can achieve cable spooling velocity of up to 0.3m/s.

(a) Cable Selection

Cable selection is carried out based on the criterion of being flexible enough to be routed, yet has negligible extension under loading. In terms of a quantitative measure, this is related to the ratio of maximum cable tension[1] over the stiffness per reciprocal unit length, and it has

[1] This refers to the maximum tension in the linear elastic region and not the maximum tension until material failure.

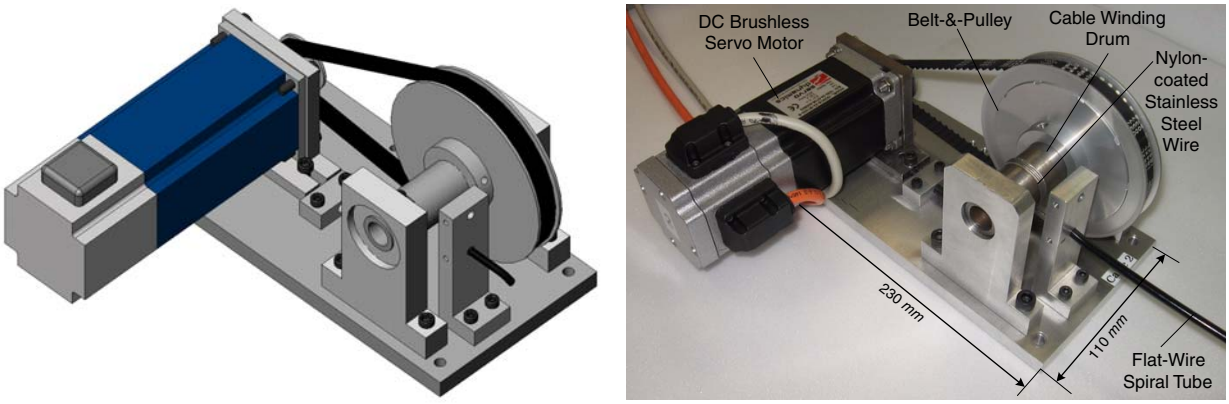

(a) CAD of cable actuation unit

(b) Fabricated cable actuation unit

Figure 5.7: Cable actuation unit

to be less than 0.5% for a cable to be considered suitable [86]. A nylon-coated stainless steel cable with loading limit of 200 lbs ($\approx$ 900N), is found to be suitable for the cable-driven prototype. An added advantage of the selected cable is the nylon coating which will minimize friction during routing, hence removing the need to manually coat the cables. A tensile test is carried out on a nylon-coated cable with diameter of $1mm$ and sample length of $150mm$. Figure 5.8 shows the tensile test plot versus the cable length elongation.

(b) Cable Routing

Cables to each CDPM are routed from the cable actuation units through flat-wire spiral tubes (see Fig. 5.9). Flat-wire spiral tubes offer the flexibility of varying the base cable attachment points, and are very suitable for cable routing to the distant elbow and wrist modules from the prototype base structure. Friction between the nylon-coated cables and the inner linings of the tube are also minimized by coating the inner linings with teflon spray.

(c) Cable Attachment Points

Cable attachment points at the base and moving platform are assumed to behave as spherical joints . This is rather challenging in practical applications, especially for base cable attach-

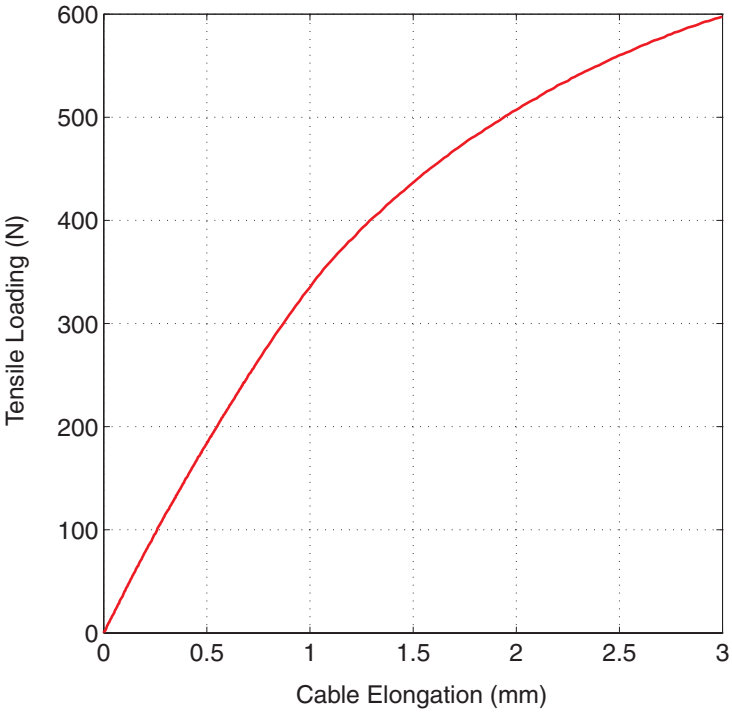

Figure 5.8: Tensile loading test of the nylon-coated stainless steel cable (sample length of $150mm$)

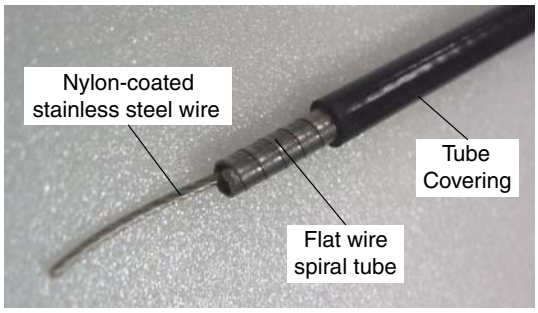

Figure 5.9: Flat-wire spiral tube for cable routing

ment points. For the 7-DOF CDRA prototype, inserts made from Delrin[2] are designed and fabricated to ensure the base cable attachment points are precise (see Fig. 5.10(a)). As for the moving platform cable attachment points, clamps are designed to ensure the pair of cables are clamped to a single point and bolted onto the moving platform to ensure the cables are not pulled apart during the motion (see Fig. 5.10(b)).

[2] Delrin® is the brand name for an acetal resin engineering plastic invented and sold by DuPont. Delrin is a lightweight, low-friction, and wear-resistant plastic, often used as a metal substitute.

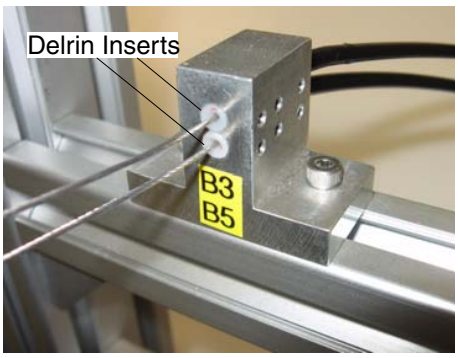

(a) Base cable attachment point with Delrin® inserts

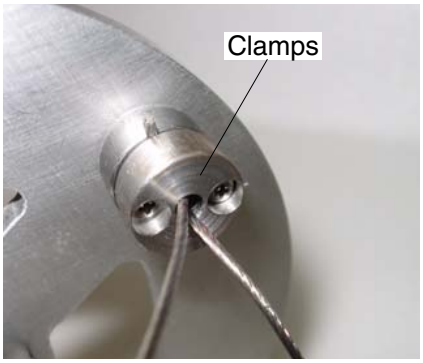

(b) Moving platform cable attachment point with a clamp design

Figure 5.10: Cable attachment point designs

5.2.2 Shoulder Module

Based on the optimization results in Section 5.1.4, the shoulder module is fabricated and it is the first module of the 7-DOF CDRA, located nearest the base. As shown in Fig. 5.11, there are three base cable attachment points. However, as it is physically impossible to actuate two cables from a single point, the three base points are in fact six points, with each pair being located as closely possible (see Fig. 5.10(a)). A spherical joint from Hephaist® (Model: SRJ 008J) is utilized as the central link spherical joint constraint.

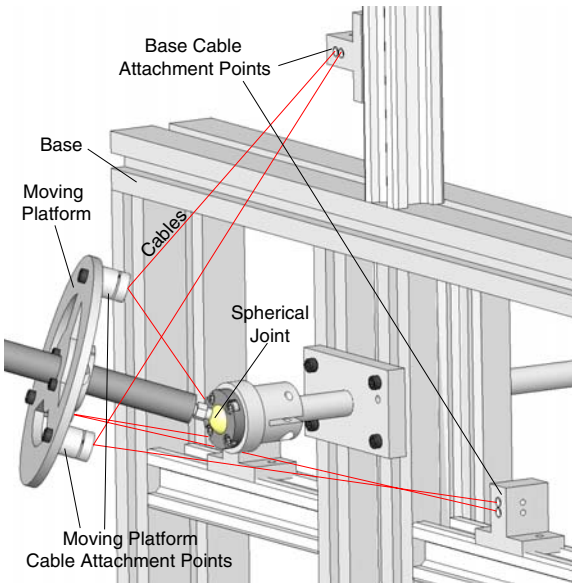

(a) CAD of shoulder module

(b) Fabricated shoulder module

Figure 5.11: 3-DOF shoulder module prototype

5.2.3 Elbow Module

The elbow module is the second module of the 7-DOF CDRA to be assembled in series with the shoulder module. As shown in Fig. 5.12, the dimensions are based on the optimization results in Section 5.1.4 and a revolute joint is fabricated to be used as the central link revolute joint constraint.

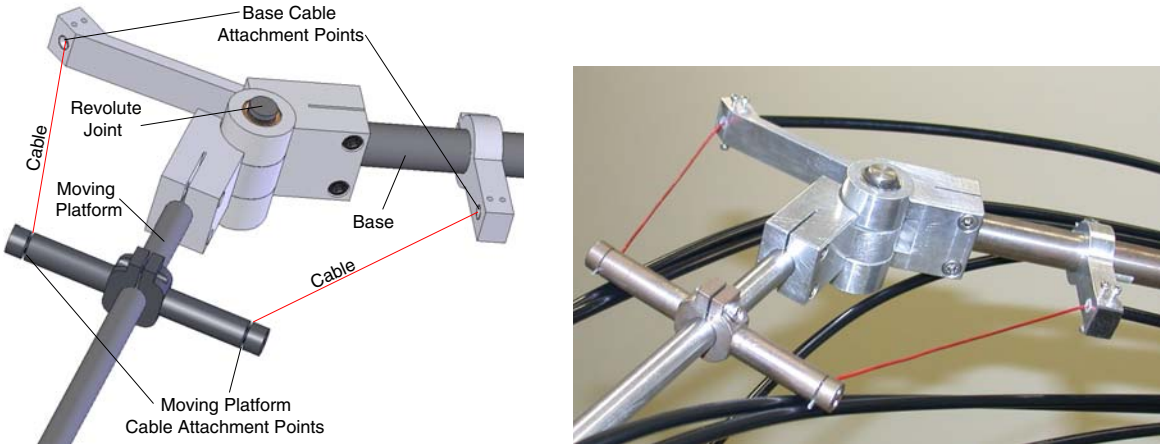

(a) CAD of elbow module

(b) Fabricated elbow module

Figure 5.12: 1-DOF elbow module prototype

5.2.4 Wrist Module

The wrist module is similarly designed as the shoulder module except for its dimensions. It is the third module of the 7-DOF CDRA to be assembled in series with the elbow module. As shown in Fig. 5.13, the dimensions are based on the optimization results in Section 5.1.4 and a smaller sized spherical joint from Hephaist® (Model: SRJ 006J) is utilized as the central link spherical joint constraint.

5.2.5 7-DOF Cable-Driven Robotic Arm Prototype

The 7-DOF cable-driven robotic arm consists of three serially connected CDPM modules. As shown in Fig. 5.14, the first module is the 3-DOF shoulder module, assembled in series with

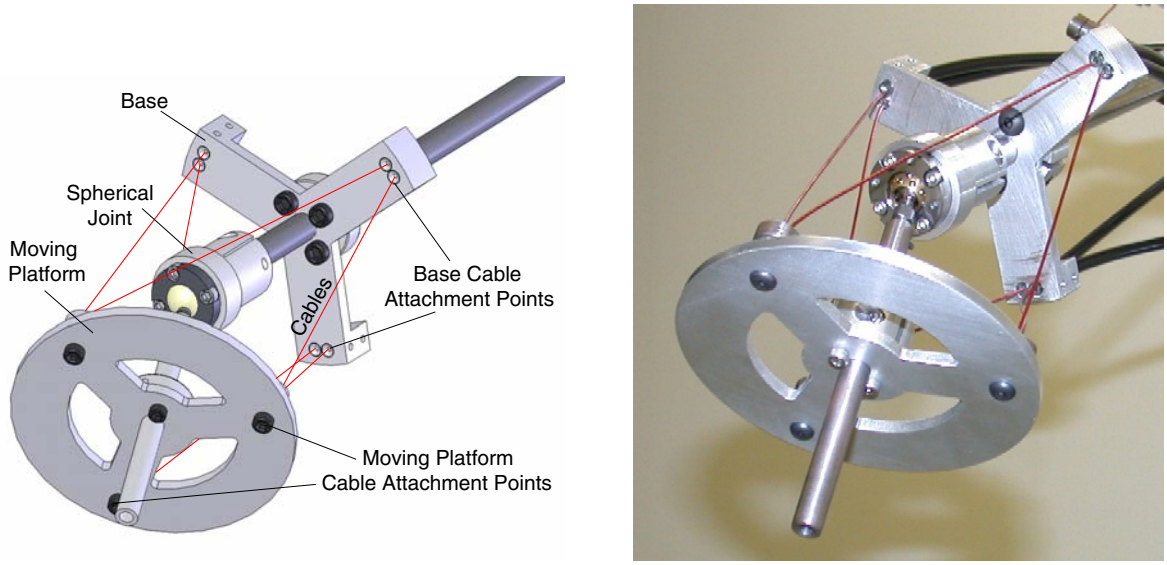

(a) CAD of wrist module

(b) Fabricated wrist module

Figure 5.13: 3-DOF wrist module prototype

the 1-DOF elbow module, which is finally assembled in series with the 3-DOF wrist module. The distance between the joints of the various CDPM modules are also similar to that of a human arm in order to have a similar reachable workspace envelope (see Fig. 5.14). The assembled arm is lightweight, weighing approximately 1 kilogram. A position-feedback based control scheme with pre-tensioning using the standard PID control scheme was implemented on the CDRA to determine its performance. From experimental studies, the CDRA was found to have repeatability of $\pm 2.5mm$, and with a payload capacity of approximately 5 kilograms at the tool-tip of the wrist module.

(a) Home Pose

In any mechanism, homing is necessary for subsequent motion tasks. For this prototype, homing clamps are fabricated to physically set the 'home' pose of the shoulder and wrist modules, while a hard stop on the elbow module sets its 'home' pose, as shown in Fig. 5.15. While we can always ensure a consistent home pose for the elbow module, the homing clamps for the shoulder and wrist modules cannot ensure the consistent home pose, especially for the twist angle (i.e., σ). In order to ensure that the twist of the shoulder and wrist modules

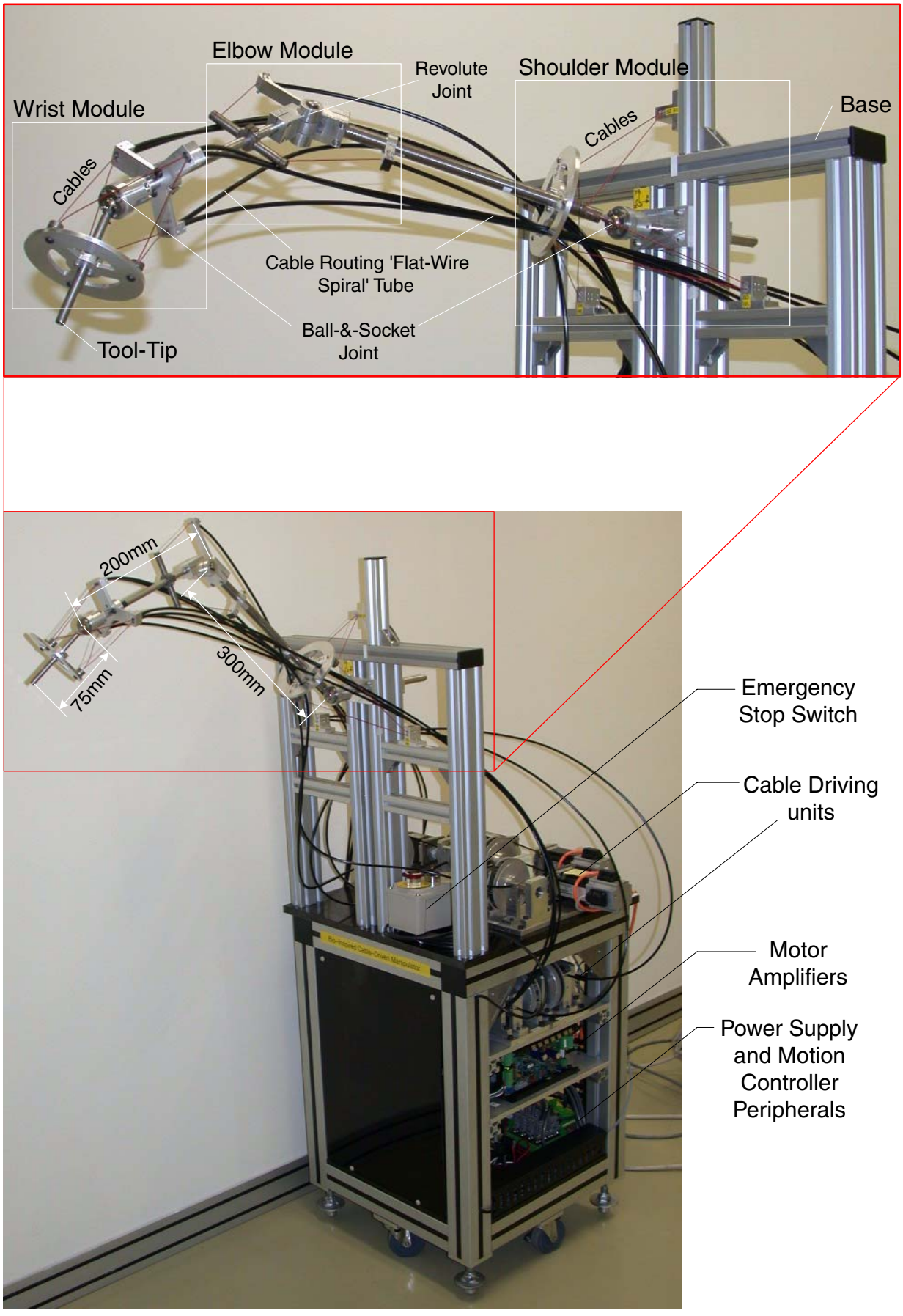

Figure 5.14: Fabricated 7-DOF cable-driven robotic arm prototype

always start from a consistent pose, the cable lengths are checked for equal length at the home pose. After being positioned in the 'home' pose, the motor encoder readings are initialized and subsequent motion are then referenced based on the cable lengths at home pose.

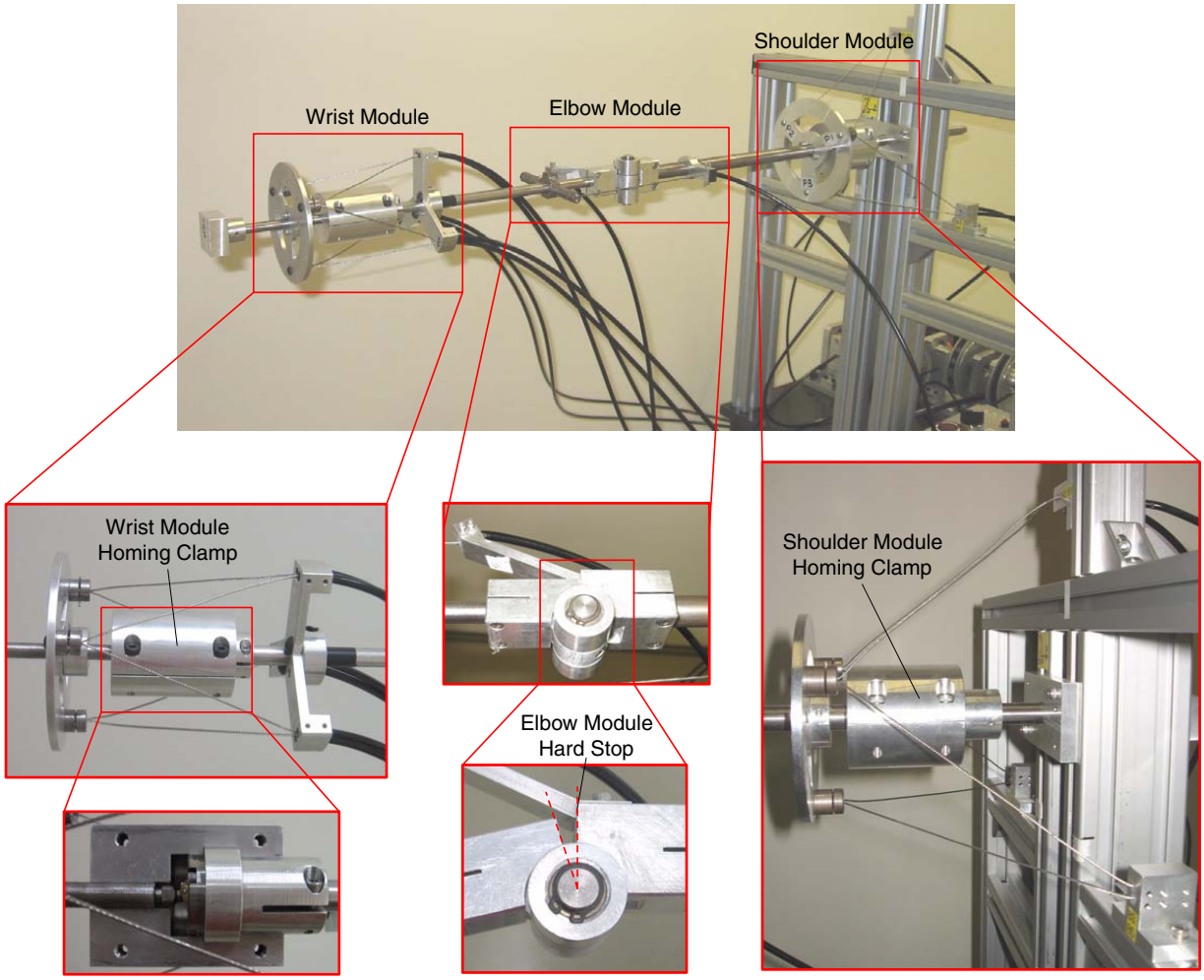

Figure 5.15: 'Home' pose of the 7-DOF CDRA prototype with its homing devices

(b) Hardware Setup

Figure 5.16 shows the hardware setup for the 7-DOF cable-driven robotic arm prototype. A computer-based motion controller from National Instruments® (Model: NI PCI-7358) is utilized. It serves as a controller for the servo motor as well as to obtain feedback (either motor encoder readings or tension sensor readings) based on the control schemes adopted. The computer functions as a host to perform high-level tasks and all commands are sent through the NI LabView® graphical user interface. The trajectory generation and control

schemes are also implemented through the LabView interface. An emergency stop switch is also installed to shut down the CAUs incase of any unforeseen events (see Fig. 5.14).

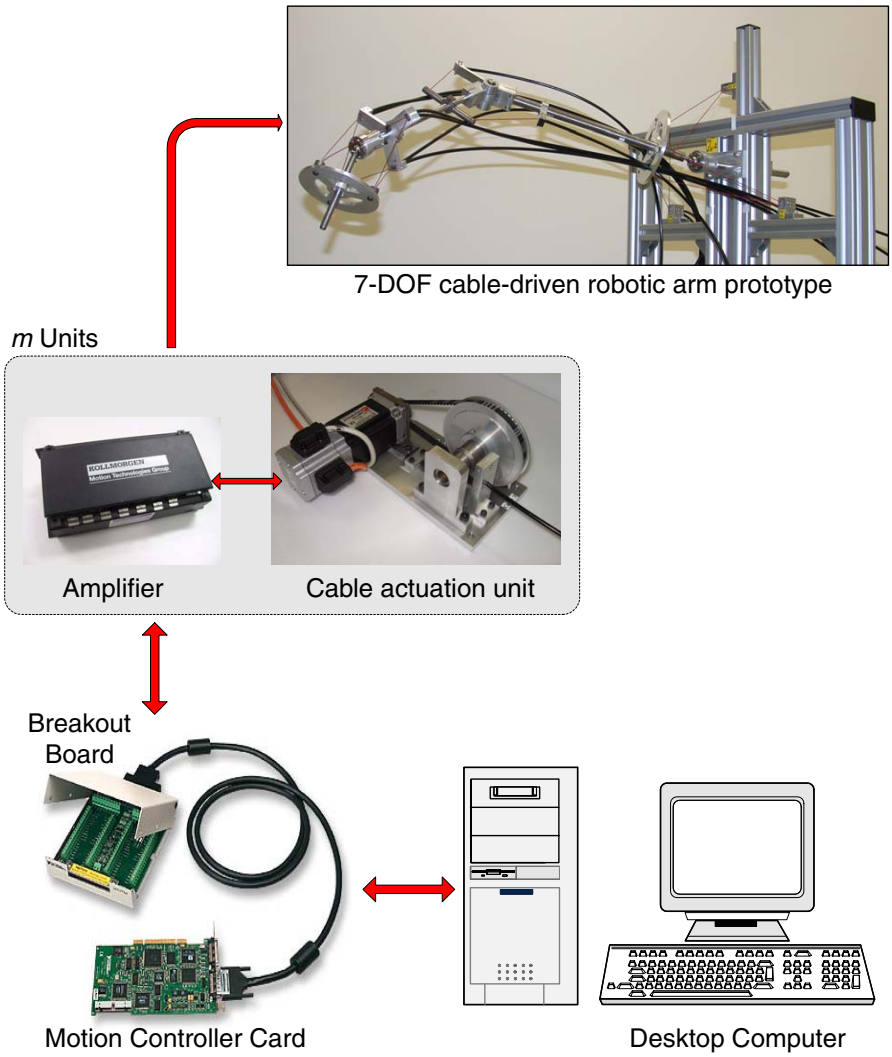

Figure 5.16: Hardware setup for the 7-DOF CDRA prototype

5.3 Proposed Tension Control

While the main focus of this thesis is on the design and development of a 7-DOF CDRA, preliminary efforts have been made to propose a unique hybrid position-force based control scheme for future work.

The unilateral driving property of cables in CDPMs prevent direct application of well-known

control approaches, and one of the critical issue to address is maintaining the positive tension in cables. Unlike incompletely-restrained CDPMs which usually rely on gravity to guarantee the positive tension in cables, sufficiently-restrained CDPMs have deterministic motions, and numerous control strategies which include the dynamics of the end-effector and the cable actuation units, have been proposed. Ming [74] implemented a PID controller for a planar four-cable CDPM which compensated its cable's elongation. Williams [138] proposed a PD controller for a planar four-cable CDPM, including its nonlinear and coupled dynamic model. Oh and Agrawal investigated the control performance of cable-suspended robots and a dual-stage cable robot by using various control approaches. These approaches included feedback controllers based on feedback linearization theory [139], Lyapunov theory [116, 117] and sliding mode control [140]. In addition to position-feedback based controllers, force-feedback based controllers have also been developed for teleoperation applications, such as a 'tension and reaction force' feedback controller implemented by Morizono [104] for a virtual sports training system.

This section will present a hybrid control scheme and the development of a novel designed tension sensor for such force-based control applications.

5.3.1 Hybrid Position-Force Based Control Scheme

For the developed 7-DOF cable-driven robotic arm prototype, a position based control scheme is insufficient as the arm's tool-tip will come in contact with environment. Hence, force based control is necessary to ensure additional compliance (as an additional safety feature) in the event of unforeseen collisions with the environment and the user. In this section, a unique hybrid position-force control scheme is proposed for such applications. This scheme utilizes n cables to determine the desired pose of the moving platform, while the remaining $m - n$ cables are utilized to ensure that all m cables are in positive tension. For any n-DOF rigid-link or cable-driven mechanism, n rigid-link lengths or cable lengths are sufficient to determine the pose of the moving-platform. The only difference is that CDPMs

require a minimum of $n+1$ cables in positive tension, to sufficiently restrain the moving platform (i.e., tension-closure condition). This can be achieved by selecting n cables to be under position based control scheme, while the remaining $m-n$ cables are under force based control scheme (see Fig. 5.17). It is also understood that tension-closure condition analysis is a pre-requisite, and if force-closure condition is satisfied, the stability of the moving platform is based on the assumption that the CAUs under position based control have a holding torque sufficient enough to withstand the maximum torques generated by the CAUs under force based control.

In order to determine the cable tensions based on the proposed hybrid position-force control scheme, the null space approach (see Section 4.3.4) is utilized as follows:

$$\begin{aligned} \mathbf{T} &= \mathbf{A}^{\#}.\mathbf{D} + \mathbf{N}\boldsymbol{\lambda} \\ \begin{Bmatrix} \mathbf{T}_{position} \\ \mathbf{T}_{force} \end{Bmatrix} &= \begin{Bmatrix} \left[\mathbf{A}^{\#}.\mathbf{D}\right]_{position} \\ \left[\mathbf{A}^{\#}.\mathbf{D}\right]_{force} \end{Bmatrix} + \begin{bmatrix} \mathbf{N}_{position} \\ \mathbf{N}_{force} \end{bmatrix} \begin{Bmatrix} \lambda_1 \\ \vdots \\ \lambda_{(m-n)} \end{Bmatrix} \end{aligned} \tag{5.1}$$

Where:

$\mathbf{T} \in \Re^{m\times 1}$: Column vector of cable tension

$\mathbf{T}_{position} \in \Re^{n\times 1}$: Column vector of cable tension under position control

$\mathbf{T}_{force} \in \Re^{(m-n)\times 1}$: Column vector of cable tension under force control

$\mathbf{A}^{\#}.\mathbf{D} \in \Re^{m\times 1}$: Particular solution of $\mathbf{T}$

$\left[\mathbf{A}^{\#}.\mathbf{D}\right]_{position} \in \Re^{n\times 1}$: Components of $\mathbf{A}^{\#}.\mathbf{D}$ for cable tension under position control

$\left[\mathbf{A}^{\#}.\mathbf{D}\right]_{force} \in \Re^{(m-n)\times 1}$: Components of $\mathbf{A}^{\#}.\mathbf{D}$ for cable tension under force control

$\mathbf{D}$: External wrench acting on the moving platform, including the dynamic terms and the gravity terms

$\mathbf{N} \in \Re^{m\times(m-n)}$: Null space (or homogeneous) solution of $\mathbf{T}$

$\mathbf{N}_{position} \in \Re^{n\times(m-n)}$: Row vector components of $\mathbf{N}$ for cables under position control

$\mathbf{N}_{force} \in \Re^{(m-n)\times(m-n)}$: Row vector components of $\mathbf{N}$ for cables under force control

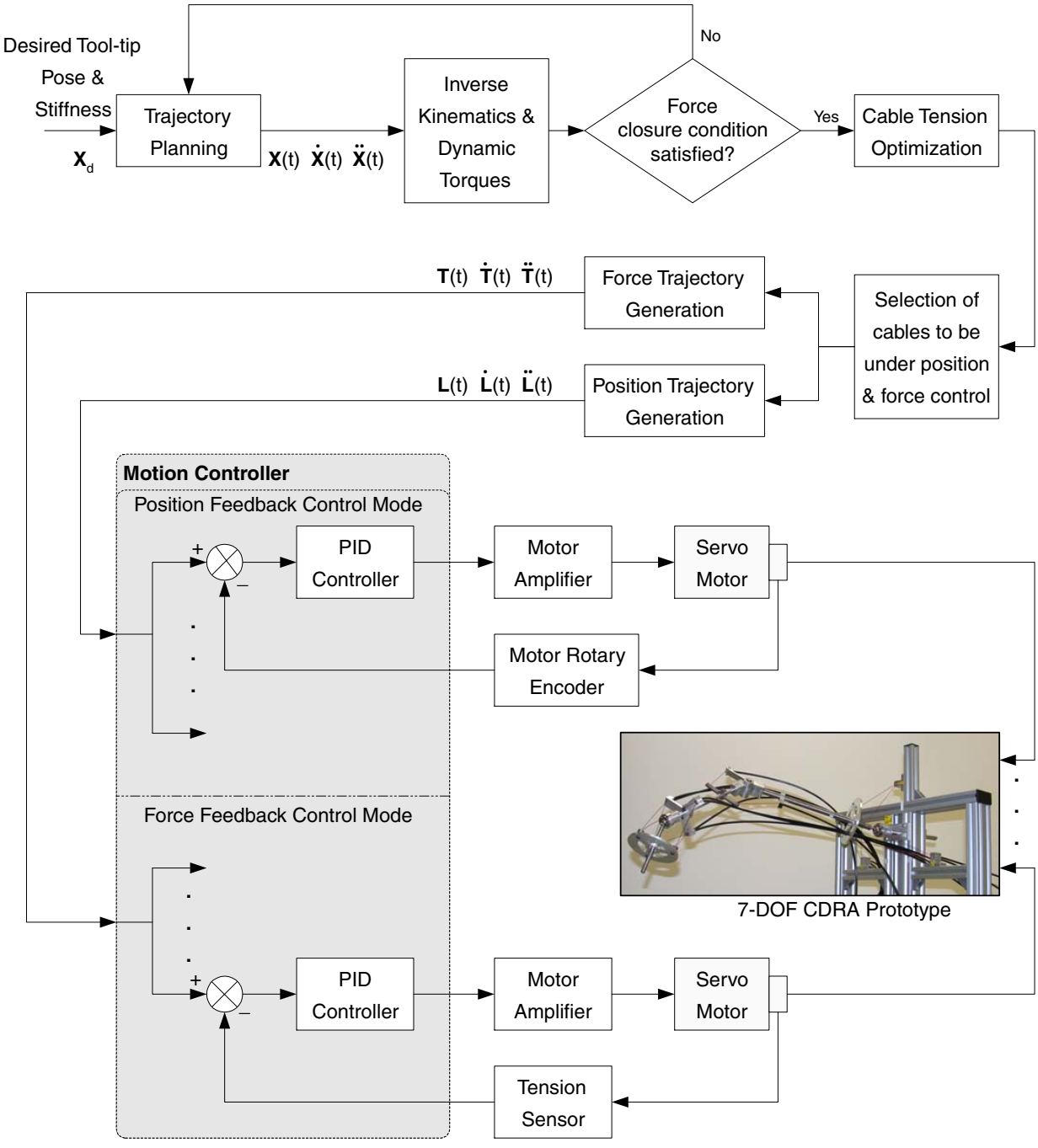

Figure 5.17: Hybrid position-force based control scheme

$\boldsymbol{\lambda} = \{\lambda_1, \ldots, \lambda_{(m-n)}\}^T$: Arbitrary scalar for the homogeneous solution of $\mathbf{T}$

For a n-DOF CDPM with m ($\geq n+1$) cables, given the tension of $m-n$ force-controlled cables[3] and combining with Eqn. (5.1), the tension in the remaining n position-controlled cables can be obtained as follows:

$$\mathbf{T}_{position} = \left[\mathbf{A}^{\#}.\mathbf{D}\right]_{position} + \mathbf{N}_{position}\mathbf{N}_{force}^{-1}\left(\mathbf{T}_{force} - \left[\mathbf{A}^{\#}.\mathbf{D}\right]_{force}\right) \tag{5.2}$$

From Eqn. (5.2), the tension of the position-controlled cables can be determined from the tensions of the force-controlled cables. This can allow the formulation of an efficient optimal cable tension algorithm with the aim of minimizing the cable tension in all m cables. Even-though we have m different cable tension parameters, the objective function will consists of only $(m-n)$ independent parameters. This is because the tension of the n cables under position control are dependent on the tension of the $(m-n)$ cables under force control, as shown in Eqn. (5.2).

For future implementation, several issues need to be investigated. The first issue is the prioritization of the feedback schemes. As a hybrid scheme, conflicts may arise if the closed-loop control parameters are set incorrectly and both are given equal priority. A feasible approach to resolve this conflict is to give prioritization to these feedback schemes, which is dependent on the task specifications. However in most cases, position feedback scheme will be given the main priority and the task would require maintaining a certain amount of force. The next important question that comes to mind is the amount of tolerances to set for both schemes to work together successfully. This will require further investigation and experimental study. Another issue that needs to be addressed is the selection of cables to be under position or force feedback schemes. Incorrect selection of cables to be under position control may result in singularity configurations, leading to instability of the moving platform under influence of external wrenches. Implementation issues such as these will be considered for future work.

[3] This is determined based on certain objective functions defined by the application or task requirements.

5.3.2 Developed Tension Sensor Prototype

For CDPMs, determination of cable tension is pertinent due to the unilateral property of cables. Hence, in order to implement a scheme to control the cable tension, a novel designed tension sensor prototype (as shown in Fig. 5.18) is developed which is lightweight, compact, has negligible extension under tensile loading, and able to measure low-range tension (i.e., in the range of zero to a few hundred Newton). Since the tension sensor is of low-range force capacity, aluminium alloys are most suitable for achieving the required strain levels, and is made of Aluminium 6061. The design for the tension sensor is proposed to be octagonal-shaped with a binocular hole to create regions of critical stress and to assist in the installation of the foil strain gauges (see Fig. 5.18(a)). Four $1mm$ 120 Ω aluminium foil strain gauges from Tokyo Sokki Kenkyujo Co., Ltd. (Model: FLA-1-23, see Fig. 5.18(b)) are utilized to form a full Wheatstone-bridge circuit. Two strain gauges are placed on the outer surface of the binocular hole which are areas of critical stresses, while the other two are placed on regions of negligible stress to serve as dummy gauges to compensate the effects of temperature, as shown in Fig. 5.18(c). Figure 5.19 shows the elongation of the tension sensor under tensile loading. Although this tension sensor can withstand high tensile loads, the recommended working range of the tension sensor should be approximately 80% of the maximum tension in the linear elastic region (i.e., this is approximately 750N, as seen from Fig. 5.19). Readers may refer to [141, 142] for more information on strain gauge technology and development.

Data Acquisition Setup

As shown in Fig. 5.20, a data acquisition setup from National Instruments is purchased in order to acquire the strain readings from the Wheatstone-bridge circuit formed on the tension sensor prototype. These readings are then be converted into an analog voltage signal and used as feedback to the motion controller in order to implement force-feedback based control schemes. Figure 5.21 shows the sensitivity plot where the average analog output signal from the tension sensor (through output analog signals from SCC-SG04) are plotted

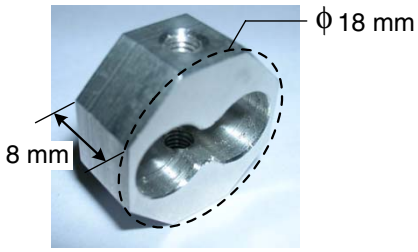

(a) Fabricated octagonal-shaped tension sensor with a binocular hole

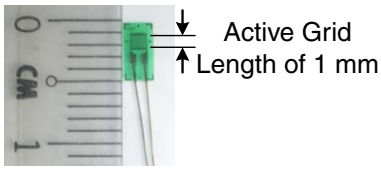

(b) $1mm$ 120 Ω aluminium foil strain gauge from Tokyo Sokki Kenkyujo Co., Ltd.

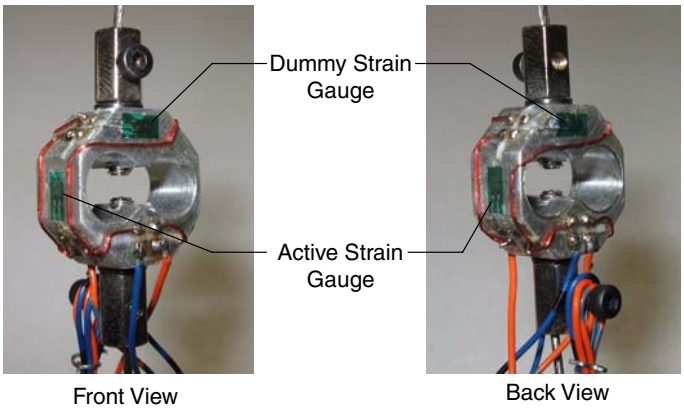

(c) Tension sensor installed with strain gauges to form a Wheatstone-bridge circuit

Figure 5.18: Components of the developed tension sensor

against the applied tensile load to the tension sensor. Tensile loads of up to 300N are plotted as the working range for the tension sensor is up to 250N, and the results show a linear trend. Hence, the developed tension sensor is suitable for use in such force based control implementation. However, further effort is required to develop the tension sensor, in terms of signal processing and its optimal design, and will be considered for future work.

5.4 Discussion

In this chapter, design optimization is carried out, followed by the prototype development. Preliminary discussions are made regarding a unique hybrid position-force based control scheme proposal and a novel designed tension sensor prototype is presented for use in such applications.

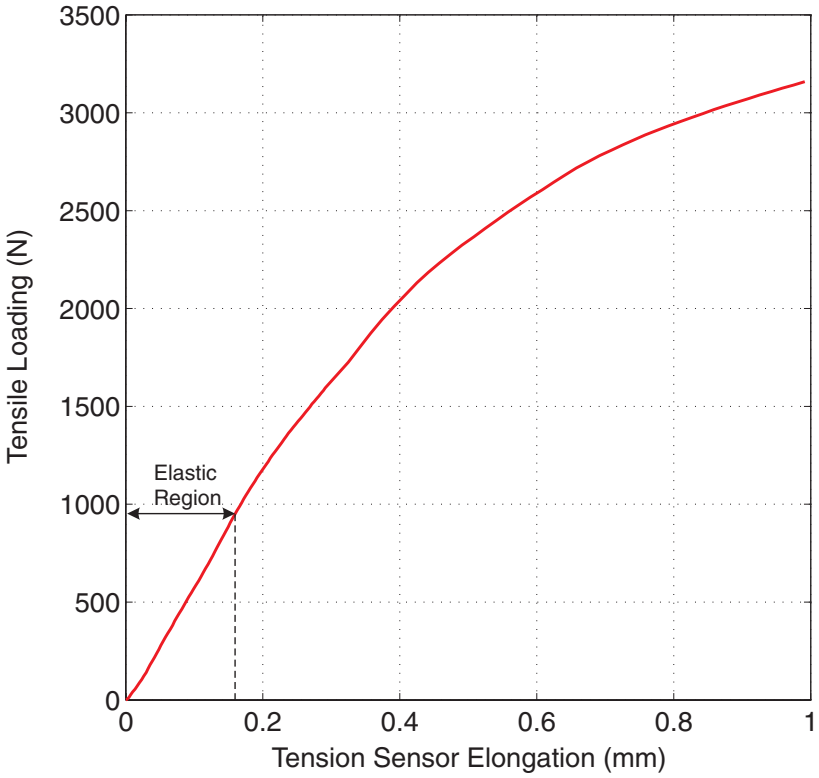

Figure 5.19: Tensile loading versus elongation plot of the fabricated tension sensor

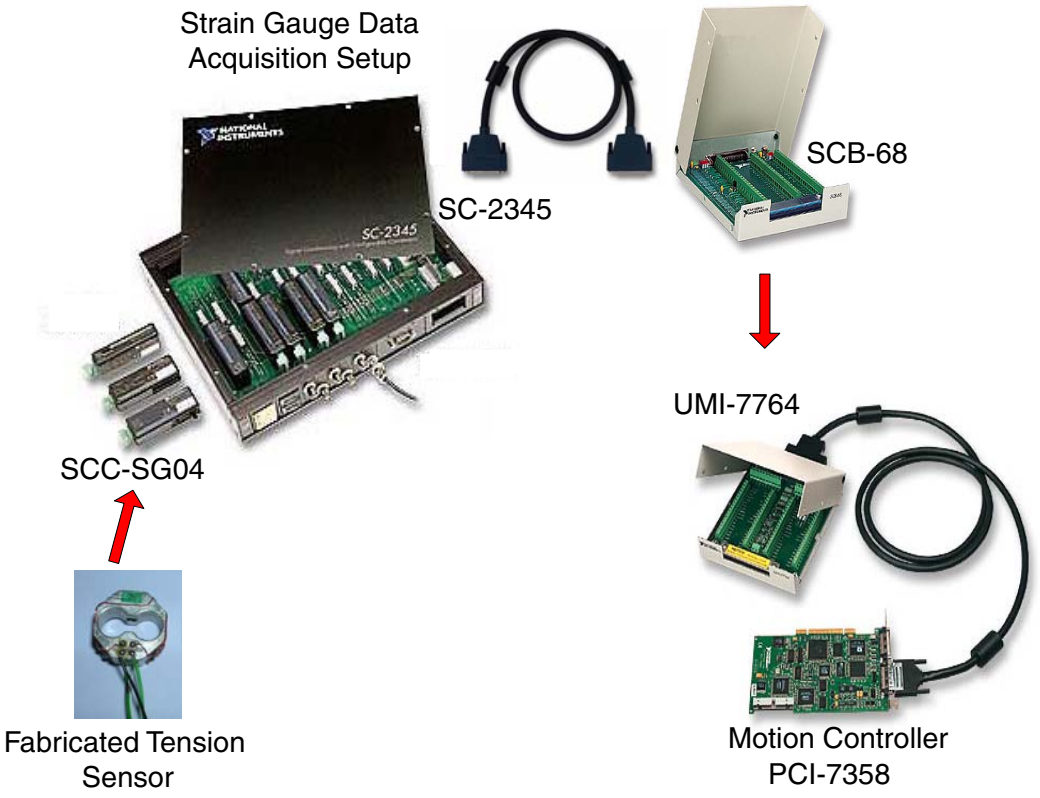

Figure 5.20: Tension sensor data acquisition setup from National Instruments

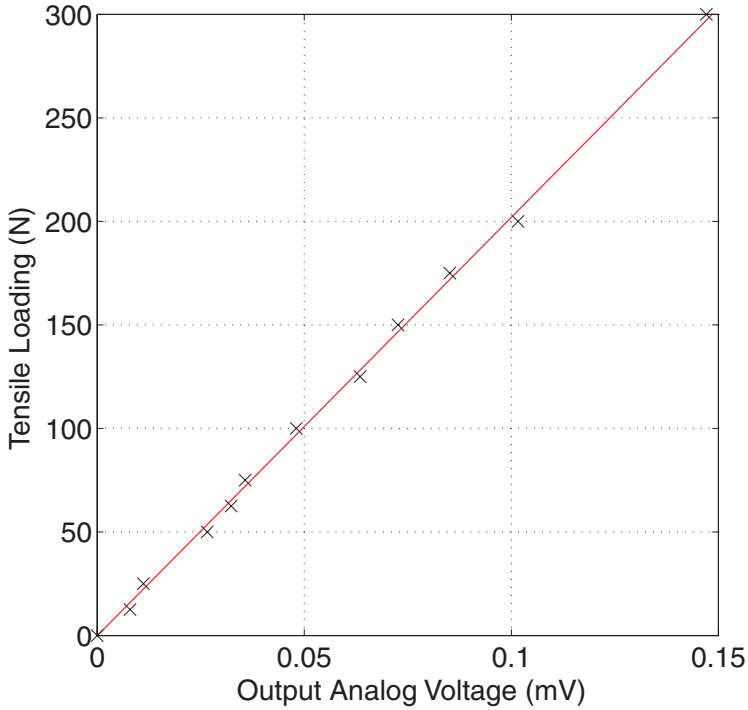

Figure 5.21: Tensile loading versus output analog voltage plot of the fabricated tension sensor

Design optimization is carried out with the aim of achieving a 7-DOF cable-driven robotic arm whose workspace will match as closely to the actual workspace of the 7-DOF human arm. However, analysis of the operational workspace of a redundant 7-DOF arm is complicated because it involves the analysis of both position workspace and orientation workspace that are often coupled with each other. In addition, there is no effective way to present and characterize the 6-dimensional operational workspace. Hence, in order to simplify the analysis, a joint-level workspace optimization approach is employed. The individual CDPM modules are optimized such that their workspace will closely match the workspace of their corresponding human arm joints' workspace (i.e., maximizing *WMI*). An optimization model is formulated and optimization is based on a modified-complex search algorithm due to the non-linearity of the objective function. The optimization resulted in shoulder/wrist modules achieving *WMI* of approximately 60 to 70%, while the elbow module achieved *WMI* of 100%. Similar to the optimization of the elbow module, *WMI* of the shoulder/wrist modules can also be improved if asymmetric designs are considered. In addition, as observed in the human arm, designs could also include crossing of cables over different joint segments. If

such an approach is employed, it is possible to obtain better *WMI*. However, this would increase complexity in the control implementation as the motion of each module is no longer decoupled. Based on the optimization results, a 7-DOF CDRA prototype is developed for subsequent experimental investigations. The various components of the prototype and its peripherals are also presented in detail. From preliminary tests, the 7-DOF arm prototype, weighing approximately 1 kilogram, has a payload capacity of approximately 5 kilograms and repeatability of $\pm 2.5mm$ at the tool-tip.

As the major focus of this thesis is the design and development of a 7-DOF cable-driven robotic arm, control aspects are not addressed. Instead, preliminary efforts are made to propose a unique hybrid position-force based control scheme for future work. This scheme utilizes n cables to determine the desired pose of the moving platform, while the remaining $m-n$ cables are utilized to ensure that all m cables are in positive tension. Given the tension of the force-controlled cables, the tension in the position controlled-cables are determined based on the null space approach. This provides with a means to optimize the cable tension based on the stiffness requirements of the tool-tip. The development of a novel designed tension sensor prototype which is lightweight, compact and with negligible extension, is also presented for use in such force-based control implementation. Preliminary tests show that the tension sensor is suitable for use as it has linear output voltage readings within its working range of up to 250N, with a linear and relatively smaller elongation (compared to the nylon-coated stainless steel cables under similar loading conditions). More efforts are still required to develop the tension sensor, in terms of signal processing and its optimal design.

Chapter 6

Calibration of Kinematic Parameters

Section 6.1-6.2 highlights the recent advancements in robot calibration and the general procedure for the calibration of the entire 7-DOF cable-driven robotic arm. Section 6.3 presents the self-calibration of the individual CDPM modules, including the self-calibration model, the self-calibration algorithm and the results. For the results, both simulation studies and experiments are carried out to verify the proposed self-calibration model. Section 6.4 presents the calibration of the whole 7-DOF cable-driven robotic arm, after assembly of the individual CDPM modules. In this section, the calibration model and algorithm are presented, followed by simulation studies and experiments. This is followed by discussion in Section 6.5, highlighting the salient points in this chapter.

6.1 Background

The positioning accuracy of a robot manipulator is significantly dependent on the kinematic model parameters. However, deviations always exist from the nominal kinematic model due to factors like manufacturing defects, assembly misalignments, compliance, wear of connecting mechanisms and thermal sensitivity, which affect the accuracy. Hence, in order to enhance the positioning accuracy, there is a need to determine the actual values of the kinematic parameters and incorporate them into the nominal kinematic model in the manipulator control software, rather than altering its physical structure. This process is known as *kinematic model-based calibration.*

In general, the calibration process consists of four basic steps [143]: modeling, measurement, parameter identification and error compensation.

(a) Modeling

'Modeling' refers to the formulation of a suitable error kinematic calibration model[1] that will relate the output of the joint displacements to the pose of the end-effector. The calibration model (i.e., usually a differential kinematic model) is based on two basic kinematic models, i.e., *forward* and *inverse* kinematic models. The forward model computes the pose from the given joint displacements, while the inverse model computes the joint displacements from the given pose. Although both basic kinematic methods relate the same sets of information (i.e., joint displacement and pose), they differ in form and complexity depending on the manipulator structure (i.e., open-loop or closed-loop kinematic chain). Results from both basic kinematic models will come into play during the calibration process. However, inverse models of serial robots and

[1] In order to obtain a good calibration model, the criterions of completeness, proportionality and equivalence, should be achieved. Completeness refers to a complete kinematic model that is able to relate the joint displacements to the end-effector poses for any manipulator configuration and should allow arbitrary placement of the inertial frame and the home pose. Proportionality implies that a differential change in the actual manipulator structure should result in a corresponding differential change in its parameters. Equivalence refers to the ability to transform the parameters of one model to other model descriptions.

forward models of parallel robots are not straightforward to determine analytically. Hence numerical methods have to be used and this significantly adds to the computational burden and reduces the robustness of the calibration model. As a result, there has been growing interest in recent years to indirectly estimate the pose errors, also known as *implicit* methods [144]. While the previous method explicitly makes use of the pose or joint displacement information, implicit methods utilizes redundant information, either by using the leg lengths [145] or by placing redundant proprioceptive sensors at the passive joints [146], to indirectly estimate the pose errors.

(b) Measurement

'Measurement' refers to the physical data collection process required by the calibration model. Pose measurement is one of the significant phases in robot calibration and there are two main measurement schemes, namely *semi-autonomous* and *fully-autonomous*. While both schemes require redundant information, it is the way these redundant information are obtained that distinguishes them. Semi-autonomous schemes (also known as external calibration) rely on complete or partial pose measurements to obtain the redundant information. This is usually done by using external pose measurement devices like coordinate measuring machines [147], laser displacement sensors [148], linear variable differential transformer (LVDT) sensors [149], double ball bar system [145], electronic theodolites [150], inclinometers [151], vision-based systems [152], and even customized fixtures [153]. On the other hand, fully-autonomous schemes (also known as self-calibration) obtain the required redundant information by either restraining the mobility of the end-effector [154], or obtaining measurement information from the existing internal sensors of the manipulator actuators and/or the additional sensors placed at the passive joints of the system [146].

Pose measurement for manipulator calibration is usually done in well-controlled laboratory environment using dedicated measurement devices. However, for systems that operate outside a controlled laboratory environment, it would be undesirable to use specialized calibration devices to update the model used for system control. As a result,

self-calibration has received significant attention in recent years as preferred solutions for such cases, and offers the following benefits [155]:

- Calibration can be carried out whenever required as the system is permanently fitted with the measurement devices.
- It is cost-effective as existing or redundant passive joint sensors are inexpensive, compared to most external pose measurement devices.
- It allows measurements to be taken over the entire workspace with high accuracy and at a fast measurement rate.
- The calibration process can be fully automated without any manual feedback to the robot controller.

(c) Parameter Identification

'Parameter Identification' refers to the use of the measurement data obtained in the previous step with various mathematical algorithms, to determine the parametric errors in the nominal geometric kinematic model. There are two types of mathematical algorithms: linear and non-linear [143]. The selection of the appropriate algorithms will depend largely on whether one chooses to ignore or include the second-order terms in the calibration model. Furthermore, in practise, the number of equations is generally larger than the number of unknown parameters, in order to reduce the sensitivity of calibration to data uncertainties. Hence, this results in an over-constrained system of equations, and one of the more common mathematical algorithms utilized is the *least-squares* approach which aims to minimize the sum of the error terms (i.e., measurement residuals).

(d) Error Compensation

'Error Compensation' refers to the process of updating the identified kinematic parameters into the manipulator controller (i.e., implementation issue). These are very important for offline-based and teaching modes. Hence, numerical solution methods (i.e., forward kinematic solution for parallel robots, and inverse kinematic solution for

serial robots), and methods of modifying the robot control software are the key research issues that have to be addressed for successful implementation.

6.2 Calibration Methodology

As shown in Fig. 6.1, the complete calibration procedure for the 7-DOF cable-driven robotic arm consists of two sequential steps: (i) Self-calibration of the various CDPM modules, followed by (ii) Calibration of the 7-DOF CDRA assembly, which requires the self-calibrated models of the individual CDPM modules.

Ideally, the measured and computed values of certain measurable parameters of a mechanism should be consistent. However, due to the errors in the nominal kinematic parameters, the solution from these two paths are not identical. Hence, the discrepancies between the two solutions can be utilized to form measurement residuals. Based on differential kinematics and the measurement residuals, calibration models can then be formulated. If the measurable parameters are sensed at sufficient number of measurement poses, the actual kinematic parameters can then be estimated by minimizing these measurement residuals and then updating the kinematic model. For the CDPM modules, the measurable parameters will be the cable end-point distance through the use of redundant cable length data from the motor encoders of the cable actuation units. For the 7-DOF CDRA, the measurable parameters will be the tool-tip pose information through the use of an external pose measurement devices.

In this chapter, the focus is mainly on the development of the various calibration models. The next few sections will present the self-calibration of the 1-DOF and 3-DOF CDPM modules, followed by the calibration of the entire 7-DOF cable-driven robotic arm assembly. These will include simulation studies and calibration experiments to verify the robustness of the proposed calibration models.

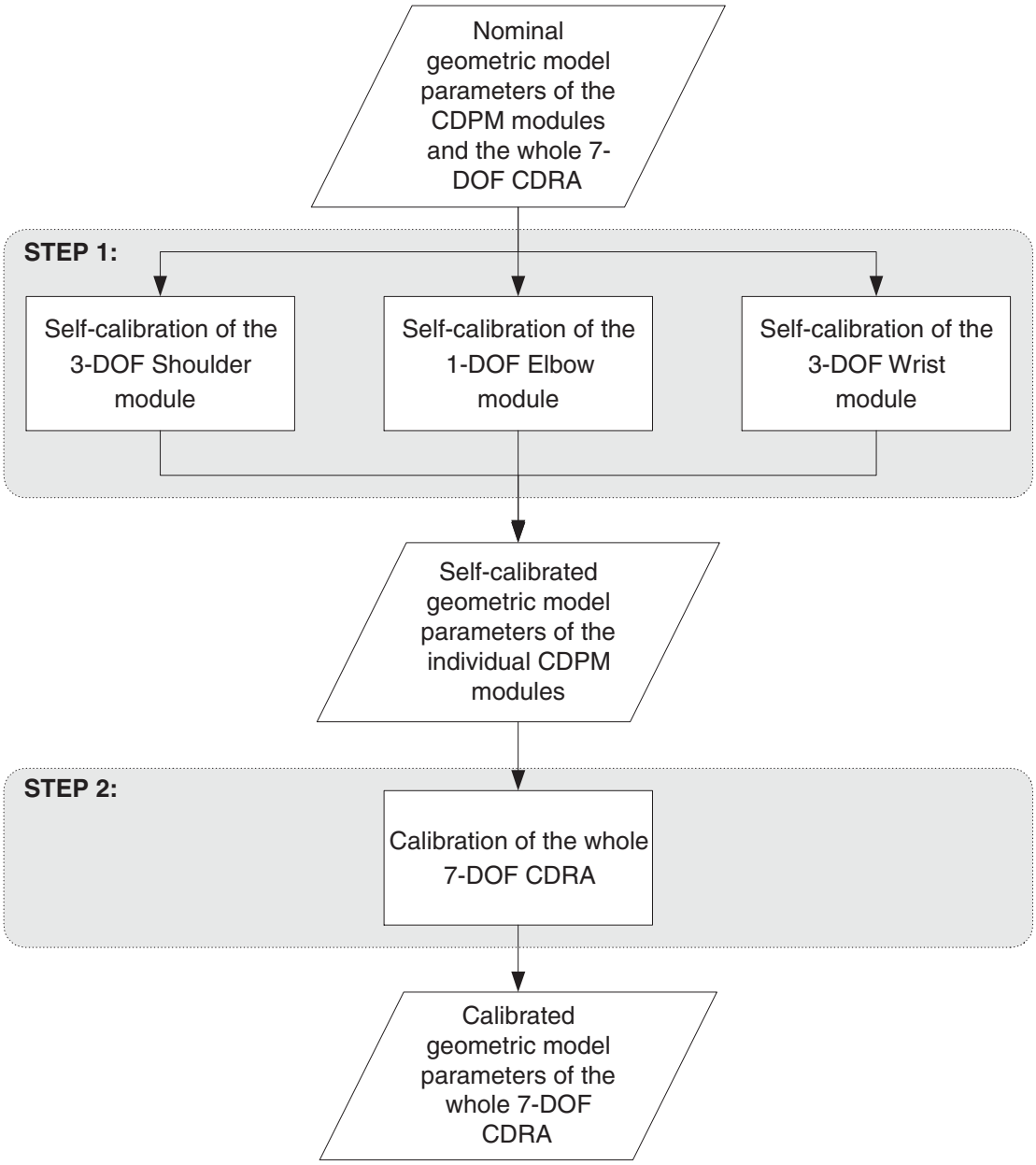

Figure 6.1: Flowchart of the calibration procedure from the individual CDPM modules to the complete 7-DOF CDRA

6.3 Self-Calibration of the CDPM Modules

This section will present the self-calibration of the 1-DOF and 3-DOF CDPM modules. This is crucial as the calibration of the whole 7-DOF CDRA requires the calibrated geometric models of the individual CDPMs.

6.3.1 Kinematic Model Description

(a) Kinematic Model of the 1-DOF CDPM Module

Two coordinate frames $\{K_O\}$ and $\{K_P\}$ are used to describe the kinematic model of the 1-DOF CDPM i.e., elbow module (see Fig. 3.1). Frame $\{K_O\}$ is the inertial coordinate frame located at the revolute joint centre. Frame $\{K_P\}$ is the local coordinate frame on the moving platform and also located at the revolute joint centre, but it undergoes a rotation R_{OP} about the y-axis of frame $\{K_O\}$. $\overrightarrow{OB_j}^{\{O\}} = \{b_{xj}, b_{yj}, b_{zj}\}^T$ $(j = 1, 2)$ are base cable attachment point position vectors that are fixed with respect to $\{K_O\}$, while $\overrightarrow{OP_i}^{\{P\}} = \{{p_{xi}}^p, {p_{yi}}^p, {p_{zi}}^p\}^T$ $(i = 1, 2)$ are the moving platform cable attachment point position vectors that are fixed with respect to $\{K_P\}$. Since this is a planar mechanism, the cable attachment points are located along $y = 0$ for convenience in formulation. The design optimization of the elbow module has resulted in 2-2 two-cable configurations, as elaborated earlier in Section 5.1.4. Since the structure of the elbow module is similar to a four-bar linkage mechanism, a closed-form forward kinematics solution exists for the elbow module, as presented in Eqn. (3.17).

(b) Kinematic Model of the 3-DOF CDPM Module

The design optimization of the shoulder and wrist modules have resulted in a 3-3 six-cable configuration, as elaborated earlier in Section 5.1.4. In the physical setup however, the six base cable attachment points have to be separated as it is physically impossible for two cables to wind/unwind through a single point, unlike the moving platform cable attachment points which can be clamped together at a single point. Hence, this will result in a 6-3 six-cable configuration (see Fig. 6.2). By observing this configuration, the cable end-points P_i $(i = 1, 2, 3)$ of the optimized configuration forms the vertex of three tetrahedrons. Thus, by utilizing this tetrahedron observation, a closed-form forward kinematics solution exist, as presented in Eqn. (3.30). Two coordinate frames $\{K_O\}$ and $\{K_P\}$ are used to describe the kinematic model of the 6-3 six-cable CDPM (see Fig. 6.2). Frame $\{K_O\}$ is the inertial coordinate frame located at the spherical joint centre. Frame $\{K_P\}$ is the local coordinate

frame on the moving platform and also located at the spherical joint centre, but it undergoes a 3-DOF orientation rotation R_{OP} about the frame $\{K_O\}$. $\overrightarrow{OB_j}^{\{O\}} = \{b_{xj}, b_{yj}, b_{zj}\}^T$ $(j = 1, \ldots, 6)$ are base cable attachment point position vectors that are fixed with respect to $\{K_O\}$, while $\overrightarrow{OP_i}^{\{P\}} = \{{p_{xi}}^p, {p_{yi}}^p, {p_{zi}}^p\}^T$ $(i = 1, 2, 3)$ are the moving platform cable attachment point position vectors that are fixed with respect to $\{K_P\}$.

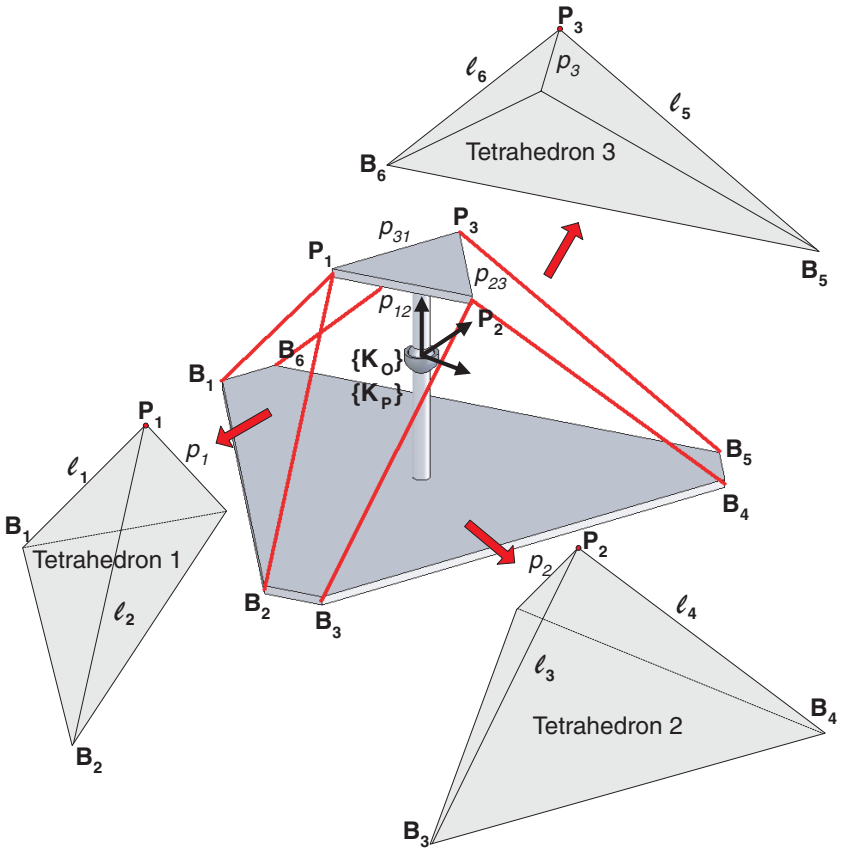

Figure 6.2: Kinematic model of the 6-3 six-cable 3-DOF CDPM with observed tetrahedrons

6.3.2 Self-Calibration Model

The objective of the self-calibration model is to identify the errors in the geometric design parameters of the nominal kinematic model through observations of measurement residues in certain parameters of the mechanism. At any feasible pose, the known measurable parameters are the set of cable lengths, and the distance between the cable end-point on the moving platform. The unknown parameters are $\overrightarrow{OB_j}^{\{O\}}$ and $\overrightarrow{OP_i}^{\{P\}}$, and these values will

be estimated in the kinematic model. Based on these parameters, the self-calibration model will describe the gross errors in the distance between the cable end-point on the moving platform, resulting from the errors in the initial estimates of $\overrightarrow{OB_j}^{\{O\}}$ and $\overrightarrow{OP_i}^{\{P\}}$.

The self-calibration model is formulated as follows:

- **Step 1:** Based on the closed-form forward kinematics solution, obtain the position vectors of the moving platform cable attachment points with respect to the inertial base frame (i.e., $\overrightarrow{OP_i}^{\{O\}}$). This requires the cable lengths l_i, $\overrightarrow{OB_j}^{\{O\}}$ and $\overrightarrow{OP_i}^{\{P\}}$.

- **Step 2:** Obtain the distance relationship equations at each cable end-point on the moving platform, which include:

  $\rightarrow\ l_i = \left\| \overrightarrow{OP_i}^{\{O\}} - \overrightarrow{OB_j}^{\{O\}} \right\|$: The cable lengths

  $\rightarrow\ p_i = \left\| \overrightarrow{OP_i}^{\{O\}} \right\| = \left\| \overrightarrow{OP_i}^{\{P\}} \right\|$: The distance from the central constraint joint centre to the moving platform cable attachment points

  $\rightarrow\ p_{ik} = \left\| \overrightarrow{OP_i}^{\{O\}} - \overrightarrow{OP_k}^{\{O\}} \right\|$: The distance between each cable end-point on the moving platform ($k \neq i$)

- **Step 3:** Differentiate the distance relationship equations formed in Step 2 and re-arrange the resulting linear differential equations to form the self-calibration model. This model describes the differential relationship between the nominal kinematic model parameters (i.e., $\overrightarrow{OB_j}^{\{O\}}$ and $\overrightarrow{OP_i}^{\{P\}}$) which contribute to the kinematic errors, and p_{ik} which is evaluates the presence of the kinematic errors.

This model is termed self-calibration because all the required information (i.e., the set of cable lengths) are readily obtained from the motor encoder readings of the cable actuation units and do not require any external pose measurement devices.

(a) Self-Calibration Model of the 1-DOF CDPM Module

This section will present the self-calibration of the 1-DOF CDPM (i.e., elbow module).

Step 1: The position vectors $\overrightarrow{OP_i}^{\{O\}}$ $(i = 1, 2)$ are obtained based on the closed-form forward kinematics solution, as presented in Section 3.2, which requires the actual cable length data (l_1, l_2), and estimated values of $\overrightarrow{OB_j}^{\{O\}}$ $(j = 1, 2)$ and $\overrightarrow{OP_i}^{\{P\}}$ $(i = 1, 2)$.

Step 2: At each point P_i, the following distance relationship equations are obtained:

At point P_1:

$$p_1 = \left\| \overrightarrow{OP_1}^{\{O\}} \right\| = \left\| \overrightarrow{OP_1}^{\{P\}} \right\| \tag{6.1}$$

$$l_1 = \left\| -\overrightarrow{OB_1}^{\{O\}} + \overrightarrow{OP_1}^{\{O\}} \right\| \tag{6.2}$$

At point P_2:

$$p_2 = \left\| \overrightarrow{OP_2}^{\{O\}} \right\| = \left\| \overrightarrow{OP_2}^{\{P\}} \right\| \tag{6.3}$$

$$l_2 = \left\| -\overrightarrow{OB_2}^{\{O\}} + \overrightarrow{OP_2}^{\{O\}} \right\| \tag{6.4}$$

The following distance relationship equation is obtained for p_{12}:

$$p_{12} = \left\| \overrightarrow{P_1P_2}^{\{O\}} \right\| = \left\| \overrightarrow{OP_1}^{\{O\}} - \overrightarrow{OP_2}^{\{O\}} \right\| \tag{6.5}$$

Step 3: The differential relationship between b_{xj}, b_{zj}, ${p_{xi}}^p$ and ${p_{zi}}^p$ (these contribute to the kinematic errors), and p_{12} (this evaluates the presence of the kinematic errors) are obtained by differentiating Eqns. (6.1)-(6.5) as follows:

(Note that $\overrightarrow{OP_i}^{\{O\}} = \{p_{xi}, 0, p_{zi}\}^T$, $\overrightarrow{OP_i}^{\{P\}} = \{{p_{xi}}^p, 0, {p_{zi}}^p\}^T$ and $\overrightarrow{OB_j}^{\{O\}} = \{b_{xj}, 0, b_{zj}\}^T$.)

$$Eqn.\ (6.1) \Rightarrow \{p_{x1}, p_{z1}\} \cdot \begin{Bmatrix} \delta p_{x1} \\ \delta p_{z1} \end{Bmatrix} = \{{p_{x1}}^p, {p_{z1}}^p\} \cdot \begin{Bmatrix} \delta {p_{x1}}^p \\ \delta {p_{z1}}^p \end{Bmatrix} \tag{6.6}$$

$$Eqn.\ (6.2) \Rightarrow \begin{Bmatrix} p_{x1} - b_{x1} \\ p_{z1} - b_{z1} \end{Bmatrix}^T \cdot \begin{Bmatrix} \delta p_{x1} \\ \delta p_{z1} \end{Bmatrix} = \begin{Bmatrix} p_{x1} - b_{x1} \\ p_{z1} - b_{z1} \end{Bmatrix}^T \cdot \begin{Bmatrix} \delta b_{x1} \\ \delta b_{z1} \end{Bmatrix} \tag{6.7}$$

From Eqns. (6.6) and (6.7), we obtain:

$$\begin{Bmatrix} \delta p_{x1} \\ \delta p_{z1} \end{Bmatrix} = {A_1}^{-1}.B_1.\{{\delta p_{x1}}^p, {\delta p_{z1}}^p, \delta b_{x1}, \delta b_{z1}\}^T \tag{6.8}$$

Where:

$$A_1 = \begin{bmatrix} \overrightarrow{OP_1}^{\{O\}T} \\ \left(\overrightarrow{OP_1}^{\{O\}} - \overrightarrow{OB_1}^{\{O\}}\right)^T \end{bmatrix}$$

$$B_1 = \begin{bmatrix} \overrightarrow{OP_1}^{\{P\}T} & \mathbf{0}_{1\times 2} \\ \mathbf{0}_{1\times 2} & \left(\overrightarrow{OP_1}^{\{O\}} - \overrightarrow{OB_1}^{\{O\}}\right)^T \end{bmatrix}$$

Similarly, from the differential equations of Eqns. (6.3)-(6.4), we obtain:

$$\begin{Bmatrix} \delta p_{x2} \\ \delta p_{z2} \end{Bmatrix} = {A_2}^{-1}.B_2.\{{\delta p_{x2}}^p, {\delta p_{z2}}^p, \delta b_{x2}, \delta b_{z2}\}^T \tag{6.9}$$

Where:

$$A_2 = \begin{bmatrix} \overrightarrow{OP_2}^{\{O\}T} \\ \left(\overrightarrow{OP_2}^{\{O\}} - \overrightarrow{OB_2}^{\{O\}}\right)^T \end{bmatrix}$$

$$B_2 = \begin{bmatrix} \overrightarrow{OP_2}^{\{P\}T} & \mathbf{0}_{1\times 2} \\ \mathbf{0}_{1\times 2} & \left(\overrightarrow{OP_2}^{\{O\}} - \overrightarrow{OB_2}^{\{O\}}\right)^T \end{bmatrix}$$

$$Eqn.\ (6.5) \Rightarrow p_{12}\delta p_{12} = \underbrace{\begin{Bmatrix} p_{x1} - p_{x2} \\ p_{z1} - p_{z2} \end{Bmatrix}^T}_{Matrix\ C_1} \cdot \begin{Bmatrix} \delta p_{x1} - \delta p_{x2} \\ \delta p_{z1} - \delta p_{z2} \end{Bmatrix} \tag{6.10}$$

Substituting (6.8) and (6.9) into Eqn. (6.10), we obtain:

$$\delta p_{12} = \underbrace{\frac{C_1 {A_1}^{-1} B_1}{p_{12}}}_{Matrix\ D_1} \begin{Bmatrix} {\delta p_{x1}}^p \\ {\delta p_{z1}}^p \\ \delta b_{x1} \\ \delta b_{z1} \end{Bmatrix} - \underbrace{\frac{C_1 {A_2}^{-1} B_2}{p_{12}}}_{Matrix\ D_2} \begin{Bmatrix} {\delta p_{x2}}^p \\ {\delta p_{z2}}^p \\ \delta b_{x2} \\ \delta b_{z2} \end{Bmatrix} \tag{6.11}$$

By rearranging the linear differential equation (6.11), the self-calibration model for a 1-DOF CDPM at any pose is described as follows:

$$Y = D \cdot X \tag{6.12}$$

Where:

$$Y = \left\{ \delta p_{12} \right\} \in \Re^{1\times 1}$$

$$D = \left[\begin{array}{cccccccc} D_1^{(1)} & D_1^{(2)} & -D_2^{(1)} & -D_2^{(2)} & D_1^{(3)} & D_1^{(4)} & -D_2^{(3)} & -D_2^{(4)} \end{array} \right] \in \Re^{1\times 8}$$

$$X = \left\{ \begin{array}{cccccccc} \delta {p_{x1}}^p & \delta {p_{z1}}^p & \delta {p_{x2}}^p & \delta {p_{z2}}^p & \delta b_{x1} & \delta b_{z1} & \delta b_{x2} & \delta b_{z2} \end{array} \right\}^T \in \Re^{8\times 1}$$

For the terms in Y, $\delta p = p_{actual} - p_{computed}$. p_{actual} is determined from the actual measurements made on the mechanism structure, while $p_{computed}$ is determined from Eqn. (6.5) using $\overrightarrow{OP_i}^{\{O\}}$ obtained in Step 1. D is the self-calibration Jacobian matrix which consists of linear terms that are functions of $\overrightarrow{OB_j}^{\{O\}}$, $\overrightarrow{OP_i}^{\{O\}}$, $\overrightarrow{OP_i}^{\{P\}}$ and p_{12}. It describes the gross error in p_{12} resulting from the errors in the estimates of $\overrightarrow{OB_j}^{\{O\}}$ and $\overrightarrow{OP_i}^{\{P\}}$. Based on Eqn. (6.12), as the initial estimates of $\overrightarrow{OB_j}^{\{O\}}$ and $\overrightarrow{OP_i}^{\{P\}}$ approach the actual values of the mechanism, the term Y will also approach zero.

(b) Self-Calibration Model of the 3-DOF CDPM Module

This section will present the self-calibration of the 3-DOF CDPM (i.e., shoulder and wrist modules). Since both modules have the same configuration, except for the mechanism dimension, the self-calibration model developed in this section can be applied for both shoulder and wrist modules.

Step 1: The position vectors $\overrightarrow{OP_i}^{\{O\}}$ $(i = 1, 2, 3)$ are obtained based on the closed-form forward kinematics solution using the tetrahedron observations (see Section 6.3.1), which requires the actual cable length data $(l_1, \ldots, l_6)$, and estimated values of $\overrightarrow{OB_j}^{\{O\}}$ $(j = 1, \ldots, 6)$ and $\overrightarrow{OP_i}^{\{P\}}$ $(i = 1, 2, 3)$.

Step 2: At each point P_i, the following distance relationship equations are obtained:

At point P_1:

$$p_1 = \left\| \overrightarrow{OP_1}^{\{O\}} \right\| = \left\| \overrightarrow{OP_1}^{\{P\}} \right\| \tag{6.13}$$

$$l_1 = \left\| -\overrightarrow{OB_1}^{\{O\}} + \overrightarrow{OP_1}^{\{O\}} \right\| \tag{6.14}$$

$$l_2 = \left\| -\overrightarrow{OB_2}^{\{O\}} + \overrightarrow{OP_1}^{\{O\}} \right\| \tag{6.15}$$

At point P_2:

$$p_2 = \left\| \overrightarrow{OP_2}^{\{O\}} \right\| = \left\| \overrightarrow{OP_2}^{\{P\}} \right\| \tag{6.16}$$

$$l_3 = \left\| -\overrightarrow{OB_3}^{\{O\}} + \overrightarrow{OP_2}^{\{O\}} \right\| \tag{6.17}$$

$$l_4 = \left\| -\overrightarrow{OB_4}^{\{O\}} + \overrightarrow{OP_2}^{\{O\}} \right\| \tag{6.18}$$

At point P_3:

$$p_3 = \left\| \overrightarrow{OP_3}^{\{O\}} \right\| = \left\| \overrightarrow{OP_3}^{\{P\}} \right\| \tag{6.19}$$

$$l_5 = \left\| -\overrightarrow{OB_5}^{\{O\}} + \overrightarrow{OP_3}^{\{O\}} \right\| \tag{6.20}$$

$$l_6 = \left\| -\overrightarrow{OB_6}^{\{O\}} + \overrightarrow{OP_3}^{\{O\}} \right\| \tag{6.21}$$

The following distance relationship equations are obtained for p_{12}, p_{23} and p_{31}:

$$p_{12} = \left\| \overrightarrow{P_1P_2}^{\{O\}} \right\| = \left\| \overrightarrow{OP_1}^{\{O\}} - \overrightarrow{OP_2}^{\{O\}} \right\| \tag{6.22}$$

$$p_{23} = \left\| \overrightarrow{P_2P_3}^{\{O\}} \right\| = \left\| \overrightarrow{OP_2}^{\{O\}} - \overrightarrow{OP_3}^{\{O\}} \right\| \tag{6.23}$$

$$p_{31} = \left\| \overrightarrow{P_3P_1}^{\{O\}} \right\| = \left\| \overrightarrow{OP_3}^{\{O\}} - \overrightarrow{OP_1}^{\{O\}} \right\| \tag{6.24}$$

Step 3: The differential relationship between b_{xj}, b_{yj}, b_{zj}, ${p_{xi}}^p$, ${p_{yi}}^p$ and ${p_{zi}}^p$ (these contribute to the kinematic errors), and p_{12}, p_{23} and p_{31} (these evaluate the presence of the kinematic errors) are obtained by differentiating Eqns. (6.13)-(6.24) as follows:

(Note that $\overrightarrow{OP_i}^{\{O\}} = \{p_{xi}, p_{yi}, p_{zi}\}^T$, $\overrightarrow{OP_i}^{\{P\}} = \{{p_{xi}}^p, {p_{yi}}^p, {p_{zi}}^p\}^T$ and $\overrightarrow{OB_j}^{\{O\}} = \{b_{xj}, b_{yj}, b_{zj}\}^T$.)

$$Eqn.\ (6.13) \Rightarrow \{p_{x1}, p_{y1}, p_{z1}\} \cdot \begin{Bmatrix} \delta p_{x1} \\ \delta p_{y1} \\ \delta p_{z1} \end{Bmatrix} = \{{p_{x1}}^p, {p_{y1}}^p, {p_{z1}}^p\} \cdot \begin{Bmatrix} \delta {p_{x1}}^p \\ \delta {p_{y1}}^p \\ \delta {p_{z1}}^p \end{Bmatrix} \tag{6.25}$$

$$Eqn.\ (6.14) \Rightarrow \begin{Bmatrix} p_{x1} - b_{x1} \\ p_{y1} - b_{y1} \\ p_{z1} - b_{z1} \end{Bmatrix}^T \cdot \begin{Bmatrix} \delta p_{x1} \\ \delta p_{y1} \\ \delta p_{z1} \end{Bmatrix} = \begin{Bmatrix} p_{x1} - b_{x1} \\ p_{y1} - b_{y1} \\ p_{z1} - b_{z1} \end{Bmatrix}^T \cdot \begin{Bmatrix} \delta b_{x1} \\ \delta b_{y1} \\ \delta b_{z1} \end{Bmatrix} \tag{6.26}$$

$$Eqn.\ (6.15) \Rightarrow \begin{Bmatrix} p_{x1}-b_{x2} \\ p_{y1}-b_{y2} \\ p_{z1}-b_{z2} \end{Bmatrix}^T . \begin{Bmatrix} \delta p_{x1} \\ \delta p_{y1} \\ \delta p_{z1} \end{Bmatrix} = \begin{Bmatrix} p_{x1}-b_{x2} \\ p_{y1}-b_{y2} \\ p_{z1}-b_{z2} \end{Bmatrix}^T . \begin{Bmatrix} \delta b_{x2} \\ \delta b_{y2} \\ \delta b_{z2} \end{Bmatrix} \tag{6.27}$$

From Eqns. (6.25)-(6.27), we obtain:

$$\begin{Bmatrix} \delta p_{x1} \\ \delta p_{y1} \\ \delta p_{z1} \end{Bmatrix} = {A_1}^{-1}.B_1.\{{\delta p_{x1}}^p, {\delta p_{y1}}^p, {\delta p_{z1}}^p, \delta b_{x1}, \ldots, \delta b_{z2}\}^T \tag{6.28}$$

Where:

$$A_1 = \begin{bmatrix} {\overrightarrow{OP_1}^{\{O\}}}^T \\ \left(\overrightarrow{OP_1}^{\{O\}} - \overrightarrow{OB_1}^{\{O\}}\right)^T \\ \left(\overrightarrow{OP_1}^{\{O\}} - \overrightarrow{OB_2}^{\{O\}}\right)^T \end{bmatrix}$$

$$B_1 = \begin{bmatrix} {\overrightarrow{OP_1}^{\{P\}}}^T & \mathbf{0}_{1\times3} & \mathbf{0}_{1\times3} \\ \mathbf{0}_{1\times3} & \left(\overrightarrow{OP_1}^{\{O\}} - \overrightarrow{OB_1}^{\{O\}}\right)^T & \mathbf{0}_{1\times3} \\ \mathbf{0}_{1\times3} & \mathbf{0}_{1\times3} & \left(\overrightarrow{OP_1}^{\{O\}} - \overrightarrow{OB_2}^{\{O\}}\right)^T \end{bmatrix}$$

Similarly, from the differential equations of Eqns. (6.16)-(6.21), we obtain:

$$\begin{Bmatrix} \delta p_{x2} \\ \delta p_{y2} \\ \delta p_{z2} \end{Bmatrix} = {A_2}^{-1}.B_2.\{{\delta p_{x2}}^p, {\delta p_{y2}}^p, {\delta p_{z2}}^p, \delta b_{x3}, \ldots, \delta b_{z4}\}^T \tag{6.29}$$

And,

$$\begin{Bmatrix} \delta p_{x3} \\ \delta p_{y3} \\ \delta p_{z3} \end{Bmatrix} = {A_3}^{-1}.B_3.\{{\delta p_{x3}}^p, {\delta p_{y3}}^p, {\delta p_{z3}}^p, \delta b_{x5}, \ldots, \delta b_{z6}\}^T \tag{6.30}$$

Where:

$$A_2 = \begin{bmatrix} {\overrightarrow{OP_2}^{\{O\}}}^T \\ \left(\overrightarrow{OP_2}^{\{O\}} - \overrightarrow{OB_3}^{\{O\}}\right)^T \\ \left(\overrightarrow{OP_2}^{\{O\}} - \overrightarrow{OB_4}^{\{O\}}\right)^T \end{bmatrix}$$

$$B_2 = \begin{bmatrix} \overrightarrow{OP_2}^{\{P\}^T} & \mathbf{0}_{1\times3} & \mathbf{0}_{1\times3} \\ \mathbf{0}_{1\times3} & \left(\overrightarrow{OP_2}^{\{O\}} - \overrightarrow{OB_3}^{\{O\}}\right)^T & \mathbf{0}_{1\times3} \\ \mathbf{0}_{1\times3} & \mathbf{0}_{1\times3} & \left(\overrightarrow{OP_2}^{\{O\}} - \overrightarrow{OB_4}^{\{O\}}\right)^T \end{bmatrix}$$

$$A_3 = \begin{bmatrix} \overrightarrow{OP_3}^{\{O\}^T} \\ \left(\overrightarrow{OP_3}^{\{O\}} - \overrightarrow{OB_5}^{\{O\}}\right)^T \\ \left(\overrightarrow{OP_3}^{\{O\}} - \overrightarrow{OB_6}^{\{O\}}\right)^T \end{bmatrix}$$

$$B_3 = \begin{bmatrix} \overrightarrow{OP_3}^{\{P\}^T} & \mathbf{0}_{1\times3} & \mathbf{0}_{1\times3} \\ \mathbf{0}_{1\times3} & \left(\overrightarrow{OP_3}^{\{O\}} - \overrightarrow{OB_5}^{\{O\}}\right)^T & \mathbf{0}_{1\times3} \\ \mathbf{0}_{1\times3} & \mathbf{0}_{1\times3} & \left(\overrightarrow{OP_3}^{\{O\}} - \overrightarrow{OB_6}^{\{O\}}\right)^T \end{bmatrix}$$

$$Eqn.\ (6.22) \Rightarrow p_{12}\delta p_{12} = \underbrace{\begin{Bmatrix} p_{x1} - p_{x2} \\ p_{y1} - p_{y2} \\ p_{z1} - p_{z2} \end{Bmatrix}^T}_{Matrix\ C_1} \cdot \begin{Bmatrix} \delta p_{x1} - \delta p_{x2} \\ \delta p_{y1} - \delta p_{y2} \\ \delta p_{z1} - \delta p_{z2} \end{Bmatrix} \tag{6.31}$$

$$Eqn.\ (6.23) \Rightarrow p_{23}\delta p_{23} = \underbrace{\begin{Bmatrix} p_{x2} - p_{x3} \\ p_{y2} - p_{y3} \\ p_{z2} - p_{z3} \end{Bmatrix}^T}_{Matrix\ C_2} \cdot \begin{Bmatrix} \delta p_{x2} - \delta p_{x3} \\ \delta p_{y2} - \delta p_{y3} \\ \delta p_{z2} - \delta p_{z3} \end{Bmatrix} \tag{6.32}$$

$$Eqn.\ (6.24) \Rightarrow p_{31}\delta p_{31} = \underbrace{\begin{Bmatrix} p_{x3} - p_{x1} \\ p_{y3} - p_{y1} \\ p_{z3} - p_{z1} \end{Bmatrix}^T}_{Matrix\ C_3} \cdot \begin{Bmatrix} \delta p_{x3} - \delta p_{x1} \\ \delta p_{y3} - \delta p_{y1} \\ \delta p_{z3} - \delta p_{z1} \end{Bmatrix} \tag{6.33}$$

Substituting (6.28) and (6.29) into Eqn. (6.31), we obtain:

$$\delta p_{12} = \underbrace{\frac{C_1 {A_1}^{-1} B_1}{p_{12}}}_{Matrix\ D_{11}} \begin{Bmatrix} \delta {p_{x1}}^p \\ \delta {p_{y1}}^p \\ \delta {p_{z1}}^p \\ \delta b_{x1} \\ \vdots \\ \delta b_{z2} \end{Bmatrix} - \underbrace{\frac{C_1 {A_2}^{-1} B_2}{p_{12}}}_{Matrix\ D_{12}} \begin{Bmatrix} \delta {p_{x2}}^p \\ \delta {p_{y2}}^p \\ \delta {p_{z2}}^p \\ \delta b_{x3} \\ \vdots \\ \delta b_{z4} \end{Bmatrix} \tag{6.34}$$

Substituting (6.29) and (6.30) into Eqn. (6.32), we obtain:

$$\delta p_{23} = \underbrace{\frac{C_2 {A_2}^{-1} B_2}{p_{23}}}_{Matrix\ D_{21}} \begin{Bmatrix} \delta {p_{x2}}^p \\ \delta {p_{y2}}^p \\ \delta {p_{z2}}^p \\ \delta b_{x3} \\ \vdots \\ \delta b_{z4} \end{Bmatrix} - \underbrace{\frac{C_2 {A_3}^{-1} B_3}{p_{23}}}_{Matrix\ D_{22}} \begin{Bmatrix} \delta {p_{x3}}^p \\ \delta {p_{y3}}^p \\ \delta {p_{z3}}^p \\ \delta b_{x5} \\ \vdots \\ \delta b_{z6} \end{Bmatrix} \tag{6.35}$$

Substituting (6.30) and (6.28) into Eqn. (6.33), we obtain:

$$\delta p_{31} = \underbrace{\frac{C_3 {A_3}^{-1} B_3}{p_{31}}}_{Matrix\ D_{31}} \begin{Bmatrix} \delta {p_{x3}}^p \\ \delta {p_{y3}}^p \\ \delta {p_{z3}}^p \\ \delta b_{x5} \\ \vdots \\ \delta b_{z6} \end{Bmatrix} - \underbrace{\frac{C_3 {A_1}^{-1} B_1}{p_{31}}}_{Matrix\ D_{32}} \begin{Bmatrix} \delta {p_{x1}}^p \\ \delta {p_{y1}}^p \\ \delta {p_{z1}}^p \\ \delta b_{x1} \\ \vdots \\ \delta b_{z2} \end{Bmatrix} \tag{6.36}$$

By combining the linear differential equations (6.34), (6.35) and (6.36), the self-calibration model for a 3-DOF CDPM at any pose is described as follows:

$$Y = D \cdot X \tag{6.37}$$

Where:

$$Y = \begin{Bmatrix} \delta p_{12} \\ \delta p_{23} \\ \delta p_{31} \end{Bmatrix} \in \Re^{3\times 1}$$

$$D = \begin{bmatrix} D1 & D2 & D3 \end{bmatrix} \in \Re^{3\times 27}$$

$$D1 = \begin{bmatrix} D_{11}^{(1)} & D_{11}^{(2)} & D_{11}^{(3)} & -D_{12}^{(1)} & -D_{12}^{(2)} & -D_{12}^{(3)} & 0 & 0 & 0 \\ 0 & 0 & 0 & D_{21}^{(1)} & D_{21}^{(2)} & D_{21}^{(3)} & -D_{22}^{(1)} & -D_{22}^{(2)} & -D_{22}^{(3)} \\ -D_{32}^{(1)} & -D_{32}^{(2)} & -D_{32}^{(3)} & 0 & 0 & 0 & D_{31}^{(1)} & D_{31}^{(2)} & D_{31}^{(3)} \end{bmatrix}$$

$$D2 = \begin{bmatrix} D_{11}^{(4)} & D_{11}^{(5)} & D_{11}^{(6)} & D_{11}^{(7)} & D_{11}^{(8)} & D_{11}^{(9)} & -D_{12}^{(4)} & -D_{12}^{(5)} & -D_{12}^{(6)} \\ 0 & 0 & 0 & 0 & 0 & 0 & D_{21}^{(4)} & D_{21}^{(5)} & D_{21}^{(6)} \\ -D_{32}^{(4)} & -D_{32}^{(5)} & -D_{32}^{(6)} & -D_{32}^{(7)} & -D_{32}^{(8)} & -D_{32}^{(9)} & 0 & 0 & 0 \end{bmatrix}$$

$$D3 = \begin{bmatrix} -D_{12}^{(7)} & -D_{12}^{(8)} & -D_{12}^{(9)} & 0 & 0 & 0 & 0 & 0 & 0 \\ D_{21}^{(7)} & D_{21}^{(8)} & D_{21}^{(9)} & -D_{22}^{(4)} & -D_{22}^{(5)} & -D_{22}^{(6)} & -D_{22}^{(7)} & -D_{22}^{(8)} & -D_{22}^{(9)} \\ 0 & 0 & 0 & D_{31}^{(4)} & D_{31}^{(5)} & D_{31}^{(6)} & D_{31}^{(7)} & D_{31}^{(8)} & D_{31}^{(9)} \end{bmatrix}$$

$$X = \left\{ \begin{array}{cccccc} \delta {p_{x1}}^p & \ldots & \delta {p_{z3}}^p & \delta b_{x1} & \ldots & \delta b_{z6} \end{array} \right\}^T \in \Re^{27\times 1}$$

For the terms in Y, $\delta p = p_{actual} - p_{computed}$. p_{actual} is determined from the actual measurements made on the mechanism structure, while $p_{computed}$ is determined from Eqns. (6.22)-(6.24) using $\overrightarrow{OP_i}^{\{O\}}$ obtained in Step 1. D is the self-calibration Jacobian matrix which consists of linear terms that are functions of $\overrightarrow{OB_j}^{\{O\}}$, $\overrightarrow{OP_i}^{\{O\}}$, $\overrightarrow{OP_i}^{\{P\}}$, p_{12}, p_{23} and p_{31}. It describes the gross errors in p_{12}, p_{23} and p_{31} resulting from the errors in the estimates of $\overrightarrow{OB_j}^{\{O\}}$ and $\overrightarrow{OP_i}^{\{P\}}$. Based on Eqn. (6.37), as the initial estimates of $\overrightarrow{OB_j}^{\{O\}}$ and $\overrightarrow{OP_i}^{\{P\}}$ approach the actual values of the mechanism, the term Y will also approach zero.

6.3.3 Self-Calibration Algorithm

Similar to the iterative calibration procedure in [156, 157], a least squares algorithm based on the proposed self-calibration model is employed to determine the actual geometric model parameters of the CDPM modules. In order to obtain reliable results, it is required to take measurements at several poses. For m sets of measurement poses, the k^{th} pose with its set of cable length data measurements will result in Y_k and its corresponding D_k. After m sets of measurement data, Y_k and D_k are stacked to form the following equation:

$$\widetilde{Y} = \widetilde{D} \cdot X \tag{6.38}$$

Where $\widetilde{Y} = \{Y_1^T, \ldots, Y_m^T\}^T$ and $\widetilde{D} = \{D_1^T, \ldots, D_m^T\}^T$. The least-squares algorithm is used since the model in Eqn. (6.38) contains m linear equations with 8 variables for the 1-DOF CDPM, while it contains $3m$ linear equations with 27 variables for the 3-DOF CDPM (Note: Eqn. (6.38) must have at least eight measurement poses for the 1-DOF CDPM, while it must have at least nine measurement poses for the 3-DOF CDPM). The least-squares solution of

X is given as:

$$X = (\widetilde{D}^T \widetilde{D})^{-1} \cdot \widetilde{D}^T \cdot \widetilde{Y} \tag{6.39}$$

Where $(\widetilde{D}^T \widetilde{D})^{-1} \widetilde{D}^T$ is the pseudo-inverse of $\widetilde{D}$. The solution of Eqn. (6.39) is further improved through iterative substitution as shown in Fig. 6.3. A refinement in the least-squares algorithm can be achieved by iterative looping. Once the kinematic error parameter vector, X is identified, estimates of $\overrightarrow{OB_j}^{\{O\}}$ and $\overrightarrow{OP_i}^{\{P\}}$ are updated after every loop k by substituting X into the following equation:

$$\begin{Bmatrix} {p_{xi}}^p \\ {p_{yi}}^p \\ {p_{zi}}^p \\ b_{xj} \\ b_{yj} \\ b_{zj} \end{Bmatrix}_{k+1} = X + \begin{Bmatrix} {p_{xi}}^p \\ {p_{yi}}^p \\ {p_{zi}}^p \\ b_{xj} \\ b_{yj} \\ b_{zj} \end{Bmatrix}_{k} \tag{6.40}$$

This procedure is repeated until the error deviation metric, δE approaches a certain tolerance limit, ε, which is close to zero. Then the final $\overrightarrow{OB_j}^{\{O\}}$ and $\overrightarrow{OP_i}^{\{P\}}$ will represent the actual parameters of the shoulder module structure. δE is the average measurement residue of p_{ik}, and is mathematically defined as:

$$\delta E = \sqrt{\frac{1}{n_y} \left(\widetilde{Y}^T \, \widetilde{Y} \right)} \tag{6.41}$$

Where n_y is the number of elements in $\widetilde{Y}$.

6.3.4 Computer Simulation

In this section, computer simulation studies were carried out on the optimized 2-2 two-cable elbow module design and the 3-3 six-cable shoulder module design. This is to demonstrate the accuracy and robustness of the self-calibration algorithm. The simulation will investigate the effects of the initial parameter guesses of $\overrightarrow{OB_j}^{\{O\}}$ and $\overrightarrow{OP_i}^{\{P\}}$. In this simulation study, it is assumed that the set of cable length measurement at each pose are noise-free (i.e.,

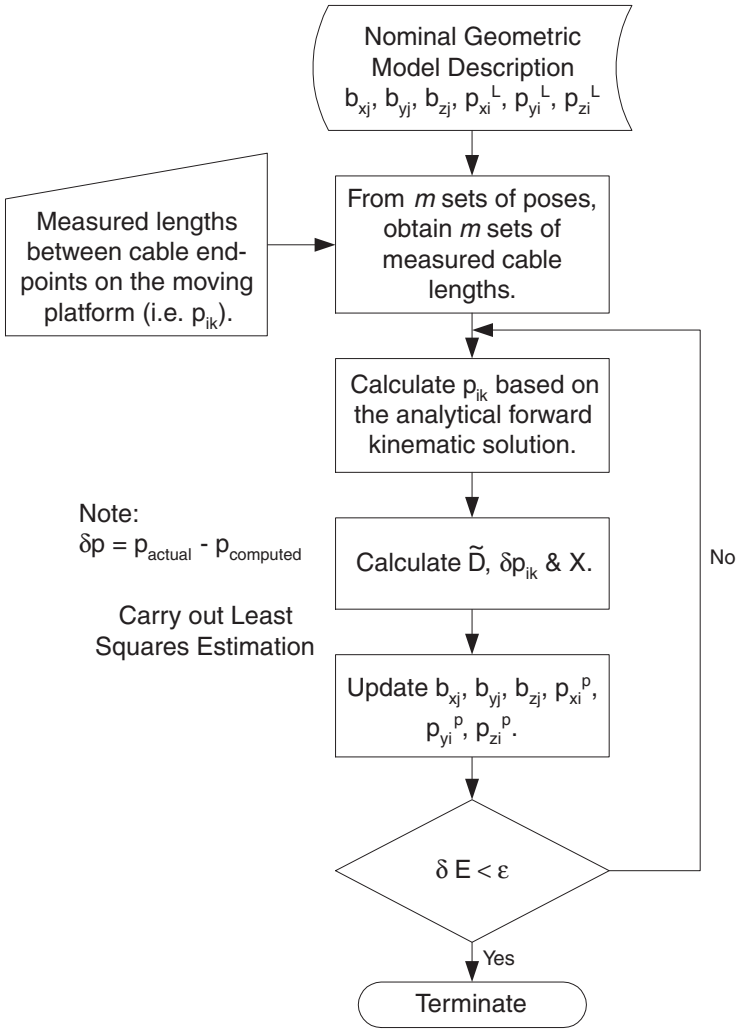

Figure 6.3: Iterative self-calibration algorithm flowchart for the individual CDPMs

ideal measurements). For the self-calibration simulation studies, the following procedure is employed:

1. Generate two sets of m random poses (within the limits of the central constraint joint motion range and satisfying tension-closure condition) and their corresponding 'simulated' cable length measurements (These are based on Eqns. (6.2) and (6.4) for the 1-DOF elbow module, and Eqns. (6.14), (6.15), (6.17), (6.18), (6.20) and (6.21) for the 3-DOF shoulder module, and their nominal kinematic parameters). The first set will be used for self-calibration, while the second set will be used for verification.

2. Assign errors in the nominal values of the kinematic parameters $\overrightarrow{OB_j}^{\{O\}}$ and $\overrightarrow{OP_i}^{\{P\}}$,

to be used as initial estimates.

3. Identify the nominal geometric model parameters using the self-calibration algorithm and the first set of m 'simulated' cable length measurements.

4. Verify the identified geometric model parameters using the second set of m 'simulated' cable length measurements.

(a) Simulation Study on the Elbow Module

The theoretical lower bound for the number of measured poses is eight but for accuracy and robustness, it is set to nine. From the viewpoint of computer simulation, the initial estimate errors $\{\delta b_{xj}, \delta b_{zj}\}$ and $\{\delta {p_{xi}}^p, \delta {p_{zi}}^p\}$ are randomly generated with uniformly distributed deviations of $\pm d$. From the simulation results, injected errors with uniformly distributed deviations of up to $\pm 10mm$ are recoverable within three to four iterations. This demonstrates the accuracy of the self-calibration model for the elbow module. Fig. 6.4 shows the self-calibration convergence plot with assigned errors of uniformly distributed deviations $\pm 10mm$ in the nominal values, used as the initial estimates. δE is driven from an initial value of 16.53 to approximately zero values within four iterations.

(b) Simulation Study on the Shoulder Module

The simulation study on the shoulder module is conducted similar to that of the elbow module. The theoretical lower bound for the number of measured poses is nine but for accuracy and robustness, it is set to ten. From the viewpoint of computer simulation, the initial estimate errors $\{\delta b_{xj}, \delta b_{yj}, \delta b_{zj}\}$ and $\{\delta {p_{xi}}^p, \delta {p_{yi}}^p, \delta {p_{zi}}^p\}$ are randomly generated with uniformly distributed deviations of $\pm d$. From the simulation results, injected errors with uniformly distributed deviations of up to $\pm 10mm$ are recoverable within three to four iterations. This demonstrates the accuracy of the self-calibration model for the shoulder module. Fig. 6.5 shows the self-calibration convergence plot with assigned errors of uniformly

distributed deviations $\pm 10mm$ in the nominal values, used as the initial estimates. δE is driven from an initial value of 17.63 to approximately zero values within four iterations.

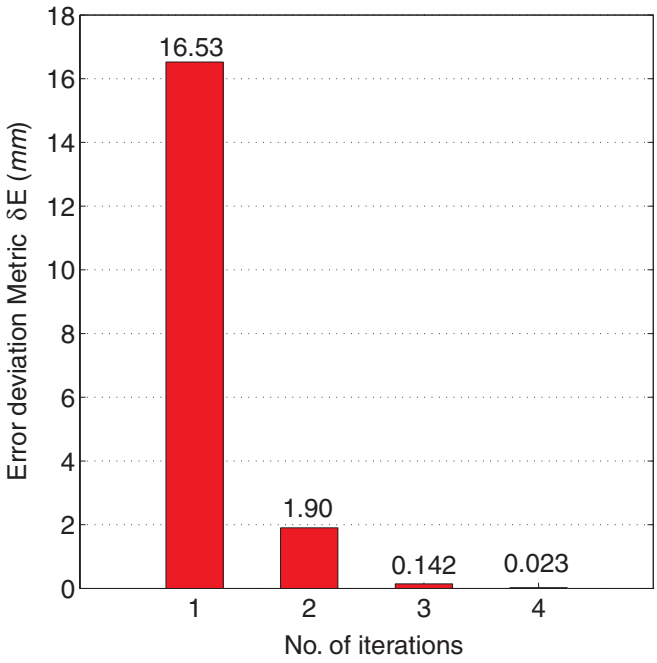

Figure 6.4: Self-calibration convergence plot for the elbow module using the 'simulated' set of cable length measurements ($d = 10mm$)

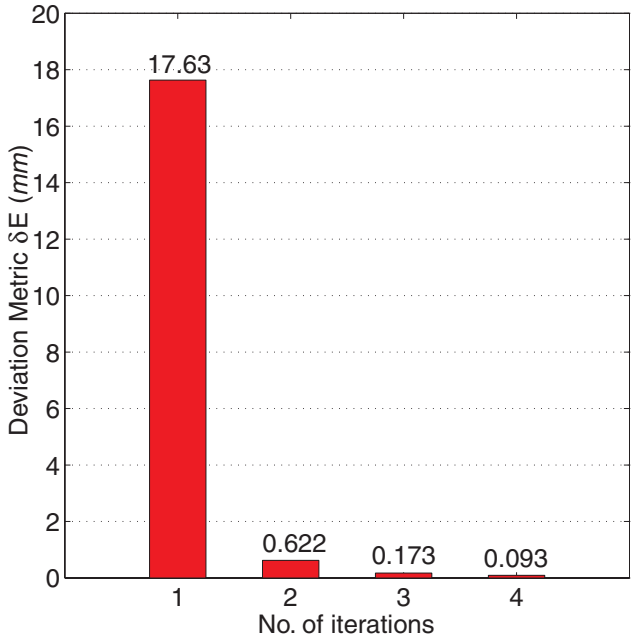

Figure 6.5: Self-calibration convergence plot for the shoulder module using the 'simulated' set of cable length measurements ($d = 10mm$)

6.3.5 Experimental Results

In this section, experimental studies were carried out on the fabricated 2-2 two-cable configuration elbow module (see Fig. 6.6) and the fabricated 3-3 six-cable configuration shoulder module (see Fig. 6.9). This is to investigate the robustness of the self-calibration algorithm in practical applications with existence of measurement noise. The experimental procedure is similar to the computer simulation procedure except that the cable length measurements are obtained from the motor encoders of the cable actuation units.

(a) Experimental Study on the Elbow Module

From this experimental study, it is found that the deviation metric becomes relatively stable when the number of measurement poses is greater than 20. Typical experimental results to verify the result of the self-calibration are shown in Figs. 6.7 and 6.8. A full recovery of the errors in the geometric model parameters is impossible due to the presence of noise in the measurements. However, partial error recovery can be achieved for nominal values of $\overrightarrow{OB_j}^{\{O\}}$ and $\overrightarrow{OP_i}^{\{P\}}$. Hence, the proposed self-calibration model for the elbow module is able to accurately and robustly identify the errors in its nominal geometric model parameters.

(b) Experimental Study on the Shoulder Module

From this experimental study, the deviation metric becomes relatively stable when the number of measurement poses is greater than 35. This is higher as compared to the elbow module, as the number of geometric model parameters for the shoulder module is also higher. Figures 6.10 and 6.11 show the typical experimental results to verify the result of the self-calibration algorithm. A full recovery of the errors in the geometric model parameters is impossible due to the presence of noise in the measurements. However, partial error recovery can be achieved for nominal values of $\overrightarrow{OB_j}^{\{O\}}$ and $\overrightarrow{OP_i}^{\{P\}}$. Hence, the proposed self-calibration model for the shoulder module is able to accurately and robustly identify the errors in its nominal geometric model parameters. (Note: Self-calibration of the wrist module will undergo the

same procedure as the shoulder module.)

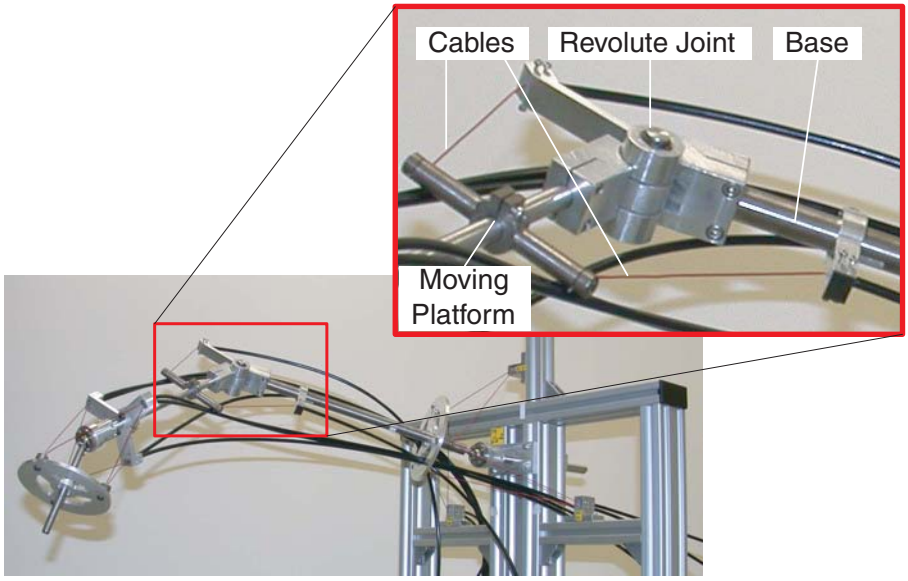

Figure 6.6: Fabricated elbow module with optimal 2-2 two-cable configuration

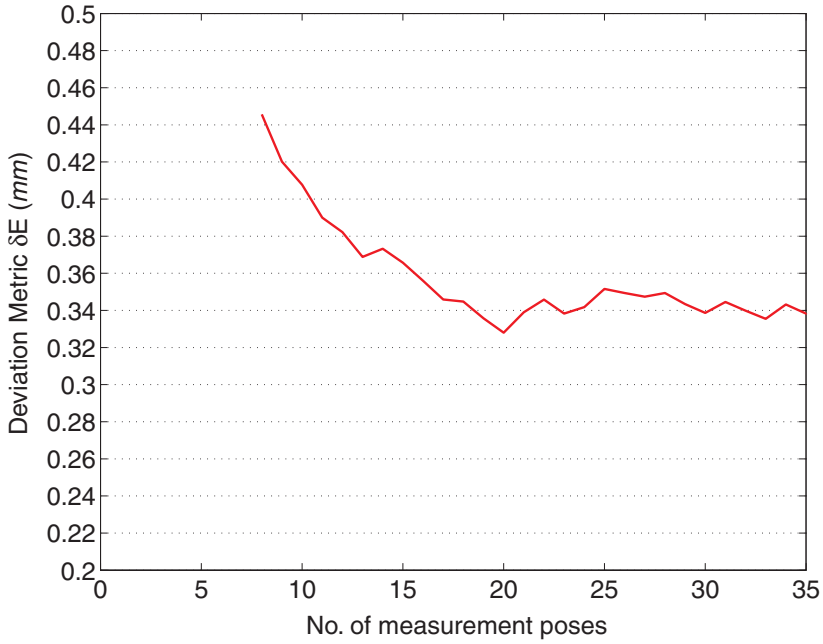

Figure 6.7: Quantified deviation metric plot versus number of measurement poses for the elbow module using the first 'experimental' set of cable length measurements

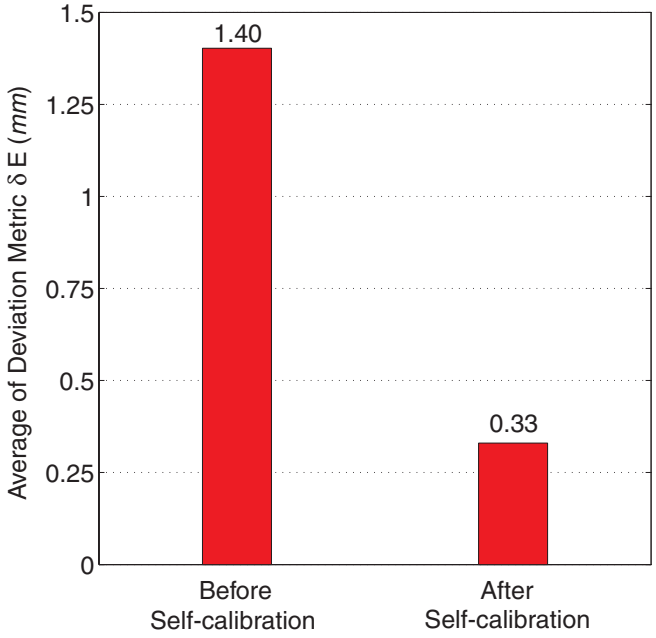

Figure 6.8: Verification plot before and after self-calibration for the elbow module using the second 'experimental' set of cable length measurements

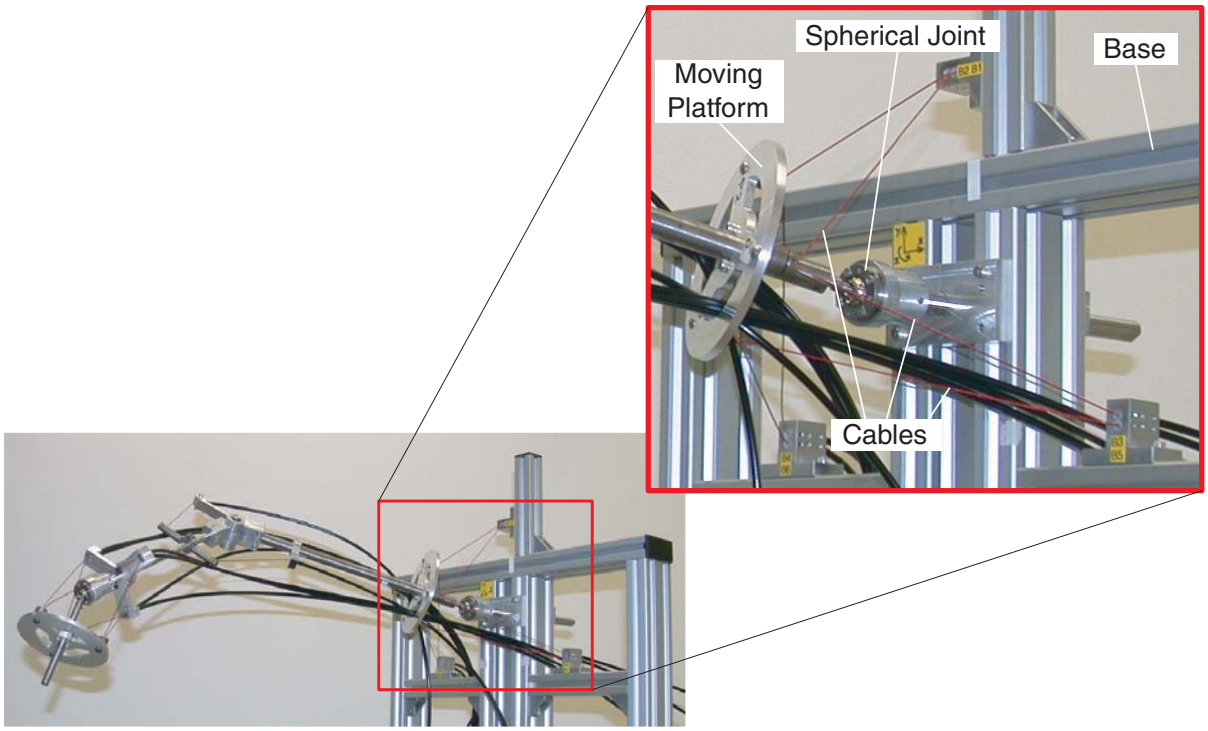

Figure 6.9: Fabricated shoulder module with optimal 3-3 six-cable configuration

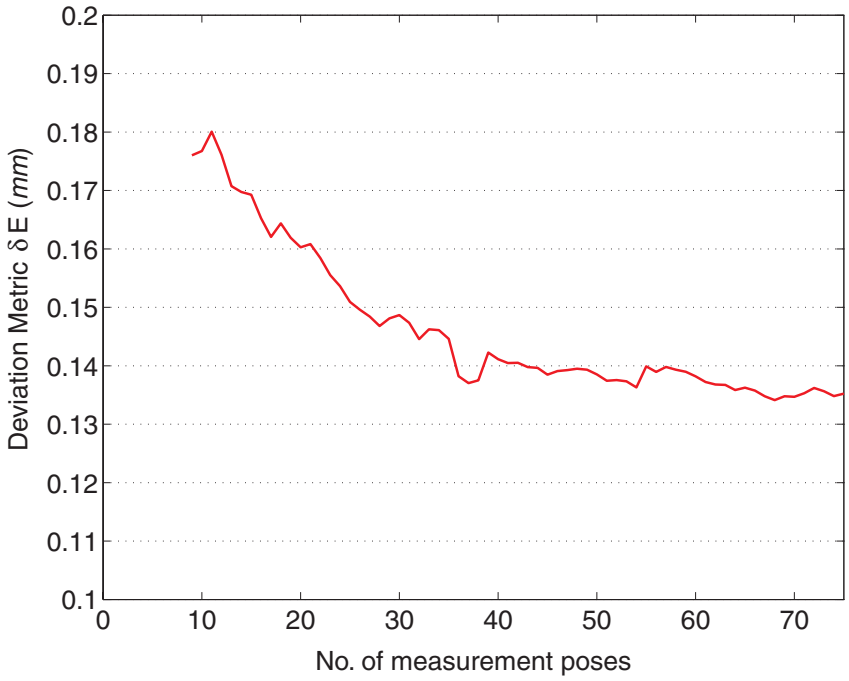

Figure 6.10: Quantified deviation metric plot versus number of measurement poses for the shoulder module using the first 'experimental' set of cable length measurements

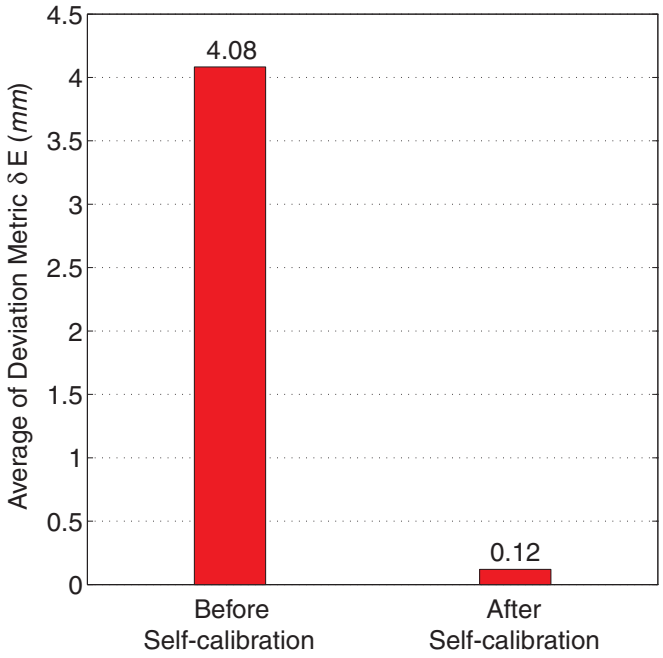

Figure 6.11: Verification plot before and after self-calibration for the shoulder module using the second 'experimental' set of cable length measurements

6.4 Calibration of the 7-DOF Cable-Driven Robotic Arm

After carrying out the self-calibration of the individual 1-DOF and 3-DOF CDPMs, the next step is to carry out the calibration of the whole 7-DOF cable-driven robotic arm. While the self-calibration dealt with the relative calibration between the inertial base frame and the moving frame of the individual CDPMs, calibration of the 7-DOF CDRA will deal with the absolute calibration among the inertial world frame, the individual CDPM coordinate frames and the body-attached frame at the tool-tip located at the moving platform of the wrist module. This is to improve the accuracy of the complete 7-DOF CDRA assembly.

6.4.1 Kinematic Model Description

The 7-DOF cable-driven robotic arm is made up of sequentially connected shoulder, elbow and wrist modules, which are individually optimized based on the workspace requirements. The kinematic model of the whole 7-DOF CDRA is described by a world coordinate frame $\{K_O\}$, and the respective base and moving platform coordinate frames of the individual CDPM modules (see Fig. 6.12).

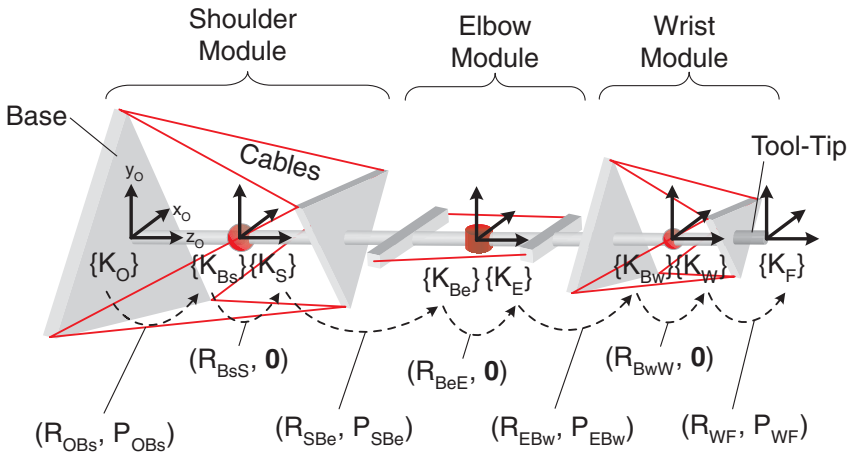

Figure 6.12: Kinematic model of the optimized 7-DOF CDRA

The forward kinematic transformation of the tool-tip coordinate frame $\{K_F\}$ relative to the

world coordinate frame $\{K_O\}$ is given as:

$$\mathbf{T}_{OF} = \mathbf{T}_{OB_s}.\mathbf{T}_{B_sS}.\mathbf{T}_{SB_e}.\mathbf{T}_{B_eE}.\mathbf{T}_{EB_w}.\mathbf{T}_{B_wW}.\mathbf{T}_{WF} \tag{6.42}$$

Where transformation matrices $\mathbf{T}_{OB_s}$, $\mathbf{T}_{SB_e}$, $\mathbf{T}_{EB_w}$ and $\mathbf{T}_{WF}$ are fixed forward kinematic transformations between the various modules attached serially to form the 7-DOF CDRA (i.e., from the moving platform frames of the individual CDPMs to the base frames of the previous modules attached in series). Transformation matrices $\mathbf{T}_{B_sS}$, $\mathbf{T}_{B_eE}$ and $\mathbf{T}_{B_wW}$ are the forward kinematic transformations of the shoulder, elbow and wrist modules respectively.

6.4.2 Calibration Model

The presence of geometric errors cause the nominal transformation frames (denoted by a superscript 'n') to shift to the actual frames (denoted by a superscript 'a'). Hence, the objective of the calibration model is to identify these errors between the nominal and actual frames, termed the calibrated frame (denoted by a superscript 'c'). A calibration model can be formulated using the various transformation representations to represent the calibrated frames. While the other representations (i.e., D-H representation) result in complicated calibration models due to the highly coupled error parameters and suffer from formulation singularity, this is easily resolved by using the POE formula. This is because it overcomes the issue of formulation singularity and a new local calibrated reference frame can be arbitrarily assigned. The kinematic errors in a fixed kinematic transformation can be treated as a twist, i.e., an element of $se(3)$. In addition, a twist has a 6-dimensional vector representation which simplifies the formulation.

According to the definition of matrix logarithm defined on $SE(3)$, there exists a $\hat{t} \in se(3)$ for a given $\mathbf{T} \in SE(3)$ such that $e^{\hat{t}} = T$. Hence, it is sufficient to let $e^{\hat{t}_{ij}} = T_{ij}$ and Eqn. (6.42) is rewritten as:

$$\mathbf{T}_{OF} = e^{\hat{t}_{OB_s}}.\mathbf{T}_{B_sS}.e^{\hat{t}_{SB_e}}.\mathbf{T}_{B_eE}.e^{\hat{t}_{EB_w}}.\mathbf{T}_{B_wW}.e^{\hat{t}_{WF}} \tag{6.43}$$

Since the individual modules have undergone self-calibration, their transformation matrices (i.e., $\mathbf{T}_{B_sS}$, $\mathbf{T}_{B_eE}$ and $\mathbf{T}_{B_wW}$) are assumed to be error-free and can be computed with sufficient accuracy. Hence, any errors that arise will be from the fixed forward kinematic transformations (i.e., $e^{\hat{t}_{OB_s}}$, $e^{\hat{t}_{SB_e}}$, $e^{\hat{t}_{EB_w}}$ and $e^{\hat{t}_{WF}}$) between the various CDPM modules attached serially to form the 7-DOF CDRA assembly. Hence their kinematic errors are denoted by $\delta\hat{t}_{OB_s}$, $\delta\hat{t}_{SB_e}$, $\delta\hat{t}_{EB_w}$ and $\delta\hat{t}_{WF}$ respectively. Since $\hat{t}_{ij}$ belongs to $se(3)$, $\delta\hat{t}_{ij}$ will also belong to $se(3)$. Hence, $\delta e^{\hat{t}_{ij}} = \delta\hat{t}_{ij}.e^{\hat{t}_{ij}}$. Linearizing Eqn. (6.43) results in:

$$\begin{aligned}\delta\mathbf{T}_{OF} &= \delta\hat{t}_{OB_S}.e^{\hat{t}_{OB_s}}.\mathbf{T}_{B_sS}.e^{\hat{t}_{SB_e}}.\mathbf{T}_{B_eE}.e^{\hat{t}_{EB_w}}.\mathbf{T}_{B_wW}.e^{\hat{t}_{WF}} \\ &\quad + e^{\hat{t}_{OB_s}}.\mathbf{T}_{B_sS}.\delta\hat{t}_{SB_e}.e^{\hat{t}_{SB_e}}.\mathbf{T}_{B_eE}.e^{\hat{t}_{EB_w}}.\mathbf{T}_{B_wW}.e^{\hat{t}_{WF}} \\ &\quad + e^{\hat{t}_{OB_s}}.\mathbf{T}_{B_sS}.e^{\hat{t}_{SB_e}}.\mathbf{T}_{B_eE}.\delta\hat{t}_{EB_w}.e^{\hat{t}_{EB_w}}.\mathbf{T}_{B_wW}.e^{\hat{t}_{WF}} \\ &\quad + e^{\hat{t}_{OB_s}}.\mathbf{T}_{B_sS}.e^{\hat{t}_{SB_e}}.\mathbf{T}_{B_eE}.e^{\hat{t}_{EB_w}}.\mathbf{T}_{B_wW}.\delta\hat{t}_{WF}.e^{\hat{t}_{WF}} \end{aligned} \tag{6.44}$$

Right-multiplying both sides of Eqn. (6.44) with $\mathbf{T}_{OF}^{-1}$ results in:

$$\begin{aligned}\delta\mathbf{T}_{OF}.\mathbf{T}_{OF}^{-1} &= \delta\hat{t}_{OB_s} + \mathbf{T}_{OS}.\delta\hat{t}_{SB_e}.\mathbf{T}_{OS}^{-1} + \mathbf{T}_{OE}.\delta\hat{t}_{EB_w}.\mathbf{T}_{OE}^{-1} \\ &\quad + \mathbf{T}_{OW}.\delta\hat{t}_{WF}.\mathbf{T}_{OW}^{-1} \end{aligned} \tag{6.45}$$

Where:

$$\mathbf{T}_{OS} = e^{\hat{t}_{OB_s}}.\mathbf{T}_{B_sS}$$

$$\mathbf{T}_{OE} = e^{\hat{t}_{OB_s}}.\mathbf{T}_{B_sS}.e^{\hat{t}_{SB_e}}.\mathbf{T}_{B_eE}$$

$$\mathbf{T}_{OW} = e^{\hat{t}_{OB_s}}.\mathbf{T}_{B_sS}.e^{\hat{t}_{SB_e}}.\mathbf{T}_{B_eE}.e^{\hat{t}_{EB_w}}.\mathbf{T}_{B_wW}$$

The definition of the *matrix logarithm* and the *adjoint representation* of $SE(3)$ results in the following representations [158]:

$$\delta\mathbf{T}_{ij}.\mathbf{T}_{ij}^{-1} = \log[\mathbf{T}_{ij}^{a}.\mathbf{T}_{ij}^{-1}] \tag{6.46}$$

$$\mathbf{T}_{ij}.\delta\hat{t}_{jk}.\mathbf{T}_{ij}^{-1} = Ad_{T_{ij}}.\delta t_{jk} \tag{6.47}$$

Where $\mathbf{T}_{ij}^{a}$ is the actual (measured) transformation pose.

Hence, Eqn. (6.45) is rewritten as:

$$\log[\mathbf{T}^a_{OF}.\mathbf{T}^{-1}_{OF}]^V = \delta t_{OB_s} + Ad_{T_{OS}}.\delta t_{SB_e} + Ad_{T_{OE}}.\delta t_{EB_w} + Ad_{T_{OW}}.\delta t_{WF} \tag{6.48}$$

Where $\log[\mathbf{T}^a_{OF}.\mathbf{T}^{-1}_{OF}]^V \in \Re^{6\times1}$ is the vector representation of $\log[\mathbf{T}^a_{OF}.\mathbf{T}^{-1}_{OF}] \in se(3)$. Similarly, δt_{jk} is the 6-dimensional vector representation of $\delta\hat{t}_{jk} \in se(3)$. Geometrically, $\log[\mathbf{T}^a_{OF}.\mathbf{T}^{-1}_{OF}]^V$ represents the gross kinematic error of the tool-tip frame $\{K_F\}$ expressed in the world frame $\{K_O\}$. From Eqn. (6.48), it is equals to the sum of kinematic errors in $\mathbf{T}_{OB_s}$, $\mathbf{T}_{SB_e}$, $\mathbf{T}_{EB_w}$ and $\mathbf{T}_{WF}$ (i.e., δt_{OB_s}, δt_{SB_e}, δt_{EB_w} and δt_{WF}), also expressed in the world frame $\{K_O\}$. In each of the 6-dimensional error vectors, the first three parameters represent the position errors $(\delta x, \delta y, \delta z)$, while the remaining three represent the orientation errors $(\delta\theta_x, \delta\theta_y, \delta\theta_z)$. Eqn. (6.48) is simplified into a linear calibration model as follows:

$$Y = D \cdot X \tag{6.49}$$

Where $Y = \log[\mathbf{T}^a_{OF}.\mathbf{T}^{-1}_{OF}]^V \in \Re^{6\times1}$, $D = [I_{6\times6}\ Ad_{T_{OS}}\ Ad_{T_{OE}}\ Ad_{T_{OW}}] \in \Re^{6\times24}$ and $X = \{\delta t_{OB_s}{}^T\ \delta t_{SB_e}{}^T\ \delta t_{EB_w}{}^T\ \delta t_{WF}{}^T\}^T \in \Re^{24\times1}$. $\mathbf{T}^a_{OF}$ is obtained by taking measurements using a coordinate measuring machine and a calibration block located at both frames $\{K_O\}$ and $\{K_F\}$. D is the calibration jacobian matrix that reflects the 24 kinematics error parameters (i.e., X) that exist in the whole system from Y. $\mathbf{T}^{-1}_{OF}$ and D are determined from the nominal kinematic model.

6.4.3 Calibration Algorithm

Based on the calibration model presented in Eqn. (6.49), an iterative least-square algorithm is employed to determine calibrated frames for the fixed forward kinematic transformation matrices $\mathbf{T}_{OB_s}$, $\mathbf{T}_{SB_e}$, $\mathbf{T}_{EB_w}$ and $\mathbf{T}_{WF}$. In order to obtain reliable results, it is required to take measurements at several poses. For m sets of measurement poses, the k^{th} pose with its set of tool-tip frame pose measurements will result in Y_k and its corresponding D_k. After m

sets of measurement data, Y_k and D_k are stacked to form the following equation:

$$\widetilde{Y} = \widetilde{D} \cdot X \tag{6.50}$$

Where $\widetilde{Y} = \{Y_1^T, \ldots, Y_m^T\}^T \in \Re^{6m \times 1}$ and $\widetilde{D} = \{D_1^T, \ldots, D_m^T\}^T \in \Re^{6m \times 24}$. Since the model in Eqn. (6.50) contains $6m$ linear equations with 24 variables, the least-squares algorithm is used (Note: Eqn. (6.50) must have at least four measurement poses). The least-squares solution of X is given as:

$$X = (\widetilde{D}^T \widetilde{D})^{-1} \cdot \widetilde{D}^T \cdot \widetilde{Y} \tag{6.51}$$

Where $(\widetilde{D}^T \widetilde{D})^{-1} \widetilde{D}^T$ is the pseudo-inverse of $\widetilde{D}$. The solution of Eqn. (6.51) is further improved through iterative substitution as shown in Fig. 6.13. A refinement in the least-squares algorithm can be achieved by iterative looping. Once the kinematic error parameter vector, X is identified, $\mathbf{T}_{OB_s}$, $\mathbf{T}_{SB_e}$, $\mathbf{T}_{EB_w}$ and $\mathbf{T}_{WF}$ are updated after every loop k by substituting X into the following equations:

$$(\mathbf{T}_{OB_s})_{k+1} = e^{\hat{t}_{OB_s}} . (\mathbf{T}_{OB_s})_k \tag{6.52}$$

$$(\mathbf{T}_{SB_e})_{k+1} = e^{\hat{t}_{SB_e}} . (\mathbf{T}_{SB_e})_k \tag{6.53}$$

$$(\mathbf{T}_{EB_w})_{k+1} = e^{\hat{t}_{EB_w}} . (\mathbf{T}_{EB_w})_k \tag{6.54}$$

$$(\mathbf{T}_{WF})_{k+1} = e^{\hat{t}_{WF}} . (\mathbf{T}_{WF})_k \tag{6.55}$$

This procedure is repeated until the norm of the error vector $\|X\|$ approaches a certain tolerance limit, ε, which is close to zero. Then the final $\mathbf{T}_{OB_s}$, $\mathbf{T}_{SB_e}$, $\mathbf{T}_{EB_w}$ and $\mathbf{T}_{WF}$ represent the calibrated kinematic transformations, denoted by $\mathbf{T}^c_{OB_s}$, $\mathbf{T}^c_{SB_e}$, $\mathbf{T}^c_{EB_w}$ and $\mathbf{T}^c_{WF}$ respectively.

After the iterative procedure, the kinematic error vector X does not represent the actual kinematic errors. Nevertheless, in order to compare the calibrated frame poses with their nominal frame poses, the actual kinematic errors can be determined with the use of the

matrix logarithm as follows:

$$\delta t_{OB_s} = \log[\mathbf{T}^c_{OB_s}.\mathbf{T}^{-1}_{OB_s}]^V \quad (6.56)$$

$$\delta t_{SB_e} = \log[\mathbf{T}^c_{SB_e}.\mathbf{T}^{-1}_{SB_e}]^V \quad (6.57)$$

$$\delta t_{EB_w} = \log[\mathbf{T}^c_{EB_w}.\mathbf{T}^{-1}_{EB_w}]^V \quad (6.58)$$

$$\delta t_{WF} = \log[\mathbf{T}^c_{WF}.\mathbf{T}^{-1}_{WF}]^V \quad (6.59)$$

After the calibration procedure, the forward kinematic equation becomes:

$$\mathbf{T}^c_{OF} = \mathbf{T}^c_{OB_s}.\mathbf{T}_{B_sS}.\mathbf{T}^c_{SB_e}.\mathbf{T}_{B_eE}.\mathbf{T}^c_{EB_w}.\mathbf{T}_{B_wW}.\mathbf{T}^c_{WF} \quad (6.60)$$

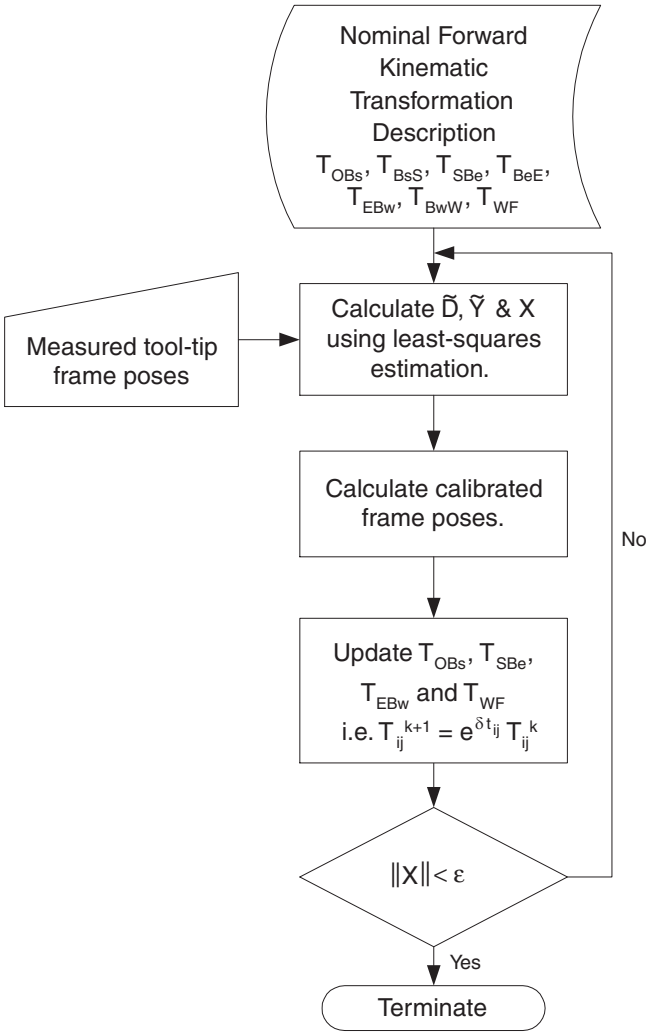

Figure 6.13: Flowchart of the iterative calibration algorithm for the 7-DOF CDRA

In order to evaluate the calibration result, two deviation metrics between the actual (measured) 'a' and calibrated 'c' tool-tip frames are mathematically defined as [159]:

$$\delta p = \sqrt{\frac{1}{m}\sum_{k=1}^{m}(P_{ak} - P_{ck})^T.(P_{ak} - P_{ck})} \tag{6.61}$$

$$\delta R = \sqrt{\frac{1}{m}\sum_{k=1}^{m}\left(\log(R_{ak}^{-1}R_{ck})^V\right)^T\left(\log(R_{ak}^{-1}R_{ck})^V\right)} \tag{6.62}$$

Where δp and δR denote the average quantified position and orientation deviation metrics respectively, between the calibrated and actual poses of the tool-tip frame.

6.4.4 Computer Simulation

In this section, computer simulation studies were carried out on the 7-DOF CDRA with the optimized individual CDPM modules. This is to demonstrate the accuracy and robustness of the calibration algorithm. The simulation will investigate the effect of kinematic errors under noise-free measurements. The units of the kinematic parameters are in radians and millimeters. For the simulation studies, the following procedure is employed:

1. Generate two sets of m random shoulder, elbow and wrist module poses, i.e., $\mathbf{T}_{B_sS}$, $\mathbf{T}_{B_eE}$ and $\mathbf{T}_{B_wW}$ respectively (within the limits of the mechanical joints motion range and satisfying tension-closure condition). One set will be used for calibration while the other will be used for verification.

2. Assign kinematic errors in the nominal poses of $\mathbf{T}_{OB_s}$, $\mathbf{T}_{SB_e}$, $\mathbf{T}_{EB_w}$ and $\mathbf{T}_{WF}$ by introducing $\delta t'_{OB_s}$, $\delta t'_{SB_e}$, $\delta t'_{EB_w}$ and $\delta t'_{WF}$ respectively.

3. Using the generated set of random poses in Step 1, calculate the two m sets of 'simulated' actual tool-tip frame poses based on:

$$\mathbf{T}^a_{OF} = \mathbf{T}^a_{OB_s}.\mathbf{T}_{B_sS}.\mathbf{T}^a_{SB_e}.\mathbf{T}_{B_eE}.\mathbf{T}^a_{EB_w}.\mathbf{T}_{B_wW}.\mathbf{T}^a_{WF}$$

Where:

$$\mathbf{T}^{a}_{OB_s} = e^{\hat{t'}_{OB_s}}.\mathbf{T}_{OB_s} = e^{\hat{t'}_{OB_s}}.\begin{bmatrix} I_{3\times3} & \mathbf{p}_{OB_s} \\ \mathbf{0} & 1 \end{bmatrix}$$

$$\mathbf{T}^{a}_{SB_e} = e^{\hat{t'}_{SB_e}}.\mathbf{T}_{SB_e} = e^{\hat{t'}_{SB_e}}.\begin{bmatrix} I_{3\times3} & \mathbf{p}_{SB_e} \\ \mathbf{0} & 1 \end{bmatrix}$$

$$\mathbf{T}^{a}_{EB_w} = e^{\hat{t'}_{EB_w}}.\mathbf{T}_{EB_w} = e^{\hat{t'}_{EB_w}}.\begin{bmatrix} I_{3\times3} & \mathbf{p}_{EB_w} \\ \mathbf{0} & 1 \end{bmatrix}$$

$$\mathbf{T}^{a}_{WF} = e^{\hat{t'}_{WF}}.\mathbf{T}_{WF} = e^{\hat{t'}_{WF}}.\begin{bmatrix} I_{3\times3} & \mathbf{p}_{WF} \\ \mathbf{0} & 1 \end{bmatrix}$$

4. Identify the preset kinematic errors using the calibration algorithm and the first set of m 'simulated' actual tool-tip frame pose measurements.

5. Verify the calibrated poses $\mathbf{T}^{c}_{OB_s}$, $\mathbf{T}^{c}_{SB_e}$, $\mathbf{T}^{c}_{EB_w}$ and $\mathbf{T}^{c}_{WF}$ (based on Eqn. (6.60)) using the second set of m 'simulated' actual tool-tip frame pose measurements.

The theoretical lower bound for the number of measured poses is four but for accuracy and robustness, it is set to five. From the viewpoint of computer simulation, the kinematic errors $\{\delta x', \delta y', \delta z'\}$ (i.e., position) and $\{\delta\theta'_x, \delta\theta'_y, \delta\theta'_z\}$ (i.e., orientation) are randomly generated with uniformly distributed deviations of $\pm d_v$ and $\pm d_\omega$. From the simulation results, injected errors with uniformly distributed deviations of d_v =1mm and d_ω =0.05rad are recoverable within three to four iterations. This demonstrates the accuracy of the calibration model for the 7-DOF cable-driven robotic arm. From Table 6.1, the preset kinematic errors are well-recovered although the preset errors are significantly large. Results from Fig. 6.14 further reinforces the calibration model, where both deviation metrics δp and δR (given in Eqns. (6.61) and (6.62)) are driven to approximately zero values within three iterations.

6.4.5 Experimental Results

In this section, experimental studies were carried out on the 7-DOF cable-driven robotic arm research prototype. This is to investigate the robustness of the calibration algorithm in

Table 6.1: Preset and identified kinematic errors in the 'simulated' calibration of the 7-DOF CDRA

$\delta t'_{ij}$	Preset Kinematic Errors	Identified Kinematic Errors
$\delta t'_{OB_s}$	$\{-6.5597, 3.8277, 8.9030,$ $0.1207, 0.1538, -0.0910\}^T$	$\{-6.5597, 3.8277, 8.9030,$ $0.1207, 0.1538, -0.0910\}^T$
$\delta t'_{SB_e}$	$\{2.0158, 6.4144, 6.0300,$ $-0.1290, 0.0207, -0.0010\}^T$	$\{1.5354, 6.1907, 6.0510,$ $-0.1290, 0.0223, -0.0011\}^T$
$\delta t'_{EB_w}$	$\{4.8284, 4.6296, 3.9088,$ $0.1285, -0.1471, 0.0130\}^T$	$\{4.8264, 4.8539, 3.8983,$ $0.1285, -0.1487, 0.0131\}^T$
$\delta t'_{WF}$	$\{6.1681, 3.6960, 5.2650,$ $0.1712, -0.0511, -0.0579\}^T$	$\{6.1681, 3.6960, 5.2650,$ $0.1712, -0.0511, -0.0579\}^T$

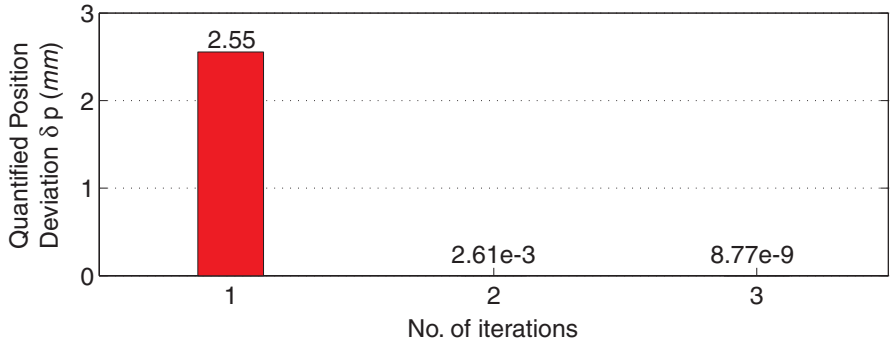

(a) Quantified position deviation metric convergence plot

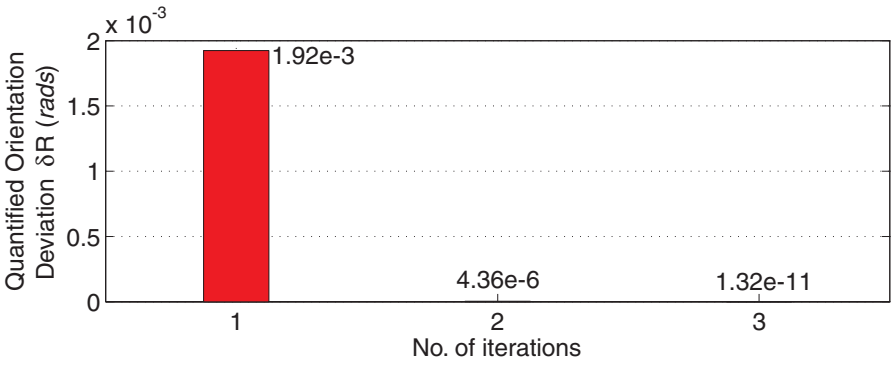

(b) Quantified orientation deviation metric convergence plot

Figure 6.14: Calibration convergence plot for the 7-DOF CDRA using the 'simulated' set of pose measurements ($d_\upsilon = 1mm$ and $d_\omega = 0.05rad$)

practical applications with the existence of measurement noise. The experimental procedure is similar to the computer simulation procedure except that the tool-tip frame poses measurements are obtained using a coordinate measuring machine (from FARO with an accuracy of 80 μm) and a calibration block located at the tool-tip of the CDRA (see Fig. 6.15).

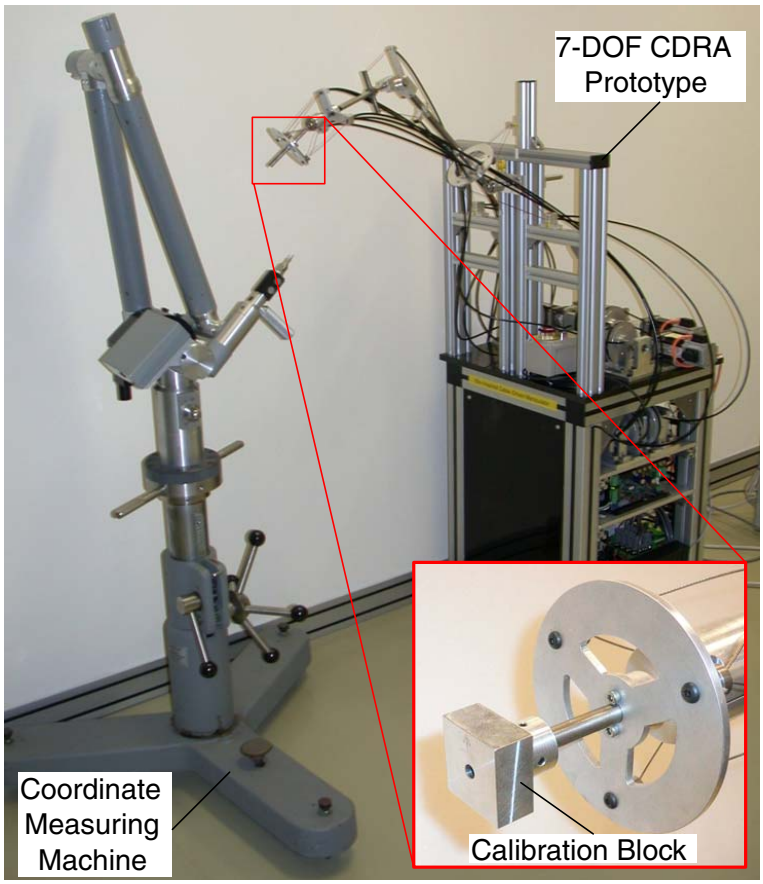

Figure 6.15: Calibration experimental setup for the 7-DOF CDRA with the FARO coordinate measuring machine and calibration block

From this experimental study, deviation metrics δp and δR became relatively stable after greater than 15 tool-tip measurement poses (see Fig. 6.16). A full recovery of the errors in the fixed forward kinematic transformations is impossible, limited by the accuracy of the measurement device as well as the CAU. However, partial error recovery can be achieved and the proposed calibration model is able to accurately and robustly identify the errors in the nominal fixed forward kinematic transformations.

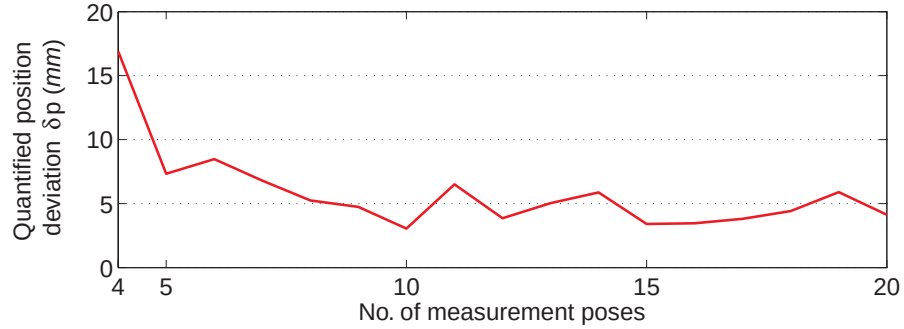

(a) Quantified position deviation metric convergence plot

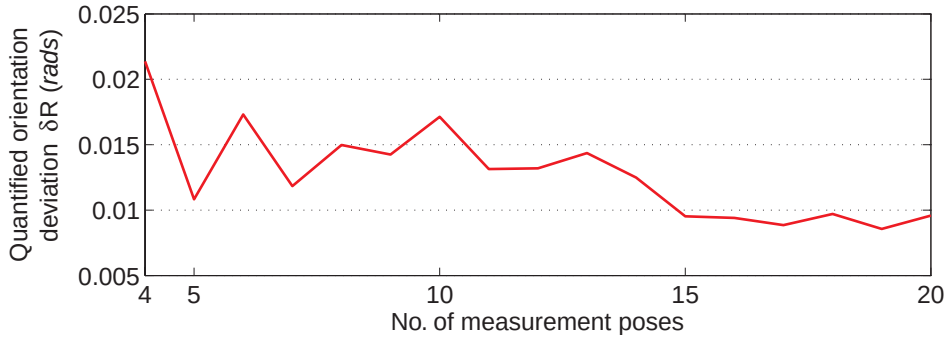

(b) Quantified orientation deviation metric convergence plot

Figure 6.16: Calibration deviation metrics convergence plot for the 7-DOF CDRA using the 'experimental' set of tool-tip measurement poses

6.5 Discussion

In this chapter, kinematic calibration is carried out with the formulation of calibration models for the CDPM modules, as well as the overall 7-DOF cable-driven robotic arm. It consists of two sequential steps. The first step is the self-calibration of the CDPM modules, followed by the second step of the entire 7-DOF CDRA assembly calibration.

Contributions are made in the formulation of self-calibration models for the individual CDPM modules. This algorithm is based on the measurement residue errors in the cable end-point distances on the moving platform and the cable length information. These models are termed 'self-calibration' as all the required information are readily obtained from the motor encoder readings of the cable actuation units and do not require any external pose measurement devices. Due to the linear nature of the self-calibration models, a least-squares algorithm is

employed to solve the calibration results iteratively. Both computer simulations and experiments were carried out to verify the accuracy and robustness of the self-calibration models. The results demonstrate that the kinematic errors with uniformly distributed deviations of upto $\pm 10mm$ can be fully recovered under noise-free measurement conditions. Under experimental conditions, the noise in measurements prevent full recovery of errors but nonetheless, these errors are precisely recovered with a minimum number of measurement poses.

For the overall 7-DOF CDRA, an effective calibration model is formulated based on the local product-of-exponential formula and the measurement residue errors in the tool-tip frame measurements. This is to account for any kinematic errors that might arise when serially assembling the individual CDPM modules to form the overall 7-DOF CDRA assembly. A least-squares algorithm is also employed to solve the calibration results iteratively due to the linear nature of the calibration model. Computer simulation studies were carried out to verify the algorithm. Simulation studies demonstrate that the preset kinematic errors in the complete arm assembly of upto $\pm 1mm$ (for position) and $\pm 0.05rad$ (for orientation), can be fully recovered under noise-free measurement conditions. Under experimental conditions, the noise in measurements prevent full recovery of errors but nonetheless, these errors are precisely recovered with a minimum number of measurement poses. Hence this calibration model is able to accurately and robustly calibrate the 7-DOF CDRA.

Chapter 7

Conclusion and Future Work

7.1 Conclusion

In this research, a novel 7-DOF assistive robotic arm based on an 'anthropomimetic' design philosophy, is designed. In addition, the fundamental tools for its systematic analysis and design optimization are established. These tools including kinematic analysis, cable tension analysis, stiffness analysis, workspace analysis, design optimization methodology and kinematic calibration. The main contributions of this thesis are summarized as follows:

- **Conceptual Design of a Cable-Driven Anthropomimetic Robotic Arm**
  The 'anthropomimetic' design philosophy is adopted in order to propose an assistive robotic arm that will offer better performance than existing ones. The human arm is observed for biological solutions, and three basic anthropomimetic modules (i.e., shoulder, elbow and wrist modules) are proposed to be arranged in series, to form the 7-DOF robotic arm design. These modules are also cable-driven in order to have a similar muscle driving scheme. The result is a lightweight, intrinsically-safe and articulate 7-DOF robotic arm suitable for healthcare assistive tasks.

- **Kinematic Formulation of the CDPM Modules and the 7-DOF CDRA**
  A closed-form forward displacement solution is formulated for the optimized 3-DOF

CDPM module with a 3-3 six-cable configuration, while an inverse kinematic algorithm based on task-decomposition approach is proposed for the 7-DOF CDRA. However, due to the redundancy of the 7-DOF CDRA, the inverse displacement problem is cast into a 1-D optimization problem, which is solved with the aim of optimizing the manipulability of the shoulder module. Given the desired tool-tip poses, suitable arm postures are achieved in computational examples for the inverse displacement of the 7-DOF CDRA.

- **Formulation of Workspace-Related Performance Evaluation Tools**

Cable-Tension Analysis

The unilateral driving property of cables makes cable-tension analysis the most crucial in the evaluation of the workspace performance of CDPMs. A computationally effective tension-closure approach based on the convex theory analysis is proposed to evaluate the positive tension conditions of the CDPMs. Computational examples demonstrate the effectiveness of the proposed approach over the conventional 'null-space' approach in terms of its computation efforts and simplicity.

Workspace Generation

Due to the complex joint motion of the human arm, an analytical approach for the workspace generation becomes complicated and ineffective. Hence, a numerical approach is adopted. Using the Tilt-&-Torsion angles parameterization, an equi-volumetric finite partitioning scheme is proposed to discretize the 3-DOF orientation workspace. This scheme ensures each element converges to its feature point when the number of elements become sufficiently large. In addition, this scheme avoids the singularity points of the T-&-T angles. Based on the joint motion limits of the human arms and the proposed workspace representation scheme, discretized workspace templates are generated for the various joints. The templates are used for the subsequent design optimization of the various CDPM modules. In addition, as the volume of $SO(3)$ is not equal to the geometric volume of the cylindrical workspace, integration measures are

introduced when computing the $SO(3)$ workspace volume from its parametric domain for a mathematically tractable solution.

Workspace Performance Evaluation Measures

A 'Workspace Matching Index' (WMI) is proposed in order to assist in the design optimization of the 7-DOF CDRA. This index measures the percentage of matching between the workspace of a CDPM module and that of its corresponding human arm joint. In addition, due to the flexible nature of cables, CDPMs have relatively low stiffness which subsequently affect the positional accuracy. Hence, a new global quality performance measure is proposed, using the conditioning index of the stiffness matrix over the entire workspace. This is critical during path planning especially when a task has certain stiffness requirements.

- **Design Optimization**

  Design optimization is carried out with the aim of achieving a 7-DOF CDRA whose workspace will match as closely as possible to the workspace of the human arm. However, analysis of the operational workspace of such a redundant 7-DOF arm is complicated as it involves both position and orientation workspace analyses. In addition, there is no effective way to present and characterize the 6-dimensional operational workspace. Hence, in order to simplify the analysis, a joint-level workspace optimization approach is employed. The optimization is based on a modified-complex search algorithm due to the non-linearity of the objective function. The optimization resulted in shoulder/wrist modules with WMI of approximately 60 to 70%. From the optimization of the elbow module, WMI of the shoulder/wrist modules can be further improved if asymmetric designs are considered.

- **Prototype of the 7-DOF Cable-Driven Robotic Arm**

  A prototype of the optimal designed 7-DOF CDRA is developed for experimental investigations. This includes the development of the cable actuation unit, the individual CDPM modules and the hardware setup for motion control. A novel designed tension

sensor prototype is also developed for force based control schemes.

- **Kinematic Calibration**

  For the individual CDPM modules, novel self-calibration models have been formulated based on the measurement residue errors in the cable end-point distances on the moving platform and the cable length information. These models are termed 'self-calibration' as all the required information are readily obtained from the motor encoder readings of the cable actuation units and do not require any external pose measurement devices. A least-squares algorithm is employed to iteratively solve the calibration result. Both computer simulations and experiments carried out verify the accuracy and robustness of the proposed calibration models. Kinematic errors are fully recovered under noise-free measurement conditions. Under experimental conditions, the noise in measurements prevent full recovery of errors. Nevertheless, these errors are precisely recovered with a minimum number of measurement poses.

  In order to improve the accuracy of the complete 7-DOF arm assembly, a linear calibration model is formulated based on the product-of-exponential formula and using the measurement residue errors in the tool-tip frame measurements. Computer simulation studies demonstrate that the preset kinematic errors in the complete arm assembly can be fully recovered under noise-free measurement conditions. Under experimental conditions, the noise in measurements prevent full recovery of errors. Nevertheless, these errors are precisely recovered with a minimum number of measurement poses.

In conclusion, our 'ultimate' goal is to come up with novel assistive robotic devices to assist the elderly and disable population, based on the 'anthropomimetic' design approach. The framework presented in this thesis can be adopted for the development of assistive robotic device spin-offs. It is envisaged that the development of such assistive robotic devices will offer whole new possibilities in the lives of the aging and disabled population and enhance their quality of life.

7.2 Future Work

Although the basic issues relating to the design of the 7-DOF cable-driven robotic arm and its individual CDPM modules have been investigated, there are still a number of unexplored aspects in this area.

- **Stiffness-Based Control Schemes and Cable Tension Optimization**

  The stiffness of the tool-tip can be controlled based on the proposed hybrid position-force control scheme presented in Section 5.3.1 and the developed tension sensor prototype. Safety measures can also be implemented through monitoring of the forces in the tension sensors. This will be critical in developing safe assistive robotic arms. Cable tension optimization can then be carried out based on the stiffness-based quality performance measure (i.e., $GSCI$) formulated in Section 4.6.2 as an objective function.

- **Improvement on the Cable Actuation Unit**

  The proposed cable actuation unit requires careful winding of the cables on the winding drum. This is to ensure that the cable length errors arising from lateral winding of cables onto the drum, are kept to a minimum. Hence, improvements can be made through designing of mechanisms to compensate for these errors without the need for careful winding of cables onto the drum.

- **Research Extension to Wearable Robotic Devices**

  A wearable arm design can be extended from the anthropomimetic design of the 7-DOF cable-driven robotic arm proposed in Section 2.3. This design synergistically combines kinematically under-deterministic 1-DOF and 3-DOF CDPMs modules with the human's bones and joints, to form a complete deterministic mechanism with a non-invasive bio-kinematic structure. This design is similar to that of the 7-DOF cable driven robotic arm, except that the mechanical joints which constraint the motion of the individual CDPM modules are substituted with the human arm joints. From Figure 7.1, the shoulder module consists of an under-deterministic 3-DOF CDPM that

combines with the shoulder joint (i.e., spherical joint) to form a deterministic cable-driven spherical mechanism. The cables will 'pull' the upper arm to rotate about the shoulder joint and generate the spherical motions. Likewise, the elbow module consist of an under-deterministic 1-DOF CDPM that utilizes the elbow joint (i.e., revolute joint) to form a deterministic 1-DOF cable-driven mechanism. The cables will 'pull' the lower arm to rotate about the elbow joint and generate the revolute motion. The wrist module is similar to that of the shoulder module. Hence, any motion that occur will be about the corresponding human joints, in which this design adapts to the human arm motion characteristics and overcomes the non-compliance issue in existing wearable robotic arms. The 3-DOF shoulder module, the 1-DOF elbow module and the 3-DOF wrist module, are then connected sequentially to form a 7-DOF cable-driven wearable arm.

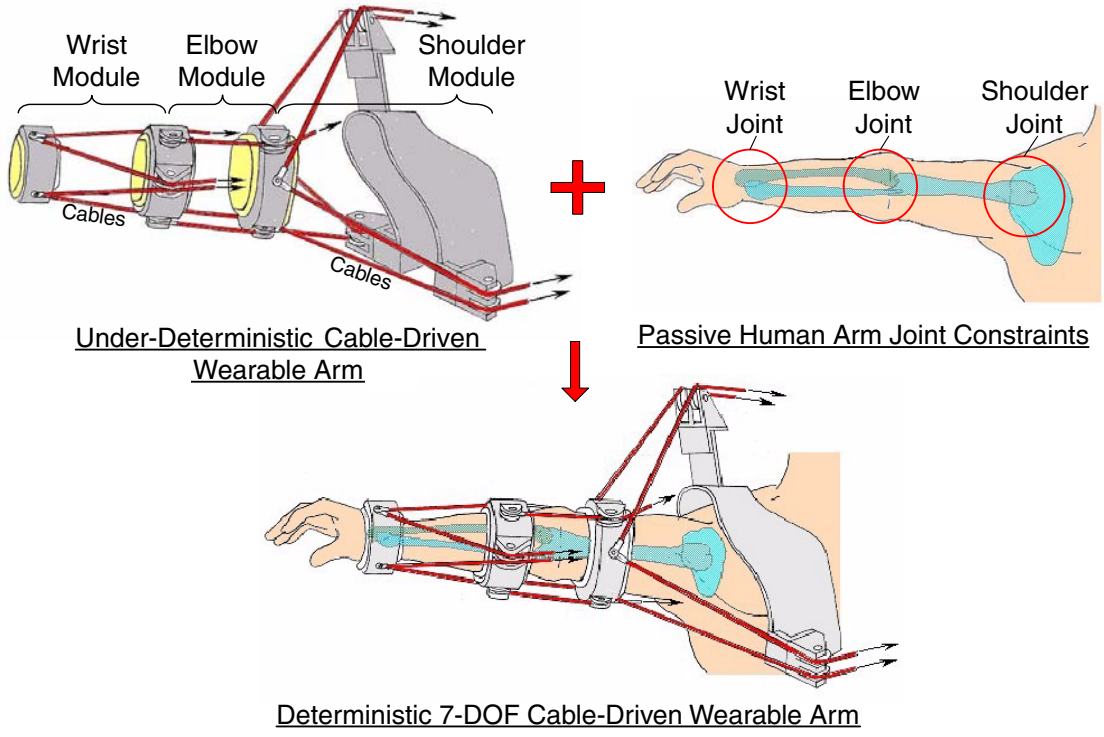

Figure 7.1: Conceptual design of the anthropomimetic wearable arm rehabilitator

This design offers the benefits of improved adaptability and comfortability due to the bio-kinematic structure of the wearable arm rehabilitator. Any motion will be about the corresponding human joints and this minimizes any mismatch between the

mechanism motion characteristics and the human joints motion characteristics. It is also lightweight with an intrinsically-safe feature due to the flexible lightweight cables (compared to the conventional actuators) and the cable actuation units can be placed away from the wearable arm through cable routing. This design also has a dexterous workspace as redundant cables can be utilized without significantly adding weight to the wearable arm. Hence, the benefits offered by the proposed cable-driven anthropomimetic wearable robotic arm offer an alternative to the conventional rigid-link and 'machine-centered' counterparts.

The design optimization procedure developed for the 7-DOF cable-driven robotic arm in Section 5.1 can be easily adopted for the design optimization of the wearable arm. The main difference in the procedure will be the dimension constraints. In this case, these constraints will be larger so as to accommodate the human arm as the central rigid-link structure. Readers may refer to a publication by the author [65] for more details on the optimal design of a anthropomimetic wearable shoulder rehabilitator.

One of the critical issues to address for such wearable robotic arms is the identification of the joint centre locations in each CDPM module which is crucial for kinematic modeling and motion control. This has been addressed by the author in [160], where a joint centre self-identification methodology is proposed, utilizing the cable length data from the available motor encoders. This eliminates the need for any external pose measurement devices and thereby reducing the hardware costs. Simulation studies are carried out for the shoulder module and the algorithm has been shown to be robust and accurate, even in the presence of measurement noise.

Eventhough the bio-kinematic structure poses additional developmental challenges, these make the cable-driven anthropomimetic wearable robotic devices to be an interesting future work to address.

List of Publications & Awards

Journal Papers

- S.K. Mustafa, G. Yang, S.H. Yeo, W. Lin, and I.-M. Chen, "Self-Calibration of a Biologically-Inspired 7-DOF Cable-Driven Robotic Arm", *IEEE/ASME Transactions on Mechatronics*, vol. 13(1), pp. 66-75, 2008.

- S.K. Mustafa, G. Yang, S.H. Yeo, and W. Lin, "Optimal Design of a Bio-Inspired Anthropocentric Shoulder Rehabilitator", *Journal of Applied Bionics and Biomechanics*, vol. 3(3), pp. 199–208, 2006.

- C.B. Pham, S.H. Yeo, G. Yang, M. S. Kurbanhusen, and I.-M. Chen, "Force-Closed Workspace Analysis of Cable-Driven Parallel Mechanisms", *Journal of Mechanism and Machine Theory*, vol. 41, pp. 53–69, 2005.

Conference Papers

- S.K. Mustafa, G. Yang, S.H. Yeo, and W. Lin, "Kinematic calibration of a 7-DOF self-calibrated modular cable-driven robotic arm", in *Proceedings of IEEE International Conference on Robotics & Automation*, Pasadena, California, 2008 (accepted).

- S.K. Mustafa, G. Yang, S.H. Yeo, W. Lin, and I.-M. Chen, "Self-Calibration of a Biologically-Inspired Cable-Driven Robotic Arm", in *Proceedings of IEEE/ASME International Conference on Advanced Intelligent Mechatronics*, Switzerland, 2007.

- S.K. Mustafa, G. Yang, S.H. Yeo, and W. Lin, "Self-Identification of the Joint Centre of a Cable-Driven Shoulder Rehabilitator", in *Proceedings of IEEE International Conference on Robotics & Automation*, Roma, Italy, 2007.

- G. Yang, W. Lin, S.K. Mustafa, I.-M. Chen, and S. H. Yeo, "Numerical Orientation Workspace Analysis with Different Parameterization Methods", in *Proceedings of IEEE International Conference on Robotics, Automation & Mechatronics*, Bangkok, Thailand, 2006.

- S.K. Mustafa, G. Yang, W. Lin, S.H. Yeo, and C.B. Pham, "Development of a Bio-Inspired Wrist Prosthesis", in *Proceedings of IEEE International Conference on Robotics, Automation & Mechatronics*, Bangkok, Thailand, 2006.

- S.K. Mustafa, G. Yang, S.H. Yeo, and W. Lin, "Design Optimization of a Shoulder Joint Rehabilitator", in *Proceedings of IEEE International Conference on Computational Intelligence, Robotics & Automation*, Singapore, 2005.

- S.K. Mustafa, G. Yang, W. Lin, S.H. Yeo, and C.B. Pham, "A Biologically-Inspired Anthropocentric Shoulder Joint Rehabilitator: Workspace Analysis & Optimization", in *Proceedings of IEEE International Conference on Mechatronics & Automation*, Niagara Falls, Canada, 2005.

- G. Yang, W. Lin, M. S. Kurbanhusen, C. B. Pham, and S. H. Yeo, "Kinematic Design of a 7-DOF Cable-Driven Humanoid Arm: a Solution-in-Nature Approach", in *Proceedings of IEEE/ASME International Conference on Advanced Intelligent Mechatronics*, California, USA, 2005.

- G. Yang, H. L. Ho, W. Chen, W. Lin, S. H. Yeo, and M. S. Kurbanhusen, "A Haptic Device Wearable on a Human Arm", in *Proceedings of IEEE Conference on Robotics, Automation & Mechatronics*, Singapore, 2004.

Awards

- "Design of a Seven Degrees-of-Freedom Cable-Driven Anthropomorphic Arm", Andrew Fraser Prize Award, Institute of Mechanical Engineers (Singapore Branch), 2007.
- Singapore Institute of Manufacturing Technology Best Student Award, Singapore, 2006.
- "Design Optimization of an Anthropocentric Shoulder Joint Rehabilitator", First Prize in the Poster Presentation Category, Inaugural A*GA-NGS Graduate Symposium, Singapore, 2005.
- "Agency for Science, Technology & Research Graduate Scholarship Award", Singapore, 2003.

Appendix A

Formulation of Jacobian associated with Tilt-&-Torsion Angles Parameterized Rotations

The time-varying rotation matrix of the 3-DOF CDPM moving frame is parameterized as:

$$\mathbf{R}(t) = \mathbf{Q}(q_1(t), q_1(t), q_1(t)) = \mathbf{Q}(\mathbf{q}(t)) \tag{A.1}$$

Applying the chain rule from calculus on Eqn. (A.1) results in:

$$\dot{\mathbf{R}}(t) = \frac{\partial \mathbf{Q}}{\partial q_1}\dot{q}_1 + \frac{\partial \mathbf{Q}}{\partial q_2}\dot{q}_2 + \frac{\partial \mathbf{Q}}{\partial q_3}\dot{q}_3 \tag{A.2}$$

Right-multiplying both sides of Eqn. (A.2) with $\mathbf{R}^T$ and extracting the vectors from both sides results in:

$$\text{vect}\left(\dot{\mathbf{R}}(t)\mathbf{R}(t)^T\right) = \mathbf{E}(\mathbf{Q}(\mathbf{q}))\dot{\mathbf{q}} \tag{A.3}$$

Where:

$\text{vect}\left(\dot{\mathbf{R}}(t)\mathbf{R}(t)^T\right) = \omega_O$: Angular velocity as seen in the inertial base frame

$\mathbf{E}(\mathbf{Q}(\mathbf{q})) = \left[\text{vect}\left(\frac{\partial \mathbf{Q}}{\partial q_1}\mathbf{Q}^T\right), \text{vect}\left(\frac{\partial \mathbf{Q}}{\partial q_2}\mathbf{Q}^T\right), \text{vect}\left(\frac{\partial \mathbf{Q}}{\partial q_3}\mathbf{Q}^T\right)\right]$: Jacobian matrix associated with the Tilt-&-Torsion Angles Parameterized Rotations

For the T-&-T angles parameterization, $\mathbf{Q}(\phi,\theta,\sigma) = \mathbf{R}_z(\phi)\mathbf{R}_y(\theta)\mathbf{R}_z(\sigma-\phi)$ and the skew-symmetric matrices whose vectors form the columns of the Jacobian matrix $\mathbf{E}$ are given as:

$$\begin{aligned}
\frac{\partial \mathbf{Q}}{\partial \phi}\mathbf{Q}^T &= \left(\dot{\mathbf{R}}_z(\phi)\mathbf{R}_y(\theta)\mathbf{R}_z(\sigma-\phi)\right)\mathbf{R}_z(\sigma-\phi)^T\mathbf{R}_y(\theta)^T\mathbf{R}_z(\phi)^T \\
&\quad - \left(\mathbf{R}_z(\phi)\mathbf{R}_y(\theta)\dot{\mathbf{R}}_z(\sigma-\phi)\right)\mathbf{R}_z(\sigma-\phi)^T\mathbf{R}_y(\theta)^T\mathbf{R}_z(\phi)^T \\
&= \dot{\mathbf{R}}_z(\phi)\mathbf{R}_z(\phi)^T - \mathbf{R}_z(\phi)\mathbf{R}_y(\theta)\dot{\mathbf{R}}_z(\sigma-\phi)\mathbf{R}_z(\sigma-\phi)^T\left(\mathbf{R}_z(\phi)\mathbf{R}_y(\theta)\right)^T \qquad \text{(A.4)} \\
\frac{\partial \mathbf{Q}}{\partial \theta}\mathbf{Q}^T &= \left(\mathbf{R}_z(\phi)\dot{\mathbf{R}}_y(\theta)\mathbf{R}_z(\sigma-\phi)\right)\mathbf{R}_z(\sigma-\phi)^T\mathbf{R}_y(\theta)^T\mathbf{R}_z(\phi)^T \\
&= \mathbf{R}_z(\phi)\dot{\mathbf{R}}_y(\theta)\mathbf{R}_y(\theta)^T\mathbf{R}_z(\phi)^T \qquad \text{(A.5)} \\
\frac{\partial \mathbf{Q}}{\partial \sigma}\mathbf{Q}^T &= \left(\mathbf{R}_z(\phi)\mathbf{R}_y(\theta)\dot{\mathbf{R}}_z(\sigma-\phi)\right)\mathbf{R}_z(\sigma-\phi)^T\mathbf{R}_y(\theta)^T\mathbf{R}_z(\phi)^T \\
&= \mathbf{R}_z(\phi)\mathbf{R}_y(\theta)\dot{\mathbf{R}}_z(\sigma-\phi)\mathbf{R}_z(\sigma-\phi)^T\left(\mathbf{R}_z(\phi)\mathbf{R}_y(\theta)\right)^T \qquad \text{(A.6)}
\end{aligned}$$

Regardless of the value of the parameter, vect $\left(\dot{\mathbf{R}}_i\mathbf{R}_i^T\right) = \mathbf{e}_i$, and using the rule vect $\left(\mathbf{R}\mathbf{X}\mathbf{R}^T\right) = \mathbf{R}\text{vect}\left(\mathbf{X}\right)$, $\mathbf{E}$ is obtained as:

$$\begin{aligned}
\mathbf{E}_{T\&T}(\phi,\theta,\sigma) &= \left[\left(1-\mathbf{R}_z(\phi)\mathbf{R}_y(\theta)\right)\mathbf{e}_z, \mathbf{R}_z(\phi)\mathbf{e}_y, \mathbf{R}_z(\phi)\mathbf{R}_y(\theta)\mathbf{e}_z\right] \\
&= \begin{bmatrix} -\cos\phi\sin\theta & -\sin\phi & \cos\phi\sin\theta \\ -\sin\phi\sin\theta & \cos\phi & \sin\phi\sin\theta \\ (1-\cos\theta) & 0 & \cos\theta \end{bmatrix} \qquad \text{(A.7)}
\end{aligned}$$

Appendix B

Formulation of the 7-DOF CDRA Velocity and Acceleration Terms

B.1 Formulation of Velocity Terms

The velocity expression is obtained by differentiating Eqn. (3.35) once, with respect to time. This results in the following adjoint representation expression:

$$V^s_{OF} = V^s_{OS} + Ad_{T_{OS}}\ V^s_{SE} + Ad_{T_{OE}}\ V^s_{EW} \tag{B.1}$$

Where:

$V^s_{OF} = \begin{bmatrix} v^s_{of} \\ \omega^s_{of} \end{bmatrix}$: Tool-tip velocity expressed in spatial frame $\{K_O\}$

$V^s_{OS} = \begin{bmatrix} v^s_{os} \\ \omega^s_{os} \end{bmatrix}$: Velocity of the moving platform of the shoulder module expressed in frame $\{K_O\}$

$Ad_{T_{OS}} = \begin{bmatrix} \mathbf{R}_{OS} & \widehat{\mathbf{p}}_{os}\mathbf{R}_{OS} \\ 0 & \mathbf{R}_{OS} \end{bmatrix}$: Adjoint mapping of $\mathbf{T}_{OS}$

$\widehat{\mathbf{p}}_{os}$: Skew-symmetric matrix of $\mathbf{p}_{os}$

$V^s_{SE} = \begin{bmatrix} v^s_{se} \\ \omega^s_{se} \end{bmatrix}$: Velocity of the moving platform of the elbow module expressed in frame $\{K_S\}$

$Ad_{T_{OE}} = \begin{bmatrix} \mathbf{R}_{OS}\mathbf{R}_{SE} & \widehat{\mathbf{p}}_{oe}(\mathbf{R}_{OS}\mathbf{R}_{SE}) \\ 0 & \mathbf{R}_{OS}\mathbf{R}_{SE} \end{bmatrix}$: Adjoint mapping of $\mathbf{T}_{OE}$

$\widehat{\mathbf{p}}_{oe}$: Skew-symmetric matrix of $\mathbf{p}_{oe}(= \mathbf{p}_{os} + \mathbf{R}_{OS}\mathbf{p}_{se})$

$V^s_{EW} = \begin{bmatrix} \upsilon^s_{ew} \\ \omega^s_{ew} \end{bmatrix}$: Velocity of the moving platform of the wrist module expressed in frame $\{K_E\}$

Based on Eqns. (3.9), (3.10), (3.21) and (3.31), the velocity terms of the various CDPM modules are expressed as follows:

$$\upsilon^s_{os} = \mathbf{p}_{os} \times \omega^s_{os} \tag{B.2}$$
$$\omega^s_{os} = \mathbf{J}^{\#}_{//S}\dot{\mathbf{L}}_S \tag{B.3}$$
$$\upsilon^s_{se} = \mathbf{p}_{se} \times \omega^s_{se} \tag{B.4}$$
$$\omega^s_{se} = \mathbf{J}^{\#}_{//E}\dot{\mathbf{L}}_E \tag{B.5}$$
$$\upsilon^s_{ew} = \mathbf{p}_{ew} \times \omega^s_{ew} \tag{B.6}$$
$$\omega^s_{ew} = \mathbf{J}^{\#}_{//W}\dot{\mathbf{L}}_W \tag{B.7}$$

Where:

$\mathbf{J}^{\#}_{//S}$: Pseudoinverse of the shoulder module Jacobian matrix $\mathbf{J}_{//S} = \begin{bmatrix} (\mathbf{p}_{sp1} \times \mathbf{l}_{s1})^T \\ \vdots \\ (\mathbf{p}_{spi} \times \mathbf{l}_{si})^T \end{bmatrix}$

$\dot{\mathbf{L}}_S = \{\dot{l}_{s1} \ \cdots \ \dot{l}_{si}\}^T \in \Re^{i\times 1}$: The spooling velocity of the shoulder module cables

$\mathbf{J}^{\#}_{//E}$: Pseudoinverse of the elbow module Jacobian matrix $\mathbf{J}_{//E} = \begin{bmatrix} (\mathbf{p}_{ep1} \times \mathbf{l}_{e1})^T \\ \vdots \\ (\mathbf{p}_{epj} \times \mathbf{l}_{ej})^T \end{bmatrix}$

$\dot{\mathbf{L}}_E = \{\dot{l}_{e1} \ \cdots \ \dot{l}_{ej}\}^T \in \Re^{j\times 1}$: The spooling velocity of the elbow module cables

$\mathbf{J}^{\#}_{//W}$: Pseudoinverse of the wrist module Jacobian matrix $\mathbf{J}_{//W} = \begin{bmatrix} (\mathbf{p}_{wp1} \times \mathbf{l}_{w1})^T \\ \vdots \\ (\mathbf{p}_{wpk} \times \mathbf{l}_{wk})^T \end{bmatrix}$

$\dot{\mathbf{L}}_W = \{\dot{l}_{w1} \ \cdots \ \dot{l}_{wk}\}^T \in \Re^{k\times 1}$: The spooling velocity of the wrist module cables

B.2 Formulation of Acceleration Terms

The acceleration expression is obtained by differentiating the velocity expression in Eqn. (B.1) once, with respect to time. This results in the following expression:

$$\dot{V}^s_{OF} = \dot{V}^s_{OS} + \dot{A}d_{T_{OS}}\ V^s_{SE} + Ad_{T_{OS}}\ \dot{V}^s_{SE} + \dot{A}d_{T_{OE}}\ V^s_{EW} + Ad_{T_{OE}}\ \dot{V}^s_{EW} \tag{B.8}$$

Where:

$\dot{V}^s_{OF} = \begin{bmatrix} \dot{v}^s_{of} \\ \dot{\omega}^s_{of} \end{bmatrix}$: Tool-tip acceleration expressed in spatial frame $\{K_O\}$

$\dot{V}^s_{OS} = \begin{bmatrix} \dot{v}^s_{os} \\ \dot{\omega}^s_{os} \end{bmatrix}$: Acceleration of the moving platform of the shoulder module expressed in spatial frame $\{K_O\}$

$\dot{A}d_{T_{OS}} = 2\ ad_{V^s_{OS}} Ad_{T_{OS}}$: First derivative of the adjoint mapping of $\mathbf{T}_{OS}$

$\dot{V}^s_{SE} = \begin{bmatrix} \dot{v}^s_{se} \\ \dot{\omega}^s_{se} \end{bmatrix}$: Acceleration of the moving platform of the elbow module expressed in spatial frame $\{K_S\}$

$\dot{A}d_{T_{OE}} = 2\ ad_{V^s_{OE}} Ad_{T_{OE}}$: First derivative of the adjoint mapping of $\mathbf{T}_{OE}$

$\dot{V}^s_{EW} = \begin{bmatrix} \dot{v}^s_{ew} \\ \dot{\omega}^s_{ew} \end{bmatrix}$: Acceleration of the moving platform of the wrist module expressed in spatial frame $\{K_E\}$

Based on the geometric background in Section 3.1.3, the differentiation of the adjoint mapping term $Ad_{T_{OS}}$ is as follows:

$$\begin{aligned}
\left(\dot{A}d_{T_{OS}}\ V^s_{SE}\right)^{\vee} &= \dot{\mathbf{T}}_{OS}\widehat{V}^s_{SE}\mathbf{T}^{-1}_{OS} + \mathbf{T}_{OS}\widehat{V}^s_{SE}(\dot{\mathbf{T}^{-1}_{OS}}) \\
&= \underbrace{\dot{\mathbf{T}}_{OS}(\mathbf{T}^{-1}_{OS}}_{V^s_{OS}\in se(3)}\underbrace{\mathbf{T}_{OS})\widehat{V}^s_{SE}\mathbf{T}^{-1}_{OS}}_{Ad_{T_{OS}}V^s_{SE}\in se(3)} + \underbrace{\mathbf{T}_{OS}\widehat{V}^s_{SE}(\mathbf{T}^{-1}_{OS}}_{Ad_{T_{OS}}V^s_{SE}\in se(3)}\underbrace{\mathbf{T}_{OS})(\dot{\mathbf{T}^{-1}_{OS}})}_{-V^s_{OS}\in se(3)} \\
&= ad_{V^s_{OS}} Ad_{T_{OS}} V^s_{SE} - ad_{Ad_{T_{OS}}V^s_{SE}} V^s_{OS} \\
&= ad_{V^s_{OS}} Ad_{T_{OS}} V^s_{SE} + ad_{V^s_{OS}} Ad_{T_{OS}} V^s_{SE} \\
&= 2\ ad_{V^s_{OS}} Ad_{T_{OS}} V^s_{SE}
\end{aligned} \tag{B.9}$$

Similarly, the differentiation of the adjoint mapping term $Ad_{T_{OE}}$ results in the following:

$$\left(\dot{A}d_{T_{OE}}\ V^s_{EW}\right)^{\vee} = 2\ ad_{V^s_{OE}} Ad_{T_{OE}} V^s_{EW} \tag{B.10}$$

In addition, from Eqn. (3.22), the acceleration terms of the various CDPM modules are

expressed as follows:

$$\dot{\upsilon}^s_{os} = \mathbf{p}_{os} \times \dot{\omega}^s_{os} \tag{B.11}$$

$$\dot{\omega}^s_{os} = \mathbf{J}^{\#}_{//S}\left(\ddot{\mathbf{L}}_S - \dot{\mathbf{J}}_{//S}\,\omega^s_{os}\right) \tag{B.12}$$

$$\dot{\upsilon}^s_{se} = \mathbf{p}_{se} \times \dot{\omega}^s_{se} \tag{B.13}$$

$$\dot{\omega}^s_{se} = \mathbf{J}^{\#}_{//E}\left(\ddot{\mathbf{L}}_E - \dot{\mathbf{J}}_{//E}\,\omega^s_{se}\right) \tag{B.14}$$

$$\dot{\upsilon}^s_{ew} = \mathbf{p}_{ew} \times \dot{\omega}^s_{ew} \tag{B.15}$$

$$\dot{\omega}^s_{ew} = \mathbf{J}^{\#}_{//W}\left(\ddot{\mathbf{L}}_W - \dot{\mathbf{J}}_{//W}\,\omega^s_{ew}\right) \tag{B.16}$$

Where:

$\dot{\mathbf{J}}_{//S}$: First order differential of the shoulder module Jacobian matrix

$\ddot{\mathbf{L}}_S = \{\ddot{l}_{s1} \ \cdots \ \ddot{l}_{si}\}^T \in \Re^{i\times 1}$: The spooling acceleration of the shoulder module cables

$\dot{\mathbf{J}}_{//E}$: First order differential of the elbow module Jacobian matrix

$\ddot{\mathbf{L}}_E = \{\ddot{l}_{e1} \ \cdots \ \ddot{l}_{ej}\}^T \in \Re^{j\times 1}$: The spooling acceleration of the elbow module cables

$\dot{\mathbf{J}}_{//W}$: First order differential of the wrist module Jacobian matrix

$\ddot{\mathbf{L}}_W = \{\ddot{l}_{w1} \ \cdots \ \ddot{l}_{wk}\}^T \in \Re^{k\times 1}$: The spooling acceleration of the wrist module cables

Appendix C

Formulation of the Integral Factor for $SO(3)$ Representation in Cylindrical Coordinates

It has been addressed in [161] that the entire rigid-body group $SO(3)$ can be visualized as a solid cylinder when the cylindrical coordinates are employed to represent the Tilt-&-Torsion angles, as shown in Fig. 4.6. However, integration measures need to be introduced when computing the volume of the orientation workspace of rigid body rotations from the T-&-T angles domain. It can be verified that if cartesian coordinates are used to represent the T-&-T angles, the integration measure will be same as that of the Euler angle representation, which is given by $\sin\theta$. In this case, the volume of the entire rigid body rotation group is given as:

$$\int_{SO(3)} dV_R = \int_0^{2\pi} \int_0^{pi} \int_0^{2\pi} \sin\theta d\phi d\theta d\sigma = 8\pi^2 \tag{C.1}$$

Equation (C.1) has the same form as when the T-&-T angles are represented with cartesian coordinates, i.e. $x \equiv \phi$, $y \equiv \theta$ and $z \equiv \sigma$. However, since the T-&-T angles are normally represented with cylindrical coordinates, i.e. $x \equiv \theta\cos\phi$, $y \equiv \theta\sin\phi$ and $z \equiv \sigma$, an additional integration measure needs to be included for the change of the coordinates representation. Geometrically, such a transformation of the coordinates representations maps the parametric domains of the T&T angles from a rectangular parallelepiped to a solid cylinder. It can be further verified that determinant of the Jacobian (i.e. the additional integration measure) for the transformation of the coordinates representations is given by $\frac{1}{\theta}$. The resultant integration measure becomes $\frac{\sin\theta}{\theta}$. It follows that the volume of the entire $SO(3)$ under cylindrical

coordinates representation of the T&T angles is given by:

$$\int_{SO(3)} dV_R = \int_{\mathcal{D}^2 \times \mathcal{R}} \frac{\sin\theta}{\theta} dxdydz \tag{C.2}$$

Where $\mathcal{D}^2 \times \mathcal{R}$ represents a solid cylinder. If the integration is computed using cylindrical coordinates, Eqn. (C.2) can be rewritten as:

$$\int_{SO(3)} dV_R = \int_0^{2\pi} \int_0^{pi} \int_0^{2\pi} \frac{\sin\theta}{\theta} \theta d\phi d\theta d\sigma = 8\pi^2 \tag{C.3}$$

Although Eqns. (C.1) and (C.3) are equivalent for the volume computation of $SO(3)$, they possess different geometrical meanings. Equation (C.1) is associated with the Cartesian coordinates representation of the T&T angles, while Equation (C.3) is associated with the Cylindrical coordinates representation of the T-&-T angles. In Eqn. (C.3), the terms $\frac{\sin\theta}{\theta}$ and $\theta d\phi d\theta d\sigma$ represent the integration measure and the differential volume element, respectively.

Equations (C.2) and (C.3) also indicate that the integration measure becomes singular when θ approaches 0 or π. However, with strategic selection of the cylindrical coordinates representation for T&T angles, singularity point at $\theta = 0$ can be avoided. This is a significant feature for the numerical volume computation of $SO(3)$ through its parametric domains.

With the equivalent integration measure derived for the cylindrical coordinates representation of T-&-T angles, the integration or convolution of a rotation-dependant function $f(R)$ over a set of rotations $S \in SO(3)$ in the T-&-T angles domain is given by:

$$\int_{R \in S} f(R) dV_R = \int \int \int_{\phi,\theta,\sigma \in Q_t} f(R\{\phi,\theta,\sigma\}) \frac{\sin\theta}{\theta} \theta d\phi d\theta d\sigma \tag{C.4}$$

Where Q_t denotes the parameter space of the T-&-T angles (with cylindrical coordinates representation), i.e., a subset of the solid cylinder.

After the finite-partition of the solid cylinder, the orientation workspace for a set of rotations $S \in SO(3)$ can be numerically computed as:

$$\int_{R \in S} dV_R \approx V_t \sum \frac{\sin\theta_{ijk}}{\theta_{ijk}} \tag{C.5}$$

Where v_t is the unit volume of the equi-volumetric partition scheme in the cylindrical coordinates representation of the T-&-T angles. Consequently, Eqn. (C.4) can be written as:

$$\int_{R \in S} f(R) dV_R \approx V_t \sum f(R\{\phi_{ijk}, \theta_{ijk}, \sigma_{ijk}\}) \frac{\sin\theta_{ijk}}{\theta_{ijk}} \tag{C.6}$$

Where $(\phi_{ijk}, \theta_{ijk}, \sigma_{ijk}) \in Q_t$.

Bibliography

[1] Regional Organization for the Western Pacific (World Health Organization), "Table 12: Dependency ratios by country (on 60+ cut-off), 2005-2010", http://www.wpro.who.int/information_sources/databases/demographic_tables, 2005.

[2] C.R. Carignan and H.I. Krebs, "Telerehabilitation robotics: Bright lights, big future?", *Journal of Rehabilitation Research & Development*, vol. 43(5), pp. 695–710, 2006.

[3] M. Meng, C. Chen, P.X. Liu, and M. Rao, "E-service robot in home healthcare", in *Proceedings of IEEE/RJS International Conference on Intelligent Robots and Systems*, Kagawa University, Takamatsu, Japan, October 31–November 05 2000, pp. 832–837.

[4] R.D. Schraft, C. Schaeffer, and T. May, "Care-o-bot: The concept of a system for assisting elderly or disabled persons in home environments", in *Proceedings of the IEEE 24th Annual Conference in IECON*, Aachen, Germany, August 31–September 04 1998, vol. 4, pp. 2476–2481.

[5] B. Preising, T.C. Hsia, and B. Mittelstadt, "A literature review: Robots in medicine", *IEEE Engineering in Medicine and Biology Magazine*, vol. 10(22), pp. 13–22, 1991.

[6] E. Garcia, M.A. Jimenez, P. Gonalez De Santos, and M. Armada, "The evolution of robotics research", *IEEE Robotics & Automation Magazine*, pp. 2–15, March 2007.

[7] International Advanced Robotics Programme, "Summary report of the international advanced robotics programme joint coordinating forum annual reports for 2004", Tech. Rep., Manchester, United Kingdom, September 10–11 2004.

[8] A.M. Cook, B. Bentz, N. Harbottle, C. Lynch, and B. Miller, "School-based use of a robotic arm system by children with disabilities", *IEEE Transactions on Neural Systems and Rehabilitation Engineering*, vol. 13(4), pp. 452–460, 2005.

[9] World Health Organization, "Concept paper: World report on disability and rehabilitation", http://www.who.int/disabilities/publications/dar_world_report_concept_note.pdf, 2006.

[10] H. Kwee, J. Quaedackers, E. van de Bool, L. Theeuwen, and L. Speth, "Pocus project: Adapting the control of the manus manipulator for persons with cerebral palsy", in *Proceedings of International Conference on Rehabilitation Robotics*, Stanford, CA, July 1–2 1999, pp. 106–114.

[11] G.R.B.E. Romer, H.J.A. Stuyt, and A. Peters, "Cost-savings and economic benefits due to the assistive robotic manipulator (ARM)", in *Proceedings of IEEE International Conference on Rehabilitation Robotics*, Chicago, IL, USA, June 28–July 01 2005.

[12] R.M. Alqasemi, E.J. McCaffrey, K.D. Edwards, and R.V. Dubey, "Analysis, evaluation and development of wheelchair-mounted robotic arms", in *Proceedings of IEEE International Conference on Rehabilitation Robotics*, Chicago, IL, USA, June 28–July 01 2005.

[13] M. Topping and J. Smith, "The development of handy 1, a robotic system to assist the severely disabled", in *Proceedings of International Conference on Rehabilitation Robotics*, Stanford, CA, July 1–2 1999, pp. 244–249.

[14] H.I. Krebs, J.J. Palazzolo, L. Dipietro, M. Ferraro, J. Krol, K. Rannekleiv, B. T. Volpe, and N. Hogan, "Rehabilitation robotics: Performance-based progressive robot-assisted therapy", *Autonomous Robots*, vol. 15, pp. 7–20, 2003.

[15] M.M. Lusardi and C.C. Nielsen, *Orthotics and Prosthetics in Rehabilitation*, Butterworth Heinemann, 2000.

[16] N. G. Tsagarakis and D. G. Caldwell, "Development and control of a 'soft-actuated' exoskeleton for use in physiotherapy and training", *Autonomous Robots*, vol. 15, pp. 21–33, 2003.

[17] K. Kiguchi, T. Tanaka, K. Watanabe, and T. Fukuda, "Design and control of an exoskeleton system for human upper-limb motion assist", in *Proceedings of IEEE/ASME International Conference on Advanced Intelligent Mechatronics*, Kobe, Japan, July 20–24 2003.

[18] K. Homma, O. Fukuda, J. Sugawara, Y. Nagata, and M. Usuba, "A wire-driven leg rehabilitation system: Development of a 4-dof experimental system", in *Proceedings of 2003 IEEE/ASME International Conference on Advanced Intelligent Mechatronics*, Kobe, Japan, 2003.

[19] D. Surdilovic and R. Bernhardt, "String-man: A new wire robot for gait rehabilitation", in *Proceedings of International Conference on Robotics and Automation*, New Orleans, LA, USA, 2004.

[20] M. Bernhardt, M. Frey, G. Colombo, and R. Riener, "Hybrid force-position control yields cooperative behaviour of the rehabilitation robot LOKOMAT", in *Proceedings of IEEE International Conference on Rehabilitation Robotics*, Chicago, IL, USA, June 28–July 01 2005.

[21] Y. Takahashi, T. Suzuki, Y. Obuchi, K. Kusakabe, K. Takahashi, and T. Sakamoto, "Evaluations of human physical burdens when using transfer aid robotic system", in *Proceedings of SICE Annual Conference in Sapporo*, Hokkaido, Japan, August 4–6 2004.

[22] B. Robins, P. Dickerson, and K. Dautenhahn, "Robots as embodied beings- interactionally sensitive body movements in interactions among autistic children and a robot", in *Proceedings of IEEE International Workshop on Robots and Human Interactive Communication*, Nashville, TN, USA, August 13–15 2005, pp. 54–59.

[23] C-G. Kang, E-J. Park, I-K. Son, Y-W. Kim, and K-S. Ryu, "Conceptual design for robotic arm wrestling", in *Proceedings of IEEE Conference on Robotics, Automation and Mechatronics*, Singapore, December 1–3 2004.

[24] N. Roy, G. Baltus, D. Fox, F. Gemperle, J. Goetz, T. Hirsch, D. Margaritis, M. Montemerlo, J. Pineau, J. Schulte, and S. Thrun, "Towards personal service robots for the elderly", in *Proceedings of Workshop on Interactive Robots and Entertainment*, Pittsburgh, PA, 2000.

[25] B. Graf, M. Hans, J. Kubacki, and R.D. Schraft, "Robotic home assistant care-o-bot II", in *Proceedings of the Second Joint Meeting of the IEEE Engineering in Medicine and Biology Society and the Biomedical Engineering Society*, Houston, Texas, October 23–26 2002.

[26] J. Pineau, M. Montemerlo, M. Pollack, N. Roy, and S. Thrun, "Towards robotic assistants in nursing homes: Challenges and results", *Robotics and Autonomous Systems*, vol. 42, pp. 271–281, 2003.

[27] C. Balaguer, A. Gimenez, A.J. Huete, A.M. Sabatini, M. Topping, and G. Bolmsjo, "The mats robot: Service climbing robot for personal assistance", *IEEE Robotics & Automation Magazine*, pp. 51–58, March 2006.

[28] T. Asfour and R. Dillmann, "Human-like motion of a humanoid robot arm based on a closed-form solution of the inverse kinematics problem", in *Proceedings of 2003*

IEEE/RSJ International Conference on Intelligent Robots and Systems, Las Vegas, Nevada, October 27–31 2003, pp. 1407–1412.

[29] M. Zinn, O. Khatib, and B. Roth, "A new actuation approach for human friendly robot design", in *Proceedings of IEEE International Conference on Robotics and Automation*, New Orleans, LA, April 26–May 01 2004.

[30] S.-S. Yoon, S. Kang, S.-J. Kim, Y.-H. Kim, M. Kim, and C.-W. Lee, "Safe arm design with mr-based passive compliant joints and visco-elastic covering for service robot applications", in *Proceedings of 2003 IEEE/RSJ International Conference on Intelligent Robots and Systems*, Las Vegas, Nevada, October 27–31 2003, pp. 2191–2196.

[31] S.-H. Jeong, T. Takahashi, and E. Nakano, "A safety service manipulator system: The reduction of harmful forces by a controllable torque limiter", in *Proceedings of 2004 IEEE/RSJ International Conference on Intelligent Robots and Systems*, Sendai, Japan, September 28–October 02 2004, pp. 162–167.

[32] B. Tondu, S. Ippolito, J. Guiochet, and A. Daidie, "A seven-degrees-of-freedom robot-arm driven by pneumatic artificial muscles for humanoid robots", *The International Journal of Robotics Research*, vol. 24(4), pp. 257–274, 2005.

[33] Z.Z. Bien and H.-E. Lee, "Effective learning system techniques for human-robot interaction in service environment", *Knowledge-Based Systems*, (Article in press) 2007.

[34] K. Tanie, "Human friendly robotics", in *Proceedings of the 6th International Symposium on Living with Robots*, Tokyo, Japan, October 4–5 2004, pp. 16–22.

[35] Q. Meng and M.H. Lee, "Design issues for assistive robotics for the elderly", *Advanced Engineering Informatics*, vol. 20, pp. 171–186, 2006.

[36] R. Bischoff and V. Graefe, "Design principles for dependable robotic assistants", *International Journal of Humanoid Robots*, vol. 1(1), pp. 95–125, 2004.

[37] K. Kawamura, R.T. Pack, M. Bishay, and M. Iskarous, "Design philosophy for service robots", *Robotics & Autonomouc Systems*, vol. 18, pp. 109–116, 1996.

[38] B. Robins, K. Dautenhahn, R. te Boerkhorst, and A. Billard, "Robots as assistive technology - does appearance matter?", in *Proceedings of the 13th IEEE International Workshop on Robot and Human Interactive Communication*, September 20–22 2004, pp. 277–282.

[39] A. Hemami, "Studies on a lightwieght and flexible robot manipulator", *Robotics*, vol. 1, pp. 27–36, 1985.

[40] H. Iwata, H. Hoshino, Y. Adachi, and S. Sugano, "Robot arm surface covers for physical interference adapting motion", in *Proceedings of 1999 IEEE/ASME International Conference on Advanced Intelligent Mechatronics*, Atlanta, USA, September 19–23 1999.

[41] B.S. Dhillon and A.R.M. Fashandi, "Safety and reliability assessment techniques in robotics", *Robotica*, vol. 15, pp. 701–708, 1997.

[42] Y. Yamada, K. Suita, K. Imai, H. Ikeda, and N. Sugimoto, "A failure-to-safety robot system for human-robot-coexistance", *Robotics and Autonomous Systems*, vol. 18, pp. 283–291, 1996.

[43] J.C. Perry and J. Rosen, "Design of a 7 dof upper-limb powered exoskeleton", in *Proceedings of first IEEE/RAS-EMBS International Conference on Biomedical Robotics and Biomechatronics*, Tuscany, Italy, February 20–22 2006.

[44] L. Zollo, C. Laschi, G. Teti, B. Siciliano, and P. Dario, "Functional compliance in the control of a personal robot", in *Proceedings of 2000 IEEE/RSJ International Conference on Intelligent Robots and Systems*, Hawaii, USA, October 29–November 03 2001, pp. 2221–2226.

[45] R. Colbaugh, H. Seraji, and K. Glass, "Direct adaptive impedence control of robot manipulators", *Journal of Robotic Systems*, vol. 2(10), pp. 217–248, 1993.

[46] V.J. Traver, A.P. del Pobil, and M. Perez-Francisco, "Making service robots human-safe", in *Proceedings of 2000 IEEE/RSJ International Conference on Intelligent Robots and Systems*, Takamatsu, Japan, October 30–November 05 2000, pp. 696–701.

[47] S. Tadokoro, Y. Ishikawa, T. Takebe, and T. Takamori, "Stochastic prediction of human motion and control of robots in the service of human", in *Proceedings of IEEE International Conference on Systems, Man and Cybernetics*, France, October 17–20 1993, pp. 503–508.

[48] Y. Wakite, S. Hirai, T. Hori, R. Takada, and M. Kakikura, "Realization of safety in a coexistent robotic system by information sharing", in *Proceedings of IEEE International Conference on Robotics and Automation*, Leuven, Belgium, May 1998, pp. 3474–3479.

[49] P. Zhang, R. Lu, and J. Zhang, "Reliability modeling and analysis of service-oriented robot management system", in *Proceedings of IEEE Asia-Pacific Conference on Services Computing*, Guangdong, China, December 12–15 2006.

[50] G. Simmons and Y.Demiris, "Biologically inspired optimal robot arm control with signal-dependent noise", in *Proceedings of IEEE/RSJ International Conference on Intelligent Robots and Systems*, Sendai, Japan, 2004, pp. 491–496.

[51] M.B. Pritts and C.D. Rahn, "Design of an artificial muscle continuum robot", in *Proceedings of*, New Orleans, LA, April 2004, pp. 4742–4746.

[52] E. Tatlicioglu, I.D. Walker, and D.M. Dawson, "Dynamic modeling for planar extensible continuum robot manipulators", in *Proceedings of IEEE International Conference on Robotics & Automation*, Roma, Italy, April 2007, pp. 1357–1362.

[53] R. Buckingham et al, "Snake-arm robots: a new approach to aircraft assembly", in *Proceedings of SAE Aerotech Congress*, Los Angeles, California, September 2007, vol. 1.

[54] G. Yang, H.L. Ho, W. Chen, W. Lin, and M.S. Kurbanhusen, "A haptic device wearable on a human arm", in *Proceedings of IEEE Conference on Robotics, Automation And Mechatronics*, Singapore, 2004, pp. 243–248.

[55] M.A. Lemay and P.E. Crago, "A dynamic model for simulating movements of the elbow, forearm and wrist", *Journal Of Biomechanics*, vol. 29, pp. 1319–1330, 1996.

[56] H. Graichen, T. Stammberger, H. Bonel, K.-H. Englmeier, M. Reiser, and F. Eckstein, "Glenohumeral translation during active and passive elevation of the shoulder-A 3D open-MRI study", *Journal Of Biomechanics*, vol. 33, pp. 609–613, 2000.

[57] K.R. Kaufman and K.-N. An, *Joint-Articulating Surface Motion in Biomechanics: Principles and Applications*, vol. 3, CRC Press, 2003.

[58] J. Lenarcic and M. Stanisic, "A humanoid shoulder complex and the humeral pointing kinematics", *IEEE Transactions on Robotics and Automation*, vol. 19, pp. 499–506, 2003.

[59] H.E.J. Veeger, "The position of the rotation center of the glenohumeral joint", *Journal Of Biomechanics*, vol. 33, pp. 1711–1715, 2000.

[60] A. Ming and T. Higuchi, "Study on multiple degree-of-freedom positioning mechanism using wires (part 1) – concept, design and control", *International Journal of Japan Social Engineering*, vol. 28(2), pp. 131–138, 1994.

[61] J.-J. Park, B.-S. Kim, J.-B. Song, and H.-S. Kim, "Safe link mechanism based on passive compliance for safe human-robot collision", in *Proceedings of IEEE International Conference on Robotics & Automation*, Roma, Italy, April 10–14 2007, pp. 1152–1157.

[62] B.-S. Kim, J.-J. Park, and J.-B. Song, "Double actuation unit with planetary gear train for a safe manipulator", in *Proceedings of IEEE International Conference on Robotics & Automation*, Roma, Italy, April 10–14 2007, pp. 1146–1151.

[63] L.W. Tsai, *Robot Analysis – The Mechanics of Serial and Parallel Manipulators*, A Wiley-Interscience Publication, 1999.

[64] S.K. Mustafa, G. Yang, S.H. Yeo, W. Lin, and C.B. Bang, "Development of a bio-inspired wrist prosthesis", in *Proceedings of IEEE Conference on Robotics, Automation And Mechatronics*, Bangkok, Thailand, July 07–09 2006, pp. 732–737.

[65] S.K. Mustafa, G. Yang, S.H. Yeo, and W. Lin, "Optimal design of a bio-inspired anthropocentric shoulder rehabilitator", *Journal of Applied Bionics and Biomechanics*, vol. 3(3), pp. 199–208, 2006.

[66] J.-P. Merlet, *Parallel Robots*, vol. 74, Kluwer Academic Publishers, 2000.

[67] C.M. Gosselin and J. Sefrioui, "Polynomial solutions for the direct kinematic problems of planar three-degree-of-freedom parallel manipulators", in *Fifth International Conference on Robots in Unstructured Environments, 91 ICAR*, June 19–22 1991, vol. 2, pp. 1124–1129.

[68] W. Lin, M. Griffis, and J. Duffy, "Forward displacement analyses of the 4-4 stewart platforms", *ASME Journal of Mechanical Design*, vol. 114, pp. 444–450, 1992.

[69] K.C. Cheok, J.L. Overholt, and R.R. Beck, "Exact methods for determining the kinematics of a stewart platform using additional displacement sensors", *Journal of Robotic Systems*, vol. 10(5), pp. 689–707, 1993.

[70] J.P. Merlet, "Closed-form resolution of the direct kinematics of parallel manipulators using extra sensors data", in *Proceedings of IEEE Conference on Robotics and Automation*, Atlanta, Georgia, USA, 1993, pp. 200–204.

[71] R.L. Williams II, "Cable-suspended haptic interface", *Journal of Virtual Reality*, vol. 3(3), pp. 13–21, 1998.

[72] J.-P. Merlet, "Direct kinematics of parallel manipulators", *IEEE Transactions on Robotics and Automation*, vol. 9(6), pp. 842–846, 1993.

[73] A. Ming, M. Kajitani, and T. Higuchi, "On the design of wire parallel mechanism", *International Journal of Japan Social Engineering*, vol. 29(4), pp. 337–342, 1995.

[74] A. Ming and T. Higuchi, "Study on multiple degree-of-freedom positioning mechanism using wires (part 2) – development of a planar completely restrained positioning mechanism", *International Journal of Japan Social Engineering*, vol. 28(3), pp. 235–242, 1994.

[75] R.C. Murray, Z. Li, and S.S. Sastry, *A Mathematical Introduction to Robotic Manipulation*, CRC Press, 1994.

[76] J.M. Selig, *Geometric Fundamentals of Robotics*, Springer, 2005.

[77] I.A. Bonev and J. Ryu, "A new approach to orientation workspace analysis of 6-dof parallel manipulators", *Mechanism and Machine Theory*, vol. 36, pp. 15–28, 2001.

[78] C. Innocenti and V. Parenti-Castelli, "Echelon form solution of direct kinematics for the general fully-parallel spherical wrist", *Mechanism and Machine Theory*, vol. 28, pp. 553–561, 1993.

[79] P. Ji and H. Wu, "Algebraic solution to forward kinematics of a 3-dof spherical parallel manipulator", *Journal of Robotic Systems*, vol. 18, pp. 251–257, 2001.

[80] S.-K. Song and D.-S. Kwon, "Efficient formulation approach for the forward kinematics of the 3-6 stewart-gough platform", in *Proceedings of 2001 IEEE/RSJ International Conference on Intelligent Robots and Systems*, Maui, Hawaii, October 2001.

[81] F. Thomas, E. Ottaviano, L. Ros, and M. Ceccarelli, "Coordinate-free formulation of a 3-2-1 wire-based tracking device using cayley-menger determinants", in *Proceedings of IEEE International Conference on Robotics & Automation*, 2003, pp. 255–363.

[82] F. Thomas, E. Ottaviano, and M. Ceccarelli, "Performance analysis of a 3-2-1 pose estimation device", *IEEE Transaction on Robotics*, vol. 21(3), pp. 288–297, 2005.

[83] E. Ottaviano and M. Ceccarelli, "Numerical and experimental characterization of singularities of a six-wire parallel architecture", *International Journal ROBOTICA*, vol. 25, pp. 315–324, 2007.

[84] D. Tolani, A. Goswami, and N.I. Badler, "Real-time inverse kinematics techniques for anthropomorphic limbs", *Graphical Models*, vol. 62, pp. 353–388, 2000.

[85] J.U. Korein, *A Geometrical Investigation of Reach*, The MIT Press, 1984.

[86] R. Verhoeven, M. Hiller, and S. Tadokoro, "Workspace, stiffness, singularities and classification of tendon-driven stewart platforms", in *International Symposium on Advances in Robot Kinematics*, Strobl, Austria, 1998, pp. 105–114.

[87] R. Verhoeven, M. Hiller, and S. Tadokoro, "Workspace of tendon-driven stewart platforms: Basics, classification, details on the planar 2-dof class", in *International Conference on Motion and Vibration Control MOVIC*, 1998, vol. 3, pp. 871–876.

[88] M. Gouttefarde, J.-P. Merlet, and D. Daney, "Wrench-feasible workspace of parallel cable-driven mechanisms", in *Proceedings of IEEE International Conference on Robotics & Automation*, Rome, Italy, April 10–14 2007, pp. 1492–1497.

[89] A. Fattah and S.K. Agrawal, "Workspace and design analysis of cable-suspended planar parallel robots", in *Proceedings of ASME 2002 Design Engineering Technical Conferences*, Montreal, Canada, Sep 29 – Oct 2 2002, pp. 1095–1103.

[90] C.M. Gosselin and G. Barrette, "Kinematic analysis of planar parallel mechanisms actuated with cables", in *Proceedings of Symposium on Mechanisms, Machines and Mechatronics*, Quebec, Canada, June 1 2001, pp. 41–42.

[91] I. Ebert and P.A. Voglewede, "On the connections between cable-driven robots, parallel manipulators and grasping", in *Proceedings of IEEE International Conference on Robotics & Automation*, New Orleans, LA, April 26–May 01 2004, pp. 4521–4526.

[92] V.-D. Nguyen, "Constructing force-closure grasps", *The International Journal of Robotics Research*, vol. 7(3), pp. 3–16, 1988.

[93] A. Fattah and S.K. Agrawal, "Design of cable-suspended planar parallel robots for an optimal workspace", in *Proceedings of the Workshop on Fundamental Issues and Future Research Directions for Parallel Mechanisms and Manipulators*, Quebec City, Canada, October 3–4 2002, pp. 195–202.

[94] J. Pusey, A. Fattah, S.K. Agrawal, E. Messina, and A. Jacoff, "Design and workspace analysis of a 6-6 cable-suspended parallel robot", in *Proceedings of IEEE/RSJ International Conference on Intelligent Robots and Systems*, Las Vegas, Nevada, October 27–31 2003, pp. 2090–2095.

[95] A.T. Riechel and I. Ebert-Uphoff, "Force-feasible workspace analysis for underconstrained, point-mass cable robots", in *Proceedings of IEEE Conference on Robotics & Automation*, New Orleans, LA, April 26–May 01 2004, pp. 4956–4962.

[96] P. Bosscher and I. Ebert-Uphoff, "Wrench-based analysis of cable-driven robots", in *Proceedings of IEEE International Conference on Robotics & Automation*, New Orleans, LA, April 26–May 01 2004, pp. 4950–4955.

[97] P. Lafourcade and M. Llibre, "First step toward a sketch-based design methodology for wire-driven manipulators", in *Proceedings of IEEE/ASME International Conference*

on Advanced Intelligent Mechatronics, Port Island, Kobe, Japan, July 20–24 2003, pp. 143–148.

[98] D. Zlatanov and S.K. Agrawal ans C. Gosselin, "Convex cones in screw spaces", *Mechanism and Machine Theory*, vol. 40, pp. 710–727, 2005.

[99] C.B. Pham, S.H. Yeo, G. Yang, M.S. Kurbanhusen, and I.M. Chen, "Force-closure workspace analysis of cable-driven parallel mechanisms", *Journal of Mechanism and Machine Theory*, vol. 41, pp. 53–69, 2006.

[100] Hotoshi Kino, "Principle of orthogonalization for completely restrained parallel wire driven robot", in *Proceedings of IEEE/ASME International Conference on Advanced Intelligent Mechatronics*, Kobe, Japan, July 20–24 2003, pp. 509–514.

[101] S. Kawamura, W. Choe, S. Tanaka, and S.R. Pandian, "Development of an ultrahigh speed robot falcon using wire drive system", in *Proceedings of IEEE Conference on Robotics & Automation*, Aichi, Japan, 1995, vol. 1, pp. 215–220.

[102] S. Kawamura, M. Ida, T. Wada, and J.L. Wu, "Development of a virtual sports machine using a wire drive system - a trial of virtual tennis", in *Proceedings of IEEE/RSJ International Conference on Intelligent Robots and Systems*, Pennsylvania, USA, August 05–09 1995, pp. 111–116.

[103] W. Choe, H. Kino, K. Katsuta, and S. Kawamura, "A design of parallel wire driven robots for ultrahigh speed motion based on stiffness analysis", in *Proceedings of Japan/USA Symposium on Flexible Automation*, Boston, MA, 1996, vol. 1, pp. 159–166.

[104] T. Morizono, K. Kurahashi, and S. Kawamura, "Analysis and control of a force display system driven by parallel wire mechanism", *Robotica*, vol. 16, pp. 551–563, 1998.

[105] S. Behzadipour and A. Khajepour, "Stiffness of a cable-based parallel manipulators with application to stability analysis", *Journal of Mechanical Design*, vol. 128, pp. 303–310, 2006.

[106] M.M. Svinin, K. Ueda, and M. Uchiyama, "On the stability conditions for a class of parallel manipulators", in *Proceedings of IEEE International Conference on Robotics & Automation*, San Francisco, CA, April 2000, pp. 2386–2391.

[107] M.M. Svinin, S. Hosoe, and M. Uchiyama, "On the stiffness and stability of gough-stewart platforms", in *Proceedings of IEEE International Conference on Robotics & Automation*, Seoul, Korea, May 21–26 2001, pp. 3268–3273.

[108] O. Ma and J. Angeles, "Architecture singularities of platform manipulators", in *Proceedings of IEEE International Conference on Robotics & Automation*, Sacramento, California, April 1991, pp. 1542–1547.

[109] L.-W. Tsai and S. Joshi, "Kinematic analysis of 3-dof position mechanisms for use in hybrid kinematic machines", *Journal of Mechanical Design*, vol. 124, pp. 245–253, 2002.

[110] G. Yang, H.L. Ho, L. Wei, and I.-M. Chen, "A differential geometry approach for the workspace analysis of spherical parallel manipulators", in *Proceedings of the 11th World Congress in Mechanism and Machine Science*, Tianjin, China, April 1–4 2003, vol. 4, pp. 2060–2065.

[111] C.M. Gosselin and J. Angeles, "A global performance index for the kinematic optimization of robotic manipulators", *Journal of Mechanical Design*, vol. 113, pp. 220–225, 1991.

[112] P. Bosscher and I. Ebert-Uphoff, "A stability measure for underconstrained cable-driven robots", in *Proceedings of IEEE International Conference on Robotics & Automation*, New Orleans, LA, April 26–May 01 2004, pp. 4943–4949.

[113] R. Verhoeven and M. Hiller, "Tension distribution in tendon-based stewart platforms", in *Proceedings of the International Symposium on Advances in Robot Kinematics*, Caldes de Malavella, Spain, 2002.

[114] E. Stump and R.V. Kumar, "Workspace delineation of cable-actuated parallel manipulators", in *Proceedings of 2004 ASME International Design Engineering Technical Conference*, Salt Lake City, UT, September 2004, vol. 2B, pp. 1303–1310.

[115] R. Verhoeven and M. Hiller, "Estimating the controllable workspace of tendon-based stewart platforms", in *Proceedings of the International Symposium on Advances in Robot Kinematics*, Portoroz, Slovenia, 2000, pp. 277–284.

[116] S.-R. Oh and S.K. Agrawal, "Generation of feasible set points and control of a cable robot", *IEEE Transactions on Robotics*, vol. 22(3), pp. 551–558, 2006.

[117] S.-R. Oh and S.K. Agrawal, "The feasible workspace analysis of a set point control for a cable-suspended robot with input constraints and disturbance", *IEEE Transactions on Control Systems Technology*, vol. 14(4), pp. 735–742, 2006.

[118] M. Ceccarelli, *Fundamentals of Mechanics of Robotic Manipulation*, Kluwer Academic Publishers, 2004.

[119] A.B. Alp and S.K. Agrawal, "Cable-suspended robots: Design, planning and control", in *Proceedings of IEEE International Conference on Robotics & Automation*, Washington, DC, May 2002, pp. 4275–4280.

[120] C.M. Gosselin and J. Wang, "Kinematic analysis and design of cable-driven spherical parallel mechanisms", in *Proceedings of 15th CISM-IFToMM Symposium on Robot Design, Dynamics and Control*, Montreal, Canada, June 14–18 2004.

[121] C.B. Pham, S.H. Yeo, and G. Yang, "Tension analysis of cable-driven parallel mechanisms", in *Proceedings of IEEE/RSJ International Conference on Intelligent Robots and Systems*, Edmonton, Alberta, Canada, August 2–6 2005, pp. 2601–2606.

[122] J.M. MacCarthy, *Introduction to Theoretical Kinematics*, MIT Press, Cambridge, 1990.

[123] F.C. Park and B. Ravani, "Smooth invariant interpolation of rotations", *ACM Transactions on Graphics*, vol. 16(3), pp. 277–295, 1997.

[124] G.S. Chirikjian and A.B. Kyatkin, *Engineering Applications of Noncommutative Harmonic Analysis with Emphasis on Rotation and Motion Groups*, CRC Press LLC, Boca Raton, 2000.

[125] G. Yang, W. Lin, S.K. Mustafa, I.-M Chen, and S.H. Yeo, "Numerical orientation workspace analysis with different parameterization methods", in *Proceedings of IEEE Conference on Robotics, Automation And Mechatronics*, Bangkok, Thailand, July 07–09 2006, pp. 720–725.

[126] R.T. Rockafella, *Convex Analysis*, Princeton University Press, 1970.

[127] G. Yang, W. Lin, M.S. Kurbanhusen, C.B Pham, and S.H. Yeo, "Kinematic design of a 7-dof cable-driven humanoid arm: a solution-in-nature approach", in *Proceedings of 2005 IEEE/ASME International Conference on Advanced Intelligent Mechatronics*, California, USA, July 24–28 2005.

[128] Y. Nakamura, *Advanced Robotics – Redundancy and Optimization*, Addison-Wesley Publishing Company, 1991.

[129] J. Duffy, *Statics and Kinematics with Applications to Robotics*, Cambridge University Press, 1996.

[130] N. Hamilton and K. Luttgens, *Kinesiology: Scientific Basis of Human Motion*, McGraw Hill, 2002.

[131] G. Strang, *Linear Algebra and its Applications*, Academic Press, New York, 1976.

[132] C.B. Pham, S.H. Yeo, and G. Yang, "Workspace analysis and optimal design of cable-driven planar parallel manipulators", in *Proceedings of IEEE Conference on Robotics, Automation And Mechatronics*, Singapore, December 1–3 2004, pp. 219–224.

[133] A. Fattah and S.K. Agrawal, "On the optimal design and workspace analysis of planar cable-suspended robots", *Journal of Mechanical Design*, vol. 127, pp. 1021–1028, 2005.

[134] Y. Li and Q. Xu, "Ga-based multi-objective optimal design of a planar 3-dof cable-driven parallel manipulator", in *Proceedings of IEEE International Conference on Robotics and Biomimetics*, Kuming, China, December 9–14 2006.

[135] S. Pheasant, *Ergonomics: Standards and Guidelines for Designers*, British Standards Institution, 1987.

[136] K. Deb, *Optimization for Engineering Design: Algorithms and Examples*, Prentice-Hall, New Delhi, 1998.

[137] S. Tadokoro, S. Nishioka, T. Kimura, M. Hattori, T. Takamori, and K. Maeda, "On fundamental design of wire configurations of wire-driven parallel manipulators with redundancy", in *Japan/Usa Symposium on Flexible Automation*, 1996, vol. 1, pp. 151–158.

[138] R.L. Williams II, P. Gallina, and J. Vadia, "Planar translational cable-direct-driven robots", *Journal of Robotic Systems*, vol. 20(3), pp. 107–120, 2003.

[139] S.-R. Oh and S.K. Agrawal, "Cable suspended planar robots with redundant cables: Controllers with positive tensions", *IEEE Transactions of Robotics*, vol. 21(3), pp. 457–465, 2005.

[140] S.-R. Oh, K. Mandala, S.K. Agrawal, and J. Albus, "Dynamic modeling and robust controller design of a 2-stage parallel cable robot", *Multibody System Dynamics*, vol. 13(4), pp. 385–399, 2005.

[141] A.L. Window, *Strain Gauge Technology*, Elsevier Applied Science, 1992.

[142] R.L. Hannah, S.E. Reed, and C.T. Bethel, *Strain Gage Users' Handbook*, Society for Experimental Mechanics, 1992.

[143] B.W. Mooring, Z.S. Roth, and M.R. Driels, *Fundamentals of Manipulator Calibration*, John Wiley & Sons, Inc., 1991.

[144] C.W. Wampler, J.M. Hollerbach, and T. Aria, "An implicit loop method for kinematic calibration and its application to closed-chain mechanisms", *IEEE Transactions on Robotics and Automation*, vol. 11(5), pp. 710–724, 1995.

[145] A.J. Patel and K.F. Ehmann, "Calibration of a hexapod macine tool using a redundant leg", *International Journal of Machine Tools & Manufacture*, vol. 40, pp. 489–512, 2000.

[146] P. Renaud, N. Andreff, P. Martinet, and G. Gogu, "Kinematic calibration of parallel mechanisms: A novel approach using leg observation", *IEEE Transactions on Robotics*, vol. 21(4), pp. 529–538, 2005.

[147] D. Cong, D. Yu, and J. Han, "Kinematic calibration of parallel robots using cmm", in *Proceedings of the Sixth World Congress on Intelligent Control and Automation*, Dalian, China, June 21–23 2006, pp. 8514–8518.

[148] P. Maurine and E. Dombre, "A calibration procedure for the parallel robot delta 4", in *Proceedings of IEEE International Conference on Robotics & Automation*, 1996, pp. 975–980.

[149] A. Nahvi, J.M. Hollerbach, and V. Hayward, "Calibration of parallel robot using multiple kinematic closed loops", in *Proceedings of IEEE International Conference on Robotics & Automation*, San Diego, CA, USA, 1994, pp. 407–412.

[150] H. Zhuang, O. Masory, and J. Yan, "Kinematic calibration of stewart platforms using pose measurements obtained by a single theodolite", in *Proceedings of IEEE/RJS International Conference on Intelligent Robots and Systems*, August 1995, pp. 329–335.

[151] S. Besnard and W. Khalil, "Calibration of parallel robots using two inclinometers", in *Proceedings of IEEE International Conference on Robotics & Automation*, Detroit, Michigan, May 1999, pp. 1758–1763.

[152] D. Daney, N. Andreff, G. Chabert, and Y. Papegay, "Interval method for calibration of parallel robots: Vision-based experiments", *Mechanism and Machine Theory*, vol. 41, pp. 929–944, 2006.

[153] A. Rauf and J. Ryu, "Fully autonomous calibration of parallel manipulators by imposing position constraint", in *Proceedings of IEEE International Conference on Robotics & Automation*, Seoul, Korea, May 21–26 2001, pp. 2389–2394.

[154] J. Ryu and A. Rauf, "A new method for fully autonomous calibration of parallel manipulators using a constraint link", in *Proceedings of IEEE/ASME International Conference on Advanced Intelligent Mechatronics*, Como, Italy, July 08–12 2001, pp. 141–146.

[155] P. Last, C. Budde, and J. Hesselbach, "Self-calibration of the hexa-parallel-structure", in *Proceedings of IEEE International Conference on Automation Science and Engineering*, Edmonton, Canada, August 01–02 2005, pp. 393–398.

[156] G. Yang, I.-M. Chen, W.K. Lim, and S.H. Yeo, "Self-calibration of three-legged modular reconfigurable parallel robots based on leg-end distance errors", *Robotica*, vol. 19, pp. 187–198, 2001.

[157] H. Zhuang, "Self-calibration of parallel mechanisms with a case study on stewart platforms", *IEEE Transactions on Robotics and Automation*, vol. 13(3), pp. 387–397, 1997.

[158] F.C. Park, "Computational aspect of manipulators via product of exponential formula for robot kinematics", *IEEE Transaction on Automation Control*, vol. 39(9), pp. 643–647, 1994.

[159] G. Yang, I.-M. Chen, W.K. Lim, , and S.H. Yeo, "Simultaneous base and tool calibration of a self-calibrated modular parallel robot", in *Proceedings of the 6th International Conference on Control, Automation, Robotics and Vision*, Singapore, 2000.

[160] S.K. Mustafa, G. Yang, S.H. Yeo, and W. Lin, "Self-identification of the joint centre of a cable-driven shoulder rehabilitator", in *Proceedings of IEEE International Conference on Robotics & Automation*, Roma, Italy, April 10–14 2007, pp. 3767–3772.

[161] I.A. Bonev and C.M. Gosselin, "Singularity loci of spherical parallel mechanisms", in *Proceedings of IEEE International Conference on Robotics & Automation*, Barcelona, Spain, April 2005, pp. 2968–2973.